A Mechanistic Study of the Formation of Peroxide in Solutions Containing the Uranyl(VI) Ion

A thesis submitted to The University of Manchester for the degree of Doctor of Philosophy in the Faculty of Engineering and Physical Sciences

2014

CHRISTOPHER PAUL GREEN

SCHOOL OF CHEMISTRY

Table of Contents

Word Count: 101,153

Table of Equations

$$V_{ee}[\rho(\mathbf{r})]=\frac{1}{2}\int\int\frac{\rho(\mathbf{r}_1)\rho(\mathbf{r}_2)}{|\mathbf{r}-\mathbf{r}_A|}d\mathbf{r}_1 d\mathbf{r}_2 \quad (25)$$ 54

$$\rho=\sum_{i<j}^{elecctrons}\langle\chi_i|\chi_j\rangle \quad (26)$$ 54

$$E[\rho(\mathbf{r})]=\sum_{i}^{electrons}\left(\langle\chi_i|-\frac{1}{2}\nabla_i^2|\chi_i\rangle-\langle\chi_i|\sum_{A}^{nuclei}\frac{Z_A}{|\mathbf{r}_i-\mathbf{r}_A|}|\chi_i\rangle\right)+\sum_{i}^{electrons}\langle\chi_i|\frac{1}{2}\frac{\rho(\mathbf{r}')}{|\mathbf{r}_i-\mathbf{r}'|}|\chi_i\rangle+E_{xc}[\rho(\mathbf{r})] \quad (27)$$ 55

$$\hat{h}_i^{KS}=-\frac{1}{2}\nabla_i^2-\sum_{A}^{nuclei}\int\frac{Z_A}{|\mathbf{r}_i-\mathbf{r}_A|}+\int\frac{\rho(\mathbf{r}')}{|\mathbf{r}_i-\mathbf{r}'|}d\mathbf{r}'+V_{XC} \quad (28)$$ 55

$$E_{XC}[\rho(\boldsymbol{r})]=\int\rho(\boldsymbol{r})\varepsilon_{XC}[\rho(\boldsymbol{r})]d\boldsymbol{r} \quad (29)$$ 55

$$E_{XC}=\int_0^1\langle\Psi(\lambda)|V_{XC}(\lambda)|\Psi(\lambda)\rangle d\lambda \quad (30)$$ 56

$$E_{XC}=E_X^{HF}+z(E_{XC}^{DFT}-E_X^{HF}) \quad (31)$$ 57

$$E_{XC}=(1-a)E_{XC}^{DFT}+aE_X^{HF} \quad (32)$$ 58

$$E_{XC}^{B3PW91}=(1-a)E_X^{LSDA}+aE_X^{HF}+b\Delta E_X^B+E_C^{LDSA}+c\Delta E_C^{PW91} \quad (33)$$ 58

$$E_{XC}^{B3LYP}=(1-a)E_X^{LSDA}+aE_X^{HF}+b\Delta E_X^B+(1-c)E_C^{LDSA}+c\Delta E_C^{LYP} \quad (34)$$ 58

$$H_{corr}=E_r+E_t+E_v+E_e+k_BT \quad (35)$$ 65

$$S_{corr}=S_r+S_t+S_v+S_e \quad (36)$$ 65

$$f_{SC}=\frac{^1<\hat{S}^2>(UKS)}{^3<\hat{S}^2>(UKS)-^1<\hat{S}^2>(UKS)} \quad (37)$$ 72

$$^1E(SCKS)=^1E(UKS)+f_{sc}[^1E(UKS)-^3E(UKS)] \quad (38)$$ 72

$$U^{VI}O_2^{2+}\xrightarrow{h\nu}{}^*U^{VI}O_2^{2+} \quad (39)$$ 100

$$^*U^{VI}O_2^{2+}+MeOH\longrightarrow U^VO_2^{+}+{}^\bullet CH_2OH+H^+ \quad (40)$$ 100

$${}^\bullet CH_2OH+O_2\longrightarrow products \quad (41)$$ 100

$$U^VO_2^{+}+O_2\longrightarrow U^{VI}O_2^{2+}+Int \quad (42)$$ 100

$$U^VO_2^{+}+Int\xrightarrow{H^+,fast}U^{VI}O_2^{2+}+H_2O_2 \quad (43)$$ 100

$$U^VO_2^{+}+O_2\longleftrightarrow[U^VO_2(O_2)]^+ \quad (44)$$ 102

$$[U^VO_2(O_2)]^+\xrightarrow{ET}[U^{VI}O_2(O_2^\bullet)]^+ \quad (45)$$ 102

$$[U^{VI}O_2(O_2^\bullet)]^++H_3O^+\longleftrightarrow[U^{VI}O_2(HO_2^\bullet)]^{2+}+H_2O \quad (46)$$ 102

$$[U^{VI}O_2(HO_2^\bullet)]^{2+}\longleftrightarrow U^{VI}O_2^{2+}+HO_2^\bullet \quad (47)$$ 102

$$U^VO_2^{+}+HO_2^\bullet\xrightarrow{OS-ET}U^{VI}O_2^{2+}+HO_2^- \quad (48)$$ 102

$${}^\bullet O_2H+{}^\bullet O_2H\longrightarrow O_2+H_2O_2 \quad (49)$$ 103

$$\Delta E=E(\text{prod})+E(H_2O)_6-E(\text{react})-E(^SO_2(H_2O)_5) \quad (50)$$ 141

$$[U^{VI}O_2(L)H_2O]^{2+}+{}^3O_2\longrightarrow[U^{VI}O_2(L)^3O_2]^{2+}+H_2O \quad (51)$$ 142

$$[U^{VI}O_2(L)H_2O]^{2+}+{}^1O_2\longrightarrow[U^{VI}O_2(L)^1O_2]^{2+}+H_2O \quad (52)$$ 142

$$[U^VOHO(L)H_2O]^{2+}+{}^3O_2\longrightarrow[U^VOHO(L)^3O_2]^{2+}+H_2O \quad (53)$$ 143

$$^4[U^VOHO(L)(^3O_2)]^{2+}\longrightarrow[U^{VI}OHO(L)(^\bullet O_2)]^{2+} \quad (54)$$ 151

$$^2[U^VOHO(L)(^3O_2)]^{2+}\longrightarrow[U^{VI}OHO(L)(^\bullet O_2)]^{2+} \quad (55)$$ 152

$$^4[U^VOHO(L)(^3O_2)]^{2+}+H_2O\longrightarrow{}^4[U^VO_2(L)(^3O_2)]^++H_3O^+ \quad (56)$$ 155

$^4[U^VO_2(L)(^3O_2)]^+ \longrightarrow [U^{VI}O_2(L)(^\bullet O_2)]^+$ (57) 155

$^2[U^VO_2(L)(^3O_2)]^+ \longrightarrow [U^{VI}O_2(L)(^\bullet O_2)]^+$ (58) 157

$[U^VOHO(L)(O_2)]^{2+} \xrightarrow{ET} [U^{VI}OHO(L)(^\bullet O_2)]^{2+}$ (59) 161

$[U^{VI}OHO(L)(^\bullet O_2)]^{2+} + H_2O \longrightarrow [U^{VI}O_2(L)(^\bullet O_2)]^+ + H_3O^+$ (60) 161

$[U^{VI}O_2(L)(^\bullet O_2)]^+ \xrightarrow{h\nu} {}^*[U^{VI}O_2(L)(^\bullet O_2)]^+$ (61) 161

$^*[U^{VI}O_2(L)(^\bullet O_2)]^+ + H_3COH \longrightarrow [U^VOHO(L)(^\bullet O_2)]^+ + H_2\dot{C}OH$ (62) 161

$[U^VOHO(L)(^\bullet O_2)]^+ \xrightarrow{ET} [U^{VI}OHO(L)(O_2)]^+$ (63) 161

$[U^{VI}OHO(L)(O_2)]^+ + H_2O \longrightarrow [U^{VI}O_2(L)(O_2)] + H_3O^+$ (64) 161

$^1[U^VOHO(L)(^\bullet O_2)]^+ + H_2O \longrightarrow {}^1[U^{VI}O_2(^\bullet L)(^\bullet O_2)] + H_3O^+$ (65) 169

$^1[U^{VI}O_2(^\bullet L)(^\bullet O_2)] \longrightarrow {}^1[U^{VI}O_2(L)(O_2)]$ (66) 169

$^1[U^VOHO(L)(^\bullet O_2H)]^{2+} \longrightarrow$ M12a-TS (67) 172

M12a-TS $\longrightarrow [U^{VI}OHO(L)(O_2H)]^{2+}$ (68) 172

$[U^{VI}OHO(L)(O_2H)]^{2+} \longrightarrow [U^{VI}OHO(L)(O_2H)]^{2+}$ (69) 172

$[U^{VI}OHO(L)(O_2H)]^{2+} + H_2O \longrightarrow [U^{VI}O_2(L)(O_2H)]^+ + H_3O^+$ (70) 172

$^1[U^VOHO(L)(^\bullet O_2H)]^{2+} + H_2O \longrightarrow {}^1[U^VO_2(L)(^\bullet O_2H)]^+ + H_3O^+$ **(71)** 178

$^1[U^VO_2(L)(^\bullet O_2H)]^+ \longrightarrow [U^{VI}O_2(L)(O_2H)]^+$ (72) 178

$[U^{VI}O_2(L)(O_2H)]^+ \xrightarrow{reorg} [U^{VI}O_2(L)(O_2H)]^+$ (73) 178

$[U^{VI}O_2(L)(O_2H)]^+ + H_2O \longrightarrow [U^{VI}O_2(L)(O_2)] + H_3O^+$ (74) 178

$U^{VI}O_2^{2+} + MeOH \xrightarrow{h\nu} U^VO_2^+ + {}^\bullet CH_2OH + H^+$ (75) 198

$U^VO_2^+ + O_2 \longleftrightarrow [U^VO_2(O_2)]^+$ (76) 198

$[U^VO_2(O_2)]^+ \xrightarrow{ET} [U^{VI}O_2(O_2^\bullet)]^+$ (77) 198

$[U^{VI}O_2(O_2^\bullet)]^+ + H_3O^+ \longleftrightarrow [U^{VI}O_2(HO_2^\bullet)]^{2+} + H_2O$ (78) 198

$[U^{VI}O_2(HO_2^\bullet)]^{2+} + U^VO_2^+ \longleftrightarrow [(U^{VI}O_2)_2(O_2)]^{2+} + H^+$ (79) 198

$[U^{VI}O_2(HO_2^\bullet)]^{2+} \longleftrightarrow U^{VI}O_2^{2+} + HO_2^\bullet$ (80) 198

$U^VO_2^+ + HO_2^\bullet \xrightarrow{OS-ET} U^{VI}O_2^{2+} + HO_2^-$ (81) 198

$2U^{VI}O_2^{2+} + HO_2^- \longleftrightarrow [(U^{VI}O_2)_2(O_2)]^{2+} + H^+$ (82) 198

$\Delta G = -RT \ln K$ (83) 199

$pH = pK_a - \log\left(\frac{[O_2^{\bullet -}]}{[HO_2^\bullet]}\right)$ (84) 199

$[U^{VI}O_2(L)(O_2^\bullet)]^+ + H_2O \rightarrow [U^{VI}O_2(L)(H_2O)]^{2+} + O_2^{\bullet -}$ (85) 204

$O_2^{\bullet -} + H_3O^+ \longrightarrow HO_2^\bullet + H_2O$ (86) 204

$[U^{VI}O_2(L)(O_2^\bullet)]^+ + H_3O^+ \longrightarrow [U^{VI}O_2(L)(HO_2^\bullet)]^{2+} + H_2O$ (87) 206

$[U^{VI}O_2(L)(HO_2^\bullet)]^{2+} + H_2O \longrightarrow [U^{VI}O_2(L)(H_2O)]^{2+} + HO_2^\bullet$ (88) 206

$[U^{VI}O_2(L)(O_2^\bullet)]^+ + H_2O \longrightarrow [U^{VI}O_2(L)(H_2O)]^{2+} + O_2^{\bullet -}$ (89) 206

$2HO_2^\bullet \longrightarrow H_2O_2 + O_2$ (90) 208

$k = \frac{k_BT}{h} e^{-\frac{\Delta G''}{RT}}$ (91) 224

$[U^{VI}OHO(\bullet O_2)]^{2+} + H_2O \longrightarrow [U^{VI}O_2(\bullet O_2)]^+ (H_3O^+) \longrightarrow [U^{VI}O_2(\bullet O_2H)]^{2+} + H_2O$ (92) 228

$[U^{VI}O_2(\bullet O_2H)]^{2+} \xrightarrow{h\nu} {}^*[U^{VI}O_2(\bullet O_2H)]^{2+}$ (93) 228

$^*[U^{VI}O_2(\bullet O_2H)]^{2+} + H_3COH \longrightarrow [U^VOHO(\bullet O_2H)]^{2+} + H_2\dot{C}OH$ (94) 228

$[U^{V}OHO(\bullet O_2H)]^{2+} \xrightarrow{ET} [U^{VI}OHO(O_2H)]^{2+}$ (95) 228

$[U^{VI}OHO(O_2H)]^{2+} + H_2O \longrightarrow [U^{VI}O_2(O_2H)]^{+} + H_3O^{+}$ (96) 228

$[U^{VI}O_2(\bullet O_2H)]^{2+} + H_2O \longrightarrow [U^{VI}O_2(\bullet O_2)]^{+} + H_3O^{+}$ (97) 228

$[U^{VI}O_2(\bullet O_2H)]^{2+} + H_2O \longleftrightarrow [U^{VI}O_2(H_2O)]^{2+} + \bullet O_2H$ (98) 229

$\bullet O_2H + \bullet O_2H \longrightarrow O_2 + H_2O_2$ **(99)** 229

$[U^{V}OHO(H_2O)]^{2+} + \bullet O_2H \longleftrightarrow [U^{V}OHO(\bullet O_2H)]^{2+} + H_2O$ (100) 230

$[U^{V}OHO(\bullet O_2H)]^{2+} + H_2O \longrightarrow [U^{V}OHO(\bullet O_2)]^{+} + H_3O^{+}$ (101) 230

$[U^{V}OHO(H_2O)]^{2+} + \bullet O_2H \xrightarrow{ET} [U^{VI}OHO(H_2O)]^{3+} + [O_2H]^{-}$ (102) 230

$[U^{VI}OHO(H_2O)]^{3+} + H_2O \longrightarrow [U^{VI}O_2(H_2O)]^{2+} + H_3O^{+}$ (103) 230

$^{1}[U^{VI}O_2(O_2)]^{2+} \xrightarrow{h\nu} *(^{1}[U^{VI}O_2(O_2)]^{2+})$ (119) 238

$*(^{1}[U^{VI}O_2(O_2)]^{2+}) + H_3COH \longrightarrow {}^{2}[U^{V}OHO(O_2)]^{2+} + H_2\dot{C}OH$ (120) 238

$^{2}[U^{VI}OHO(^{\bullet}O_2)]^{2+} \xrightarrow{PT} {}^{2}[U^{VI}O_2(^{\bullet}O_2H)]^{2+}$ (121) 240

$[U^{VI}OHO(O_2H)]^{2+} + H_2O \longrightarrow [U^{VI}OHO(O_2)]^{+} + H_3O^{+}$ (122) 242

$[U^{VI}O_2(L)(H_2O)]^{2+} + HO_2^{-} + U^{VI}O_2(NO_3)_2(H_2O) \longrightarrow [(U^{VI}O_2)_2(O_2)(L)(NO_3)_2] + H_3O^{+} + H_2O$ (123) 246

$[U^{VI}O_2(L)(O_2)] + U^{VI}O_2(NO_3)_2(H_2O) \longrightarrow [(U^{VI}O_2)_2(O_2)(L)(NO_3)_2] + H_2O$ (124) 248

$[U^{VI}O_2(L)(O_2H)]^{+} + U^{VI}O_2(NO_3)_2(H_2O) \xrightarrow{PT} [(UO_2)_2(O_2)(LH)(NO_3)_2]^{+} + H_2O$ (125) 249

$[(UO_2)_2(O_2)(LH)(NO_3)_2]^{+} + H_2O \longrightarrow [(UO_2)_2(O_2)(L)(NO_3)_2] + H_3O^{+}$ (126) 249

$[U^{V}OHO(L)(\bullet O_2)]^{+} + U^{VI}O_2(NO_3)_2(H_2O) \longrightarrow [(U^{V}OHO)(U^{VI}O_2)(^{\bullet}O_2)(L)(NO_3)_2]^{+} + H_2O$ (127) 250

$[(U^{V}OHO)(U^{VI}O_2)(\bullet O_2)(L)(NO_3)_2]^{+} \xrightarrow{ET} [(U^{VI}OHO)(U^{VI}O_2)(O_2)(L)(NO_3)_2]^{+}$ (128) 250

$[(U^{VI}OHO)(U^{VI}O_2)(O_2)(L)(NO_3)_2]^{+} + H_2O \longrightarrow [(UO_2)_2(O_2)(L)(NO_3)_2] + H_3O^{+}$ (129) 250

$(H_2O)_{7(aq)} + H^{+}_{(gas)} \xrightarrow{\Delta G_{hyd}(H^{+})} [H(H_2O)_7]^{+}_{(aq)}$ (130) 276

$\Delta G_{hyd}(H^{+}) = G_{gas}([H(H_2O)_7]^{+}) - G_{gas}(H_2O)_7 - G_{gas}(H^{+}) + \Delta G_{solv}([H_3O(H_2O)_6]^{+}) - \Delta G_{solv}(H_2O)_7$ (131) 276

$[O_2(H_2O)_5]^{2-} + [H_3O(H_2O)_6]^{+} \leftrightarrow [HO_2(H_2O)_5]^{-} + (H_2O)_7$ (132) 282

$[O_2(H_2O)_5]^{-} + [H_3O(H_2O)_6]^{+} \leftrightarrow [HO_2(H_2O)_5] + (H_2O)_7$ (133) 282

Table of Figures

Table of Tables

Abbreviations

ACM	Adiabatic Connection Method
AE	All-Electron
AO	Atomic Orbital
BDE	Bond Dissociation Energy
BO	Born-Oppenheimer (approximation)
BSSE	Basis Set Superposition Error
BTPhen	*$CyMe_4$-BTPhen*
CASPT2	Complete Active Space Perturbation Theory
CASSCF	Complete Active Space Self-Consistent Field
CCDC	Cambridge Crystallographic Data Centre
CCR	Carbon-Centred Radical
CCSD	Coupled Cluster Singles and Doubles
CI	Configuration Interaction
CMPO	Octyl(phenyl)-N, N-dibutyl Carbamoylmethyl Phosphine Oxide
CP	Counterpoise
CPCM	Conductor Polarised Continuum Model
CSD	Cambridge Structural Database
CSF	Computational Shared Facility
CT	Charge Transfer
DFT	Density Function Theory
DFT	Density Functional Theory
ECP	Effective Core Potential
ELF	Electron Localisation Function
EPR	Electron Paramagnetic Resonance
ESI	Electrospray Ionisation
ET	Electron Transfer
EXAFS	Extended X-Ray Absorption Fine Structure
FP	Fission Products
GANEX	Group Actinide Extraction
GGA	Generalised Gradient Approximation
GTO	Gaussian Type Orbital
HF	Hartree-Fock
HOMO	Highest Occupied Molecular Orbital
IS-ET	Inner Sphere Electron Transfer
KS	Kohn-Sham
LC-ECP	Large Core-Effective Core Potential
LDA	Local Density Approximation
LMCT	Ligand-to-Metal Charge Transfer
LS	Russell-Saunders
LSDA	Local Spin Density Approximation
LUMO	Lowest Unoccupied Molecular Orbital
MCCT	Metal Centred Charge Transfer
MO	Molecular Orbital
MP	Model Potentials
MS	Mass Spectrometry
NBO	Natural Bonding Orbital
NMR	Nuclear Magnetic Resonance
OK	Odourless Kerosene
OS-ET	Outer Sphere Electron Transfer
O_{yl}	Uranyl Oxygen
PA	Proton Affinity
PC-ET	Proton-Coupled Electron Transfer
PES	Potential Energy Surface
POM	Polyoxometallate
PP	Pseudopotential
PT	Proton Transfer
PUREX	Plutonium and Uranium Recovery by Extraction
QM	Quantum Mechanics
QM/MM	Combined Quantum Mechanics-Molecular Mechanics

RMS	Root Mean Square
RT	Room Temperature
SANEX	Selective Actinide Extraction
SC-ECP	Small Core-Effective Core Potential
SCF	Self Consistent Field
SD	Slater Determinant
SHO	Simple Harmonic Oscillator
SNF	Spent Nuclear Fuel
SO	Spin-Orbit
SOMO	Singly-Occupied Molecular Orbital
SP	Single Point
STO	Slater Type Orbital
TBP	Tributyl Phosphate
TRUEX	Transuranic Extraction
TS	Transition State
UA0	United Atom Model
UEG	Uniform Electron Gas
UREX	Uranium Extraction
UV	Ultraviolet
UV-vis	Ultraviolet-Visible
UV-vis-nIR	Ultraviolet-Visible and Near Infra-Red
WB	Wood-Boring (equation)
XRD	X-Ray Diffraction
ZORA	Zeroth Order Regular Approximation

Abstract

A Mechanistic Study of the Formation of Peroxide in Solutions Containing the Uranyl(VI) Ion

Christopher Paul Green

The University of Manchester

2014

This body of work concerns the formation of peroxide in solutions containing the uranyl(VI) ion and a ligand proposed for use in next generation nuclear fuel reprocessing technologies, *CyMe*$_4$-BTPhen.[1] The uranyl(VI) ion is known to readily form insoluble complexes in the presence of the peroxide anion and hence the formation of peroxide under process conditions could lead to increased rates of fouling of plant equipment.[2] It is therefore of importance to determine the mechanisms by which peroxide can form in such solutions so these processes may be controlled. To this end this report initially focusses on determining the speciation of actinyl(VI) ions in solutions containing *CyMe*$_4$-BTPhen in order to establish a baseline computational model against which the formation of peroxide may be probed. The synthetic research presented in this thesis predominantly focusses on the coordination chemistry of the plutonyl(VI) ion in solutions containing *CyMe*$_4$-BTPhen. The analogous speciation in solutions containing the uranyl(VI) ion is covered explicitly briefly, although much of the chemistry of this specific species is known and hence is inferred from the studies of a collaborator, D.M. Whittaker.[3] The limiting species formed in both solutions is a complex with 1:1 stoichiometry and this complex is observed to not dissociate readily, as determined by competition experiments in the presence of the chloride anion. With reference to kinetic studies carried out by the likes of Bakac et al.[4] and Burrows et al.[5] in the period between the 1970s and 1990s two mechanistic routes to form peroxide in solutions containing the uranyl(VI) ion, the ligand *CyMe*$_4$-BTPhen and methanol are identified as feasible processes in RT solutions when exposed to sunlight. These mechanisms proceed via the initial formation of an excited state uranyl(VI) species which subsequently is able to abstract a hydrogen atom from the methanol solvent in order to generate a formally uranyl(V) species. This species subsequently reacts with molecular oxygen via an inner-sphere electron transfer reaction to form a solvated uranyl(VI)-superoxide complex. Following this point the favoured mechanisms diverge, where one follows a path to the peroxide bound product that proceeds via a second iteration of the inner-sphere electron transfer process whilst in the other peroxide is formed via an outer-sphere electron transfer between the aquated uranyl(V) ion a a solvated hydroperoxyl radical.

Declaration

No portion of the work referred to in the thesis has been submitted in support of an application for another degree or qualification of this or any other university or other institute of learning.

Copyright Statement

Acknowledgements

For Mum, Dad, Andrew and Rose

Quotes that have inspired aspects of this work:

"Chemistry is nothing more than the study of the games electrons play."

--This is a statement that has stuck with me throughout my degree. I remember hearing it during one of my first undergraduate lectures in Manchester. It has since transpired that these are the immortal words of Dr Joseph McDouall.

" $\frac{Kinetics}{Mechanism} = \frac{Fact}{Fiction}$ "

-- A poignant quote generated at the end of a Gaussian 09[6] run carried out during the study of the mechanism of formation of peroxide.

"*Life is short. Eat dessert first*"

--A second quote generated by Gaussian 09.[6]

"Dah-dah-dah-da-de-da-de-dadadito-dah-dah-dah-da-de-da-de-dadadito-dah-dah-dah-da-de-da-de-dadaditio da-da-da-di-da-da-da-de-dah!"

--El Jarabe Tapatio, a.k.a "The Mexican Hatdance". The melody that repeats *ad infinitum* as the brain idles. In memory of a good friend, big foodie, scathing grammar and punctuation pedant and the most vehement atheist I'll ever know, Alex Chew. Sound mate.

1 GENERAL INTRODUCTION

1.1 The Significance of Actinide Chemistry in Nuclear Reprocessing

The UK is committed to a new generation of nuclear power plants to succeed current civil reactors, all but one of which will be retired by 2023.[7] In order to decommission these 'legacy' sites and wastes, whilst efficiently managing the waste generated by future generations, a fundamental understanding of the chemistry of the actinide elements is required.

The UK currently reprocesses spent nuclear fuel (SNF) arising from recent civil activity. There are many proposed methods to separate the components of SNF arising from generation IV reactors,[8] but currently the most widely implemented processes use solvent extraction, specifically the plutonium and uranium recovery by extraction (PUREX) process. The history of PUREX, as the name suggests, is in plutonium extraction for military use and to this purpose the PUREX process is predictably efficient. However, following reclassification of military managed reprocessing facilities such as Sellafield and La Hague as civil sites, the focus has shifted from a means to purify plutonium, to a process to allow separation of long-term radiological hazards and useful fuels from short-lived waste as part of a closed fuel cycle. Current research is directed towards modifying the PUREX process to meet this change of specification.

1.1.1 PUREX

The fundamental basis of solvent extraction is that it is possible to partition different chemical species as a function of their relative solubilities in immiscible liquids. Solvent extraction is a mature technology widely employed in the production of pharmaceuticals, refined ores, vegetable oils and biodiesels.

The two solvent phases in PUREX are aqueous nitric acid (> 0.5 M) and a mixture of tributyl phosphate (TBP) and odourless kerosene (OK) (usually ~30% TBP in OK)[3]. The process exploits the greater solubility of uranium and plutonium in the organic phase than in the aqueous. When an aqueous nitric solution of irradiated fuel is contacted with a TBP/OK mixture, uranium and plutonium concurrently diffuse into the organic phase to form metal-TBP-nitrate complexes which are better solvated than their hydrated analogues. The majority of the remaining fission products (FPs) remain in the aqueous phase where they are more soluble. Solvent extraction is a reversible process and so the magnitude of the partition

between the phases is governed by an equilibrium constant, specific to each metal-solvent system.

The affinity of a solvated metal ion for a neat solvent phase can be 'fine-tuned' by incorporating molecules capable of forming dative covalent bonds with Lewis acids. These ligands or phase modifiers coordinate metal ion solutes and form complexes that display the solvation behaviour of neither the freebase nor the metal ion, thus altering the metal distribution between the phases. It is also possible to modify the distribution of metals by varying solute concentration and controlling redox speciation.[9] For example, the relative solubility of uranium and plutonium varies as a function of nitric acid concentration and the oxidation state of the metal. This permits the separation of uranium and plutonium in the latter stages of the PUREX process through reduction of *Pu(IV)* to *Pu(III)* using a soft agent such as acetohydroxamic acid which selectively reduces plutonium over uranium. *Pu(III)* is more soluble in the aqueous phase than *Pu(IV)* and UO_2^{2+}, so the products partition between the phases allowing their physical separation. Following separation, it is possible to back-extract the uranium from the organic phase into the aqueous by reducing the nitric acid concentration below 0.2 M.[10] Alternatives and modifications to the PUREX solvent system have been suggested in order to tailor the metals extracted to the needs of future fuel cycles. In some cases these alterations have been implemented at both pilot plant and industrial level. These processes are generally described by an acronym that explains the purpose of the process. A selection of processes are described below along with an example of implementation, if available:

1.1.2 Uranium Extraction (UREX)

The UREX process suppresses the extraction of plutonium from the aqueous SNF solution by reducing *Pu(IV)* and *Pu(VI)* species to *Pu(III)* before the primary extraction stage. As described above, *Pu(III)* has a reduced solubility in TBP/OK and so in the UREX process plutonium is not isolated from the SNF solution. This is beneficial as it provides proliferation resistance. Hence, UREX is an attractive process to apply to non-nuclear states as part of the non-proliferation treaty (NPT).[9]

1.1.3 Transuranic Extraction (TRUEX)

Addition of the complexant octyl(phenyl)-N, N-dibutyl carbamoylmethyl phosphine oxide (CMPO) into the TBP/OK phase allows concurrent extraction of americium and curium with the typical PUREX extracts. This is beneficial as it reduces the long-lived alpha activity of the aqueous raffinate from which actinides have been extracted, thereby facilitating its disposal. This process also extracts the lanthanide elements.[10]

1.1.4 Selective Actinide Extraction (SANEX) and Group Actinide Extraction (GANEX)

Development of SANEX and GANEX processes is ongoing. Generation IV fuel cycles endeavour to increase the efficiency of nuclear power by generating more thermal energy per tonne of heavy metal. One method to achieve this is to extract fissionable and fertile actinides generated by the first pass through a reactor and incorporate them into a fuel form suitable for a second pass; thereby increasing the energy output per tonne of heavy metal used.

As stated above, the TRUEX process extracts the trivalent actinides americium and curium as well as uranium and plutonium from SNF solutions.[10] However, this process provides no selectivity for actinides over lanthanides and so many lanthanide elements are also stripped into the organic phase. Lanthanides have large neutron cross sections across a range of energies and so they act as reactor poisons.[10] This complicates fuel and reactor design as the inventory of lanthanides in SNF varies with fuel burnup. Therefore, it is desirable to develop an extraction process to selectively partition actinides from lanthanides. It is for this purpose that the *CyMe₄-BTPhen* (BTPhen) ligand, discussed in Chapter 1.6, has been designed.

1.2 Spherical Coordinates and the Hydrogenic Orbitals

In the periodic table of the elements, the lanthanide and actinide elements make up the *f*-block. The name of each block of the periodic table refers to the designation of the orbital being filled as the series is traversed. As with orbitals of lower angular momentum, it is also useful to project hydrogenic orbitals to represent the *f*-series. The general expression used to define the wave function, ψ, of a hydrogenic atomic orbital is presented as **Equation 1**.[5]

$$\psi(r,\theta,\varphi) = R_{nl}(r) \cdot Y_l^{m_l}(\theta,\varphi) \qquad \textbf{(1)}$$

In this expression n, l and m_l represent the principal quantum number, angular momentum quantum number and magnetic quantum number, respectively. The term $R_{nl}(r)$ represents the radial component of the orbital and the term $Y_l^{m_l}(\theta,\varphi)$ represents the angular component.

Equation 1 defines the wave function using a spherical coordinate system instead of the better known Cartesian system. It is advantageous to use spherical coordinates in this instance as they allow the electronic wave function to be described as the product of three functions, two angular and one radial, all of which are dependent on a single coordinate in three-dimensional space. This is in contrast to the three numerical coordinate pairs required by the Cartesian system. This represents a significant simplification when analysing

symmetric systems, as a sphere described by the Cartesian equation $c^2 = x^2 + y^2 + z^2$ can be described by the equation $r = c$ in spherical coordinates.

1.2.1 Spherical Harmonics (Orbital Angular Nodality)

Equation 1 decomposes the orbital wave function, $\psi_{nlm}(r,\theta,\varphi)$, into a radial and angular terms. The angular term predominantly determines the shape and directionality of the orbital when viewed externally and so this term predominantly contributes to the reactivity of each orbital. Further separation of variables decomposes $Y_l^m(\theta,\varphi)$ to provide **Equation 2**. In this instance, orbital shapes are the solutions found for $Y_l^m(\theta,\varphi)$ and are referred to as spherical harmonics[5].

$$Y_l^{m_l}(\theta,\varphi) = \Theta_{lm_l}(\theta) \cdot \Phi_{ml}(\varphi) \qquad \textbf{(2)}$$

Equation 2 represents a special case of Laplace spherical harmonics as it necessitates l to be an integer, where there are $2l + 1$ independent solutions to the argument; one for each value of m from $-l \leq m_l \leq l$. These constraints define the allowed values of the azimuthal and magnetic quantum numbers; hence, **Equation 2** is the standard method used to define the shape of orbitals.[11] In the equation, $\Phi_m(\varphi)$ is a periodic function able to represent a full 2π azimuthal rotation about the z-axis and $\Theta_{lm}(\theta)$ denotes a function of the angle of inclination, of value 0 to π.

1.2.2 The General Set of *f*-Orbitals

On evaluating **Equation 2**, for $l=3$, seven independent solutions are generated.[11] These orthogonal solutions are presented in **Figure 1** as the *general* set of *f*-orbitals. When unoccupied or in an isotropic environment these orbitals are degenerate in energy. However, when in a ligand field global *f*-orbital degeneracy is broken and the orbitals of the *general* set form three doubly degenerate sets and one non-degenerate orbital.[10,11]

As would be expected, the degenerate orbitals are related by symmetry and generally a 90° or 45° rotation about one axis is sufficient to convert one representation into another. For example, a 45° rotation about the z-axis transforms the real function f_{xyz} into $f_{z(x^2-y^2)}$, see **Figure 1**. The *f*-orbitals are generally classified by the number of angular nodes or lobes they exhibit, the point group of the orbital, or more accurately, a shorthand representation of the real Cartesian function that describes orbital shape and orientation. **Figure 1** indicates appropriate nomenclature in each instance.

1.2.3 The Cubic Set of *f*-Orbitals

When considering the *d*-orbitals, i.e. the spherical harmonics calculated for all values of m_l, where $l=2$, group theory stipulates that in ligand fields of relatively high intrinsic symmetry, the degeneracy of the *d*-orbitals will be broken into one doubly degenerate set and one triply degenerate set; governed by the shape and orientation of each orbital relative to the ligand field.[10,11] This is what leads to the characteristic and distinct *d*-orbital ordering experimentally confirmed for transition metal complexes in octahedral, O_h, and tetrahedral, T_d, ligand environments.[10,11] However, when this treatment is applied to the *f*-orbitals, group theory states that the degeneracy must be broken into two triply degenerate orbital sets and one non-degenerate orbital and clearly, the *general* set does not meet this requirement.[10,11] Hence, in cubic ligand fields, such as O_h and T_d, the orbitals of the *general* set are allowed to mix to form a second set of seven representative *f*-orbitals, known as the *cubic* set, which satisfies group theory.[10,11] The orbitals of the *cubic* set are presented in **Figure 2**.

1.3 Actinide Redox Chemistry

1.3.1 Electronic Structure of the 5*f*-Elements

As alluded to previously, the ability of an element to access a range of oxidation states is governed by the strength of the interaction between the atomic nucleus and the valence electrons. Elements in their group valence oxidation state are defined as having no remaining electrons in the valence region. Generally the valence region defines the orbitals from which electrons which must be removed in order to allow the element to reach noble gas configuration. In the case of the actinides the valence electronic configuration can be described by the expression [Rn] $5f^{x-y}\,6d^{y}\,7s^{2}$.

Orbital ordering for elements in the *f*-block is not as clear cut as for groups earlier in the periodic table due to the relative degeneracy of the *f* and *d* orbitals. **Table 1** presents the ground state elemental electronic configurations of the actinide elements.[10,12]

The ordering of actinide electronic configurations is complicated due to the influence of relativistic effects for the actinide series. Relativity acts to destabilise the *f*-orbitals relative to the *d*- and leads to a greater degree of *d*-orbital penetration into the actinide valence region than would be expected compared to other groups in the periodic table. The causes and effects of relativity are elaborated on in Chapter 1.4.2.

The *General* Set of *f*-orbitals

Symmetry Related f-orbital Sets

Eight Lobe Orbitals of δ Symmetry

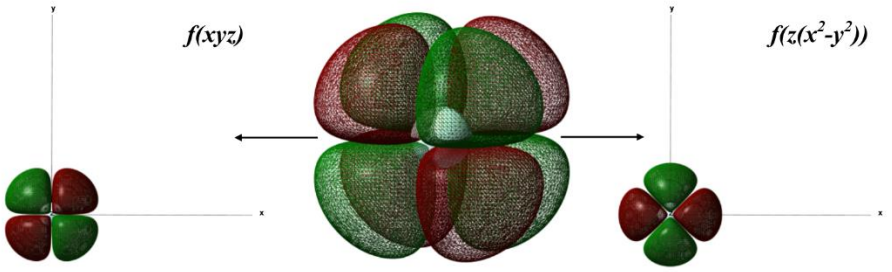

Six Lobe Orbitals of φ Symmetry

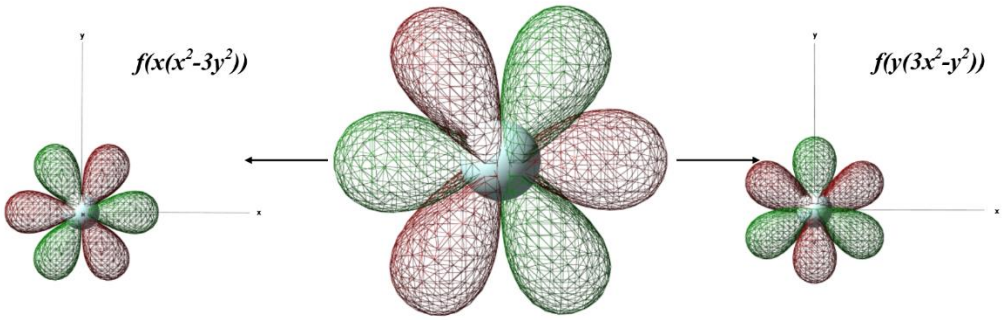

Six Lobe Orbitals of π Symmetry

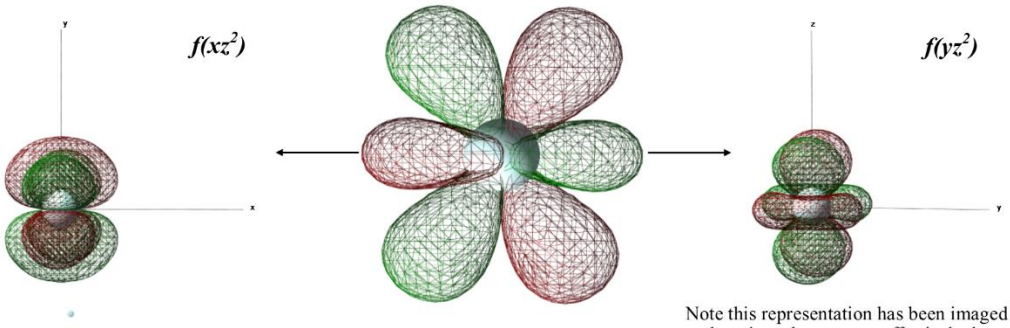

Note this representation has been imaged in the *zy* plane in order to more effectively demonstrate the difference between the lobes of this orbital.

Double Toroidal Orbital of σ Symmetry

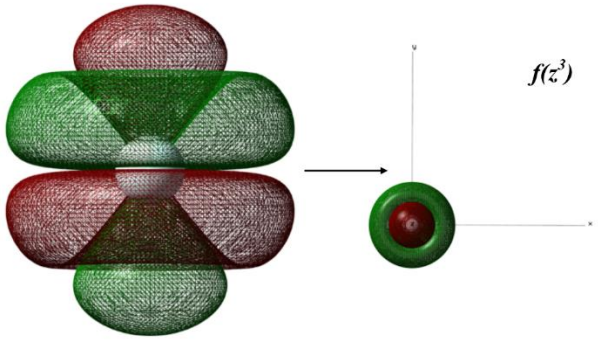

Figure 1: Represents the seven spatially distinct *f*-orbitals of the *general* set as generated using Gaussian 09[6] and GaussView 05.[13] The orbitals have been grouped into sets in terms of point group and number of lobes. The general shape of each AO is shown for each set, along with representations that indicate orientation and the terms used to identify each within 3D Cartesian space. AO diagrams were generated from a helium atom model. The functional employed was B3LYP using a unitary basis set of single *s*, *p*, *d*, *f*, *g*, *h* and *i* functions, symmetry was minimised to visualise the *general* set. Each orbital has been plotted at the 0.02 isosurface.

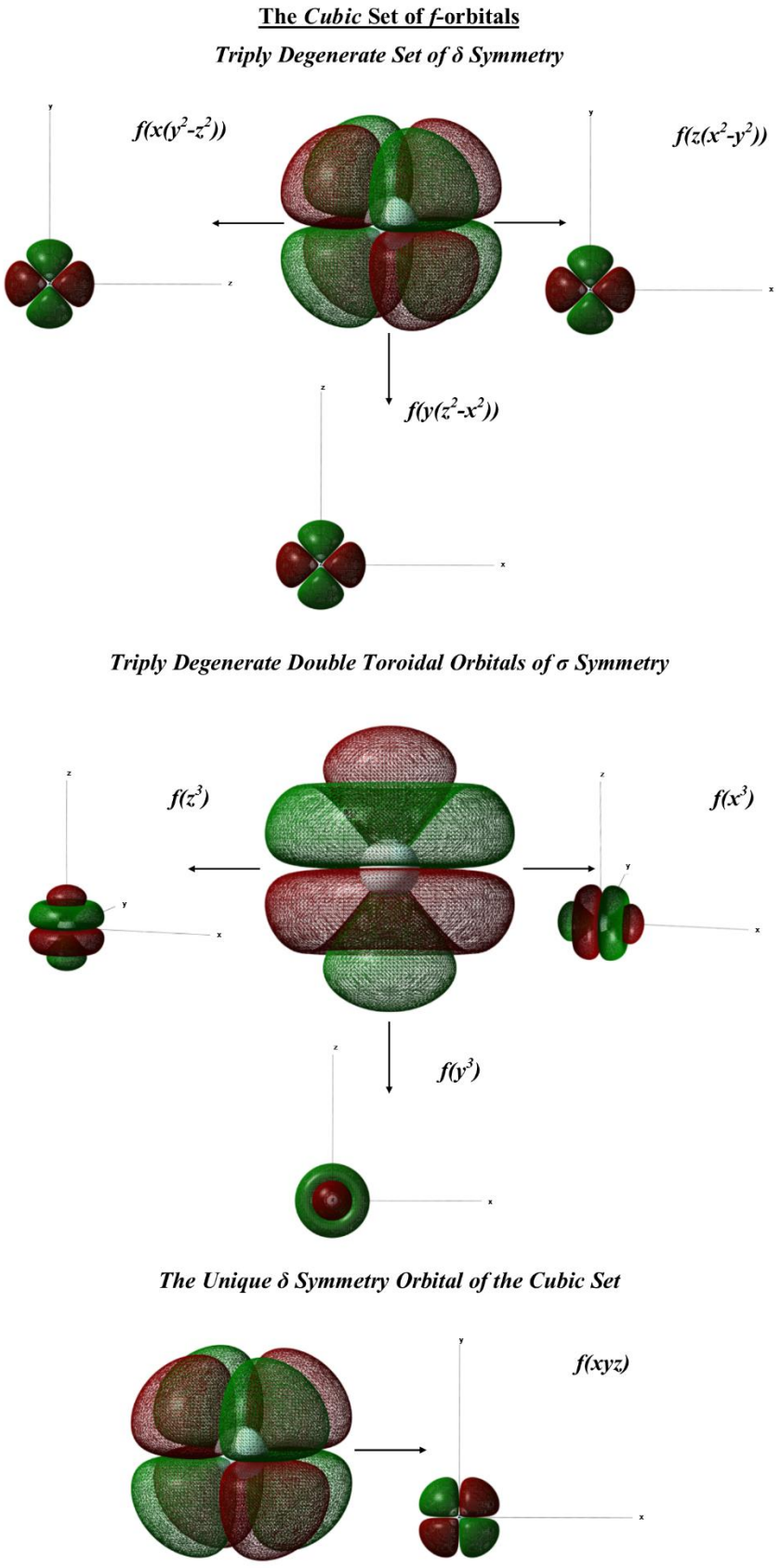

Figure 2: Represents the *f*-orbitals of the *cubic* set as generated using Gaussian 09[6] and GaussView 5.[13] The orbitals have been grouped into degenerate sets; defined as orbitals with similar angular nodality, which can be transformed into each other by a single 90º rotation about one Cartesian axis. AO diagrams were generated from a helium atom model modified by a set of *f*-functions. The functional employed was B3LYP using a unitary basis set of single *s*, *p*, *d*, *f*, *g*, *h* and *i* functions, symmetry was constrained to visualise the *cubic* set. Each orbital has been plotted at the 0.02 isosurface.

Table 1: Table characterising the actinides by atomic number, ionic radius and ground state neutral atom electronic configurations.[a]

Symbol	Atomic number	Electronic Configuration
Ac	89	[Rn] $6d^1\ 7s^2$
Th	90	[Rn] $6d^2\ 7s^2$
Pr	91	[Rn] $5f^2\ 6d^1\ 7s^2$
U	92	[Rn] $5f^3\ 6d^1\ 7s^2$
Np	93	[Rn] $5f^4\ 6d^1\ 7s^2$
Pu	94	[Rn] $5f^6\ 7s^2$
Am	95	[Rn] $5f^7\ 7s^2$
Cm	96	[Rn] $5f^7\ 6d^1\ 7s^2$
Bk	97	[Rn] $5f^9\ 7s^2$
Cf	98	[Rn] $5f^{10}\ 7s^2$
Es	99	[Rn] $5f^{11}\ 7s^2$
Fm	100	[Rn] $5f^{12}\ 7s^2$
Md	101	[Rn] $5f^{13}\ 7s^2$
No	102	[Rn] $5f^{14}\ 7s^2$
Lr	103	[Rn] $5f^{14}\ 6d^1\ 7s^2$

[a] The actinide ionic radii presented are for ions in the +3 oxidation state and octahedral environment.

1.3.2 Actinide Oxidation States

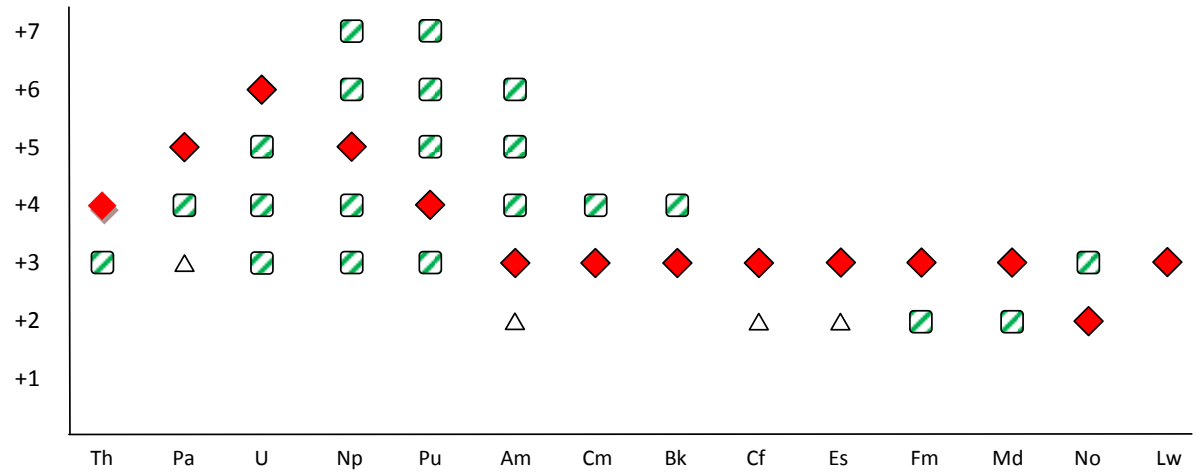

Figure 3: Diagram indicating the accessible oxidation states of the actinide elements in solid and liquid phases. Red diamonds represent the most stable oxidation state adopted by each element in solution; green striped squares represent other accessible oxidation states. Open triangles represent oxidation states only found in solids. Adapted from similar diagram in *The f-elements* (Kaltsoyannis and Scott).[10]

A diagram of the oxidation states available to the actinide elements is presented as **Figure 3**. The range of oxidation states accessible to the actinide elements varies as the group is traversed. Whilst the early elements tend to be most stable in high oxidation states, for example the elements *Th*, *Pr* and *U* are most stable in their group valence oxidation states of +4, +5 and +6, respectively, this trend inverts following uranium. This is demonstrated by the fact that whilst neptunium is able to access its group valence state it is most stable in the +5 state. Plutonium follows suit, being most stable in the +4 state and americium the +3 state. Americium is the last actinide able to readily access more than two oxidation states in solution. The latter actinides *Cm-Lr* are only able to access low oxidation states of +4, +3

and +2, with the most stable being the +3 state for all but nobelium. Therefore, the latter actinides behave more like lanthanide elements than they do the early actinides.

This change in character across the actinide series, from elements displaying oxidation states similar to a transition metal series to ones mimicking the lanthanide series, is assigned to the effects of *actinide contraction* and *relativity*, both of which will be dealt with in the next chapter.

1.3.3 The Redox Chemistry of Plutonium

Of all of the chemical complexity posed by the actinide elements, it is debatable that no aspect is as rich as the redox chemistry of plutonium. As stated, the plutonium ion can access six oxidation states in solution ranging from +3 through to +7. Of these, the +4 oxidation state is that typically encountered in SNF solutions in nitric acid, although the near degeneracy of the reduction potentials between the different oxidation states means that in effect multiple oxidation states of plutonium can coexist in solution at the same time. A Latimer diagram presenting the similar reduction potentials of plutonium in aqueous perchloric acid is presented in **Figure 4**.

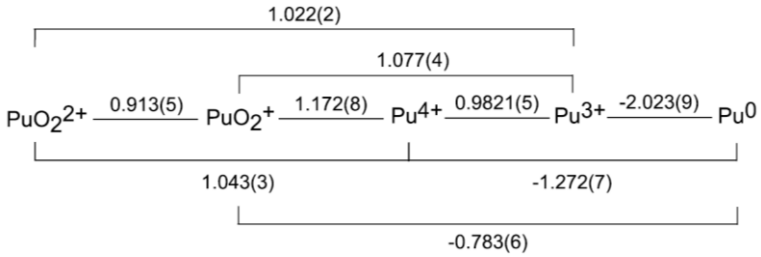

Figure 4: Latimer diagram presenting the formal redox potentials of plutonium ions in 1M aqueous perchloric acid at 25 °C relative to the standard hydrogen electrode. Image reproduced from reference (Clark, 2000)[14], data as published by Lemire et al.[15]

The practical effect of this is that the oxidation state of plutonium is exceedingly difficult to control in solution as multiple equilibria between oxidation states often establish themselves in a system after a period ranging from hours to days following the initial redox conditioning process. This difficulty is compounded by the large specific activity of certain plutonium isotopes that leads to the generation of redox active species through radiolysis of the solvent and subsequent loss of control of the oxidation state.

Fortunately, however, the differing oxidation states of the plutonium ion all interact in a different way with light owing to their dissimilar electronic structures, this thereby imbues each oxidation state with a spectral fingerprint that allows the composition of a solution to be monitored simply and quickly by quantifying the amount of ultraviolet to near infrared light that a sample absorbs as a function of wavelength using UV-vis-nIR spectroscopy.

Examples of the colours of plutonium ions in different oxidation states are presented in **Figure 5** and examples of their characteristic electronic absorption spectra are presented in **Figure 6**. **Figure 5** is reproduced exactly as found in reference (Clark, 2000)[16] and **Figure 6** is reproduced exactly as found in reference (Clark, 2005)[14].

Figure 5: Figure reproduced from reference (Clark, 2000)[16]. Image showing the characteristic colours of plutonium ions in aqueous media. The specific composition of the solutions used is described in the caption of **Figure 6**, below.

The electronic transitions responsible for these characteristic spectra of each of the plutonium ions are transitions between *f* orbitals. These transitions are therefore formally forbidden by the Laporte selection rule. The forbidden nature of these transitions provides somewhat of a blessing, however, as it results in the absorptions being sharp well defined transitions between the two states as opposed to the wide absorption 'smears' typically associated with the electronic absorption spectra of organic compounds. Furthermore, the forbidden nature of these transitions results in the intensity of the absorptions being intrinsically linked to the symmetry of the orbitals in the species being probed, hence they provide an indication of the geometry of the complex present in solution. This concept is exemplified by the absorption spectra recorded by Runde[17] for an aqueous perchloric acid solution of the plutonyl(VI) ion at different concentrations of chloride. These spectra have been reproduced exactly as presented in reference (Runde, 2000)[17] in **Figure 7**.

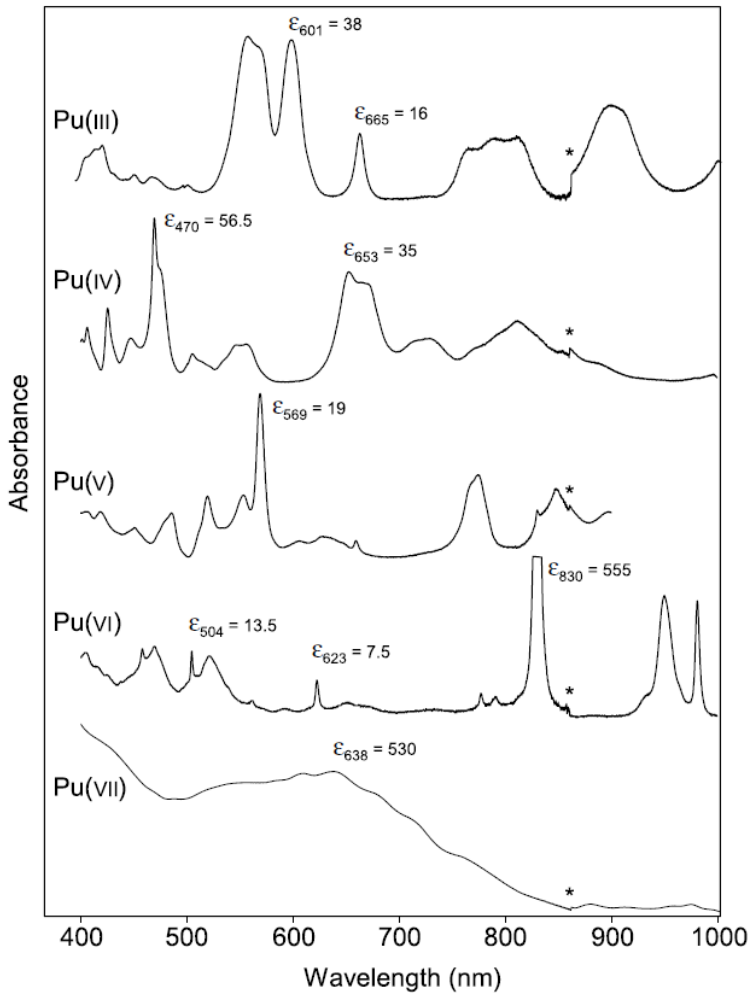

Figure 6: Figure and caption reproduced exactly from reference (Clark, 2005)[14]. "*Electronic absorption spectra of major plutonium aqua ions recorded at 25 °C. The asterisk marks a spectrophotometer grating change. Plutonium(III) recorded on 1.89 m solution in 1 M $HClO_4$ using 1 cm cell. Plutonium(IV) recorded on 2.91 mM solution in 1 M $HClO_4$ using 1 cm cell. Plutonium(V) recorded on 10.2 mM solution in 1 M $(Na,H)ClO_4$ solution using 1 cm cell. Plutonium(VI) recorded on 0.89 mM solution in 1 M $HClO_4$ solution using 1 cm cell. Plutonium(VII) recorded on 20 mM solution in 2.5 M NaOH solution using 1 cm cell. (spectra courtesy of Phillip D. Palmer of Los Alamos National Laboratory).*"

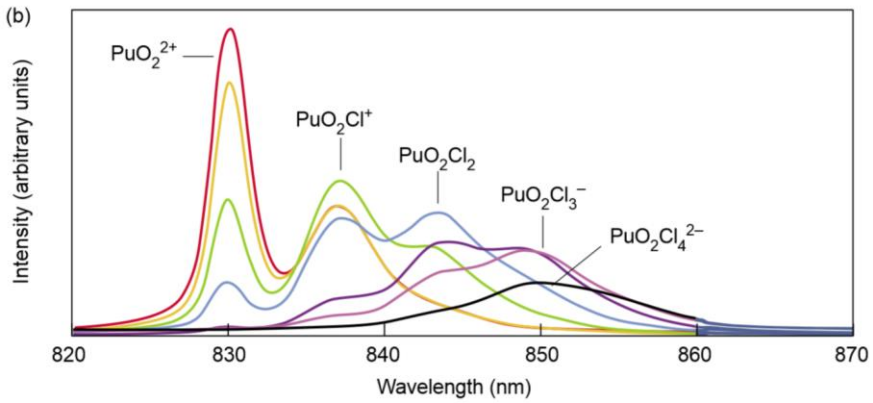

Figure 7: Figure reproduced exactly as presented in reference (Runde,2000).[17] The figure depicts the electronic absorption spectra in the region of 820 nm to 870 nm of aqueous 1 M $HClO_4$ solutions containing the plutonyl(VI) ion and chloride at differing concentration. The chloride concentrations employed range from 0 M Cl^- (red line) to 15 M Cl^- (black line).

As **Figure 7** shows, as the concentration of chloride in solution is increased, the intensity of the sharp absorption maxima at 830 nm ascribed to the aquated $[PuO_2(H_2O)_5]^{2+}$ complex decreases and there is the appearance of adjacent maxima that are red shifted relative to the absorption of the aquated complex. As the concentration of chloride in the solution is increased, progressively further red-shifted additional maxima are observed that are indicative of the formation of higher order plutonyl(VI) chloride complexes. This study by Runde[17] was coordinated with an extended X-ray absorption fine structure (EXAFS) study of the system that allowed each of the absorption maxima in the UV-vis-nIR experiments to be correlated to a single plutonyl chloride complex. In this way, Runde[17] was able to confirm that as the concentration of chloride increases, higher order chloride complexes of the plutonyl(VI) ion up to and including $[PuO_2Cl_4]^{2-}$ are formed and that these complexes all exhibit unique absorption maxima. Furthermore, the higher symmetry octahedral $[PuO_2Cl_4]^{2-}$ complex was shown to have a smaller extinction coefficient than the lower symmetry pentagonal bipyramidal $[PuO_2(H_2O)_5]^{2+}$ species, thereby indicating that the extinction coefficient of the Laporte forbidden transitions in these solutions provides information about the symmetry of the complex. This boils down to the fact that visual-near IR electronic absorption spectra of plutonyl(VI) solutions are incredibly useful tools to the synthetic radiochemist.

1.4 Aspects of the Electronic Structure of the Actinides

1.4.1 The Actinide (and Lanthanide) Contraction

The term *lanthanide contraction* relates to the physical observation that the metallic radius of hafnium is similar to that of zirconium, 159 pm and 160 pm respectively.[18] This contradicts the general trend of the periodic series, which suggests that atomic radii should increase down each group. This similarity between the metallic radii of *Zr* and *Hf* persists for other pairs of elements from the fifth and sixth transition series and is due to the occurrence of the first *f*-electrons between these two *d*-block periods.[19] The term *actinide contraction* is typically applied to describe the analogous process occurring across the actinide series due to the appearance of 5*f* orbitals.

Both actinide and lanthanide contractions act to increase the density of orbitals in the valence region, as it is only electrons higher in energy than the more core-like *f*-electrons that are affected. In some cases, this valence orbital contraction permits *d*-orbital involvement in actinide ground state configurations and along with relativistic effects this factor leads to the wide range of oxidation states accessible to the early actinides.

1.4.2 Scalar Relativistic Effects

In this context, relativity refers to Einstein's theory of special relativity and specifically the relativistic mass increase the theory explains. Special relativity confirmed the speed of light to be a constant and showed that energy and mass can be interconverted.[10,19] Hence, as an object is accelerated close to the speed of light a greater proportion of the energy input is converted into mass, so as $v \rightarrow c$, $m \rightarrow \infty$. Where v is the velocity of the object, c is the speed of light, m is the mass of the moving object and m_o is the rest mass of the object. The equation which describes this relativistic mass increase is presented in **Equation 3**.

$$m = \frac{m_0}{\sqrt{1-(v/c)^2}} \qquad \textbf{(3)}$$

The radial velocity of a 1*s* electron is approximately Z in Hartree atomic units, where Z is the proton number of the atom. Hence, the 1*s* electron of a uranium has a radial velocity of approximately 97 *c*/137, or 67 % of the speed of light. Substituting this into the relationship presented in **Equation 3** it is possible to calculate the relativistic mass increase for a 1*s* electron of uranium as $1.35m_e$.

The radial extent of an orbital is inversely proportional to the electronic mass, m_e, hence a $1.35m_e$ increase in mass leads to a contraction of the 1*s* orbital and so also an energetic stabilisation. In contrast to the heavy metals, the relativistic stabilisation observed for lighter elements is significantly reduced. For example the relativistic mass increase for the 1*s* electron of hydrogen is $1.00003m_e$, and so for light elements the effects of relativity are often regarded as insignificant.[10,19]

The effects of relativity do not stop with the electronic core. Due to the orthogonality constraint, contraction of the 1*s* orbital will lead to contraction of all *s*-orbitals, regardless of principal quantum number. This is known as *direct relativistic contraction* and albeit to a lesser extent, *p*-orbitals are also stabilised in this manner.

This direct contraction leads to a secondary effect, known as the *indirect relativistic expansion*. Here, the contraction of *s*- and *p*-orbitals more effectively shields the valence *f*- and *d*-electrons from the nuclear charge causing their radial extents to increase accordingly.[10,16,19] This ultimately results in the 5*f* electrons being more chemically available than would be expected in comparison to the core-like 4*f* electrons of the lanthanide series.

Similarly to the actinide contraction, the effect of relativity on the 5*f* orbitals is to increase their radial penetration of the valence region. These combined effects go some way to

explain why actinide coordination complexes are typically observed to have more covalent character than would be expected when compared to the lanthanide series.[20,21]

1.4.3 Spin-Orbit Coupling

Relativistic effects and actinide contraction are able to explain certain aspects of the complex orbital ordering observed for the actinides, however further complexity is added due to the coupling of orbital and electronic angular momentum. This is termed spin-orbit (SO) coupling and gives rise to the fine structure observed in atomic spectra.

Electrons are charged particles of spin quantum number $s=½$. As an electron moves about an atom, it generates a magnetic moment. The magnitude of the moment generated is associated with the total angular momentum of the electron. This is a quantity not solely due to its spin, but also the motion of the orbital it occupies about a charged nucleus. The coupling of these two sources of angular momentum gives rise to the SO effect, which breaks the degeneracy of orbitals sharing the same azimuthal quantum number, leading to the fine structure observed spectroscopically. [4]

The degeneracy is broken by two effects; the first is that for a given set of orbitals, l, the orbital specific angular momenta are not necessarily equal. For example, an f_{xyz}-orbital has a greater angular nodality than an f_{z^3}-orbital, hence an electron occupying the former has a greater angular momentum then the latter and so will generate a greater orbital moment. This difference is quantified using the orbital magnetic quantum number, m_l, where m_l can have values $-l \leq m_l \leq +l$. Therefore in the case of the *f*-orbitals, the allowed values of m_l are -3, -2, -1, 0, 1, 2 and 3, where orbitals of greater angular momentum are represented by the greatest magnitude m_l quantum numbers. The second magnetic effect that breaks degeneracy is due to the fact that a magnetic moment is a vector quantity. Thus, the magnetic moment due to the electronic spin may be aligned parallel to the moment due to orbital motion or the two could be oppositely aligned. Each combination produces a distinct energetic state, thereby breaking the degeneracy between orbitals of similar angular momentum. The only allowed spin quantum number of an electron is $s=½$, therefore the only spin magnetic quantum numbers allowed are $m_s = ±½$.

There are two methods used to quantify the degree of SO coupling; Russell-Saunders (LS) coupling and *j-j* coupling. The former is most appropriate for systems where SO coupling is weak relative to interelectronic repulsion and *j-j* coupling is more appropriate when SO coupling is strong in relation to interelectronic repulsion.[4]

1.4.3.1 LS Coupling

LS coupling treats electron spin-spin interactions and orbital-orbital interactions separately in order to calculate total atomic angular momentum. It achieves this by defining two new quantum numbers; **L** and **S. L** describes the moment solely due to individual orbit-orbit interactions, $\boldsymbol{l_i}$, and **S** describes the moment due to individual electron spin-spin interactions, $\boldsymbol{s_i}$. These two quantum numbers are then combined, as per **Equation 4** to give a spin-orbit quantum number, **J**.

$$\mathbf{J} = \mathbf{L} + \mathbf{S} \qquad \mathbf{(4)}$$

Where:

$$\mathbf{L} = \sum_i \mathbf{l}_i \qquad \mathbf{(5)}$$

And:

$$\mathbf{S} = \sum_i \mathbf{s}_i \qquad \mathbf{(6)}$$

This new quantum number allows orbitals with the same principal, azimuthal, orbital magnetic and spin magnetic quantum numbers to have different **J** quantum numbers, thereby breaking the degeneracy of states in systems where SO coupling is not considered.

1.4.3.2 *j-j* Coupling

The *j-j* coupling model treats the individual electronic spin and orbital angular momenta together, to give a total angular momentum for each electron, $\boldsymbol{j_i}$. These individual $\boldsymbol{j_i}$ values are then coupled to calculate the total atomic angular momentum, **J**, equation *(1.9)*[4].

$$\mathbf{J} = \sum_i \mathbf{j}_i = \sum_i (\mathbf{l}_i + \mathbf{s}_i) \qquad \mathbf{(7)}$$

The SO interaction in the lanthanides is weak enough relative to the inter-electronic repulsion that lanthanide SO coupling can be described satisfactorily using a **LS** scheme. However, the case for the actinides is not as straight forward as the degree of SO coupling is increased to the point a pure **LS** description is often inadequate. Despite this limitation of the **LS** model, SO coupling in actinide elements does still not dominate over inter-electron repulsion and so a *j-j* model is also lacking. The increasing influence of SO coupling for the actinide elements complicates the interpretation of their electronic and magnetic spectra as well as their theoretical prediction.

It is common in the literature to apply a SO correction to calculated energies of actinide systems in order to save the computational expense related to their calculation. These

corrections are specific to the oxidation state of the actinide modelled as well the computational method employed.[22,23]

1.5 Coordination Chemistry of the Actinides

1.5.1 The Actinyl Ion

As stated previously, the light actinide elements are able to exist in a range of oxidation states, up to and including group valence in some cases. As the oxidation state of a metal ion increases there is a net stabilisation of the remaining occupied electronic orbitals, which leads to a decrease in the ionic radius of the metal ion. This decrease in ionic radius with increasing cationic charge increases the charge density of the ion, a property which acts to polarise the electronic distribution of other molecules in the vicinity of the ion. In aqueous solution, the charge density of the high oxidation state early actinides is great enough to polarise the water *O-H* bonds to the point of dissociation, the driving force for which is the formation of actinide-oxygen triple bonds. Two water molecules are split per metal ion affording unusually trans-dioxo cations, known as actinyl ions.

Actinyl ions are described by the general formula AnO_2^{n+}, where n= 1 or 2, for this reason actinyl ions are only readily observed for elements able to access oxidation states greater than +4. Actinyl ions of uranium, neptunium and plutonium are the most widely studied, but americyl and protactinyl ions are also possible.[24,25]

The actinyl ions exist as linear *O-An-O* species, which is incongruent with their dioxotransition metal analogues, which preferentially form bent species such as MoO_2^{2+}.[4] The reason actinyl ions form *trans*-oxo species rather than *cis* is explained by the participation of *f*-orbitals in the metal-ligand bond, which this is not possible for transition metal ions, where *d*-orbital overlap with ligands dominates the chemistry.[16]

1.5.2 Electronic Structure of the An(VI) Ion

The bonding in the actinyl(VI) ion, AnO_2^{2+}, is due to σ and π overlap of the metal centred *d*- and *f* -orbitals with the 2*p* orbitals centred on each oxygen atom. Each oxygen atom possesses three orthogonal *p*-orbitals, therefore there are six unique linear combinations of these orbitals with the *d* and *f* metal centred orbitals able to form bonding interactions; two π_g, two π_u, one σ_g and one σ_u as shown in **Figure 8**.[26] These six constructive AO interactions across the actinyl ion relate to the formation of a formal triple bond between the actinide atom and each of the oxygen ligands. These triple bonds are characterised by the very short actinide to actinyl oxygen (*An-O*$_{yl}$) bond distances which are typically on the order of ~1.75 Å, as determined by DFT and X-ray diffraction (XRD) studies.[27–30]

In **Figure 8**, the six bonding MOs of the actinide ion are described by their appropriate symmetry label for the linear $D_{\infty h}$ point group. Whilst it is not technically correct to describe actinide MOs using this syntax when in lower symmetry ligand fields, it does provide a useful point of reference. Hence, in this study the six symmetry labels presented in the figure will be used to describe the analogous actinyl bonding orbitals regardless of the specific point group of the system.

Figure 8 also presents a schematic of the energetic ordering of the actinyl MOs. In this schematic, the highest occupied MO (HOMO) of the uranyl(VI) ion is the σ_u orbital. This MO has a node in its equatorial plane and hence it is only able to undergo π-bonding interactions with the equatorial ligand field. This results in this MO being relatively invariant towards ligand field effects, especially when the equatorial ligands are exclusively σ donors. In addition, the σ_u MO of the actinyl ion is heavily destabilised relative to the other uranyl bonding MOs via a mechanism known as the 'pushing up from below' effect.[26,31,32] It is thought that this effect is predominantly due to the σ_u MO being formed of a superposition of an oxygen 2*p* and actinide $5f_{z^3}$ bonding interaction and an oxygen 2*p* and actinyl 6*p* anti-bonding interaction. Thereby the admixture of the actinide 6*p* AO with the oxygen 2*p* MOs overall acts to destabilise the actinyl σ_u MO in a manner that does not occur for the other bonding MOs.[33] When teamed with the insusceptibility of this MO to crystal field effects, this destabilisation results in the fact that the σ_u MO is always observed as the HOMO in appropriately modelled complexes of the actinyl(VI) ion.[26,31,33]

In contrast to the energetically distant actinyl HOMO, the remaining five bonding MOs all have relatively similar energies. Furthermore, many of these remaining bonding MOs are able to interact strongly with the equatorial ligand field of the actinyl ion meaning their relative ordering typically falls subject to ligand field effects.[26,33] For this reason, in **Figure 8**, the specific ordering of the HOMO-1 to HOMO-5 orbitals of the actinyl ion has been left ambiguous.

Only three of the seven actinide *5f* orbitals are of the correct symmetry to form bonding interactions with the axial dioxygen ligands in the actinyl ion, and hence the lowest unoccupied MOs (LUMOs) of the actinyl ion are a manifold of near degenerate non-bonding metal centred MOs. Similar to their bonding MO analogues, these MOs are typically known by their $D_{\infty h}$ symmetry labels. As shown in **Figure 8**, the non-bonding actinyl MOs are the δ_u and φ_u orbitals and there are two of each that differ only in their orientation with respect to the ligand field. This means that in a $D_{\infty h}$ species these MOs are exactly degenerate, although, their relatively short radial extent means that they are only able to form weak

interactions with equatorial ligand fields and so typically retain their near degeneracy in lower symmetry complexes. Higher in energy than the non-bonding MOs, lie the anti-bonding analogues of the actinyl bonding MOs. A discussion of the character of these MOs and how they may be accessed on excitation is beyond the scope of this report.

1.5.3 Common Geometries of Actinyl(VI) Coordination Complexes

The strong covalent interaction associated with the *trans*-configuration of the oxygen ligands in the uranyl ion, as well as other actinyl species, limits their coordination chemistry somewhat by directing all further coordination to occur equatorially. Equatorial coordination is generally mediated by the *d*- and *f*-orbitals not involved in bonding with the axial oxygen atoms, however should no orbital of correct symmetry exist out of the remaining *f*-orbitals then competition between the equatorial and axial ligand fields for the uranyl bonding MOs may be observed.[10,16,34]. Equatorially, it is usual to observe AnO_2^{2+} coordinated by four, five or six donor atoms in the aqueous and organic phases. Including the axial coordination, these modes relate to formal coordination numbers of 6, 7 and 8 and relate to octahedral, pentagonal bipyramidal and hexagonal bipyramidal coordination geometries, respectively. Of these geometries, the pentagonal bipyramidal structure is most commonly observed for monodentate ligands. The equatorial coordination number of an actinyl ion is predominantly determined by the steric bulk of the coordinating species. Therefore, large and bulky ligands such as chloride anions may direct the actinyl complex to take an octahedral geometry, whilst smaller ligands, such as fluoride may allow the coordination of five ligands to the actinyl centre, permitting pentagonal bipyramidal geometry. The pentagonal bipyrimidal geometry is that typically observed for actinyl(V) and actinyl(VI) complexes.[23,35,36] The hexagonal bipyramidal geometry is only adopted when multidentate ligands are present, such as carbonate, in which the bidentate binding mode of the ligands presumably stabilise the hexadentate equatorial coordination by the chelate effect.[16] With very strained or sterically demanding ligands, it is possible for actinyl ions to exist in trigonal bipyramidal geometry. Examples of such complexes are rare, but include the strained macrocyclic calixarene uranyl(VI) complex described by P.Thuéry *et al.*[37] and the sterically congested uranyl(VI) complex formed with three bis(trimethylsilyl)amido ligands, discovered by Burns *et al.*,[38] see **Figure 9**. In the latter example, it is thought that the anionic ligands stabilise the traditionally unsaturated trigonal equatorial coordination mode of the uranyl using a combination of strong σ-donation and steric congestion.[38]

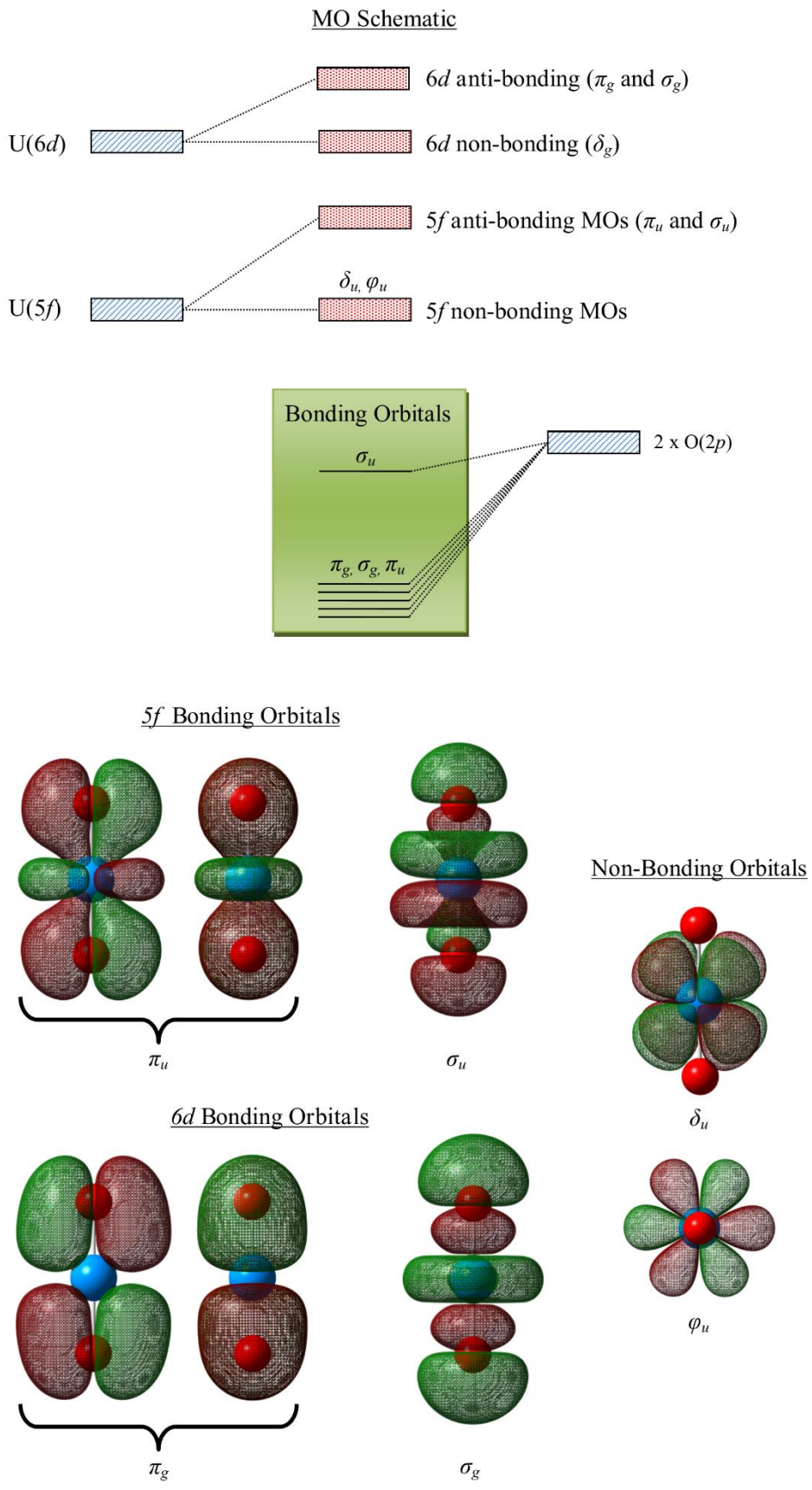

Figure 8: Schematic of the frontier MOs of the actinyl ion along with the images of the 6 actinyl bonding MOs and two non-bonding LUMOs pictured at the 0.02 isosurface. To allow assignment of the MOs pictured to their points in the MO schematic symmetry labels specific to the $D_{\infty h}$ point group have been included.

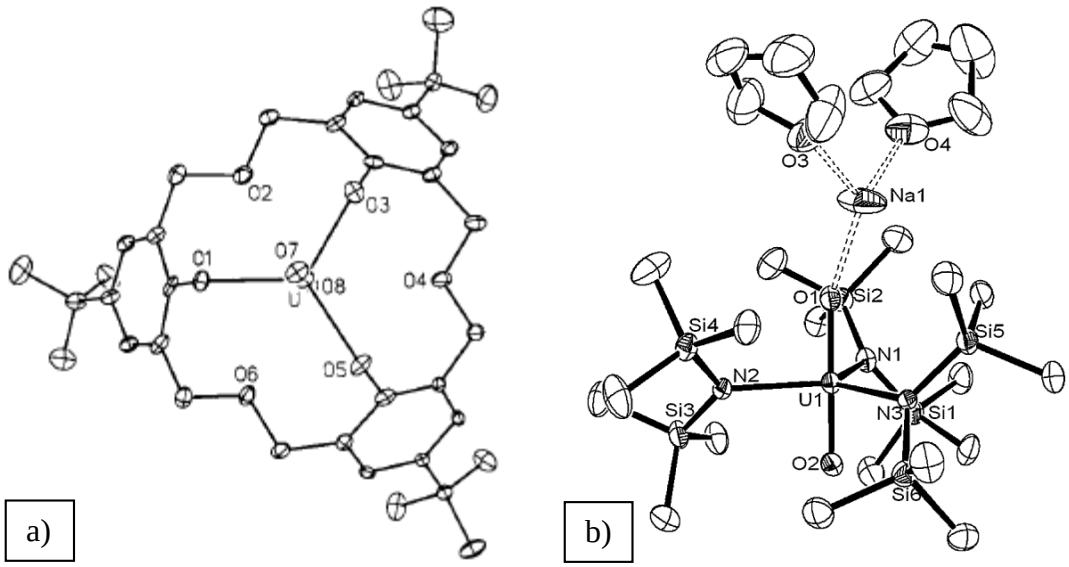

Figure 9: Two examples of uranyl(VI) complexes with trigonal bipyramidal geometry; a) p-tert-butylhexahomotrioxacalix[3]arene complex of uranyl(VI)[16] and b) the complex *[Na(THF)$_2$][UO$_2$(N(SiMe$_3$)$_2$)$_3$]*.[38] Both images are reproduced directly as published in the original articles of Thuiery *et al*.[16] and Burns *et al*.[38]

Despite the fixed axial oxygen atoms constraining a large part of actinyl coordination to occur in the equatorial plane, actinyl chemistry is relatively varied. Considering uranyl(VI) complexes alone, monodentate, bidentate and higher orders of ligand denticity have been observed with a range of immediate donor atoms. Chelating ligands are able to direct the most stable complex geometry away from those of high symmetry and most efficient orbital overlap by imposing the coordinating atom *bite angles* inherent of the chelating ligand structure. This leads to additional chemical complexity, in that the stability of actinyl complexes with such rigid ligands will be much more dependent on the size and charge of the metal ion than previously. This provides an additional tool towards designing ligands that selectively coordinate one metal over another.

Figure 10 shows the crystal structures of two actinide complexes; a) is an example of an uranyl(VI) complex with a large tetradentate ligand.[29] This ligand is not able to saturate the uranyl coordination sphere sterically or electronically and so a monodentate solvent molecule occupies the spare site. The average bite angle inherent of each N_x-*U*-N_x unit of this chelating ligand is 63.8°, this steric requirement forces the geometry of the complex away from the pentagonal bipyramidal geometry expected for analogous monodentate complexes, resulting in the pyridine solvent ligand approaching approximately perpendicular to the *N1-U-N4* chelating bite angle.[29] In contrast, **Figure 10** b) shows the crystal structure of a heteroleptic uranyl(VI) complex that is not dependent on direct coordination by solvent.[39] In this complex, uranyl has an equatorial coordination number of 4. Here, the steric bulk afforded by the β-ketiminate and β-diketonate ligands congests the

uranyl equatorial plane, preventing coordination by auxiliary solvent molecules. This stabilises the tetracoordinate complex despite the non-ideal metal-ligand orbital interactions. In this complex the β-ketiminate and β-diketonate bite angles are 71.6° and 72.8° respectively, this therefore forces the donor atom bite angles between the two ligands (O_x-*U1*-N_x angles) to be in the order of 108°.[39]

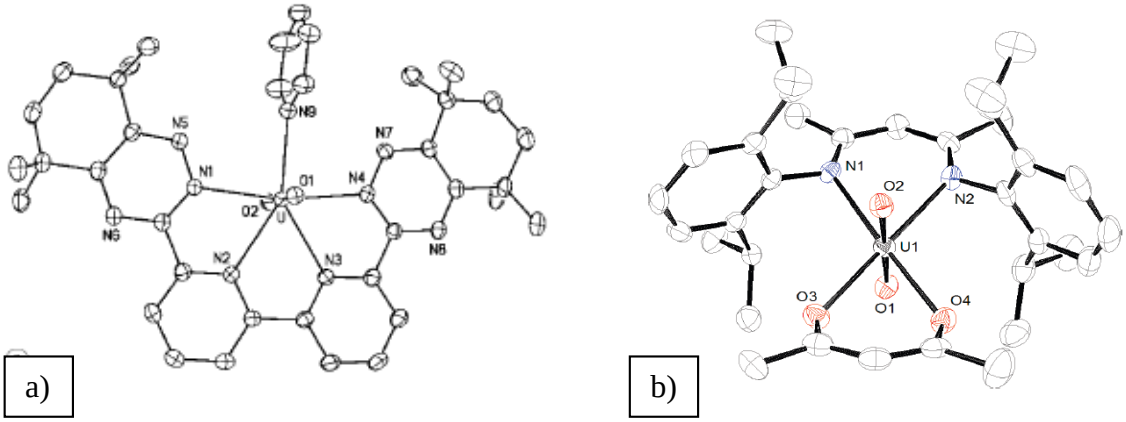

Figure 10: Two examples of uranyl(VI) complexes with multidentate ligands. In a) the chelating ligand fails to sterically occupy the whole equatorial coordination plane, hence a pyridine solvent molecule occupies the fifth coordination site because it is electronically favourable to do so;[29] b) represents the crystal structure of a more sterically demanding complex in which the uranyl equatorial plane is sterically saturated by a two bidentate ligands. These ligands prevent direct uranyl(VI) coordination by monodentate solvent molecules, despite the uranyl ion being electronically unsaturated.[39]

1.6 Introducing *CyMe$_4$-BTPhen*

As stated, recently there has been considerable interest in the community to design a ligand that could selectively extract the actinide elements from the lanthanide elements in order to design a next generation reprocessing procedure compatible with Gen IV reactor designs.[40] One such ligand that has shown promise in this regard is the CyMe$_4$-BTPhen ligand.[1] As shown in **Figure 11**, this is a tetradentate nitrogen donor ligand based on a phenanthroline moiety with two pendant 1,2,5-triazinyl arms pre-organised in a manner to envelop a metal cation in the cavity. On the end of each arm of the ligand is a cyclohexane group substituted with four methyl groups, dubbed a *CyMe$_4$* group. This functionality is purely to increase the solubility of the ligand in organic solvents, although its specific design does protect it somewhat against radiolysis.[41] BTPhen was developed at Reading University by Lewis et al.[1] and this group is actively involved in all aspects of the research into the coordination chemistry of this species through the MBASE consortium, of which the author is also affiliated.

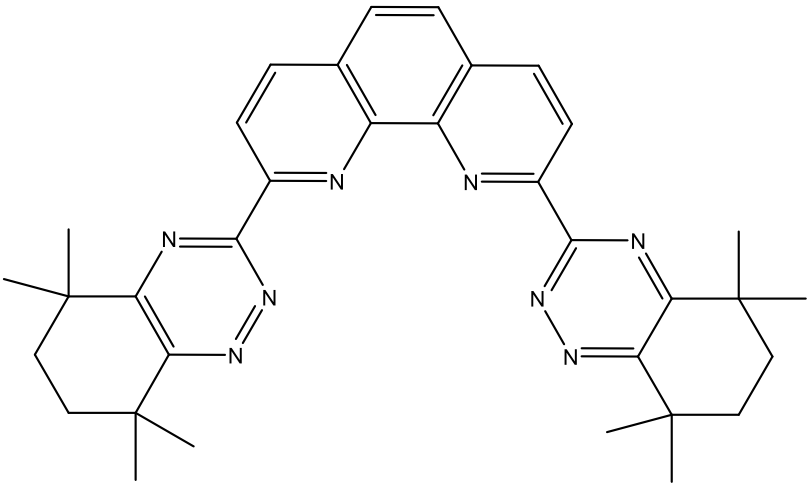

Figure 11: Structure of *CyMe*$_4$-BTPhen. Image generated using ChemBioDraw.[42]

This ligand was borne out of a quantitative structure activity relationship study that used a combinatorial technique more traditionally applied to medical screening research to identify ligand types that were likely to demonstrate the properties desired.[43] Over multiple synthetic iterations of the ligand backbone (to control structure) and periphery (to control solubility) the ligand presented in **Figure 11** was identified as a suitable target for a process.[44–49] Such a process employing the bipyridine bridged analogue of BTPhen, *CyMe*$_4$-BTBP, has since been developed and refined by Aneheim et al.[50] on pilot scale. Over the past few years a large amount of data about the speciation of the phenanthroline derivation of this ligand and its structural relatives has been amassed as part of the thesis of a colleague, D.M. Whittaker (DMW).[3] Chapter 4.2, acts as a complement to the thesis of DMW by way of studying the solution phase chemistry of the BTPhen in systems containing actinyl ions in the presence of competing ligands, specifically chloride in order to provide a molecular understanding of the speciation observed and the nature of the electronic interactions occurring in these coordination complexes.

1.7 An Introduction to Computational Chemistry

This chapter introduces the implementation of electronic structure theory used to model the complexes discussed in this report, density functional theory (DFT), with an aim to highlight the major assumptions in the derivation which lead to discrepancies between theoretically and experimentally derived quantities.

1.7.1 Fundamentals of Molecular Orbital Theory

The quantised nature of elemental absorption and emission spectra demonstrates that bound electrons have discrete energies.[51] This phenomenon has no analogy in classical mechanics,

where the energy of each electron can vary continuously. This discrepancy relates to the ability of an electron to display wave-like behaviour in addition to the classically assumed particle-like behaviour. The field of quantum mechanics (QM) was developed to address this dichotomy.

The basis of QM is the electronic wave function, Ψ, which contains all the information about the particle it represents. The nature of the wave function is difficult to comprehend, however it is useful to note that when dealing in real numbers the square of the wave function relates to the electronic probability density. Hence, the integral of $|\Psi^2|$ over a region of three dimensional space within a molecule or atom represents the probability an electron will be found within that region. When integrated over all space, this probability must be unity, hence **Equation 8**.

$$\int \Psi^2 d\mathbf{r} = 1 \qquad \textbf{(8)}$$

1.7.1.1 The Hamiltonian Operator

The time-independent Schrödinger equation, shown in **Equation 9**, can be used to obtain the wave function. The Hamiltonian operator acts on the wave function in order to return the associated energy (eigenvalue).

$$\hat{H}\Psi = E\Psi \qquad \textbf{(9)}$$

The electronic Hamiltonian, $\hat{H}$, is constructed from the individual energetic interactions which contribute to the overall energy of the system. The main contributors to this energy are shown in atomic units in **Equation 10**. The first term represent the total kinetic energy of all of the electrons in the system, the second term represents the total Coulombic attraction between the electrons and nuclei in the system and the third term represents is the total inter-electronic repulsion in the system.

$$\hat{H} = -\frac{1}{2}\sum_{i}^{electrons}\nabla_i^2 - \sum_{i}^{electrons}\sum_{A}^{nuclei}\frac{Z_A}{r_{iA}} + \sum_{i<j}^{electrons}\frac{1}{r_{ij}} \qquad \textbf{(10)}$$

In **Equation 10**, the indices i and j run over electrons, and A runs over nuclei; Z is the number of protons in the nucleus, r_{ij} is the distance between the electrons i and j, R_{iA} is the distance between electron i and nucleus A and ∇^2 is the Laplacian operator.

1.7.1.2 Approximations

The Schrödinger equation can only be solved exactly for one nucle, one electron systems, so it is necessary to enforce some approximations in order to render the equation soluble for many electron cases. One of the most important approximations is the Born-Oppenheimer

(BO) approximation, which states that since the electrons move much faster than the nuclei, they can be assumed to move within a static field of nuclei. The direct implication for the Hamiltonian operator is that the kinetic energy of the nuclei can be ignored and the repulsion between nuclei simply evaluated as a constant. The Schrödinger equation now becomes the *electronic* Schrödinger equation. Application of the BO approximation is justified in most cases as under standard conditions nuclear motion is negligible relative to the movement of electrons.

Another issue is that calculating the interaction between electrons becomes very expensive in systems which have many electrons. In order to simplify these interactions, we make a second assumption that each electron moves within a static field of all others. This is the *independent electron model*, which assumes that each electron in a molecular or atomic system can be treated individually; hence, the total electronic Hamiltonian, $\hat{H}$, can be expressed as the sum of the individual electron Hamiltonians. Unfortunately this assumption is more detrimental than the former, and many quantum computational methods make attempts to recover this lost 'correlation energy'.

1.7.1.3 Hartree Product

In the independent electron model, electrons are considered to be uncorrelated. This allows the total many electron Hamiltonian to be decomposed into its component one electron Hamiltonians which consider some degree of inter-electronic repulsion without explicitly treating the correlated motion of any two electrons.[51] In **Equation 11**, below, h_i represents the one electron Hamiltonian operator.

$$\hat{H} = \sum_i h_i \qquad \textbf{(11)}$$

Each single electron Hamiltonian has a related one electron wave function, ψ_i, which it acts upon to give a one electron eigenvalue, ε_i. Another name often given to a one electron wave function is a molecular orbital (MO), the square of which represents the probability that the electron will be found at a particular position.[52] The one electron eigenvalue represents the energy of the MO, which is equivalent to the energy of the electron.[52,53] Therefore, this assumption directly allows the construction of MO diagrams in which the quantised nature of electronic structure is most apparent.

If it is assumed that the one electron Hamiltonians may be summed to provide the many electron Hamiltonian, then the same must be true of the one electron energies. In the equation below, ε_i are the one electron energies.

$$E = \sum_{i}^{N} \varepsilon_i \qquad \textbf{(12)}$$

The assumed equivalent operation to combine the one electron wave functions into a many electron wave function is to find their product, as shown in **Equation 13**. This is known as the Hartree Product.

$$\Psi = \prod_{i}^{N} \psi_i \qquad \textbf{(13)}$$

However, this is not sufficient since wave functions constructed in this manner violate a set of constraints fundamental to relativistic QM; the Pauli Exclusion Principle.

1.7.1.4 The Pauli Exclusion Principle

Not only are electrons specified by their coordinates in space, they have an additional property; spin. The Pauli exclusion principle takes into account this additional property by stating that any two electrons must be antisymmetric upon their exchange in a molecular system.[51,52] An example of this antisymmetric principle is provided in **Equation 14**, in which the effect on the wavefunction of exchanging the positions of two electrons in a two electron system is demonstrated. In essence, the antisymmetric principle means that no two electrons can share the same set of quantum numbers.

$$\Psi(x_1, x_2) = -\Psi(x_2, x_1) \qquad \textbf{(14)}$$

In order to include this effect in the calculations, a Slater determinant (SD) must be used (see **Equation 15**), which mathematically enforces the following points on the system:

- All electrons are indistinguishable: in the SD, all *N* electrons occupy all *N* spin orbitals.
- Electrons must be antisymmetric upon exchange of their coordinates: if two rows of the SD are interchanged, the sign of the determinant changes.
- Pauli principle: if two electrons occupy the same orbital, this means two columns of the SD are equal and the value of the determinant is zero.

$$\Psi(x_1, x_2, \ldots x_N) = \frac{1}{\sqrt{N!}} \begin{vmatrix} \phi_1(x_1)\ \phi_2(x_1) \cdots \phi_N(x_1) \\ \phi_1(x_2)\ \phi_2(x_2) \cdots \phi_N(x_2) \\ \vdots \quad\ \vdots \quad \ddots \quad \vdots \\ \phi_1(x_N)\phi_2(x_N) \cdots \phi_N(x_N) \end{vmatrix} \qquad \textbf{(15)}$$

In Hartree-Fock (HF) theory, individual electrons feel the presence of other electrons as a mean field as well as through the effects of electron exchange, also known as the Fermi

correlation. In this way, parallel electron spins are correlated but not antiparallel spins. The correlation of electrons with parallel spins results in the notion of a 'Fermi hole', which describes the repulsion of said electron pairs so that they are less likely to be found in close proximity to one another.

1.7.1.5 Hartree-Fock Theory

Conveniently, the variation theorem states that the energy of a trial wave function will always be greater than or equal to the actual ground state; the energy is effectively *bounded from below*.[52,53] With this in mind, it is necessary to consider the most effective way to represent a trial wave function. A convenient procedure is the linear combination of atomic orbitals (LCAO) approach, in which exact functions that describe the shapes of the hydrogenic orbitals about each nucleus in a molecular system are used.[51,52] It is assumed a linear combination of these basis functions, which are a mathematical analogy for the atomic orbitals, are appropriate building blocks to use to construct the MOs.[52] This operation is described by **Equation 16**.

$$\Phi = \sum_{i=1}^{N} c_i \phi_i \qquad \textbf{(16)}$$

Where Φ represents the trial molecular wave function formed as a linear combination of exact atomic wave functions, ϕ_i, which are weighted according to the coefficients, c_i.

$$\hat{f}_i \phi_i = \varepsilon_i \phi_i \qquad \textbf{(17)}$$

Once a trial wave function has been constructed, the HF equation (shown above in **Equation 17**) is solved via a self-consistent field (SCF) procedure. In this equation, $\hat{f}_i$ represents the one electron Fock operator, where the sum of all of the one electron operators provides the Fock operator for the system as a whole, $\hat{F}$. The one electron Fock operator has the form shown in **Equation 18**, in which the first term represents the kinetic energy of the i^{th} electron, the second term represents the Coulombic attraction between the i^{th} electron and the A^{th} nucleus and the third term represents the Hartree-Fock potential, υ_i^{HF} . The Hartree-Fock potential represents the averaged field seen by the i^{th} electron due to all the other electrons in the system. In this way υ_i^{HF} accounts for a degree of electron correlation not accounted for in the Hartree product. The introduction of υ_i^{HF} into the Fock operator complicates the process of solving the Hartree-Fock equation, in that the external potential, υ_i^{HF} , depends on the orbitals of all of the other electrons in the system, yet in order to

calculate the orbitals of the system, υ_i^{HF} itself must be known. Thus, the HF equations must be solved iterative manner by generating an initial guess of the orbitals, then using this ansatz to calculate the average field for the system, thereby allowing the HF eigenvalue equation to be solved in order to generate a new set of orbitals. The process may then be iterated until self-consistency is achieved, as per a pre-determined set of criteria. This is known as the self-consistent field (SCF) procedure.

$$\hat{f}_i = -\frac{1}{2}\nabla_i^2 - \sum_A^{nuclei} \frac{Z_A}{r_{iA}} + \upsilon_i^{HF} \qquad \textbf{(18)}$$

The final set of orbitals obtained is the best single determinantal orbital set within the size of basis set employed.

1.7.2 Basis Sets

As explained previously, in the LCAO procedure the exact functions used are the one-electron-one nucleus solutions to the Schrödinger equation, solved for the set of quantum numbers thought to best describe the atom modelled. For example, to model a proton it may be sufficient to only localise a single hydrogenic *s* function at its centre, whereas more complicated atoms such as carbon may be best represented by multiple *s* and *p* type functions. In theory, a set of basis functions can be infinite in size as its only purpose is to provide enough mathematical flexibility to allow electrons to arrange themselves in the lowest energy configuration. However, in practice basis sets must be limited due to computational constraints and thus the problem arises of how to accurately describe the whole molecular space using the minimum number of basis functions, since increasing the number of basis functions scales the computational expense as N^4 in the HF method.[51] Different groups have offered solutions to this conundrum using atom-centred functions specifically; this includes the work by the groups of Dunning[54,55] and Pople.[56–58]

The most accurate functions able to describe the hydrogenic orbitals are those originally described by Slater.[59] The radial decay of Slater type orbitals (STOs) is described by **Equation 19**, where *r* represents the radius of the atomic centred function.

$$STO \propto e^{-r} \qquad \textbf{(19)}$$

Whilst accurate, STOs are computationally expensive to evaluate, hence S. F. Boys[60] proposed the use of Gaussian type orbitals (GTOs) for this purpose. Although individually, GTOs are a poor description of the hydrogenic orbitals, several may be combined in order to generate a reasonable approximation to a single STO. It is worthwhile to construct basis functions from multiple GTOs as opposed to a single STO, as GTOs are much more easily

evaluated analytically. This is an important means of making HF calculations more efficient, however in other applications, such as density functional theory (DFT), GTOs are typically solved numerically across an integration grid for practical reasons, thereby significantly reducing the benefit of using these functions over STOs. The radial decay of GTOs is described by **Equation 20**.

$$GTO \propto e^{-r^2} \qquad \textbf{(20)}$$

The act of combining several Gaussian primitives to represent an AO is known as *contraction*.

1.7.2.1 Zeta and Split Valence Basis Sets

The original basis sets developed represented the core and valence electrons using the same contraction scheme, thus drawing no differentiation between their relative involvements in bonding.[61] As computational methods developed, Pople et al. proposed that quantum chemical calculations could be made more efficient by allowing more flexibility in the valence region than the core, since the valence region of an AO is more susceptible to perturbation by external stimuli. This resulted in the development of the split valence type basis sets.[56,58] Additional flexibility is afforded by representing the valence region as a weighted mixture of two functions, one tight and one more diffuse. These functions have different orbital exponents, ζ, and therefore penetrate different regions of space more effectively. This orbital description is referred to as a split valence double-ζ basis set. This principle may be extended by putting more functions into the valence region; when three basis functions are used to represent the valence region it is known as a triple-ζ basis set, four functions – quadruple-ζ etc.

The notation introduced by the Pople group is used to describe many basis sets. This notation describes how many Gaussian primitives are used to represent the core and valence regions as well as how many are included in each contraction. The notation 6-31G indicates that on each atom the core orbitals are represented as a contraction of six primitive Gaussian functions and the valence region is represented as a weighted linear combination of three contracted Gaussians and a primitive, both with different exponents. On the other hand, 6-311G represents the valence region as weighted linear combination of three contracted primatives and two additional individual primatives each with a different exponent. In this way, 6-311G is an example of a triple-ζ basis set.

1.7.3 Fundamentals of Density Functional Theory

Since the development of the Schrodinger equation, people have looked for methods to calculate the energy of a molecule without relying on the abstract concept of a wave function. One such methodology is DFT which uses an observable quantity; the electron density, ρ, **Equation 21**. The fact that the electron density integrated over all space is equal to the total number of electrons, N, is an indication that this quantity may be appropriate for the formation of the Hamiltonian operator.

$$N = \int \rho(\mathbf{r})\, d\mathbf{r} \qquad \mathbf{(21)}$$

1.7.3.1 The Hohenberg-Kohn Existence Theorem

The Hohenberg-Kohn existence theorem states that the ground state electron density determines the external potential and thus, the energy, by demonstrating that contrary assumptions lead to impossible results. This is a conceptually reasonable result, as one would expect the distribution of electron density about a molecule to mimic the positions and charges of the nuclei. Hohenberg and Kohn also showed that the ground state energy can be obtained variationally, analogous to the variation theorem in MO theory.

1.7.3.2 The Kohn-Sham Self-Consistent Field Methodology

The methodology defined so far still relies on finding the energy as an expectation value of the Hamiltonian, therefore to this point DFT represents no simplification over MO theory. In order to avoid the two-electron integrals that are the bottle neck of MO theory, Kohn and Sham proposed that the Hamiltonian operator of DFT should be one describing a non-interacting system.[53] This is useful because, in a manner analogous to HF MO theory, for a non-interacting system:

1) The Hamiltonian can be expressed as the sum of the one electron Hamiltonians;
2) The total energy of the system can be calculated as the sum of the one electron eigenvalues and;
3) The one electron eigenvectors may be combined into a Slater determinant to represent the wavefunction of the system as a whole.

Kohn and Sham thereby proposed a route to provide the interacting energy of a real system by initially calculating the energy of a fictitious non-interacting system that has the same density as the real interacting system. As the functional forms of the classical kinetic energy and Coulombic interactions are known and easily calculated, this allowed Kohn and Sham to separate the functional into the constituent parts, as shown in **Equation 22**. The functionals shown in **Equation 22** may be separated into two broad groups; known classical

functionals and unknown exchange-correlation functionals. Where the latter account for all interactions in the real system that are not described by the classical non-interacting description of the system.

$$E[\rho(\boldsymbol{r})] = T_{ni}[\rho(\boldsymbol{r})] + V_{ne}[\rho(\boldsymbol{r})] + V_{ee}[\rho(\boldsymbol{r})] + \Delta T[\rho(\boldsymbol{r})] + \Delta V_{ee}[\rho(\boldsymbol{r})] \quad \textbf{(22)}$$

In the above equation, the first three terms on the right hand side of the equation refer to the kinetic energy of the non-interacting electrons, the Coulombic attraction between the nuclei and the electrons and the classical electron-electron repulsion, respectively. The remaining two terms are corrections applied to the non-interacting energy in order to account for the interaction of electrons in a real system. These terms thereby encompass all of the error in the functional associated with describing the system as non-interacting. These terms represent, respectively, the required correction to the kinetic energy and all non-classical corrections required to describe inter-electronic repulsion. Collectively, these corrections are known as the exchange correlation potential, V_{XC}. Where V_{XC} is the functional derivative of the exchange correlation energy with respect to the density of the system, as defined in **Equation 23.**

$$V_{XC} = \frac{\delta E_{XC}}{\delta \rho} \quad \textbf{(23)}$$

The terms describing classical nuclear-electron and electron-electron interactions are calculated using the integrals presented in **Equations 24** and **25**, respectively.

$$V_{ne}[\rho(\boldsymbol{r})] = \sum_{A}^{nuclei} \frac{Z_A}{|\boldsymbol{r} - \boldsymbol{r_A}|} \rho(\boldsymbol{r})\, d\boldsymbol{r} \quad \textbf{(24)}$$

$$V_{ee}[\rho(\boldsymbol{r})] = \frac{1}{2} \int\int \frac{\rho(\boldsymbol{r}_1)\rho(\boldsymbol{r}_2)}{|\boldsymbol{r} - \boldsymbol{r_A}|} d\boldsymbol{r}_1 d\boldsymbol{r}_2 \quad \textbf{(25)}$$

Where, Z_A represents the nuclear charge on atom A, and $\boldsymbol{r_1}$ is an integration variable running over all space. By analogy to the wave function of MO theory, it is reasonable to assume that the density can be represented as a combination of orbitals, χ_i. This leads to **Equation 26**, which allows the energy functional in **Equation 22** to be rewritten in terms of operators that act on density orbitals, **Equation 27**.

$$\rho = \sum_{i<j}^{elecctrons} \langle \chi_i | \chi_j \rangle \quad \textbf{(26)}$$

$$E[\rho(\mathbf{r})] = \sum_{i}^{electrons}\left(\langle\chi_i|-\frac{1}{2}\nabla_i^2|\chi_i\rangle-\langle\chi_i|\sum_{A}^{nuclei}\frac{Z_A}{|\mathbf{r}_i-\mathbf{r}_A|}|\chi_i\rangle\right)+ \sum_{i}^{electrons}\langle\chi_i|\frac{1}{2}\frac{\rho(\mathbf{r}')}{|\mathbf{r}_i-\mathbf{r}'|}|\chi_i\rangle+E_{xc}[\rho(\mathbf{r})] \quad \textbf{(27)}$$

It is possible to break down **Equation 27** further, by assuming that the many electron Kohn-Sham (KS) Hamiltonian, H^{KS}, may be constructed from the one-electron KS Hamiltonians, $\hat{h}_i^{KS}$, as shown in **Equation 28**.

$$\hat{h}_i^{KS} = -\frac{1}{2}\nabla_i^2 - \sum_{A}^{nuclei}\int\frac{Z_A}{|\mathbf{r}_i-\mathbf{r}_A|}+\int\frac{\rho(\mathbf{r}')}{|\mathbf{r}_i-\mathbf{r}'|}d\mathbf{r}'+V_{XC} \quad \textbf{(28)}$$

Equation 28 thereby represents the KS one electron Hamiltonian. As stated, this operator may be used in an analogous way to the Fock operator of HF theory in order to calculate the total energy of the interacting system. The similarity between the HF and KS approaches do not end here as in order to calculate the exchange correlation energy of the system the density must be known, but in order to calculate the density of the system an appropriate set of orbitals must be known and these depend on the potential of the system, thus the KS equations must also be solved iteratively. This is the basis of the KS-SCF procedure.

1.7.3.3 Approximating E_{XC}: The Exchange Correlation Energy

As previously stated, the many body nature of the integrals which describe electron correlation and exchange are often too complex to evaluate explicitly. Therefore, these corrections as well as other inter-electronic effects not accounted for by the exact non-interacting KS operators are lumped together into an exchange-correlation energy operator, V_{XC}, defined in **Equation 23**.

The functional dependence of the exchange correlation energy, E_{XC}, on the electron density is defined as the interaction between the electron density and the 'energy density', ε_{XC}. Where the energy density is a per particle density dependent on the electron density at a point.[51] This relationship is expressed in **Equation 29**.

$$E_{XC}[\rho(\boldsymbol{r})] = \int\rho(\boldsymbol{r})\varepsilon_{XC}[\rho(\boldsymbol{r})]d\boldsymbol{r} \quad \textbf{(29)}$$

1.7.3.4 The Local Density Approximation

An early approximation made to evaluate the functional in **Equation 29** was the local density approximation (LDA). A fictitious system known as the uniform electron gas (UEG) is taken, defined as containing N uniformly distributed electrons in a homogeneous positive charge. The LDA assumes that the energy density, ε_{XC}, at a molecular position, $\boldsymbol{r}$, may be

calculated using only the electron density, ρ, at that position. The LDA can be extended to account for spin, which is known as the local spin density approximation (LSDA).

1.7.3.5 The Generalised Gradient Approximation

An obvious limitation of the LDA lies in the anisotropy of the exchange-correlation energy density across a molecule. In order to account for local changes in electron and energy densities, the LDA may be corrected by accounting for the gradient of the electron density about a position, ***r***, which is known as the generalised gradient approximation (GGA).

A widely used GGA exchange functional of this form is 'B' and was developed by Becke.[62] This exchange functional incorporates a single parameter which has been optimised to reproduce the known exchange energies of the noble gas atoms He - Rn.

GGA correlation functionals need not merely correct the LDA. For example, Lee Yang and Parr's GGA correlation functional, LYP, computes the correlation energy entirely without applying the LDA.[63] LYP is fitted to the helium atom and contains four empirical parameters.

The wide array of separate exchange and correlation functionals derived in the literature provides a great amount of choice to the computational chemist as to which combination to use. Exchange and correlation functionals tend to be used in tandem, for example, the combination of the two above gives the BLYP exchange-correlation functional.

1.7.3.6 Adiabatic Connection Methods

To this point, we are aware of two distinct states of correlation and exchange in a system; the non-interacting reference system and the interacting real system. As opposed to this discrete model, imagine that the extent a system interacts with itself is continuously variable. Such a model would be bounded by the exchange energy of the non-interacting system and the exchange-correlation energy of the fully interacting system. Between these boundaries, there is a number of states where some degree of electron exchange and correlation is accounted for and some is neglected. The Hellmann-Feynman theorem defines the degree of interaction using a variable, λ, where $\lambda=0$ represents the non-interacting KS reference system and $\lambda=1$ represents the totally interacting real system, see **Equation 30**.[51]

$$E_{XC} = \int_0^1 \langle \Psi(\lambda) | V_{XC}(\lambda) | \Psi(\lambda) \rangle d\lambda \qquad \textbf{(30)}$$

Should this relationship be plotted graphically, it may take a form similar to that in **Figure 12**.

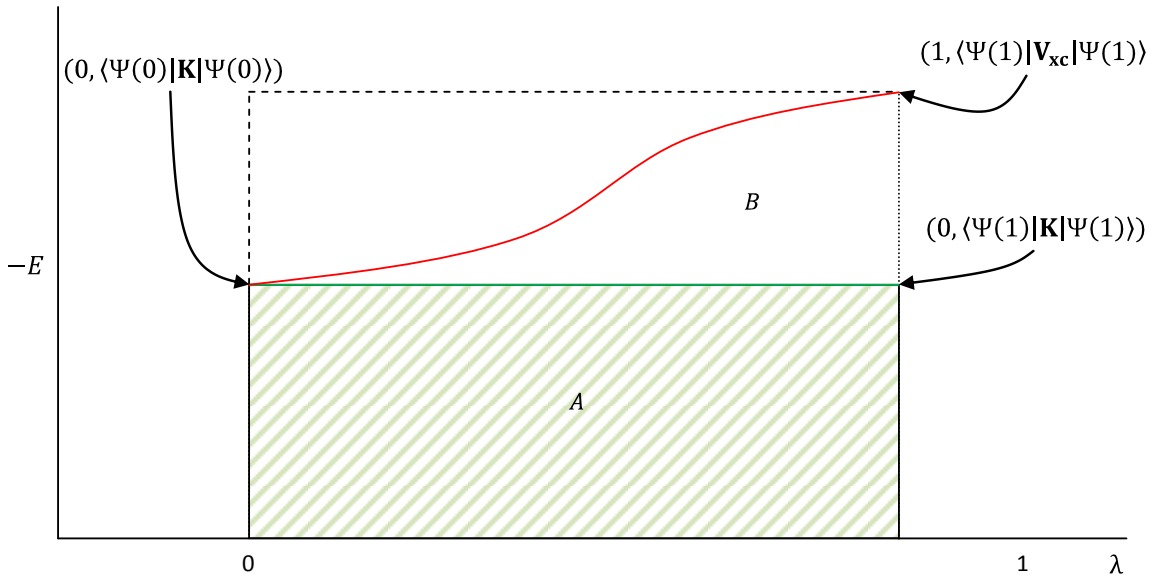

Figure 12: Geometrical schematic used to aid the interpretation of the Hellmann-Feynmann equation, **Equation 30**. The area underneath the curve is defined as the sum of the areas *A* and *B*. The area of *A* is computed as the expectation value of the HF exchange operator acting on the SD wave function of the non-interacting system. The area of *B* is approximated as some fraction of the dotted rectangle, where the solution to $\langle \Psi(1)|V_{XC}|\ \Psi(1)\rangle$ has been approximated using a DFT calculation. Diagram adapted from Cramer, *Essentials of Computational Chemistry*.[51]

In **Figure 12**, the area under the curve is defined by the expectation value of $V_{XC}(\lambda)$, i.e. E_{XC}. The lower bound on this system where $\lambda=0$ can be determined exactly by solving the KS SCF equations to calculate the ground state orbitals. When these orbitals are acted upon by the HF exchange operator the expectation value is the exact exchange energy of the system, also known as the HF exchange, E_X^{HF}. This HF exchange energy is equal and exact in both interacting and non-interacting systems. Graphically, E_X^{HF} defines the area of a rectangle, *A*.[51]

Following on, in order to calculate E_{XC}, the whole area under the expectation value curve between the limits of λ must be determined. This area includes that covered by rectangle *A*, thus $E_{XC}=E_X^{HF}+B$.

It is not known how E_{XC} varies as a function of λ, therefore the shape of the curve in **Figure 12** is essentially unknown. Despite this, it can be approximated as some fraction, *z*, of the area of the upper rectangle. Since we do not know the expectation value of the interacting system, $\langle\Psi(1)|V_{XC}|\Psi(1)\rangle$, it must be approximated. Assuming *z* to be an empirical constant that can be optimised, one may approximate $\langle\Psi(1)|V_{XC}|\Psi(1)\rangle$ using a DFT exchange-correlation functional, denoted E_{XC}^{DFT} (see **Equation 31**). This defines the second rectangle as having area E_{XC}^{DFT}-E_X^{HF} when integrated between 0 and 1 with respect to λ.[51]

$$E_{XC} = E_X^{HF} + z(E_{XC}^{DFT} - E_X^{HF}) \qquad \textbf{(31)}$$

Introducing the constant a to this expression, defined as a=(1-z), leads to **Equation 32**. This expression suggests that hybridised HF and DFT functionals may be better approximations to E_{XC} those generated using pure HF or DFT procedures.

$$E_{XC} = (1-a)E_{XC}^{DFT} + aE_{X}^{HF} \qquad \textbf{(32)}$$

Though the adiabatic connection method (ACM) is by no means exact, it does account for the majority of the exchange-correlation energy in a system, thereby significantly reducing the error associated with pure DFT approaches.[51]

The initial work into the ACM was conducted by Becke and he approximated the curve in **Figure 12** to be a straight line, thereby giving a an initial value of 0.545.[64] Over time the value of a has been optimised by different groups using different functionals for use in different chemical situations. Indeed the number of empirical parameters used to define E_{XC} has also been varied in order to allow exchange and correlation to be treated separately using the ACM. Becke pioneered this work by developing the three parameter functional expression, **Equation 33**. This functional is constructed using Becke's exchange functional and the PW91 correlation functional, the combination is usually known as B3PW91.

$$E_{XC}^{B3PW91} = (1-a)E_{X}^{LSDA} + aE_{X}^{HF} + b\Delta E_{X}^{B} + E_{C}^{LDSA} + c\Delta E_{C}^{PW91} \qquad \textbf{(33)}$$

Becke optimised the three parameters a, b and c to 0.2, 0.72 and 0.81, respectively.[51]

Functionals designed using the ACM are generally referred to as *hybrid functionals*, owing to the use of both HF exchange and DFT exchange-correlation in their design. One of the most widely used hybrid functionals today was developed by Stevens *et al.*[65] and is based on the model proposed by Becke with his B3PW91 functional. This functional is known as B3LYP and as the name suggests it is a three parameter combination of the B exchange functional with the LYP correlation functional. Stevens et al. did not optimise the parameters for B3LYP, instead opting to use those optimised for B3PW91. However, the performance of B3LYP is still remarkably good for a wide range of applications. The B3LYP model is defined by **Equation 34**.[65]

$$E_{XC}^{B3LYP} = (1-a)E_{X}^{LSDA} + aE_{X}^{HF} + b\Delta E_{X}^{B} + (1-c)E_{C}^{LDSA} + c\Delta E_{C}^{LYP} \qquad \textbf{(34)}$$

1.7.4 Pseudopotentials

The assumptions stated to this point are sufficient to allow relatively inexpensive calculations to be performed on light atoms. However, heavy atoms still pose a computational challenge owing to the large number of basis functions required to model the increased number of electrons. For this reason, certain groups have developed effective core

potentials (ECPs).[66,67] The theory behind ECPs is based on the frozen core approximation, which states that the core region of an atom is less sensitive to the external environment than the valence electrons and therefore can be represented using a lower level of theory.[68]

The definition of the core region is vague, but it generally refers to the electrons that are perturbed a negligible amount on approach of an external stimuli. Hence, the definition of the ECP core electrons changes across the periodic table. For example, defining the core electrons of an early actinide element as *those that occupy completely filled electronic shells* leads to significant errors in predicted properties. For example, using this standard core definition, the general formula representing the valence electronic structure of uranium would be [Rn] $7s^2\ 5f^3\ 6d^1$. However, in both transition metals and actinides it has been shown that there are significant correlation effects between the valence electrons and those of the fully occupied 'semi-core' orbitals of similar radial extent.[66,69] This correlation leads to errors in the molecular properties predicted using this core definition. These findings have led to a contraction of the ECP core size for actinides through the development of so called 'large core' (LC) and 'small core' (SC) ECPs, which include 78 and 60 electrons in the core respectively.[66,70]

For the case of uranium, the valence region of a LC ECP model has the electronic structure $6s^2\ 6p^6\ 5f^3\ 6d^1\ 7s^2$, whereas a SC ECP model considers the electrons $5s^2\ 5p^6\ 5d^{10}\ 6s^2\ 6p^6\ 5f^3\ 6d^1\ 7s^2$ explicitly. It should be clear that an increase in the number of electrons considered explicitly leads to a concomitant increase in the computational effort required.

There are two categories of ECP in wide usage; model potentials (MPs) and pseudopotentials (PPs). Both types of ECP are parameterised in order to represent the orbitals of all electron (AE) calculations.[68] A major difference between the two is that MPs aim to replicate the radial nodal structure of the AE valence region exactly, whereas PPs further reduce the number of basis functions required to represent the ECP by simplifying the atomic radial nodal structure.

PPs in turn fall into two categories, known as energy consistent and shape consistent PPs.[68] Energy consistent PPs are parameterised in order to reproduce the energetic properties of an atomic system as generated using a high level of AE theory, generally an excitation spectrum. Conversely, shape consistent PPs are fitted to the shape of the orbitals generated using an AE model.

1.7.4.1 Pseudopotentials and Relativity

PPs have found widespread use recently not only as a method to reduce computational expense, but also as a vessel to introduce the most important relativistic effects into calculations using standard non-relativistic codes.[51,70] This is achieved using parameterisation; if an energy consistent PP is fitted to a quasi-relativistic or fully relativistic calculation, then relativistic effects are intrinsically incorporated into the PP, and will be accounted for in the calculated orbital energies. Here, the term quasi-relativistic refers to PPs fitted to appropriate solutions of the scalar relativistic Wood-Boring (WB) equation, which accounts for mass-velocity and Darwin terms, but does not explicitly consider the effects of SO coupling.[66,70] As the name suggests fully relativistic PPs are fitted to calculations in which all the effects of relativity are explicitly accounted for as solutions to the four component Dirac equation or two component approximations to it.[70] Each PP is provided with a bespoke basis set that is optimised for computational efficiency and accuracy.

2 COMPUTATIONAL DETAILS

2.1 Computational Acknowledgements

All of the calculations presented in this study were carried out using the Gaussian 09 software, revision B.01.[6] Population analyses have been carried out under the natural bonding orbital (NBO) framework (version 3.1)[71,72] as incorporated in Gaussian 09.[6] The corresponding visualisation package GaussView 5[13] was used to construct input decks and visualise results alongside the text editor Notepad++.[73] All of the calculations presented here were carried out using the Computational Shared Facility (CSF), of the University of Manchester, to this end the author would like to acknowledge the assistance provided by IT Services, University of Manchester.

2.2 Defining the B3LYP/B1 Functional-Basis Set Combination

All models discussed in this report were optimised using DFT, specifically an unrestricted formalism of the B3LYP functional[63,64,65,75] as parameterised in Gaussian 09,[6] unless stated otherwise. Scalar relativistic properties of the uranium atom were taken into account using the Stuttgart 60 electron SC-ECP parameterised to be energetically consistent with quasi-relativistic calculations.[66,76] In all calculations this SC-ECP was used along with its recommended basis set.[76,77] The *g*-functions in this basis were retained in order to act as polarisation functions for the *f*-manifold occupied in the reduced models studied. SO effects were not taken into account in the calculations explicitly, although the effect of including SO corrections on the calculated energies (as calculated by others) is discussed.[78,79] Unless otherwise stated, all other atoms were optimised using the Pople-type 6-31G(d,p) basis set that includes a set of *d*-type polarisation functions on second row atoms as a set of *p*-type polarisation functions on first row atoms.[80–84] In calculations where a proton was attached to a hydrogen bond donor atom i.e. *O* or *N*, it was described using the Pople-type 6-311++G(d,p) basis in order to provide the proton with the diffuse function it may require to describe the hydrogen bonding interaction.[85]

The above combination of basis sets will be referred to as the B1 basis set from this point onwards. Furthermore, when used in conjunction with the B3LYP functional, as is typically the case in this study, this pairing will be denoted as the B3LYP/B1 functional-basis set combination. The B3LYP/B1 combination will typically be used for structural optimisations owing to its relatively compact basis set. Using the B1 basis set, a typical uranyl-BTPhen complex will be described by around 1000 basis functions. As is necessary, the frequency

calculations required to confirm that the optimised structures lie within potential minima and that are used to generate thermodynamic corrections will be carried out at the same level of theory as the optimisation procedure.

2.3 Defining the B3LYP/B2 Functional-Basis Set Combination

In this study, single point (SP) calculations of the absolute energy of a system were carried out using a larger basis set on the *C, H* and *N* atoms and uranyl O_{yl} atoms than used for structural optimisations. The basis set employed is the def2-TZVP basis set as defined by Ahlrichs et al.[86,87] As explained in Appendix 1, the *O* atoms of the dioxygen species in the complexes studied (dioxygen, superoxide, hydroperoxyl radical, peroxide, hydroperoxide) were described using a bespoke def2-TZVP basis set that had been augmented by a set of diffuse functions in order to aid in the description of the anionic character of this ligand in certain models. The standard diffuse function augmented def2-TZVPD[88] basis was employed initially, but this basis set was found to inadequately describe the anionic character of the peroxide ligand in counter-poise (CP) calculations.[89] This was corrected somewhat on inclusion an additional diffuse *s*-function on these atoms, two additional *p*-functions and one *d*-function with exponents with a value 1/3 of the next most diffuse. Thus creating a bespoke 'aug-def2-TZVPD' basis set that reduced the BSSE error as calculated using the counterpoise (CP) methodology to more reasonable values without complicating SCF convergence procedures to the point they were no longer practicable. The validity of the use of this basis and of the CP procedure as applied to this system in general is discussed in Appendix 1. As stated previously, the treatment of the uranium atom did not vary between the optimisation and single point calculations.

2.4 General Computational Methodology

Structures were optimised using Gaussian 09.[6] Initial guess structures were either generated using chemical intuition, a previously optimised structure or a crystallographically determined structure. When optimising to ground state geometries, the converged models were confirmed as minima on the potential energy surface (PES) by conducting an analytic frequency analysis as coded in Gaussian 09.[6] This procedure calculates the second derivative of the energy with respect to the nuclear coordinates, following which the absence of any negative modes in the predicted spectrum indicates the structure resides in a potential well, i.e. the standard 'second derivative test'. Conversely, when a reaction transition state (TS) was coveted, the correct geometry was confirmed by the presence of a single negative frequency mode that detailed the transformation of the geometry from one of predominantly

reactant character to one more closely resembling the desired product. No geometric symmetry constraints were employed during any optimisation unless otherwise stated.

The SCF calculations converged within geometry optimisation procedures were minimised to meet the 'conver=8' criterion in Gaussian 09,[6] which specifies root mean squared (RMS) changes in the density matrix must be lower than 1.0×10^{-8} and the maximum change in the density matrix and changes in the energy of the system must be lower than 1.0×10^{-7}. Conversely, the SCF calculations used to provide SP energies were converged to meet the 'conver=9' criterion as specified in Gaussian 09,[6] which tightens up each of these requirements by an order of magnitude.

Where possible, geometries were optimised to the 'tight' criterion in Gaussian 09,[6] which specifies convergence thresholds of the maximum force, RMS force, maximum displacement and RMS displacement of 1.5×10^{-5} Hartrees/Bohr, 1.0×10^{-5} Hartrees/Bohr, 6.0×10^{-5} Bohr and 4.0×10^{-5} Bohr, respectively. Such convergence typically gives rise to structures that differ in energy by around 1.0×10^{-9} Hartrees. Despite this aim, for some structures this level of convergence was not possible. In such cases geometries were converged to the standard convergence criterion as defined in Gaussian 09,[6] which specifies thresholds of the maximum force, RMS force, maximum displacement and RMS displacement of 4.5×10^{-4} Hartrees/Bohr, 3.0×10^{-4} Hartrees/Bohr, 1.8×10^{-3} Bohr and 1.2×10^{-3} Bohr, respectively. Such criteria typically result in structures that differ in energy by around 1×10^{-7} Hartrees.

Calculations were carried out using an unpruned integration grid of 200 radial shells with 434 angular points per shell on all atoms. This is in line with grids similar to the 'ultrafine' and 'superfine' grids in Gaussian 09 that have 99 radial and 590 angular points and 225 radial and 794 angular points per heavy atom, respectively. This 200434 integration grid is known within our group to treat the electronic structure of the actinides accurately at a reasonable computational cost.

Solvent calculations were carried out using the polarisable conductor continuum model (CPCM) implemented in Gaussian 09,[6] using the standard solute and solvent radii defined under the united atoms model (UA0). Use of this model allowed explicit spheres to be added to hydrogen atoms thought to be involved in intramolecular hydrogen bonds or otherwise deemed to require explicit treatment in the definition of the cavity. The standard solvent parameters for methanol were used in all the calculations detailed. Tests were conducted in which the solvent properties were modified to represent water in order to probe the

robustness of the solvent parameters chosen (see discussion below). This was necessary because the empirical results were gleaned from a mixed aqueous-methanolic solution. The change in dielectric on shifting the solvent model from methanol to water was shown to not change the calculated energies of the most highly charged species by more than 1.5 kcal mol^{-1}. Considering this deviation is relative to a typical solvation energy on the order of 100 kcal mol^{-1}, it is deemed an acceptable uncertainty. By way of consolation, this particular uncertainty will also likely benefit from a partial cancellation of errors in this study as the solvated energies will be used to calculate free energy changes between chemically similar species, thus accuracy of absolute solvation energy of each species is not paramount.

Population analyses were conducted using the NBO 3.9[71,72] and Mulliken schemes as implemented in Gaussian 09.[6]

2.5 A note on Single Point and Thermodynamic Energies

Single point SCF energies carried out on optimised structures provide the BO electronic energy of the system modelled. As such calculations are generally modelled in a vacuum, this is a technically a gas phase electronic energy and so is only of limited use when comparing models to empirical solution phase data. In order to aid comparison to experiment it is often prudent to utilise the principles of statistical thermodynamics in order to correct these electronic energies for the effects of temperature and disorder on their reactivity. This is achieved by calculating the enthalpy and entropy of the species involved and by using these quantities to calculate Gibbs free energy changes for the desired transitions at a given temperature. The thermodynamic quantities required to correct the electronic energy are automatically calculated by the Gaussian 09 program on specifying the frequency keyword. However, as will be discussed, in particular systems such quantities can be found in considerable error owing to the assumptions used to facilitate their evaluation, hence reducing confidence in the applicability of the corrections proposed.

The output of a thermochemistry analysis[90] in Gaussian provides corrections to the electronic energy in order to account to the molecular zero-point energy (ZPE), the thermal energy, the enthalpy (ΔH), the entropy (ΔS) and ultimately the Gibbs free energy, calculated as $\Delta G = \Delta H - T\Delta S$. Of these, only the ZPE has a firm basis in QM. Hence, the ZPE is the only quantity that can be added to all SCF electronic energies without fear of incorporating considerable error into the calculated energies.

The enthalpic correction corrects the electronic energy for the effects of temperature, pressure and volume. It is calculated as the sum of $k_B T$ and the rotational, translational,

vibrational and electronic corrections to the energy, E_r, E_t, E_v and E_e, respectively. Hence, **Equation 35**, below.

$$H_{corr} = E_r + E_t + E_v + E_e + k_B T \qquad \textbf{(35)}$$

In Gaussian 09[6] the quantities E_r and E_t are reduced to equal *3/2RT*, and $E_e = 0$. The latter is the result of the assumption in Gaussian 09 that the energy required to reach the first and higher excited states of the system in question is much greater than k_bT, and are hence inaccessible. Whilst this is likely to be a reasonable assumption for the complexes studied here, *cf* the silent UV-vis absorption spectrum for the uranyl(VI)-BTPhen complexes in reference,[3] it is a potential source of error in systems with low lying excited states. The vibrational correction to the energy is calculated by treating all vibrational modes of the system as simple harmonic oscillators (SHO). This is also generally a reasonable approximation, however, in systems containing hindered internal rotations this assumption can present a source of error in the calculated enthalpy. Despite this, as hindered internal rotations are by necessity low energy modes and because the contribution of a mode to the total enthalpy is directly proportional to its vibrational frequency, inclusion of such modes in error tends to have only a minor effect on the corrected enthalpy at room temperature (RT). As a result, the enthalpic corrections calculated by such an approach to thermochemistry are marginally less reliable than the ZPE corrected quantities in terms of sources of error, but importantly include some of the effects of temperature, pressure and volume on the species studied.

The entropy of the system is calculated similarly to the enthalpic terms, in that the corresponding entropic rotational, translational, vibrational and electronic terms, S_r, S_t, S_v and S_e, respectively, are calculated and summed to provide the total entropy of the system, **Equation 65**.

$$S_{corr} = S_r + S_t + S_v + S_e \qquad \textbf{(36)}$$

However, unlike the enthalpic correction, the contribution of a mode to the total entropy, with respect to its energy, follows an inverse proportionality. Thus, low energy modes that incorrectly describe hindered internal rotations as vibrations in the automated frequency analysis have an increased influence over the total entropy correction as compared to the enthalpic correction. Hence, if such modes are included in the correction, the incorporated error is able to alter the feasibility of reactions that proceed with intrinsically small changes in energy. This uncertainty therefore typically results in considerable doubt over the quality of calculated free energies in systems with many low frequency modes. Such doubt over

whether the calculated Gibbs free energies are a reasonable parameter to assay the feasibility reactions in computational chemistry has led to reaction pathways being described in the literature in a rather inconsistent manner, varying from some groups favouring to quote only the ZPE corrected energies,[91] whilst others provide reaction enthalpies[92] and those remaining proffer the free energy changes alone[93] or in combination with one of the other thermodynamic quantities.[94]

Despite such doubt in calculated free energies, it is possible to improve on their reliability by subtracting the contribution of modes that describe hindered internal rotations from the total enthalpy and entropy of the molecular system. This can be done in an automated manner to some extent in Gaussian 09 using the procedure described by Schlegel,[95] invoked in by the keyword 'freq=hindrot'. However, in some instances this procedure also fails, leaving the operator with the onus to manually inspect all low lying modes and determine whether they represent a hindered internal rotation. Following the definition in Gaussian 09, there are typically ~80 low frequency modes in each of the models studied herein and so a manual search for hindered rotations in this work would be time consuming. Such a search would be further complicated by the fact that modes containing hindered internal rotations are often coupled to the normal modes of the system. This means it would be inappropriate to completely subtract the contribution of this mode from the total enthalpy and entropy and warrants that a corrected hindered rotor free mode be calculated in its place. Hence, manual analysis and computation of the corrected partition functions for all low lying modes is a laborious process and furthermore through such a manual treatment is possible that even greater uncertainty would be introduced. For this reason, this study does not act to manually correct the calculated thermodymanic quantities. Instead, it is assumed that many of the errors due to breakdown of the SHO will cancel out due to the similar nature of the systems studied. For this reason, it is pertinent to consider the free energies changes quoted in this work with significant error bars and only use them only as a guide to the relative feasibility of comparable processes and not as an absolute gauge. The automated hindered rotor analysis in Gaussian 09 was used to study a selection of systems considered in this work. The corrections proffered by the analysis concerned only hindered rotations of the methyl groups and failed to identify many of the very low energy modes representing hindered internal rotations of the BTPhen ligand. For this reason and owing to the relatively removed and non-interacting nature of the methyl groups, the calculated corrections were of a similar magnitude in each of the models studied, leading to only minor modifications in the calculated free energies of each reaction (on the order of 0.1 kcal mol^{-1} for the lowest free

energy change electron transfer (ET) reactions). Hence, it was deemed unnecessary to compute the correction for all the species studied.

2.6 BSSE and the CP Method

The calculations in this study were necessarily carried out using a basis set significantly smaller than the complete basis set limit. This necessity leads to the possibility that the basis set provided to some atoms may be inadequate to describe their ground state electronic structure alone and this in turn may lead such atoms to borrow functions from other nuclear centres, thereby leading to over binding of the system under study. The energy related to this erroneous stabilisation is known as the basis set superposition error (BSSE) and it is particularly problematic when the basis set centred on one atom is significantly more complete than those centred on its neighbours or when diffuse functions are present. Both of these features are typical of calculations of heavy metal coordination complexes, as studied here. Having said this, BSSE as it is technically defined is of concern only when modelling non-covalent interactions. Hence, its consideration in studies of coordination complexes that display a degree of covalency, such as uranyl(VI)-peroxide complexes,[96] is technically in error as inherent of this interaction is some degree of basis set sharing.[97] Nevertheless, it is typical in the literature to calculate the BSSE when modelling such species.[98,99] Hence, the application of BSSE correction methods to this study has been considered.

The only *a posteriori* method of calculating the BSSE is the CP method by Boys et al.[89] In this method, the molecular system under study is redefined as a collection of fragments. The BSSE for each fragment is then estimated by subtracting the energy calculated for each fragment using its own basis set (i.e. the monomer-centred basis set) from the energy calculated when it has the basis set of the whole complex available to it (i.e. the multimer centred basis set). The latter is typically calculated by anchoring the basis functions centred on neighbouring fragments to ghost atoms with the same nuclear coordinates, with no charge or electrons associated. Once the BSSE for each fragment has been calculated in this way, they are summed to provide an estimate of the BSSE of the whole system.

Whilst it can prove a useful tool to gauge the BSSE of a system, the procedure used by the CP method is not without its flaws. In particular, the total BSSE calculated for a system is completely dependent on how the fragments are initially defined and if carried out in an inconsistent manner the CP method can generate wildly different BSSE corrections for the same system. The fragmentation scheme proposed when the method was devised by Boys and Bernardi[89] was an individual atom approach. Clearly, this would lead to intractable

calculations for larger systems and hence a simplified fragmentation scheme based on chemical reasoning is often required. However, as previously shown by others, even conceptually reasonable fragmentation schemes can lead to significant discrepancies that preclude an accurate assessment of the BSSE in a system using the CP method.[97,100]

In this study, the CP method has been used to assess the BSSE in all the models studied. Unless otherwise stated, the fragmentation scheme used for the CP calculation defined all molecular species in the model as separate fragments. The CP calculations were conducted at the same level of theory as was used to calculate the SP energies of each system. In this work, that meant carrying out the calculations using two slightly different basis sets; one that used the def2-TZVP basis set on all *C*, *H*, *O* and *N* atoms and a second in which the basis on the oxygen atoms in the dioxygen species had additional diffuse functions added to them. This modification to the dioxygen species basis was carried out specifically following calculation of large BSSEs for the peroxide dianion as modelled using the standard def2-TZVP basis. This large BSSE was heeded as an indication of possible significant inadequacies in the basis set initially chosen to represent this system, as discussed in Appendix 1. Despite this initial concern, the study described in Appendix 1 indicated that there was no significant dependence of the energies and geometries of the complexes modelled in this study on the size of the basis set used to describe the dioxygen ligand. Thus the use of a larger basis affected only the BSSE predicted using the CP method as implemented. Furthermore, even when utilising the large augmented basis set described to model the peroxide ligand the BSSE predicted still did not converge. Hence, the BSSEs presented in this study should be viewed with caution and are provided only as a bounding figure to the likely magnitude of the BSSE in such systems. For this reason, as the report progresses and the complexity increases, the calculated BSSE for the systems in question are omitted in the name of clarity.

2.7 Concerning Solvation

Following application of the thermodynamic corrections to the reaction energies calculated in Chapter 4.3, as discussed earlier, the effects of solvation have been accounted for in an implicit manner using CPCM[101,102] solvation corrections parameterised for the solvent, methanol. This method uses spheres of a predefined geometry centred at the atomic coordinates to construct a molecular cavity. The surface of this cavity is subsequently broken down into tessellating fragments, known as *tesserae*, and the electrostatic potential of the solute at the distance of the defined surface is mapped onto these *tesserae* as point charges.[103] The point charges localised on this surface are then allowed to relax on exposing the cavity

to a dielectric continuum representing the dielectric properties of a particular bulk solvent. In this manner, the system resembles the behaviour of a capacitor, in that when the solute cavity is immersed in a solvent with a low dielectric constant, the solvent will effectively behave as an insulator and the molecular system will be forced to retain much of its charge. If a solvent of high dielectric is used, the mutual polarisation of the solvent and the point charges on the 'molecular surface' will lead to an overall stabilisation of the energy of the system. When applying continuum models to quantum chemical methods, the exponential decay of the wave function typically results in a proportion of charge penetrating the predefined cavity and escaping into the continuum. In this way, a proportion of the polarisation charges of the system may be lost leading to error in the calculated quantities. In all calculations in this study that utilise the CPCM solvation model, this quantity has been monitored in order to ensure this error is not excessive. The threshold denoting excessive error in the polarisation charges is defined as 5 %, although typically in this study the error observed was close to 1 %.

As stated, the CPCM method is able to correct the model for the polarising nature of the solvent-solute interaction, but it fundamentally fails to incorporate specific directional interactions, such as hydrogen bonding, that could lead to error under certain circumstances. A second source of error of this type may be introduced by the neglect of solvation during geometry optimisations. The possibility of such errors significantly affecting the reaction pathway is reduced somewhat by the fact that many of the models of importance to this report are similar in structure. Therefore, on calculating reaction energies these systems will benefit form a partial cancellation of errors. The possibility of errors in the solvation model contributing significantly to the calculated reaction profile is further reduced by the fact that in all the models studied the uranyl species has a hydrophobic exterior, provided by the chelating ligand, BTPhen. Hence certain vulnerable moieties in the complexes are likely to form very few directional interactions with the bulk solvent. Despite this, the uranyl oxygen atoms in the systems studied are typically exposed and hence there is a finite possibility that the neglect of explicit solvation could lead to significant error in the model. Such an error has been the subject of a combined quantum mechanic-molecular mechanic (QM/MM) study of solvation of uranyl by Tsushima et al.[79] in which it was demonstrated that the error in the calculated uranyl(VI) ion reduction potential that was introduced by neglecting explicit consideration of the secondary solvation sphere of the uranyl(V) and (VI) ions (i.e. the sphere that includes amongst others all of the O_{yl}-H_2O interactions) results in a discrepancy of less than 5 kcal mol^{-1} with respect to the experimentally determined potential.[79] In this

light, they conclude that inclusion of second and higher order coordination spheres is not necessary to study such reaction energy calculations with reasonable accuracy.

Nevertheless, in studies that describe acid-base reactions, the accurate description of solvation is often paramount. For this reason, in Chapter 4.3.3 the effect of implicit and explicit solvation of vulnerable moieties in the modelled complexes, such as the uranyl(V) oxygen atoms, is considered with reference to the predicted geometries of the complexes of interest and their relative energies.

Despite this caveat, as demonstrated in Chapter 4.3.3 and Appendix 2, for many of the reactions described (particularly those which do not require the transfer of protons between species), the presence of solvent during the optimisation procedure is not necessary as the majority of the stabilisation afforded to the system by the solvent may be recovered by conducting a CPCM SP calculation at the gas phase optimised geometry. This observation has been made frequently by others as described in a review by Schreckenbach et al.[104] For this reason, this is the typical approach to solvation taken in this study.

2.8 Concerning Spin-Orbit Coupling

As an actinide element, when in different oxidation states uranium houses differing numbers of *f*-electrons. Of particular importance to this study is the fact it houses zero in the +6 oxidation state and one in the +5 state. The 5*f* orbitals, have $-3 < m_l < +3$ and hence occupation of the 5*f* orbitals by unpaired electronic spins can give rise to non-negligible SO coupling effects. Such SO effects act to stabilise the UO_2^{+} species relative to UO_2^{2+}, and could therefore change the predicted feasibility of the ET reactions. The explicit treatment of SO effects in the models of the present study would lead to calculations unfeasible with existing resources. Despite this, previous work by Hay et al.[78] and Tsushima et al.[79] has provided a rough estimate of the SO coupling for the early actinides in different oxidation states, thereby allowing the effects of SO coupling to be considered in an approximate manner. The SO correction presented by Hay et al. was calculated using configuration interaction (CI) and CI-SO calculations for the free actinyl unit, whereas Tsushima et al. utilised a complete active space self-consistent field (CASSCF) approach based on a hydrated model of the uranyl cation. Despite their different approaches, both studies yielded reasonably similar corrections of -7.15 kcal mol^{-1} and -6.76 kcal mol^{-1}, respectively. This is therefore a non-trivial contribution, however due to the uncertainties associated with its inclusion in the computational model as an adjunct correction factor, it is not be explicitly considered in the study. In all calculations that occur between systems in which the uranyl

ion remains in the same oxidation state it is likely that the errors due to the neglect of the SO interaction will cancel out. However, when describing reactions that involve the system transitioning from a system containing *U(V)* to one containing *U(VI)* the effect of neglecting SO coupling will be compounded and significantly affect the calculated reaction energies. This is the case when modelling the ET reactions of importance to this study. For this reason, when drawing conclusions based on the feasibility of the modelled ET reactions, it is worthwhile to consider the error bars associated with neglect of SO coupling. Despite the implications of neglect of SO coupling on the predicted reaction energetics it has been shown previously that in similar systems modelling similar reactions neglect of SO does not preclude the model from describing the correct chemistry.[105,106]

As a final note, as radical species, the superoxide anion and hydroperoxyl radical are both also subject to SO effects. However, owing to the lower angular momentum of the orbitals in these oxygen-based systems the magnitude of the appropriate correction is much lower, on the order of 0.5 kcal mol^{-1}.[107]

2.9 Spin Contamination

Studies of open shell compounds are complicated by the possibility of spin contamination in the resulting wavefunction. Spin contamination is the mixing of higher order multiplicity states into the state desired and is an artefact of permitting the alpha and beta orbitals of the wavefunction to differ spatially in unrestricted calculations. The artificial mixing of higher order multiplicity states into the unrestricted wavefunction may lead to a lowering or heightening of the energy of the system, dependent on the relative energies of the states involved. Spin contaminated wavefunctions are readily identified on evaluation of the spin operator, as they are no longer eigenfunctions of $<\hat{S}^2>$, where $<\hat{S}^2> = S(S+1)$. Hence, if the value of $<\hat{S}^2>$ for a given wavefunction differs greatly from what would be expected for the 'spin pure' single multiplicity solution it is likely that the solution is spin contaminated. The $<\hat{S}^2>$ values of spin contaminated wavefunctions can typically be represented by weighted linear combinations of $S(S+1)$ terms of differing multiplicity, where S is the total unpaired spin in the system. In this manner it is often possible to determine the fraction of the higher order multiplicity term(s) that is contaminating the desired state of the system and subsequently estimate the energy of the system in the absence of spin contamination. One such method to achieve this is known as the Yamaguchi spin projection method, as described in reference.[108]

The Yamaguchi method employs the expression in **Equation 37** to calculate the fraction of spin contamination that defines the proportion of the lower order multiplicity component of the wavefunction relative to the proportion of the higher order multiplicity contaminant.

$$f_{SC} = \frac{^{1}<\hat{S}^{2}>(UKS)}{^{3}<\hat{S}^{2}>(UKS) - ^{1}<\hat{S}^{2}>(UKS)} \qquad \textbf{(37)}$$

In which $^{x}<\hat{S}^{2}>(UKS)$ is the spin expectation value of the spin state, *x*, acting on the KS orbitals. Following on the expression in **Equation 38** is used to estimate the energy of the 'spin pure' multiplicity state of the system.

$$^{1}E(SCKS) = ^{1}E(UKS) + f_{sc}[^{1}E(UKS) - ^{3}E(UKS)] \qquad \textbf{(38)}$$

Where $^{1}E(SCKS)$ represents the spin corrected energy of the singlet state of the system, $^{1}E(UKS)$ represents the spin contaminated energy of the singlet state of the system and $^{3}E(UKS)$ represents the energy of the triplet state of the system. Although this spin projection procedure is able to provide an estimate of the energy of the system in the absence of spin contamination, it should not be considered an absolute correction as it is known that this method typically overcorrects the energy of the spin pure state.[109] Hence, as opposed to an absolute correction, it is most appropriate to use the spin contaminated and spin corrected energies of the system as upper and lower bounds of the energy of the spin pure wavefunction, respectively.

Unfortunately, the Yamaguchi spin projection method as described does not take into account the possibility that the geometry of the pure spin system may be different to that of the spin contaminated system. Hence, it is possible that even the bounded range identified by the spin projection method could still be in considerable error if the structure of the spin pure system is significantly different to that of the spin contaminated system.

It is worthwhile to note that the expression presented in **Equation 38** is only fit for use with wavefunctions that are contaminated by the next highest order multiplicity state and no others, as it assumes that the spin operator is described by only two components. Regarding the validity of this assumption, following completion of the SCF procedure the Gaussian 09[6] programme performs a spin annihilation procedure that removes the contamination due to the next highest order multiplicity state from the wavefunction and provides a corrected value of $<\hat{S}^{2}>$. Hence, if following this annihilation procedure the resulting value of $<\hat{S}^{2}>$ is very close to what would be expected for the spin pure lower multiplicity system then it is reasonable to assume that it is reasonable to apply the Yamaguchi spin projection procedure as described.

2.10 Treatment of Secondary Species Playing a Role in the Reaction Profiles

In addition to the treatment of the uranyl-BTPhen models in this study, in order to calculate the reaction energy profiles desired, optimised structures and energies of all secondary species involved such as water, triplet and singlet dioxygen, superoxide, the hydroperoxyl radical, peroxide, the hydroperoxide anion and the proton were required to be calculated at the same level of theory as the uranyl analogues in order to allow the construction of a sequence of reaction schemes that can be used to calculate reaction free energy changes. Furthermore, unlike in the uranyl complexes studied where a large degree of the relaxation due to explicit solvation is accounted for by the mutual interaction between the metal and the primary ligand field, the isolated nature of these small species results in large errors in their calculated solvated energies should specific interactions between the solute and the polar solvent be ignored. Appendix 2 describes the procedure employed to model the solvated energies of the secondary species required to construct the desired mechanistic schemes. Appendix 2 achieves this by walking through a worked example of the procedure employed to model the energy of the hydrated proton. In general, the procedure is similar to that applied to the uranyl complexes, consisting of a gas phase optimisation using uB3LYP/B1, followed by a SP calculation using the B2 basis set in a CPCM for methanol. However, the differences lie in a number of explicitly defined water molecules included that were found to be necessary in order to describe the solvation energy of these species.

The short study concludes that optimising the structure of the secondary molecules in the gas phase embedded in a cluster of five explicitly defined water molecules and then performing a SP calculation at the gas phase optimised geometry using a CPCM is sufficient to reclaim a large degree of the solvation energy that would otherwise materialise as error. Using this approach, it was possible to predict the solvation energy of a proton to within 3 kcal mol^{-1} of the experimentally determined value. This approach was then extended to describe all of the small molecules that play a role in the mechanism to form peroxide. It was noted that the error associated with the solvation of the superoxide anion exceeded the desired 3 kcal mol^{-1} threshold and amounted to a minimum deviation of 6 kcal mol^{-1} relative to the empirical solvation energy (dependent on which experimental value was considered). It was therefore proposed that in all calculations conducted in which the solvation energy of the superoxide anion would be utilised, two values for the reaction would be presented, one in which the computationally pure solvation energy would be used and one in which an empirical correction factor of 6 kcal mol^{-1} had been considered.

The absolute energies and images of the optimised secondary species modelled are presented in Appendix 2 for reference.

3 A Study of the Speciation of the Uranyl(VI) and Plutonyl(VI) ions in the Presence of *CyMe$_4$*-BTPhen

3.1 Introduction

The envisaged use of the BTPhen ligand is as an organic phase modifier in next generation solvent extraction processes that aim to separate the actinide elements from the lanthanide elements in a one pot process. For this purpose, this ligand has been shown to behave admirably.[3,110,111] In order to understand the electronic and molecular basis for the observed separation and direct the design of ligands that are even better suited to this purpose, it is necessary to characterise the specific species responsible for the observed separation factors. A study of specifically this topic has recently been published as the thesis of DMW,[3] in which the complexes formed between the BTPhen ligand and ions in oxidation states relevant to the separation process were studied. This body of work serves as an addendum to this study in that it seeks to utilise the equatorially chelating BTPhen ligand as a means to study ternary complex formation between actinyl(VI) ions and monodentate ligands in solution. To this end, the BTPhen ligand is well suited, as it has been shown to coordinate actinyl ions equatorially using four coordinate bonds, but yet provide space for the approach of a second ligand on the fifth coordination site of the actinyl ion., as per **Figure 13**. In this way it is possible to use the BTPhen ligand as a blocking species able to control the coordination environment about the actinyl ion and limit the approach of ligands to all but one coordination site, thereby facilitating the construction of computational models of the species formed.

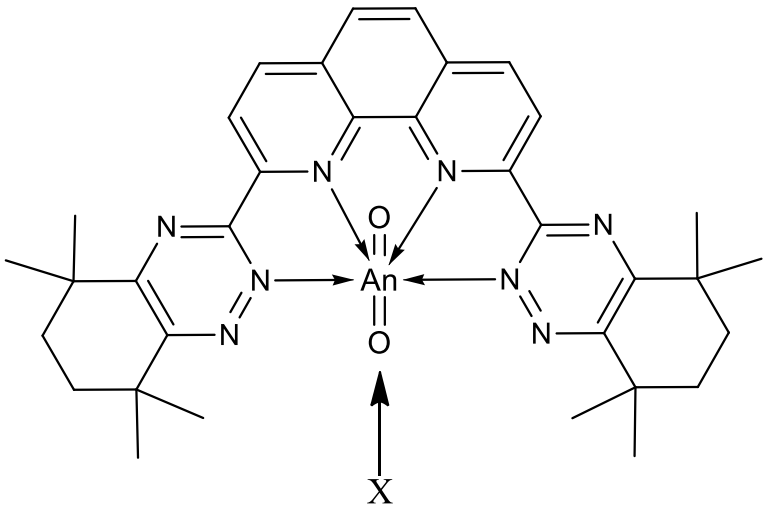

Figure 13: Schematic of the mode in which the BTPhen ligand equatorially binds to actinyl ions. As BTPhen only has four nitrogen donor atoms it is inherently structured to leave a fifth coordination site accessible to other ligands in solution. One such ligand is represented by the species X in this figure.

3.2 Experimental Details

Purification and Preparation of the Plutonium(VI) Stock Solution in Triflic Acid

Solutions of plutonium in nitric acid were obtained from the laboratory stock solution (Lab LN1, Atalante, CEA Marcoule). Nitric acid solutions were purified of the americium that had built up during prolonged storage of the material due to radioactive decay using ion exchange chromatography. The purified plutonyl nitrate solutions were subsequently oxidised to the +6 oxidation state using controlled additions of silver(I/III) oxide (sometimes colloquially known as silver(II) oxide) interspersed with spectrophotometric analysis until the characteristic absorption of the plutonium(IV) ion at 470 nm was no longer observed. In the event that too much silver oxide was added, hydrogen peroxide was added to the batch to lower the oxidation state once more, followed by the obligatory spectrophotometric analysis. Subsequently, 4 M ammonium hydroxide was added to the plutonyl(VI) nitrate solution to precipitate green plutonyl(VI) hydroxide. The suspension was immediately centrifuged and the supernatant liquor was decanted, to yield a small mass of green plutonium hydroxide. Care was taken to not compact this product excessively or allow it to completely dry since plutonium(VI) hydroxide will polymerise under such conditions forming a product that will resist dissolution even in strong acid. The green product formed was washed thrice with water in order to reduce the amount of residual nitrate and was subsequently dissolved in neat >10 M triflic acid to yield a straw coloured solution. This solution was subsequently charged with ammonium hydroxide once more to precipitate the green plutonyl(VI) hydroxide product. The washing procedure was then repeated and then the washed solid was once again dissolved in neat triflic acid. This procedure was repeated a final time so as to minimise the possibility of nitrate carryover, before finally being left as a straw coloured triflic acid solution of concentration 0.16 M with respect to plutonium(VI) and 6 M with respect to triflic acid. An image showing the colour of the plutonyl(VI) triflate stock solution following purification and the vis-nIR electronic absorption spectrum that confirms the purity of the solution with respect to oxidation state is presented in **Figure 14**. Assuming no loss of plutonium during the oxidation and washing procedures carried out, an extinction coefficient for the 830 nm absorption of the plutonyl(VI) ion in triflic acid was calculated. This was found to be 400 M^{-1} cm^{-1}. This compares favourably to the extinction coefficient of the plutonyl(VI) ion in perchloric acid of 555 M^{-1} cm^{-1} published previously by Cohen.[112]

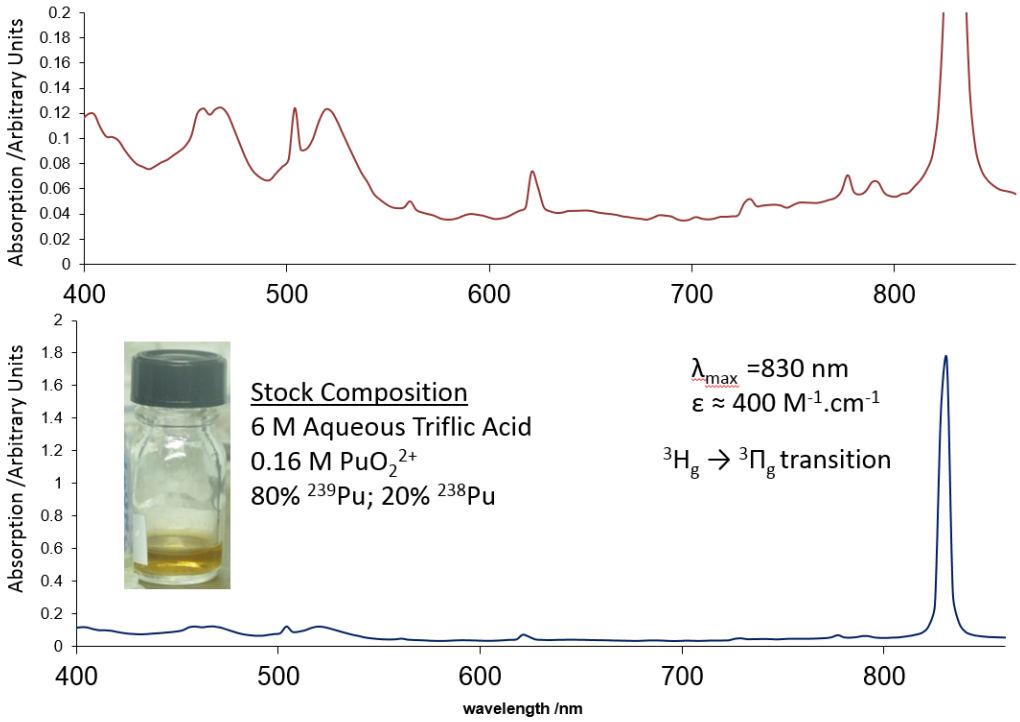

Figure 14: Image of the staw-coloured plutonyl(VI) triflate stock solution along with the vis-nIR absorption spectrum, confirming the purity of the soltion with respect to oxidation state.

UV-vis Experimental Procedure

UV-vis titration experiments were carried out using a Cary 100 Spectrophotometer equipped with fibre optic cables that ran into a glovebox containing the plutonium samples. The experiments were carried out over a path length of 1 cm. Titrations were typically carried out on a scale of 600 µL – 1 mL using solutions that were 2.5 mM to 5 mM concentration with respect to *Pu(VI)*. To these solutions was added aqueous hydrochloric acid of varying concentration. The concentration of hydrochloric acid was varied dependant on the initial volume of *Pu(VI)* solution in order to keep the error associated with small volume (<10 µL) additions to a minimum. When titrating solutions of BTPhen into the batch, these solutions were acidified to the same concentration as the experimental solution in order to minimise error in the spectrophotometric titration experiment due to changing the ionic strength of the solution. Titration experiments were carried out using two different solvent systems, neat aqueous triflic acid and a mixed solvent system that was 90 %v/v acetonitrile (*MeCN*) and 10 %v/v water acidified to the desired concentration with triflic acid.

Mass Spectrometric Sample Preparation

Samples destined for mass spectrometry (MS) were prepared as either neat aqueous or 90 %v/v acetonitrile (MeCN) and 10 %v/v water solutions of ~2.5 mM concentration with respect to *Pu(VI)* or *U(VI)*. For this reason many of the solutions studied were those initially prepared for UV-vis-nIR spectroscopy. MS analysis was carried out using a Bruker

electrospray ionisation (ESI) quadrupole ion trap mass spectrometer that allowed fragmented ions to be collided post separation to allow firm assignment of the fragment ions and the species formed.

Proton NMR Experimental Procedure

NMR samples were prepared using neat deuterated *MeCN* solutions of *U(VI)* or volume ratios of 9:1 deuterated *MeCN*:heavy water solutions of *Pu(VI)* in the presence or absence of a stoichiometric quantity of BTPhen. These solutions were typically at a concentration of ~20 mM in order to achieve a reasonable signal to noise ratio in the proton NMR spectrum. NMR spectra were collected using a Bruker 400 MHz spectrometer.

XRD Crystallography

XRD structures were collected using a Bruker Nonius diffractometer at 77 K. Crystals containing plutonium were grown in polystyrene vessels in a glove box, single crystals were selected using a microscope fitted with a polarising filter in the glove box. Crystals were mounted on a goniometer tip inside a glove box and placed in a cellulose envelope designed to fit snugly over the top of the goniometer tip and provide a means of primary containment.

3.3 Results and Discussion

A Spectrophotometric Study of the Formation of Plutonyl(VI) Chloride Complexes in Aqueous Solution

As has been stated, the chemistry of plutonium is often complex and unpredictable, furthermore the number of institutions worldwide where it is possible to conduct such chemistry are extremely limited. Hence, as a first step into the study of the formation of ternary complexes of the plutonyl(VI) ion it was decided to first attempt to reproduce previous work carried out in order to 1) provide confidence in the experimental set up and the purity of the reagents and 2) demonstrate reproducibility of an experiment carried out previously. The experiment identified was that of Runde,[17] as outlined in Chapter 1.3.3. This experiment was a spectrophotometric titration of chloride into an aqueous perchloric acid solution of the plutonyl(VI) ion. The perchlorate anion is typically used in coordination chemistry owing to the fact that in many systems it acts as a non-coordinating (or spectator) anion, hence in aqueous solution the use of perchlorate as the counter ion typically allows the properties of the wholly aquated analogue of the metal ion in question to be probed. It is of further benefit to plutonyl(VI) ion chemistry that perchloric acid is a super acid and under radiolysis generates oxidising species and hence provides a level of resilience to the stock solution with respect to reduction as well as suppressing the formation of insoluble

plutonyl(VI) hydroxide polymers. Despite these benefits, perchlorate salts are typically explosive and hence there is always an unwanted element of danger when working with this compound. The triflate anion provides a reasonable substitute in this respect as it is also a super acid and is only weakly nucleophilic, hence under the majority of experimental circumstances the triflate ion will be out-competed by other species present to coordinate the metal ion. In this regard its use is becoming increasingly wide spread, although to date the author is unaware of any other studies in which triflic acid solutions of the plutonyl(VI) ion have been utilised. This uncertainty in the behaviour of the triflate counterion compared to perchlorate compounded the decision that the work of Runde[17] was worth repeating.

In order to achieve this titration experiments were carried out (as detailed in the experimental details, above), in which a solution of hydrochloric acid was titrated into an aqueous triflic acid solution of the plutonyl(VI) ion. Between each titration, a trace of the electron absorption spectrum of the solution was measured in the region of the most intense forbidden absorption of the metal ion, around 830 nm, in order to observe any changes in speciation of the system. The titration was carried out between a concentration of 1.8 M [Cl^-] to 11.9 M [Cl^-], i.e. from neat aqueous triflic acid solution to neat hydrochloric acid solution, in order to generate the spectrophotometric titration spectrum presented in **Figure 15**.

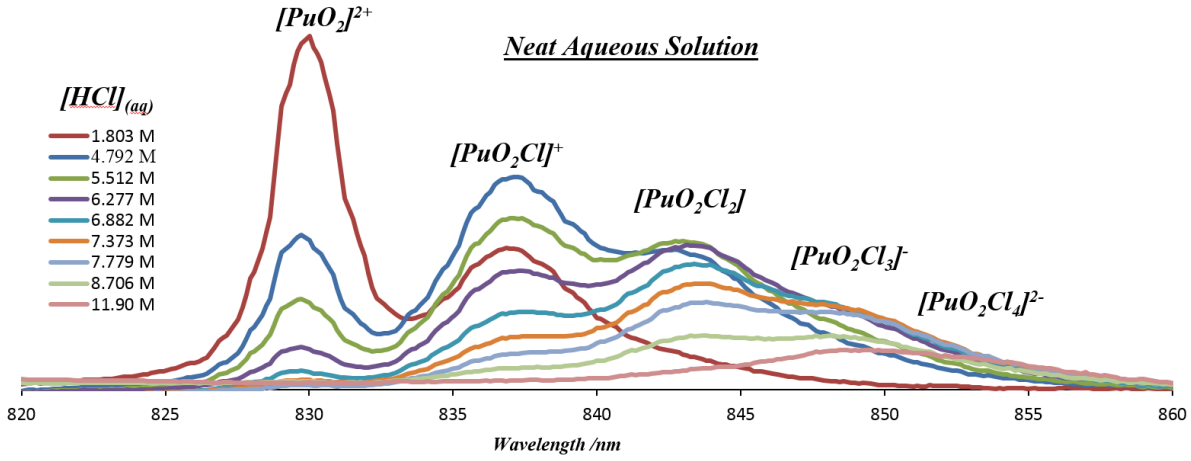

Figure 15: Electronic absorption spectra describing the titration of chloride into an aqueous triflic acid solution of the plutonyl(VI) ion. In line with assignments made by Runde, the plutonyl(VI) species responsible for each of the absorption maxima have been labelled.

As can be seen on comparison of **Figure 15** and the work of Runde presented previously in **Figure 7** (Chapter 1.3.3) the spectra recorded in triflic acid solution and perchloric acid solution are broadly the same. In the triflic acid solution, absorption maxima were observed at wavelengths of 830 nm, 837 nm, 843 nm and 849 nm along with a broad absorption centred around 855 nm, which was assigned as the octahedral plutonyl(VI) tetrachloride complex, whereas in perchloric acid solution Runde found these absorption maxima to lie at

830 nm, 838 nm, 843 nm and 849 nm along with a broad absorption centred around 855 nm. The agreement between the two studies is therefore excellent, indicating that in both solutions the species probed is the aquated plutonyl(VI) ion, $[PuO_2(H_2O)_5]^{2+}$ and hence, like the perchlorate anion the triflate anion also acts as a spectator species in these solutions.

A Spectrophotometric Study of the Formation of Plutonyl(VI) Chloride Complexes in a Mixed Acetonitrile : Water Solvent System

Due to the low solubility of the ligand of interest (BTPhen) in water and the aqueous nature of the plutonyl(VI) triflate stock selected, it was quickly identified that a mixed solvent system of acetonitrile and water would be required in order to study the coordination chemistry of the system of interest. Through multiple small scale validation tests it was possible to identify that a per volume ratio of 9:1 acetonitrile:water was found to adequately solvate the starting materials and products alike across the ligand and metal concentration ranges required to conduct the experiment.

Prior to carrying out the planned titrations with BTPhen, it was important to establish the behaviour of the plutonyl(VI) ion in the mixed solvent system with respect to the neat aqueous triflic acid system described previously. To this end, the spectrophotometric titration described in the previous chapter was repeated using the modified 90% v/v acetonitrile solvent system. It is important to note that in order to reduce the effects of solvatochromism on the spectra recorded, the hydrochloric acid was charged to this system as a 90 % v/v acetonitrile/water solution.

The overlaid spectra resulting from this titration of hydrochloric acid into the mixed acetonitrile-water solution of plutonyl(VI) triflate are presented in **Figure 16**.

Interestingly, in the mixed solvent system, the first plutonyl(VI) chloride complex is observed to form at chloride concentrations that are three orders of magnitude lower than observed in the neat aqueous system (0.001 M as compared to 1 M previously). Despite this change being surprisingly large, it may be rationalised that the chloride ion will be less effectively solubilised by a mixed acetonitrile-water system than a neat aqueous phase, due to the lower effective dielectric constant of the former. This will thereby promote the charged species in solution to solvate each other via the electrostatic stabilisation afforded on complexation of the oppositely charged ions. In addition to this unexpected concentration phenomenon, in the mixed solvent system it is only possible to observe the absorption due to two plutonyl(VI) chloride species, presumably the $[PuO_2Cl]^+$ and $[PuO_2Cl_2]$ species, as the ^3H to $^3\Pi$ transition for the plutonyl(VI) tri- and tetrachloride species is non-absorptive

under these conditions. This change in absorption behaviour may indicate an increase in the symmetry of the tri and tetra chloride complexes in the mixed solvent system relative to neat aqueous system. Such a difference may also be rationalised considering the reduced ability of the mixed solvent system to solvate the charged species because this would act to make the chloride ligand less labile and thereby decrease the rate of exchange of the ligand field about the plutonyl ion. This would correspondingly affect the ability of the more symmetric complexes to be detected sincce the means of detection is forbidden and is therefore only observed due to such rapid fluctuations in the ligand field that break the symmetry of the orbitals between which the electron transitions.

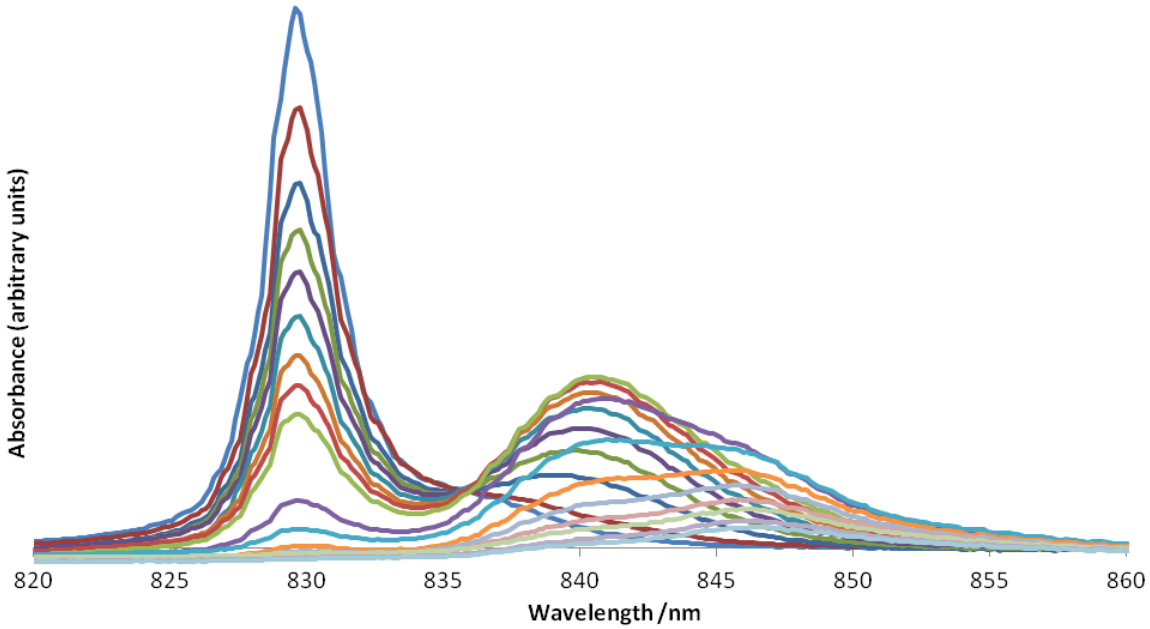

Figure 16: Overlaid electronic absorption spectra obtained on titrating a mixed acetonitrile-water solution of hydrochloric acid to a triflic acid solution of the plutonyl(VI) ion of the same solvent composition. The total hydrochloric acid concentration varies from 0 M to 0.05 M across the spectra presented. At concentrations above 0.5 M no absorbance was observed that could be assigned as the ^{3}H to $^{3}\Pi$ transition of the plutonyl(VI) ion.

In the mixed system, the wavelength of maximum absorption in the absence of chloride remains at 830 nm, suggesting that the dominant species in a 9:1 acetonitrile:water system is the same as in the neat aqueous solution, i.e. the purely aquated plutonyl(VI) ion. However, the similarity between the spectra ends here as there is a significant shift in the wavelength of maximum absorption of the first and second chloride complexes observed on moving to the mixed solvent system. Assuming that these two species are the mono- and dichloride complexes, this amounts to a bathochromic shift of the $[PuO_2Cl]^+$ species absorption from 837 nm to 841 nm on moving to the mixed solvent system and a shift from 843 nm to 846 nm for the dichloride species. This change is indicative of a change in the equatorial coordination environment of the plutonyl(VI) complex in the mixed system relative to the

pure aqueous phase, which could be rationalised by incorporation of acetonitrile into the equatorial coordination sphere of PuO_2^{2+} or by a change in the number of equatorial water molecules bound. Despite this assignment, it cannot be discounted that the two species observed are not the odd numbered chloride complexes as one may assume that both the di- and tetrachloride complexes exhibit octahedral symmetry and hence may be silent transitions in this mixed solvent system.

A Spectrophotometric Study of the Formation of Plutonyl(VI) BTPhen Complexes in a Mixed Acetonitrile : Water Solvent System

Following the successful study of plutonyl(VI) speciation in the mixed solvent system, the effect of titrating BTPhen into the designer solution was studied, initially in the absence of chloride. An overlaid spectrum of the titration of BTPhen into a plutonyl(VI) triflate solution from 0 to 2 molar equivalents is presented as **Figure 17**. On increasing the concentration of BTPhen, a decrease is observed in the absorption due to the aquated plutonyl(VI) ion at 830 nm along with a concomitant increase in an absorption at 833 nm due to the formation of a new complex.

Following the addition of 1 equivalent of BTPhen to the reaction mixture, the absorption spectrum ceases to change, suggesting the presence of a 1:1 plutonyl(VI) to BTPhen complex. Furthermore, the single isosbestic point observed throughout the titration suggests this process is a simple equilibrium involving only two species, i.e. the aquated plutonyl(VI) complex and the BTPhen bound species, $[PuO_2(CyMe_4\text{-}BTPhen)H_2O]^{2+}$.

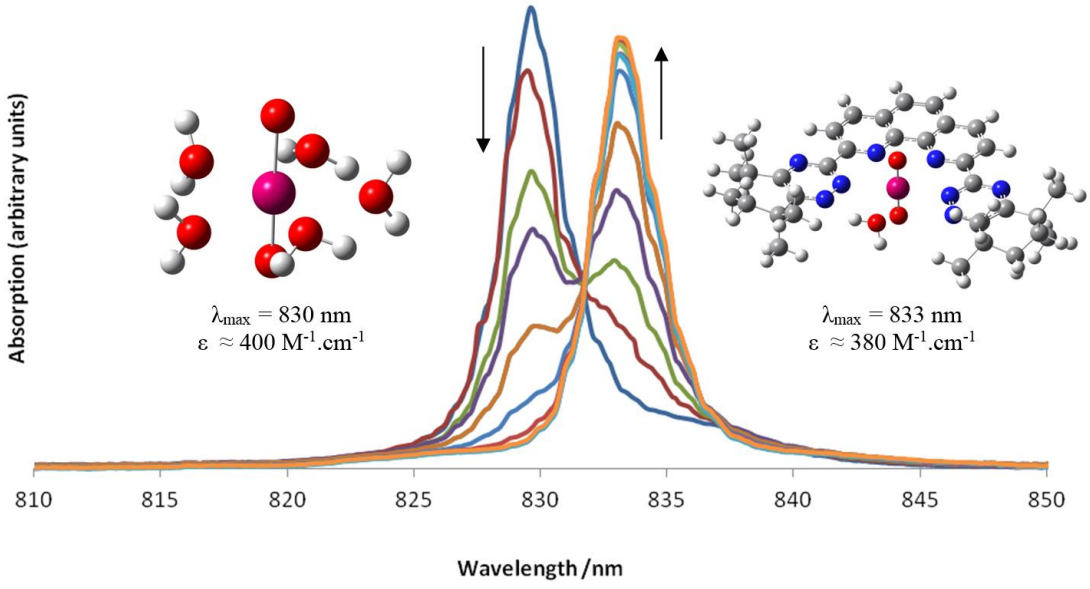

Figure 17: Overlaid electronic absorption spectra obtained on titrating BTPhen into a mixed acetonitrile-water solution from 0 to 2 equivalents with respect to the concentration of plutonyl(VI). An approximate extinction coefficient and a schematic have been provided for each proposed species.

As the titration was performed in such a manner that the concentration of the species present in solution at each point was known, it was possible to calculate a stability constant for the $[PuO_2(CyMe_4\text{-}BTPhen)H_2O]^{2+}$ species formed using the Hyperspec spectral analysis software package.[113] This stability constant was calculated to be 4.66 ± 0.1. This compares favourably to the corresponding log*K* calculated by DMW for the stability constant of the corresponding uranyl(VI)-BTPhen complex of 6.48 ± 0.064.[3] The trend is also as would be expected considering that the plutonyl ion is a marginally harder acid than the uranyl ion owing to the effects of the actinide contraction on the *f*-orbitals and hence the soft BTPhen ligand would be expected to interact more strongly with the latter.

A Spectrophotometric Study of the Formation of Ternary Complexes Between the Plutonyl(VI) ion, BTPhen and the Chloride Anion in a Mixed Acetonitrile : Water Solvent System

The observation of a discrete $[PuO_2(BTPhen)H_2O]^{2+}$ complex forming in the experimental solution permitted further analysis of the system in order to see if BTPhen was able to outcompete chloride for coordination of the plutonyl(VI) ion in this system. To test this, hydrochloric acid was titrated into a solution containing stoichiometric amounts of BTPhen and the plutonyl(VI) ion in a manner analogous to the experiments described previously. As with previous experiments, the ratio of acetonitrile to water and 0.2 M acidification with respect to triflic acid were held constant across all solutions used. **Figure 18** presents the overlaid spectra recorded during this titration of hydrochloric acid into a solution containing the plutonyl(VI) ion and BTPhen.

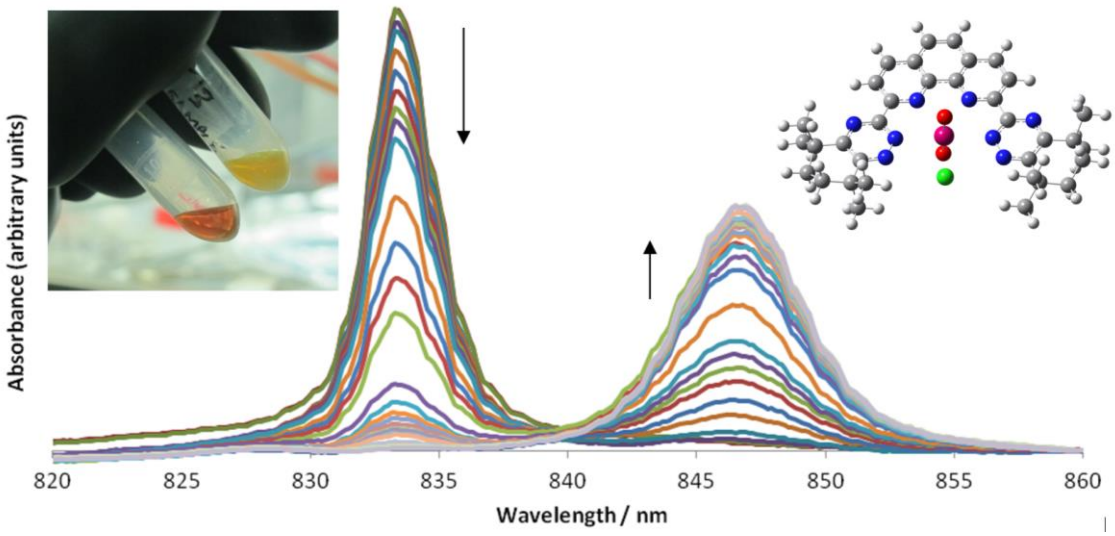

Figure 18: Overlaid electronic absorption spectra recorded on titrating hydrochloric acid into a solution containing equimolar amounts of BTPhen and the plutony(VI) ion. Also presented is a photograph of a solution containing the $[PuO_2(BTPhen)H_2O]^{2+}$ (bottom vial in image, orange solution) and $[PuO_2(BTPhen)Cl]^{+}$ (top vial in image, yellow solution) and an image of $[PuO_2(BTPhen)Cl]^{+}$.

Once again, only two species were observed throughout the titration from a concentration of 0 M [Cl^-] up to 0.02 M [Cl^-], as indicated by the well resolved absorptions at 833 nm and 847 nm sharing a mutual isosbestic point. The new absorbance was preliminarily assigned as the complex $[PuO_2(BTPhen)Cl]^+$ on the basis that the concentration of chloride was the variable being altered. Despite this preliminary assignment, comparison of these absorption spectra to those gleaned from the analogous titration in the absence of BTPhen, it is apparent that the absorption assigned as due to $[PuO_2(BTPhen)Cl]^+$ appears at a similar wavelength as the absorption due to the PuO_2Cl_2 species, at 847 nm and 846 nm, respectively. Despite this similarity, the fact that only one new absorbance is observed in the titration where BTPhen is present across a range of chloride concentrations wider than that studied in the absence of BTPhen suggests only the mono-chloride complex exists in this solution and that this change in speciation must be due to the formation of a plutonyl(VI) complex that incorporates BTPhen. As an item of further evidence in favour of this theory, it should be noted that on titration of BTPhen into a plutonyl(VI) mixed acetonitrile-water solution acidified to 0.24 M with hydrochloric acid (a solution which exhibits very little absorbance in the region of the ^3H to $^3\Pi$ transition due to the previously discussed non-absorptive nature of the higher order plutonyl(VI) chloride complexes in this solvent system) a single absorbance is observed to increase in intensity at around 847 nm, which is indicative of the displacement of multiple chloride ions from the equatorial plane of the plutonyl(VI) ion on chelation by BTPhen to form $[PuO_2(BTPhen)Cl]^+$. It is also interesting to note that should water be added to this solution in order to reduce the effective concentration of chloride present, a small increase in absorption at 833 nm is observed, which is indicative of competition between water and chloride for coordination of the $[PuO_2(BTPhen)]^{2+}$ reference Lewis acid.

Mass Spectrometric Characterisation of the Species Observed During the Solution Phase Studies

In an attempt to confirm that the limiting species formed in solution was in fact the 1:1 plutonyl(VI):BTPhen complex, the gaseous speciation of the complexes prepared were studied using an ESI mass spectrometer fitted with a quadrupole ion trap. On passing the solutions used for the electron absorption spectroscopic study through the mass spectrometer, mass ion peaks were observed that suggested the formation of a $[PuO_2(BTPhen)H_2O]^{2+}$ complex in the gas phase. There was no indication of the formation of any higher order coordination complexes with respect to BTPhen. Furthermore, in solutions containing the chloride anion, a mass ion peak corresponding to the $[PuO_2(BTPhen)Cl]^+$ was observed in addition to the aquated analogue. These species were

identified alongside the triflate adduct of the mono-BTPhen complex, $[PuO_2(BTPhen)OTf]^+$, which has an increased stability in the gas phase due to the ionic nature of its components and the poor screening of these charges when vapourised. **Figure 19** and **Figure 20** present the positive ion mass spectra recorded when analysing the 9:1 acetonitrile:water solutions containing the plutonyl(VI) ion and BTPhen only and the analogous solution also containing hydrochloric acid, respectively. It is worthwhile to note that the major species observed were not dependent on the solvent system analysed, whether neat aqueous solution or mixed solvent.

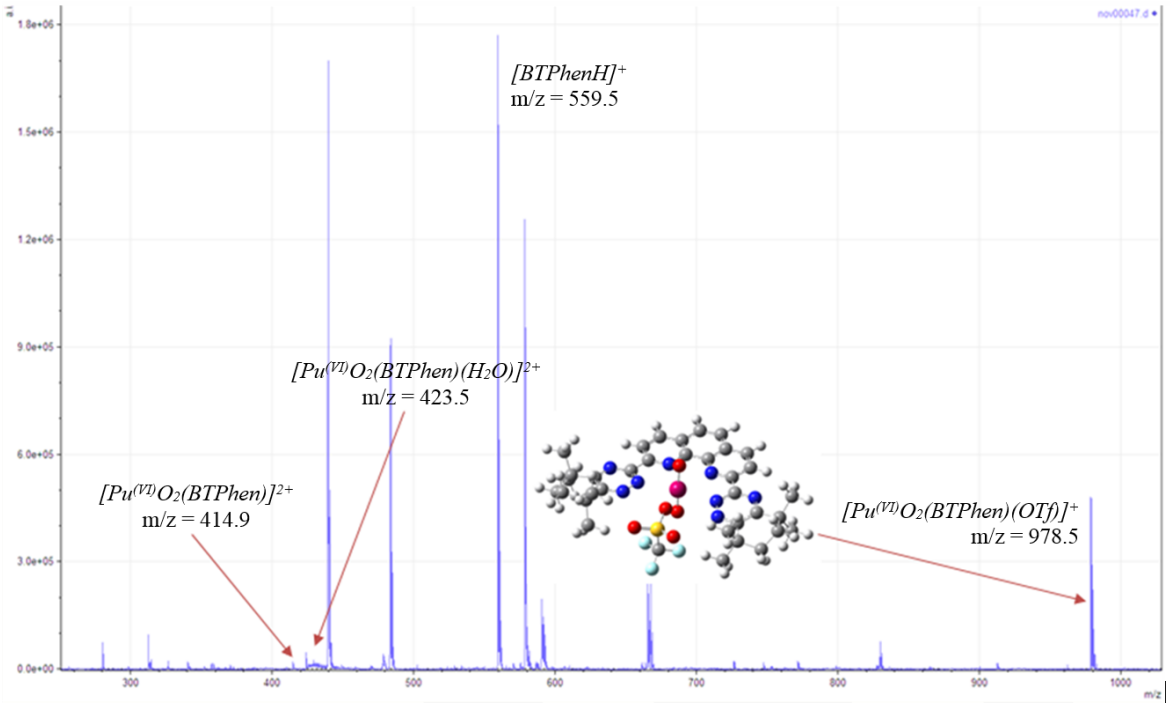

Figure 19: ESI mass spectrum of a solution containing $[PuO_2(BTPhen)H_2O]^{2+}$ as the major species. It is interesting to note that the relative abundance of the water adduct and the triflate adduct in the gas phase is drastically different than in solution where no evidence of direct coordination of the plutonyl(VI) ion by triflate is observed. This shift derives from the relatively low Lewis basicity of discrete water molecules in the gas phase and the electrostatic stabilisation afforded on coordination of the triflate anion to the plutonyl dication.

The presence of an inline ion trap allowed the more abundant ternary complexes of interest present to be isolated and further fragmented in order to confirm their initial assignment. In the case of the chloride adduct, this confirmation was exemplified by the loss of 35 m/z units (i.e. Cl) following further fragmentation of the $[PuO_2(BTPhen)Cl]^+$ complex, giving rise to a formally plutonyl(V)-BTPhen reference complex.

In addition to these expected species, it was also possible to observe the fluoride adduct of the plutonyl(VI)-BTPhen complex, $[PuO_2(BTPhen)F]^+$ formed via a fluoride abstraction reaction from a bound triflate anion occurring in the spectrometer, **Figure 21**. The occurrence of this process was confirmed by fragmenting the mass ion peak corresponding to the $[PuO_2(BTPhen)OTf]^+$ complex which was observed to degrade by losing 130 m/z

units, indicative of fluoride abstraction from the triflate anion to form *[PuO$_2$(BTPhen)F]$^+$ in situ*, followed by loss of 19 m/z units (i.e. F) to form the previously observed plutonyl(V) BTPhen reference complex.

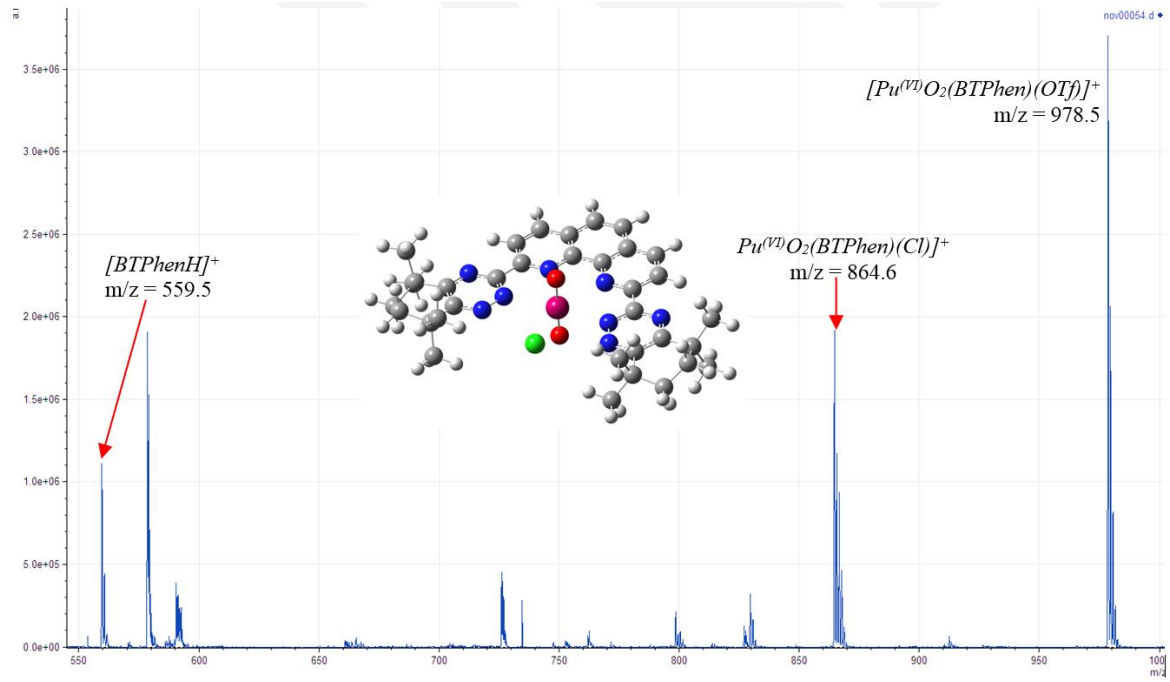

Figure 20: ESI mass spectrum of a solution containing *[PuO$_2$(BTPhen)Cl]$^+$* as the major species. Species pertinent to the present discussion have been annotated.

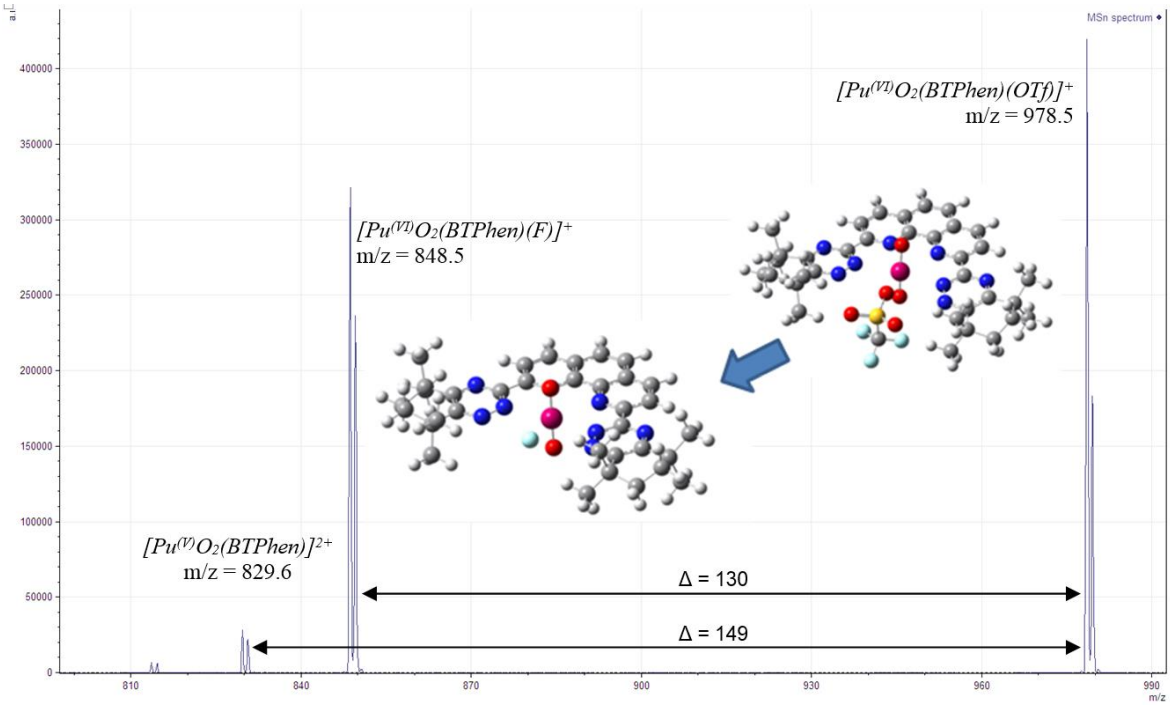

Figure 21: MS^2 mass spectrum recorded on further fragmentation of a peak of 978.5 m/z units, i.e. the complex *[PuO$_2$(BTPhen)OTf]$^+$*. Further fragmentation of this ion confirms the proposed assignments as fragments are observed with m/z representing loss of the triflate anion (m/z of 149) as well as loss of a triflate anion from which the plutonyl ion has abstracted a fluoride (m/z 130) to form the fluoride adduct of the reference complex.

Solid State Characterisation of the Plutonyl(VI)-BTPhen Complex

Whilst the previously discussed forms of characterisation were being carried out, various crystallisation experiments were set up in the hope of identifying a solvent system from which single crystals of XRD quality could be grown. Eventually, such crystals were grown from a mixed acetonitrile-water system on reduction of its volume by slow evaporation. One of the red crystals afforded was analysed using X-ray diffraction and the data was of sufficient quality to identify the diffracting species as $[PuO_2(BTPhen)H_2O][OTf]_2$. Interestingly, the radioactivity of the sample resulted in the frames recorded towards the end of the collection exhibiting significant powder rings, indicative of amorphisation of the crystal due to the radioactive decay. A schematic presenting photographs of the crystallisation and crystal selection processes and an image of the crystal structure elucidated from the grown crystals are provided as **Figure 22**. Although the statistics of the refinement of this crystal structure indicate the model is a publishable fit of the data, there is a chemical anomaly in the structure that indicates that this model is likely flawed. This anomaly is that the $Pu\text{-}O_{yl}$ bonds are of different lengths. As these should be chemically equivalent without further refinement of the data in the absence of the amorphous diffraction images, it is likely that this data will remain flawed. Despite the limited use of this structure to provide structural parameters, it is of sufficient quality to firmly assign the species ligating the plutonyl(VI) ion as a water molecule and in addition confirm the formation of a stable 1:1 complex between the plutonyl(VI) ion and BTPhen.

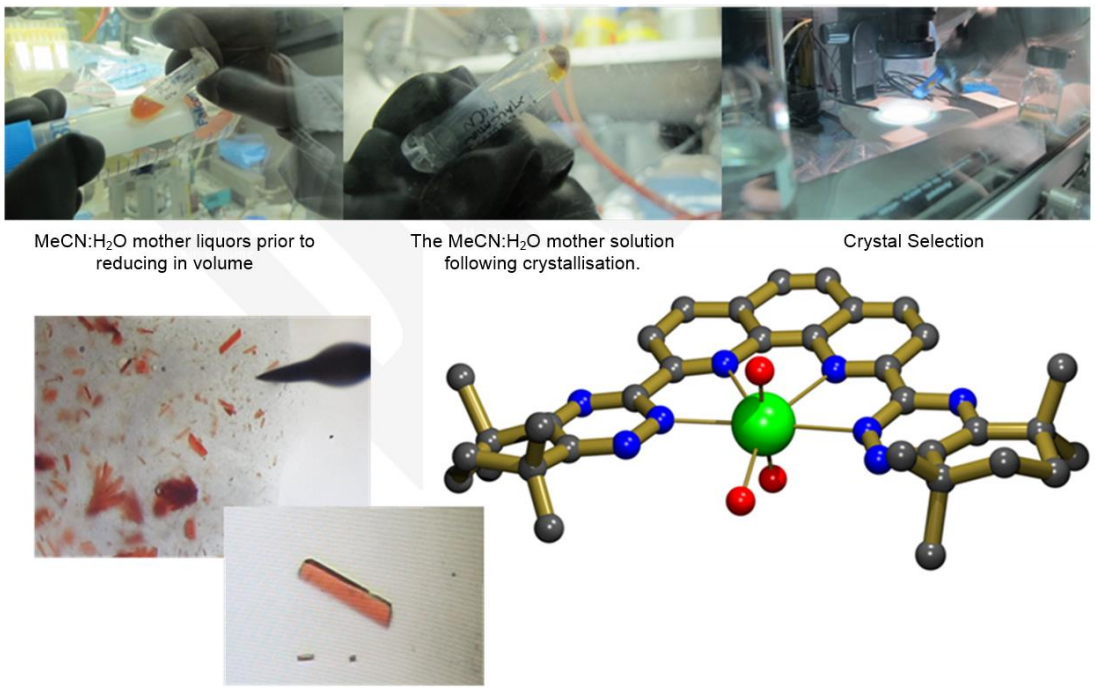

Figure 22: Schematic showing selected pictures of the crystallisation process (above) and the crystal analysed by XRD (bottom left) to provide the refined model presented on the right of the complex $[PuO_2(BTPhen)H_2O]^{2+}$.

Subsequent to XRD confirmation of the structure of the crystals grown from the aqueous acetonitrile solution, IR spectroscopy was also used to analyse the contents, in particular to analyse the frequency of the asymmetric stretch of the plutonyl(VI) ion in the BTPhen complex as compared to the frequency of this mode in aqueous solution. This is a significant quantity to determine for actinyl complexes in particular, as the relative strength of the equatorial coordination environment can be gauged by the degree to which the strength of the actinyl bonds is disrupted relative to the aquated complex. The IR absorption spectra for the crystalline material determined by XRD to be $[PuO_2(BTPhen)H_2O]^{2+}$ is presented in **Figure 23** for reference, this figure also presents the absorption spectra recorded for the relevant background solutions, i.e. an acetonitrile-aqueous triflic acid solution; the plutonyl(VI) triflate aqueous stock solution and solid BTPhen. Due to the poor solubility of BTPhen in many solvents it was not possible to record a solution phase spectrum for this sample. In addition, it was not possible to analyse the plutonyl(VI) starting material in the solid state as it proved difficult to crystallise. The weak absorbance observed of the usually strongly absorbing asymmetric stretching mode of the plutonyl ion in solution is rationalised by considering the relatively low concentration of plutonyl present relative to triflic acid (0.16 M and 6 M respectively), which also absorbs strongly in this region. The values obtained compare favourably to those of other plutonyl(VI) complexes in the literature. For example the asymmetric stretching frequency of the plutonyl(VI) ion in perchloric acid solutions has been quantified by Jones and Penneman[14] as 962 cm^{-1}. This compares favourably to the 959 cm^{-1} frequency of the ν_3 mode of the plutonyl(VI) complex observed in triflic acid solutions during this study.

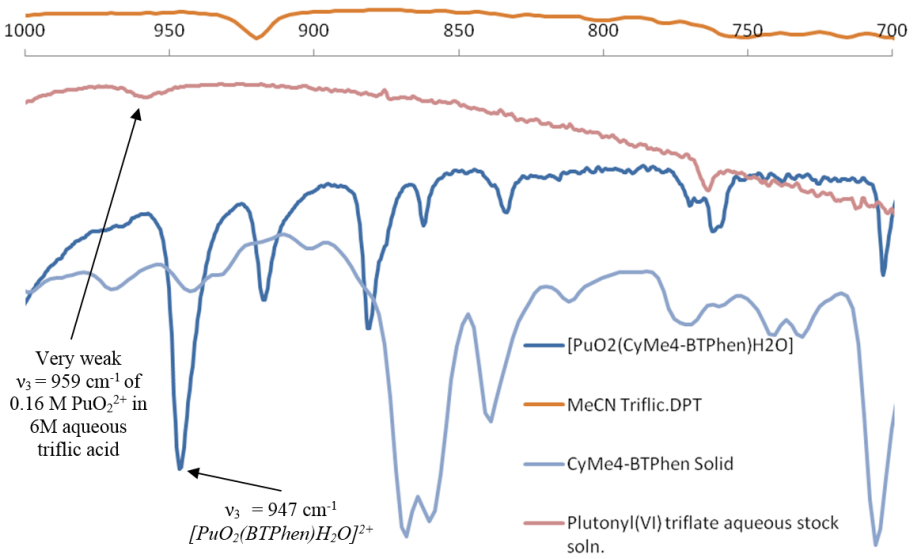

Figure 23: IR absorption spectrum of the $[PuO_2(BTPhen)H_2O]^{2+}$ complex and the spectra of the component species for comparison.

NMR Spectroscopy of the Plutonyl(VI) Ion

In light of the fact that solid state and gas phase analysis of the plutonyl(VI)-BTPhen systems had definitively indicated the formation of a stable 1:1:1 plutonyl(VI):BTPhen:H_2O complex it was decided to return to solution phase characterisation in order to gather additional information about the behaviour of this species. NMR spectroscopy was identified as an excellent target to extract additional information from this system due to the paramagnetic nature of the plutonyl(VI) ion and the novelty that is presented by trying to replicate the interaction of the unpaired spin on the metal ion with the nuclear spins of the protons on the BTPhen ligand. To this end the NMR spectrum of a solution containing plutonyl(VI) triflate and BTPhen in a solution of deuterated *MeCN* was recorded. The proton NMR spectrum of the BTPhen ligand on its own in deuterated acetonitrile is presented in **Figure 24**, whilst the proton NMR spectrum of the paramagnetically shifted proton resonances in the corresponding plutonyl(VI) complex of the uranyl ion are presented in **Figure 25**.

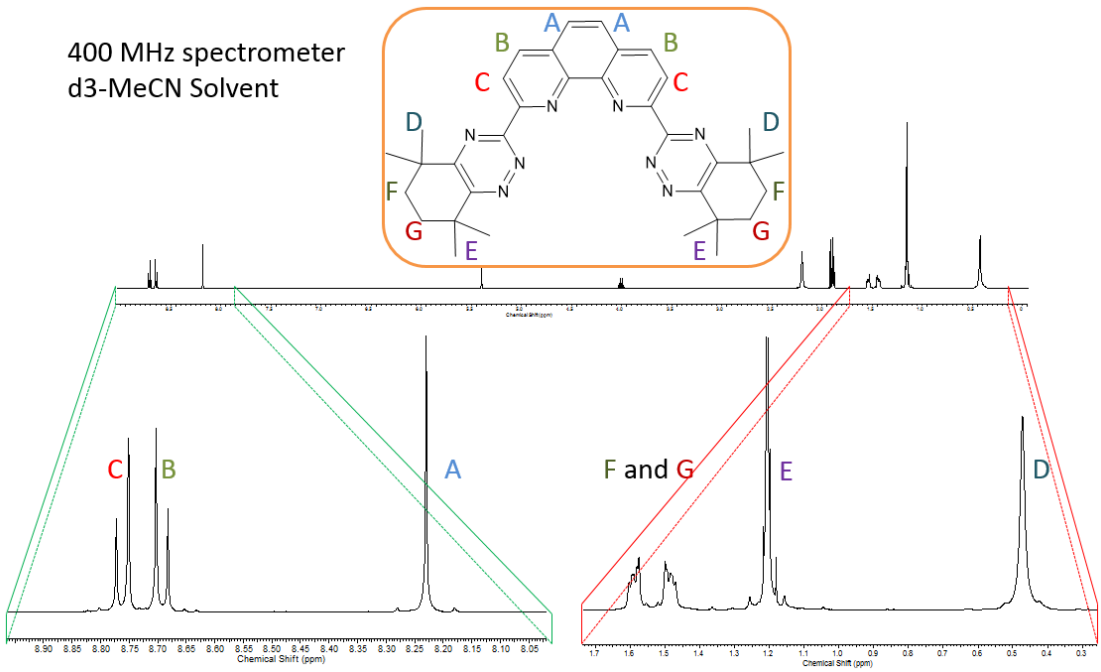

Figure 24: Proton NMR Spectrum of the free BTPhen ligand in deuterated *MeCN*.

As can be seen, when present as a free ligand the resonances corresponding to the protons on the phenanthroline backbone of the BTPhen ligand fall into the aromatic region of the spectrum, whilst the protons that reside in the tetra-methyl cyclohexane group fall into the aliphatic region, as would be expected. Conversely, on coordinating the paramagnetic plutonyl(VI) ion these proton resonances are shifted significantly upfield due to the interaction of the unpaired spin on the metal ion and the nuclear spin of the precessing

protons. The computational prediction of such interactions provides an interesting technical challenge that goes far beyond the typical (although still problematic) prediction of the magnetic properties of closed shell systems. With this in mind it is an academic curiosity that leads this author to wonder how far relatively simple and economical computational models may go towards replicating these complex magnetic interactions. To this end a future report is planned that explores the ability of all electron and ECP DFT to predict these experimental spectra. As may be expected, in general the absolute agreement between the DFT predicted paramagnetic spectra and the experimental spectrum is far from perfect, however the broad trends in the data are correctly predicted.

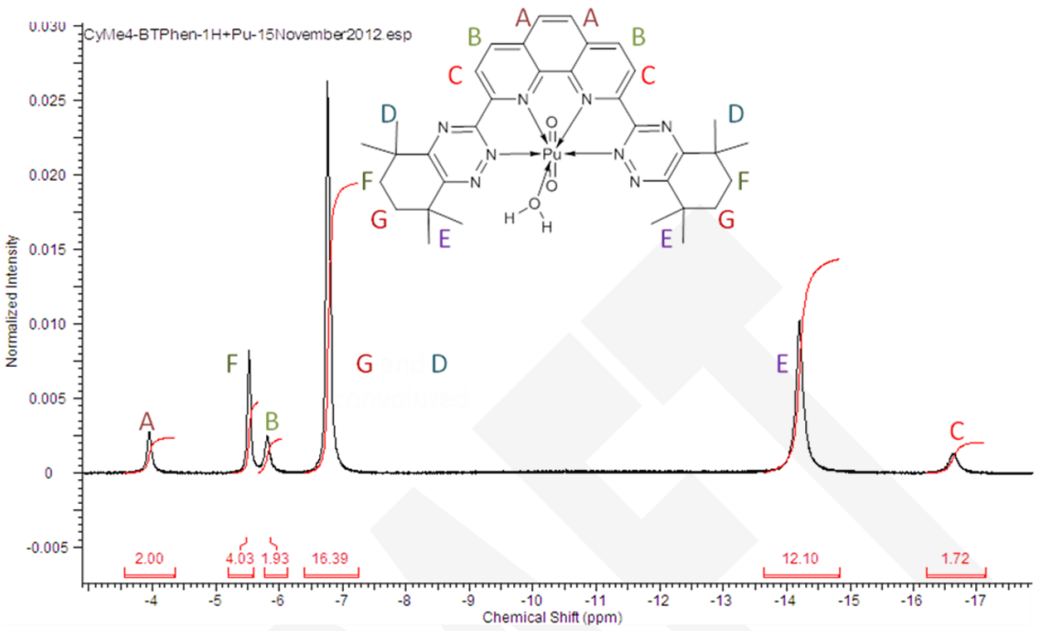

Figure 25: Paramagnetically shifted region of the proton NMR spectrum of a solution containing the species $[PuO_2(BTPhen)H_2O]^{2+}$. The proton positions have been assigned based on 2D COSY experiments and 1D TOCSY experiments conducted.

Comparison of the Behaviour of the Plutonyl(VI) Ion to the Uranyl(VI) Ion

In order to provide a suitable reference point for the behaviour of the plutonyl(VI) ion in systems containing the BTPhen ligand and chloride where practicable the previously described experiments were repeated for the uranyl(VI) ion. Unfortunately, as stated previously, the uranyl(VI) ion does not have any *f*-electrons and hence its solution phase speciation is not as easily studied using UV-vis-nIR spectroscopy as the plutonyl(VI) ion. Nevertheless, in line with studies of the plutonyl(VI) ion the changes in the chemical shift of the protons in the ligating BTPhen ligand are still able to provide an indirect probe of the chemistry occurring at the metal ion.

NMR Titration Experiment to Determine the Stoichiometry of the Uranyl(VI) Complex Formed in Solution

In order to probe the speciation in solutions containing the uranyl(VI) ion, BTPhen and chloride an NMR titration experiment was carried out in which a solution of uranyl(VI) chloride in deuterated acetonitrile was titrated into an acetonitrile solution of BTPhen up to a four molar equivalent excess. Overlaid spectra resulting from this experiment are presented in **Figure 26**.

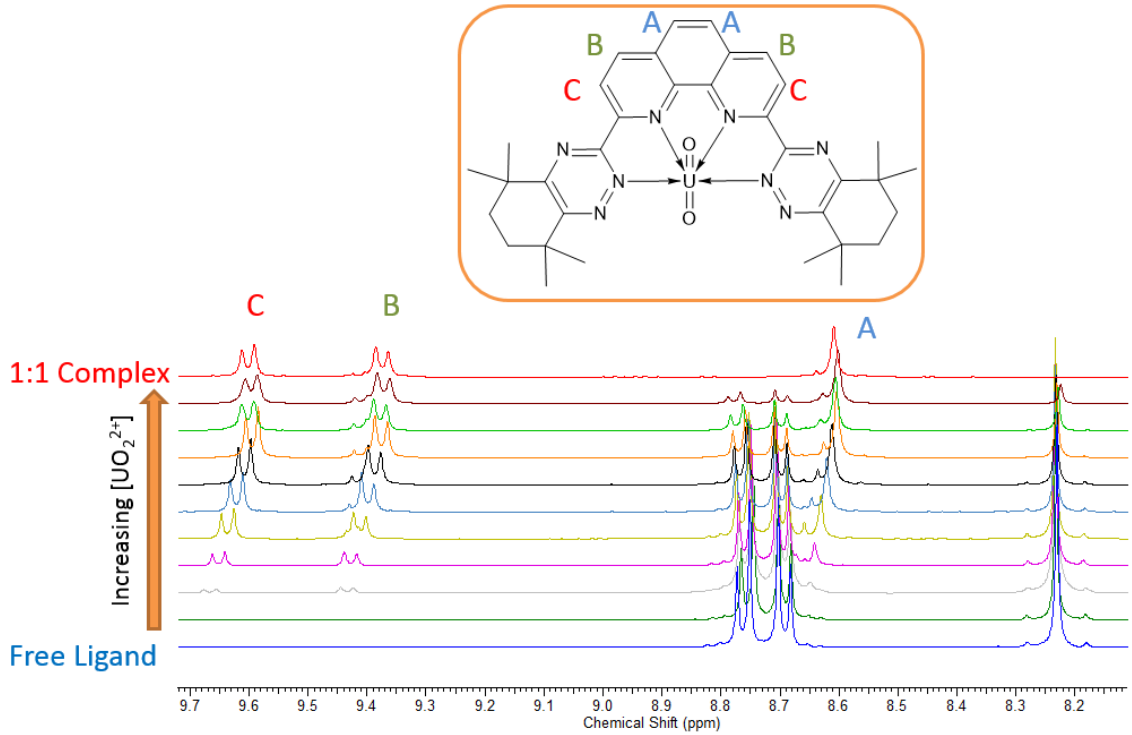

Figure 26: NMR titration in deuterated acetonitrile of uranyl(VI) chloride into a solution of BTPhen. The reaction proceeds from a neat solution of BTPhen to a solution containing an equimolar proportion of uranyl(VI) and the BTPhen ligand. The protons on the BTPhen ligand responsible for the signals in the aromatic region are described with reference to the presented structure.

Figure 26 focusses specifically on the aromatic region of the spectrum in which the resonances due to the phenanthroline based protons are found. The spectra have been offset in order to allow the progression of the complexation reaction to be easilily visualised as the concentration of the uranyl(VI) ion increases in solution, from a neat solution of the BTPhen complex in *MeCN* at the bottom of the figure to a 1:1 molar equivalent mixture of the uranyl(VI) ion and BTPhen at the top. As the concentration of the uranyl ion is increased there is a decrease in the intensity of the signals due to the free ligand (the singlet at 8.23 ppm and the doublet of doublets centred at 8.73 ppm) and there is a concomitant increase in the intensity of a new set of signals shifted downfield due to the formation of the uranyl(VI)-BTPhen complex. These signals are seen to increase in intensity until one molar equivalent of the uranyl(VI) ion has been added to the solution, at which point the signals

due to the free ligand are no longer observed. This indicates that the complex formed in solution is considerably stable and does not undergo a process of fast exchange on the timescale of the NMR experiment conducted. Furthermore, on increasing the relative concentration of BTPhen in excess of the uranyl ion, no additional signals are observed, suggesting that as was observed when studying the plutonyl ion, the limiting complex in this solution is a 1:1 complex.

This suggestion was corroborated by MS analysis of acetonitrile solutions of uranyl(VI) triflate in the presence and absence of chloride, which, similarly to the analogous experiments with the plutonyl(VI) ion, present mass charge fragments representative of the 1:1:1 aquated:plutonyl(VI):BTPhen complex, the monochloro:plutonyl(VI):BTPhen complex and the triflate:plutonyl(VI):BTPhen complex.

These findings are in line with those published by others for similar solutions containing the uranyl(VI) ion and BTPhen[3] or structurally related ligands.[29]

3.4 Conclusion

The coordination chemistry of the plutonyl(VI) ion has been studied using spectrophotometry in aqueous and mixed phase solutions. The triflate anion was found to behave as a non-coordinating anion with respect to the plutonyl(VI) ion in a manner analogous to the perchlorate anion. The formation of chloride complexes in a mixed acetonitrile-water solvent system was found to occur at much lower concentrations than in neat aqueous solution owing to the reduced ability of the mixed system to solvate the liberated ions. This solvation effect was observed to impact on the intensity of the Laporte forbidden *f-f* transitions for the chloride complexes formed resulting in only two of the four chloride complexes characterised in aqueous solution being observed. Spectrophotometric titration studies of BTPhen into solutions containing the plutonyl(VI) ion demonstrated that the BTPhen ligand bound the metal ion rapidly to form a complex with a stability constant of 4.66 ± 0.1. This suggests the BTPhen ligand binds the plutonyl(VI) ion less strongly than the uranyl(VI) ion which has previously been identified as forming a complex with BTPhen with log$K$ = 6.48 ± 0.064.[3] Spectrophotomeric studies indicated it was not possible to form a 2:1 or higher order complex of BTPhen:PuO_2^{2+}, this result was corroborated by gas phase MS and solid state XRD analyses. Addition of chloride to solutions containing the 1:1 BTPhen: PuO_2^{2+} complex resulted in the formation of a 1:1:1 ternary complex with the formula $[PuO_2(BTPhen)Cl]^+$. Even in large molar excesses of chloride the BTPhen ligand was not displaced indicating it is a much stronger ligand for the plutonyl(VI) ion that chloride

anions. The formation of the 1:1:1 ternary complex was confirmed by gas phase MS analysis. Analogous studies were carried out with the uranyl(VI) ion. This system was found to behave similarly to the plutonyl(VI) system, in line with work presented elsewhere.[3] NMR analysis of the plutonyl(VI) and uranyl(VI) systems in acetonitrile provided a set of data against which the ability of computational methods to replicate these complex interactions may be evaluated. This will be the focus of another study.

4 A STUDY OF URANIUM PHOTOCHEMISTRY AND URANYL(VI) PEROXIDE COMPLEXES

4.1 Introduction to Uranium Photochemistry

4.1.1 Historic Uses of Uranium

Uranium was first discovered in 1789 by Martin Klaproth.[114] The element was isolated as an oxide, formed on treating a nitric acid solution of the mineral pitchblende with potash. The vivid yellow uranium oxide formed was coveted as a colourant by the contemporary dye industry for use in ceramic and porcelain glazes and as a result the production of dinnerware containing uranium exploded during the 19th century.[115] The use of uranium was favoured not only for its vibrancy, but also the range of colours its oxides and salts exhibited. By varying the uranium oxidation state, colours of black, green, yellow and the characteristic red-orange colouration of Fiestaware were achieved. The first reported use of uranium in a ceramic glaze dates back to 79 AD to an ancient Roman mosaic tile, although, despite being quoted in the literature frequently,[116–118] it is exceedingly difficult to identify the primary source for this reference. In addition to its use in glazes, historically uranium in its hexavalent oxidation state has been used to produce luminescent yellow and green 'vaseline' glasses that emit green light when exposed to ultra-violet (UV) radiation.[115,117] Slightly more novel applications of the photochemical properties of the uranyl ion include its use as a photographic toner in place of silver nitrate[118] and as a dopant in porcelain teeth where its luminescence supposedly helps the dentures more closely mimic the pearlescence of their natural analogues.[119] More recently, interest has piqued once again in the photochemical properties of the uranyl ion for various applications, including its use as a marker for trace actinide detection and a probe of solution composition;[120,121] as the active species in a 'zero discharge' photochemical redox process to generate *U(IV)*;[122] as the absorbing species in processes exploiting the magnetic isotope effect to direct the course of so called 'spin selective' reactions to separate the isotopes ^{235}U and ^{238}U[123] and as a relatively powerful oxidant to destroy atmospheric and aqueous carcinogens.[124,125] All such applications are owed to the vast wealth of chemistry and physics of one species, the uranyl ion (UO_2^{2+}), and its interaction with light.

4.1.2 Photochemistry of the Uranyl(VI) Ion

The electronic structure of the uranyl ion was described in Chapter 1. Upon irradiation, the uranyl ion absorbs UV and blue light ($\lambda_{max}(UO_2^{2+})$ = 414 nm[4,126]) to form the excited state

uranyl species, $^{*}UO_2^{2+}$. The initial transition is from the mostly oxygen character σ_u MO to the predominantly metal localised δ_u or φ_u orbital to give an open shell singlet state. Formally then, this is a ligand-to-metal charge transfer (LMCT) transition. Following excitation, the uranyl ion has two pathways available to it; it may decay back to the ground state near instantaneously by emitting a photon, i.e. fluorescence, or it can undergo a process of intersystem crossing towards the more stable excited triplet state followed by emission of a photon i.e. phosphorescence. The latter path gives rise to a much longer lived species owing to the spin forbidden nature of the transition back to the closed shell singlet ground state and it is this significantly increased lifetime (of up to 100 µs in phosphate solutions, but typically on the order of 2 µs) that allows much of the photochemistry of the uranyl ion to occur.[125,127–129]

Despite the lifetime of the triplet excited state of the uranyl(VI) ion being appreciably longer than that of its singlet state, it is still much shorter than is typical of other phosphorescent triplet state species. For example, the analogous excited triplet state of benzoquinone has a lifetime on the order of 0.9 ms.[130] This difference historically led to much debate over the nature of the reactive excited state of the uranyl ion, with many describing it as a phosphorescent process and many as a fluorescent process in reference to the short lifetime of the observed excited state. However, seminal work by the likes of Bell et al.,[126] Burrows et al.,[5,128,131] Bakac et al.[4,124,125,132] and Formosinho et. al.[127,133,134] between the mid-1960s and 1990s paved the way to the confirmation that the luminescent state of the uranyl ion is a triplet state and hence any appreciable reduction in the phosphorescent lifetime of this species is due to quenching of the excited state owing to interactions occurring in solution. Predominantly, the excited state of the uranyl ion is known to decay via three processes:

1) hydrogen atom abstraction
2) electron transfer (ET)
3) exciplex formation

The process that is dominant in a particular solution depends on the nature of the other species present.

4.1.2.1 Quenching by Hydrogen Atom Abstraction

The propensity of the excess energy of the excited state uranyl ion to be dissipated by abstracting a hydrogen atom from another species in solution correlates with the *R-H* bond energy of the vulnerable complex, where *R* may be a *C*, *N* or *O* atom. The standard reduction

potential of the excited state uranyl ion, $^{*}UO_2^{2+}$, is +2.6 eV.[135,136] Hence, this is sufficient to abstract a hydrogen atom from most aliphatic hydrocarbons.[132,136] In 1995 Wang et al.[132] studied the rate of oxidation of aliphatic alcohols and aldehydes using the uranyl(VI) ion as a photocatalyst. They found that the excited state uranyl ion facilitated the oxidation of alcohols to aldehydes and ketones, aldehydes to carboxylic acids and alkanes to ketones. Furthermore, they found that varying the excitation wavelength between 423 nm (blue) and 355 nm (UV) did not affect the distribution of products formed. This indicated that the same oxidative mechanism was occurring at both excitation wavelengths. Initial studies identified that the rate of oxidation of isopropyl alcohol was faster than that of methanol with rates on the order of 10^6 M^{-1} s^{-1} and 10^7 M^{-1} s^{-1}, respectively. Such a trend would be expected for a process occurring via a hydrogen atom abstraction as the secondary carbon-centred radical (CCR) formed by the abstraction from isopropyl alcohol would be more effectively stabilised by the inductive effect of the adjacent methyl groups than the corresponding methanol derived radical. The involvement of hydrogen atoms in the oxidation process was confirmed by repeating the study using deuterated methanol, during which a kinetic isotope effect was observed. Furthermore, plots of the bond dissociation energies (BDEs) of the oxidised species against the rates observed exhibited reasonable correlation, whereas the corresponding plot of the ionisation energy of the species studied against the measured rates provided no such correlation. These findings clearly indicate that the oxidation of simple alcohols, aldehydes and the sp^3 hybridised *C-H* bonds of alkanes and alkenes in solution by $^{*}UO_2^{2+}$ occurs via a mechanism of hydrogen atom abstraction. These findings are corroborated by earlier work by Matsushima.[137]

4.1.2.2 Quenching by ET

Similar studies performed to elucidate the dominant quenching mechanism of $^{*}UO_2^{2+}$ in solutions containing alcohols, aldehydes and saturated hydrocarbons were carried out by other groups focussing on the oxidation of simple alkenes and aromatic hydrocarbons. In a study of the oxidation of simple linear mono- and dienes of varying substitution pattern led McCleskey et al.[136] to the conclusion that these species quenched $^{*}UO_2^{2+}$ via an electron transfer (ET) mechanism. In this experiment the series of alkenes studied were selected to fall into two broad series, one across which the BDEs of the species contained remained constant but the ionisation potential (IP) varied and a second across which the IP remained constant, but the BDE varied. On plotting the rates of oxidation of the organic species in each set against either the BDE or the IP, McKleskey et al. were able to identify that the rate of oxidation of alkenes was independent of the BDE and strongly correlated with the IP of the species studied. This suggested the quenching mechanism utilised by alkenes occurs via

ET to the excited state uranyl(VI) ion. These findings were echoed by Mao et al.[125] who studied the oxidation of naphthalene by the excited state uranyl ion. These studies identified that the naphthalene was oxidised via an outer sphere electron transfer (OS-ET) process that reduced the excited uranyl(VI) ion, forming a protonated uranyl(V) ion, $U^{V}OHO^{+}$. The identification of this process as an ET was corroborated by the lack of an observed kinetic isotope effect in these solutions. Despite OS-ET being observed in solutions containing naphthalene and $^{*}UO_2^{2+}$, the efficiency of formation of the naphthalene radical cations, indicative of the occurrence of ET, was only 30 %. Hence, this suggested that a second means of quenching was out-competing the ET process in these solutions.

4.1.2.3 Quenching by Exciplex formation

As stated, the quenching of uranyl(VI) phosphorescence by ET in solutions containing naphthalene was observed by Mao et al.[125] to have a quantum yield of only 0.3. This thereby suggested that 70 % of excited state uranyl ions, formed in the naphthalene-containing solutions studied, were quenched via an alternative mechanism. The competing mechanism proposed was quenching via exciplex formation. Exciplex is a contraction of the term excited state complex and typically refers to non-covalently bound molecules that only favourably associate when one of the species is in an electronically excited state. Quenching by exciplex formation is typically characterised by a dissipation of the energy associated with the excited state species in a manner that does not involve chemical reaction. Thus, the energy is either dissipated via luminescence if the exciplex has an accessible lower lying electronic state to relax into, though this is typically not the case for small aromatic molecules and olefins[138], or thermal dissipation if no such electronic state is available, typically through *C-H* stretching modes.[134] In the absence of additional oxidisers, Mao et al. found that the quenching of $^{*}UO_2^{2+}$ in the presence of benzene occurred exclusively via a radiationless exciplex formation mechanism that regenerated the reactant UO_2^{2+} and benzene species without any chemical modification.[124] Matsushima et al.[137] suggested that the favourable formation of an exciplex in this system was due to perturbation of the π-electron cloud of the benzene ligand which permitted the formation of a δ^{-} δ^{+} associated pair. This pair is lower in energy than free $^{*}UO_2^{2+}$ and ground state benzene systems combined or a system in which an electron is formally abstracted from benzene creating a radical pair. In this way an exciplex may be described as a partial charge transfer (CT) state. Therefore, similarly to the ET quenching mechanism described above, the probability of exciplex formation is somewhat dependent on the IP of the reductant species involved.

4.1.3 Application of DFT to Model the Quenching of the Luminescent state of $*UO_2^{2+}$

Recently Tsushima et al. have invested a considerable amount of time into studying the quenching mechanisms of the uranyl(VI) excited state using DFT. In particular, they have demonstrated that using an unrestricted formalism of B3LYP in the absence of corrections for the BSSE and SO effects they are able to reproduce the experimentally observed trends in uranyl photochemistry.[79,105,106,116] This is somewhat surprising as whilst the uranyl(VI) is not subject to SO effects, the excited state of the uranyl(VI) ion and its reduced analogue, the uranyl(V) cation, are. Despite this technically incorrect neglect of SO coupling for these species, Tsushima et al. conclude that the non-bonding and near-degenerate nature of the δ_u and φ_u orbitals of the uranyl ion means that the geometric and luminescent properties calculated when neglecting SO coupling are broadly invariant between the two states. Furthermore, they suggest that the use of an unrestricted formalism of DFT allows the calculation to converge upon a state averaged solution which, whilst describing neither electronic state of the uranyl ion correctly, generates a solution with broadly similar properties to the true system owing to the near-degeneracy of the two non-bonding states.

In their study, Tsushima et al.[116] initially probed the quenching of $*UO_2^{2+}$ via halide ions. Experimentally it had been noted that heavier halide anions were able to quench the luminescence of the uranyl ion more effectively than smaller halides. This series was bounded by the fluoride and the iodide anions. In the presence of fluoride, no premature quenching of the uranyl ion luminescence is observed. On the other hand, in the presence of iodide efficient quenching of the excited state is observed. The calculation took advantage of the differing spin states of the excited and ground state systems in order to constrain the solution to describe the chemistry of interest. In this way, solution phase optimisations were carried out for the singlet and triplet multiplicities of aquated mono-halide complexes of the uranyl ion in order to represent the ground and excited states, respectively. Following optimisation, spin density and MO analyses of the electronic structure were carried out in order to identify any possible differences between the models that may explain the difference in quenching behaviour. To this end, Tsushima et al. identified that excitation of the fluoride complex of the uranyl ion gave rise to only a slight redistribution of the electron density. This was characterised by a metal centred charge transfer (MCCT) excitation and correspondingly, the excited state of the uranyl ion housed two unpaired spins following excitation. In contrast, on excitation of the iodide analogue of this complex a considerable redistribution of the charge in the system was observed. This was characterised as an LMCT process in which excitation essentially led to the formation of a uranium(V)-iodine radical

pair, $[UO_2^{+}X\cdot]$. The formation of this state was characterised by the spin density analysis of the excited state indicating that the two unpaired spins in the system were localised on the uranium atom and the iodine atom. The identification of the quenching in the iodide bound system as via the formation of a uranyl(V)-radical pair, validated the mechanism previously proposed by Burrows et al.[139] based on empirical findings. In line with these two bounding species, analogous studies of the uranyl-chloride and -bromide complexes yielded intermediate results.

In a similar manner, Tsushima et al.[106,116] also studied the quenching of $*UO_2^{2+}$ via hydrogen atom abstraction from methanol. In this study it was shown that, similar to the uranyl-iodide analogue, excitation gave rise to a redistribution of charge in the system indicative of quenching and the formation of a radical pair. In this case, excitation of the uranyl ion generated a protonated uranyl(V) ion, $U^{V}OHO^{2+}$ and a CCR. As observed in the case of uranyl iodide, a Mulliken spin density analysis of the system reflected this result, with near unit sharing of the two unpaired spins between the uranyl ion and the CCR. Following on from this point, Tsushima et al. conducted an energetic analysis of the reaction that occurs between a ground state uranyl(VI) ion and the CCR formed during the initial reaction that generates a second mole of $U^{V}OHO^{2+}$ and formaldehyde. When modelling this process Tsushima et al. considered the reaction proceeding via a mediating water molecule in order to act as a buffer and ensure the process proceeded by an intramolecular procedure in order to bypass the geometric constraints that a directly bound reaction would require. In line with the kinetic considerations of Nagaishi et al.[140] this process was found to be exergonic. In order to probe the geometric dependence of the energy of the ground state and excited state uranyl(VI)-methanol system on the nature of the hydrogen bond between the O_{yl} atom and the methanol methyl group, Tsushima et al. carried out a rigid PES scan. This scan varied the separation between the oxygen atom of the uranyl ion (O_{yl}) and the bridging hydrogen atom in both the singlet and triplet states in order to examine the topology of the PES for the hydrogen abstraction process. These surfaces were then compared to the analogous scans conducted for a uranyl-water analogue of this system, in the knowledge that water is a much less efficient hydrogen donor than methanol.[138] This study identified that the triplet surface that describes the MCCT transition is distinct from the surface that describes the hydrogen atom abstraction and that in order for the system to cross between these two surfaces and allow the ET from the methanol molecule to the excited state uranyl ion, a degree of structural reorganisation is required. In this way, the hydrogen atom abstraction process in this system is reminiscent of Marcus's theory of ET.

In addition to studying the quenching behaviour of $*UO_2^{2+}$ it is worth noting that Tsushima et al.[105] have since successfully utilised the same methodology to study the photochemistry of the uranyl(VI)-oxalate complex. In this study, the computational methodology correctly described the experimental observation that this complex decomposes to release carbon dioxide at high pH and carbon monoxide at low pH. Thereby further validating the use of B3LYP to study photochemical reactions of the uranyl ion.

4.1.4 Empirical Kinetic Studies of Peroxide Formation and Suggested Mechanisms

Whilst carrying out studies into the quenching of uranyl luminescence in different solutions, several authors have commented on the effect of oxygen on the reaction. Primarily, it was noted that oxygen had no effect on the rate of quenching of the excited state of the uranyl(VI) ion itself.[138] However, despite the fact that no direct interaction could be identified, the presence of oxygen was observed to increase the quantum yield of the photolysis reaction,[141] indicating dioxygen was playing a role at another point in the mechanism. With the discovery of hydrogen peroxide in photolysed solutions containing the uranyl ion, Bakac et al. subsequently identified that the role of dioxygen was to act as an oxidant to the uranyl(V) ion, thereby regenerating the starting uranyl(VI) ion and making the process catalytic.[4,125,132] The general mechanistic scheme as originally proposed by Bakac et al. is presented in **Equations 39-43**.

$$U^{VI}O_2^{2+} \xrightarrow{h\nu} *U^{VI}O_2^{2+} \quad \textbf{(39)}$$

$$*U^{VI}O_2^{2+} + MeOH \longrightarrow U^{V}O_2^{+} + {}^{\bullet}CH_2OH + H^{+} \quad \textbf{(40)}$$

$${}^{\bullet}CH_2OH + O_2 \longrightarrow products \quad \textbf{(41)}$$

$$U^{V}O_2^{+} + O_2 \longrightarrow U^{VI}O_2^{2+} + Int \quad \textbf{(42)}$$

$$U^{V}O_2^{+} + Int \xrightarrow{H^{+},\, fast} U^{VI}O_2^{2+} + H_2O_2 \quad \textbf{(43)}$$

In this scheme *Int* is a placeholder for an intermediate species that was proposed by Bakac et al. to be either the superoxide anion, ${}^{\bullet}O_2^{-}$, its conjugate acid the hydroperoxyl radical, ${}^{\bullet}O_2H$ or a uranyl(VI)-hydroperoxyl radical complex, $[U^{VI}O_2({}^{\bullet}O_2H)]^{2+}$. From their initial studies of the autoxidation of the uranyl(V) ion, Bakac et al.[4,132] were able to draw multiple conclusions that along with contributions from other groups[128,131] allow the physical characterisation of the catalytic process as follows:

1) the formation of $*UO_2^{2+}$ from UO_2^{2+} is a monophotonic process.[141]

2) The process proceeds with a stoichiometry of 2:1 $[UO_2^+]$:$[O_2]$ and generates UO_2^{2+} and H_2O_2 in quantitative yield. Therefore, two molecules of UO_2^{2+} must be excited to form each molecule of hydrogen peroxide.[4]

Furthermore, on the basis of their understanding of similar reactions, the following inferences about the mechanistic route were made:

3) the ET between $U^VO_2^+$ and O_2 is likely to proceed via the formation of an inner sphere complex as the standard redox potentials of these species suggest that an outer sphere process would be unfeasible.[4]
4) Following the initial ET, it is likely that the uranyl(VI)-superoxide complex formed rapidly protonates to form $[UO_2(^\bullet O_2H)]^{2+}$. Bakac et al. propose this to be the intermediate species described. This complex may then dissociate yielding free $U^{VI}O_2^{2+}$ and $^\bullet O_2H$.[4]
5) It is probable that the second ET between $U^VO_2^+$ and $^\bullet O_2H$ will occur as an OS process, as the standard reduction potentials for these species suggest this is a feasible reaction.[4]

Despite these conclusions, Bakac et al. were keen to demonstrate that these mechanistic considerations are borne out of a kinetic study, and hence there is an uncertainty inherent in the assignment of the specific actors in the mechanism described. Despite this, owing to the acidic pH of the experimental set up, they state that it is conceptually appealing that the intermediate species is the hydroperoxyl radical complex of the uranyl(VI) ion, $[UO_2(^\bullet O_2H)]^{2+}$.

The initial studies of Bakac et al.[4] were not the first time that the kinetics of the complex formed in solutions containing the uranyl(VI) ion and the hydroperoxyl radical had been studied. In the early 1970s, Meisel et al. published a suite of papers studying the UV-vis and electron paramagnetic resonance (EPR) spectroscopic properties of this complex.[142,143] This combination of techniques allowed the stability constant of the paramagnetic complex formed in such solutions to be determined. The stability constant of the species observed was calculated to be ~1.5 x 10^3 M^{-1} and was independent of the spectroscopic technique employed. This rate corresponds to a moderate free energy change for the reaction of -4.3 kcal mol^{-1}. Similarly to Bakac et al., Meisel et al. conducted their studies in a 0.1 M acidic solution. Hence, as the pK_a of $^\bullet O_2H$ is known to be 4.86[142,144,145] in aqueous solution,[144,146] Meisel et al. also suggested that the paramagnetic complex formed in their solutions was $[UO_2(^\bullet O_2H)]^{2+}$.

Despite this perceived consensus, not everyone held the same opinion about the coordination chemistry of the superoxide anion and its conjugate acid. In particular, Berdnikov et al.[147–149] stated that the superoxide most likely forms complexes with transition metal ions as the conjugate base species, i.e. complexes of the type $[UO_2(^{\bullet}O_2)]^+$. This difference of opinion has since been documented in a review of superoxide chemistry by Afanas'ev.[144]

Disregarding this controversy over the identity of the intermediate species for the moment and bringing back to the fore the conclusions about the process drawn by Bakac et al.[4] it is possible to present Scheme 1 in which the general mechanism as proposed by Bakac et al. has expanded in order to incorporate their inferred conclusions.

$$U^{VI}O_2^{2+} \xrightarrow{h\nu} {}^*U^{VI}O_2^{2+} \quad \textbf{(39)}$$

$${}^*U^{VI}O_2^{2+} + MeOH \longrightarrow U^{V}O_2^{+} + {}^{\bullet}CH_2OH + H^+ \quad \textbf{(40)}$$

$$U^{V}O_2^{+} + O_2 \longleftrightarrow [U^{V}O_2(O_2)]^+ \quad \textbf{(44)}$$

$$[U^{V}O_2(O_2)]^+ \xrightarrow{ET} [U^{VI}O_2(O_2^{\bullet})]^+ \quad \textbf{(45)}$$

$$[U^{VI}O_2(O_2^{\bullet})]^+ + H_3O^+ \longleftrightarrow [U^{VI}O_2(HO_2^{\bullet})]^{2+} + H_2O \quad \textbf{(46)}$$

$$[U^{VI}O_2(HO_2^{\bullet})]^{2+} \longleftrightarrow U^{VI}O_2^{2+} + HO_2^{\bullet} \quad \textbf{(47)}$$

$$U^{V}O_2^{+} + HO_2^{\bullet} \xrightarrow{OS-ET} U^{VI}O_2^{2+} + HO_2^{-} \quad \textbf{(48)}$$

This reaction scheme is therefore initiated by the photoexcitation of the uranyl ion in order to form its excited state analogue in **Equation 39**. Following on, this species abstracts a hydrogen atom from a molecule of nearby methanol solvent leading to the formation of a uranyl(V) species, a CCR and a proton (**Equation 40**). The uranyl(V) ion formed then goes on to form a transient complex with dissolved dioxygen which undergoes ET to form a uranyl(VI)-superoxide complex, see **Equation 44**. This species is then rapidly protonated in acid leading to the corresponding hydroperoxyl radical bound analogue (**Equation 46**). Subsequently this species dissociates thereby releasing the regenerated uranyl(VI) photocatalyst and a hydroperoxyl radical as shown in **Equation 47**. Finally, the hydroperoxyl radical encounters a uranyl(V) ion, formed by a subsequent photoexcitation and hydrogen atom abstraction process, and an OS-ET occurs between these species in order to generate a molecule of hydroperoxide as per **Equation 48**, which may then be protonated to form hydrogen peroxide. The standard reduction potential of the uranyl(VI) ion is +0.16 V[4,5,150] and those of the hydroperoxyl radical and the superoxide anion are +1.44 V[150] and +0.20 V,[150] respectively. These relate to reaction free energies for the reduction of the hydroperoxyl radical and superoxide anion by a uranyl(V) ion of -36.9 kcal mol^{-1}

and -8.3 kcal mol^{-1}, respectively. Hence, these standard potentials suggest that both the hydroperoxyl radical and its conjugate base are reduced spontaneously via an OS-ET reaction with the uranyl(V) ion. This compares to the standard reduction potential of dioxygen of -0.33 V,[150] which relates to a reaction free energy change of +3.9 kcal mol^{-1} and is therefore predicted not to be a spontaneous process under standard conditions. In addition to the OS-ET process suggested by Bakac et al.[4] to be the final step of the reduction of dioxygen to peroxide, there are two other reduction pathways that are likely to compete with this process in solution. The first of these processes is the corresponding IS-ET reaction that occurs via formation of a discrete uranyl(V)-superoxide complex, analogous to the initial uranyl(VI)-dioxygen complex described. The second is the disproportionation of the hydroperoxyl radical, as per **Equation 49**.

$$^{\bullet}O_2H + {}^{\bullet}O_2H \longrightarrow O_2 + H_2O_2 \qquad \textbf{(49)}$$

Despite disproportionation typically being the predominant method of termination of the hydroperoxyl radical in neat aqueous solution, the fact that the photochemical experiments of Bakac et al.[4] identified a reaction stoichiometry of 2:1 $[UO_2^{+}]$:$[O_2]$ suggests that reduction of dioxygen via an IS or OS electron transfer from a uranyl(V) ion is likely to be the dominant pathway in solutions containing the uranyl ion.

Since these initial studies, interest in the superoxide chemistry of the uranyl ion has died down, only to be revived relatively recently. Thus, there is still considerable dispute in the literature over the nature of the 'intermediate species' as defined by Bakac et al. In particular, this debate focusses on whether it is a uranyl(VI) complex of the hydroperoxyl radical or of the superoxide anion. In a recent publication by Bühl, Sieffert and Wipff[35] a combination of quantum chemical techniques including DFT (B3LYP), QM/MM and Car-Parrinello molecular dynamics were used to identify the nature of the complex that persists in analogous solutions containing the uranyl(VI) ion and hydrogen peroxide. This study concluded that the polarising nature of the solvent favours the formation of the deprotonated uranyl(VI) peroxide complex as opposed to the hydroperoxide analogue. Hence, in addition to highlighting the importance of solvation in directing the chemistry of these systems, this paper also contributes to the debate over the nature of the species formed between the uranyl(VI) ion and anionic dioxygen species that empirical studies have, to date, failed to determine.

4.1.5 Uranyl(VI)-Peroxide Complexes in the Solid State

Recently, interest in uranyl photochemistry has surged across a few labs due to the characterisation of peroxide in solutions that were previously assumed to be innocuous. As

explained, in certain academic circles the photoreactivity of the uranyl ion has been known and studied for decades, however the prevailing view of many radiochemists is that the uranyl ion is an essentially inert species. Despite this, the repeated characterisation of uranyl peroxide complexes crystallised from solutions to which no peroxide was added directly, and in which peroxide formed by radiolysis is in short supply, is forcing the general community to change its stance.

A recent addition to this group of peroxide bridged complexes observed to form on allowing access of molecular oxygen to solutions of the uranyl ion, is the bisuranyl peroxide bridged 'pacman' complex described Arnold et al.[151] This complex displays two uranyl(VI) ions bridged by a peroxide anion housed within the novel macrocyclic 'pacman' ligand. When published in 2012, the authors claimed that this complex was "*the first uranyl peroxide complex formed by a redox reaction"*[151] although a quick search of the literature (including some of the papers referenced by Arnold et al.[151]) indicates this not to be the case as many of the peroxide bound complexes identified prior to this point, for example Rose et al.,[152] Doyle et al.[153] and John et al.[154] (and references within) all invoke a two electron reduction of dioxygen by uranyl(V) as the mechanism of formation of the peroxide bridge. This is not an isolated example of confusion in the mainstream literature in this field and whilst there are groups who are unaware of the breadth of knowledge of this topic there are others who even fail to grasp the nature of the complex they are characterising. A prime example of this is the bisuranyl(VI) peroxide bridged bipyridine complex structurally characterised by Wang et al.[155] This complex was originally characterised as a bis-oxo bridged bisuranyl complex when it was published in 2012, despite the 1.48 Å separation of the two bridging oxygen atoms, however this oversight has since been corrected in the data deposited in the Cambridge Structural Database (CSD), as maintained by the Cambridge Crystallographic Data Centre (CCDC).

Despite the inaccuracy of the previous claim made by Arnold et al.,[151] the identification of the formation of peroxide in their solutions does provide a result of note. Much of the work of this group is centred around characterisation of uranyl(V) complexes, specifically those that have been functionalised on the O_{yl} atom. For this purpose the 'pacman' ligand has been identified as surprisingly apt and hence the identification of peroxide bridged complexes forming following ingress of molecular oxygen into solutions that have previously been shown to contain macroscopic amounts of the uranyl(V) ion, gives additional credence to the mechanism proposed by Bakac et al.[4] to form peroxide. In addition, Arnold et al.[156] have recently confirmed the formation of a remarkably stable protonated uranyl(V) ion in solution

by nuclear magnetic resonance (NMR) spectroscopy. As discussed previously, the protonated uranyl(V) ion is likely to be the species formed directly following the quenching of the uranyl(VI) excited state by hydrogen atom abstraction. In the mechanism proposed by Bakac et al.,[4] the protonated uranyl(V) ion was assumed to dissociate immediately following its formation to generate an acidic proton and a uranyl(V) ion which goes on to reduce molecular oxygen. In this respect, it is likely that Bakac et al. were a product of their time and the prevailing perception of the uranyl ion as a relatively inert three atom system. Despite this, as suggested by the identification of a "*remarkably stable*"[156] protonated uranyl(V) complex isolatable in macroscopic quantities, one could suggest that Bakac et al. may have been mistaken in this respect and the protonated uranyl(V) ion may persist through to later reactions in the peroxide forming mechanism than previously proposed.

In addition to formation of peroxide through a two electron reduction of molecular oxygen, recent work by McGrail et al.[157] suggests that the uranyl ion is also able to oxidise water to generate peroxide bridged complexes. This study crystallographically identified a bisuranyl(VI)-peroxide bridged complex of the formula $[(UO_2)_2(O_2)(NO_3)_2(py)_4]$ in photolysed pyridine solutions of uranyl nitrate. Initially the group assumed that this species was formed via the reduction of molecular oxygen as described by Bakac et al,[4] however, the product was also isolated when the photolysis occurred under an inert argon atmosphere thereby suggesting an alternative mechanism was at play. Subsequent identification of molecular hydrogen in the ullage of the reaction vessel and labelling studies employing ^{18}O labelled water led McGrail et al.[157] to suggest that the mechanism was proceeding via a two electron oxidation of a bishydroxide bridge in a bisuranyl dimeric complex stimulated by two single photon absorptions. In this way, it was proposed that the excited state of the uranyl ion in such a bisuranyl-bishydroxide bridged complex is quenched by hydrogen atom abstraction from the hydroxide bridge. This leads to the formation of two protonated uranyl(V) ions which lose their excess electron and proton on forming molecular hydrogen, whilst the two bridging oxygen radicals generated mutually terminate yielding a bridging peroxide moiety.

It seems the chemistry of the uranyl ion is not as mature as many believe, and its ability to surprise is proving interesting to many contemporary experimentalists and theoreticians alike. Despite this, the peroxide coordination chemistry of the uranyl(VI) ion has been studied purposefully since the mid-2000s, with the crystallographic characterisation of the first mineral containing peroxide, Studtite.[158] This mineral consists of infinite 1D chains of $[UO_2(O_2)_2(H_2O)_2]^{2-}$ polyhedra linked by edge sharing peroxide anions and whilst found

naturally in geologies containing high concentrations of uranium, it also thought to be an important alteration phase of nuclear fuel.[158,159] The mineral is thought to form spontaneously in aquifers with a minority peroxide constituent, from natural processes in contact with high concentrations of uranium, but has also been observed on the surface of nuclear waste containers stored in an aqueous environment.[158,159] In the latter case it is thought that the intense radiation field of the waste gives rise to reactive oxygen species such as peroxide in the contacted water and subsequently, any breach of the waste containment releasing uranium will promote the formation of these stable mineral phases. This is not where the study of uranium peroxide phases ends however, as recent work by the same group has led to the characterisation of many more systems built from uranium peroxide polyhedra, ranging in structure from isolated uranyl peroxide species,[160–162] bridged dimers,[151,157,162,163] 2D lattices[2] and cage clusters containing up to 124 uranyl ions.[163] All these phases are observed to form spontaneously in solutions containing the uranyl(VI) ion and peroxide and exhibit a strong pH dependence analogous to the polyoxometallate (POM) clusters of the transition metals. Considering the prevalence of cement and other high pH materials in the nuclear industry, specifically its planned use in geological disposal facilities, it is likely that the formation of such complexes will strongly affect the environmental transport of uranium and so they represent a worthwhile area of study.[164]

At the time of writing, there were 34 structures in the CSD that include a uranyl(VI)-peroxide-uranyl(VI) bonding motif. Of these 34 structures, 21 describe isolated peroxide bridged bisuranyl units and 13 represent extended structures built by combining the individual uranyl peroxide polyhedra. Now that a reasonably large number of uranyl peroxide species have been characterised it is possible to comment on their structural similarities and hypothesise as to the origins of their differences, be they electronic, steric or crystal packing phenomena. In this respect, quantum chemistry has been employed by this author, as well as those of other groups, in order to rationalise the experimental structure identified. This introduction will conclude with a summary of the structural properties of the peroxide bridged bisuranyl complexes crystallographically characterised to date and the key findings of others who have applied the computational chemistry to elucidate the reasons behind these structural differences.

4.1.5.1 Uranyl(VI) Peroxide Monomers

There is only one structure in the CSD of an isolated uranyl ion bound by a peroxide unit. This is a dicarbonato-peroxo-uranylate complex based on the $[UO_2(CO_3)_2(O_2)]^{4-}$ unit. This structure was characterised in 1984,[160] and although it is the only structure of its kind in the

CSD a similar structure built around the same anionic unit, but containing a different charge balancing cation has recently been published by Runde[161] The peroxide unit in these structures are 1.52 Å and 1.50 Å in length, respectively, and they both bind the uranyl ion in a bidentate fashion at mean distances of 2.23 Å and 2.25 Å, respectively. The carbonate units are similarly bound in a bidentate mode and exhibit slightly longer mean distances to the uranyl centre of 2.42 Å and 2.45 Å. The uranyl ions display the near linearity characteristic of the species (176.9° and 175.3°) as well as the expected short uranium to O_{yl} (U-O_{yl}) contacts of 1.79 Å and 1.81 Å, respectively. To aid visualisation of these species, an image of the structure identified by Mikhailov et al.[160] as generated from their published crystallographic information file (CIF) deposited in the CSD is presented in **Figure 27**.

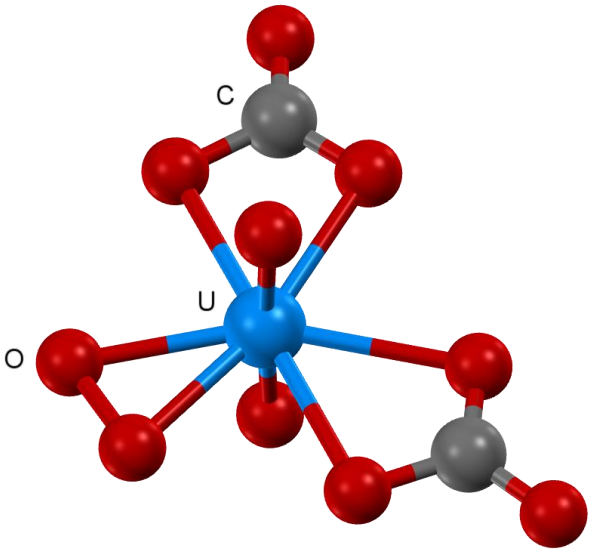

Figure 27: Structure of the $[UO_2(CO_3)_2(O_2)]^{4-}$ anion as determined by Mikhailov et al.[160] using XRD. This image was generated using the CIF deposited in the CSD by Mikhailov et al.[160] using the Mercury visualisation package[165–168] provided by the CCDC.

These structures of monouranyl-monoperoxide complexes may also be compared to an analogous anionic species isolated and characterised by Kubatko et al.[162] This structure differs from those above in that the uranyl ion in the systems characterised by Kubatko et al. describes a uranyl(VI) ion equatorially coordinated by three bidentate peroxide ligands. The uranate anion formed thereby takes on D_{3h} symmetry and hence rather aptly resembles a trefoil when viewed along the axis of the uranyl ion, **Figure 28**.

Kubatko et al. identified two systems which contained these isolated $[UO_2(O_2)_3]^{4-}$ units, but that differed in the charge balancing counterion; sodium or calcium. Despite this difference both structures were very similar. In the uranyl trisperoxo complexes the average peroxide bond length was found to be 1.49 Å and 1.51 Å for the sodium and calcium containing systems, respectively. Similarly to the carbonate bearing system the peroxide ligands were

all found to bind the uranyl ion in a bidentate manner, however, the lengths of these interactions compared to the $U\text{-}O_{perox}$ interactions in the carbonate complex were found to be significantly shorter at 2.31 Å and 2.30 Å for the sodium and calcium complexes respectively, as compared to 2.42 Å and 2.45 Å for the corresponding peroxide interaction in the carbonate complexes of Mikhailov et al.[160] and Runde,[161] respectively. As suggested by Kubatko et al.[162] this short interaction is likely permitted by the small bite angle of the peroxide anion that reduces steric crowding in the equatorial binding plane of the uranyl ion and thus permits a closer approach of the strongly binding peroxide anion. The increased strength of the binding interaction with the equatorial ligand field in the trisperoxide complexes relative to the monoperoxide complexes is reflected in the length of the $U\text{-}O_{yl}$ bonds of the uranyl ion which typically compete with the equatorial ligands for uranium bonding orbitals of correct symmetry. In this example the trisperoxide complexes display $U\text{-}O_{yl}$ bond lengths of 1.85 Å and 1.84 Å for the sodium and calcium containing complexes, respectively as compared to an average $U\text{-}O_{yl}$ bond length of 1.80 Å in the monoperoxide analogues.

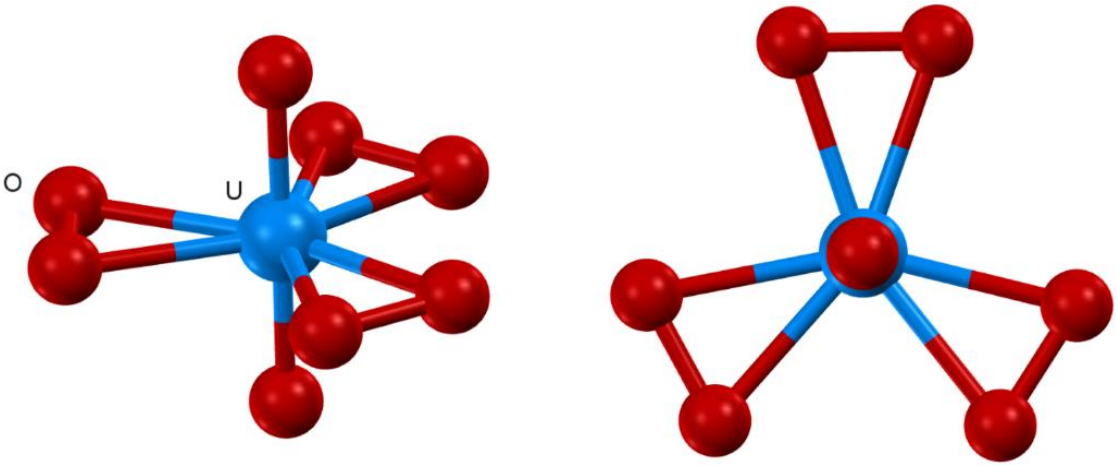

Figure 28: Structure of the $[UO_2(O_2)_3]^{4-}$ anion as determined by Kubatko et al.[162] using XRD. The right image is a plan view of the structure demonstrating the similarties of the appearance of this complex to the radioactive trefoil. This image was generated using the CIF deposited in the CSD by Kubatko et al.[162] using the Mercury visualisation package[165–168] provided by the CCDC.

4.1.5.2 Uranyl(VI) Trisperoxide Dimers and Higher Order Structures

The uranyl(VI)-trisperoxide structures characterised by Kubatko et al.[2,162] take the form of distorted hexagonal bipyrimidal polyhedra. In subsequent studies conducted by Kubatko et al., these polyhedra have been shown to polymerise generating 2D planes and 3D cages built from the $[UO_2(O_2)_3]^{4-}$ monomeric building blocks. Examples of such

structures characterised by Kubatko et al.[2,162] and Sigmon et al.[163,169] are presented in **Figure 29**.

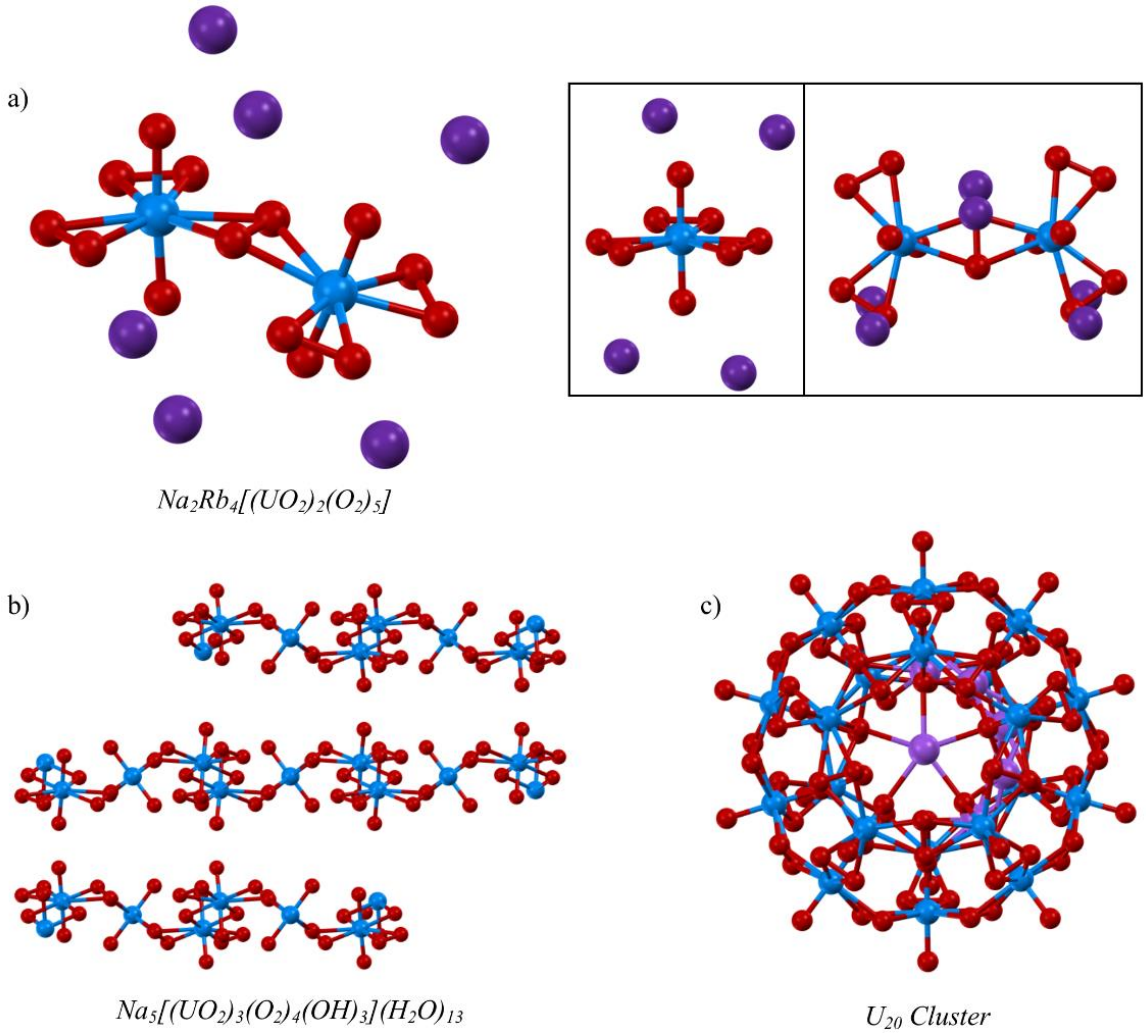

Figure 29: Examples of the different secondary structures that may be formed using uranyl(VI)-peroxide building blocks. Images generated from the CIF documents deposited in the CSD by the original authors; a) the 1D bisuranyl(VI)-pentaperoxide complex isolated by Kubatko et al.[162] (counterions included as purple spheres), b) the 2D sheet arrangement of uranyl(VI)-trisperoxide complexes as characterised by Kubatko et al.[2] (counterion layers that interleave the uranyl-peroxide layers have been omitted for clarity), c) the 20 membered uranyl(VI)-trisperoxide spherical structure characterised by Sigmon et al.[163] All images were generated using Mercury.[165–168]

As shown above, the secondary structures that may be constructed from these distorted hexagonal bipyrimidal polyhedra building blocks are varied. However, the complexes formed all exhibit characteristic primary structural motifs that are relatively invariant to the secondary structure of the material. **Table 2** presents structural parameters covering the gamut of uranyl(VI)-trisperoxide complexes identified by Kubatko et al. and Sigmon et al. The principal investigator in all of these studies is P. Burns, University of Notre Dame, IN, USA.

Table 2: Table of structural parameters of trisperoxide bound uranyl(VI) complexes characterised by Burns et al. (see table for specific references) .

Structure	Bridging Peroxide *O-O* Bond length /Å	Non-Bridging Peroxide *O-O* Bond length /Å	Ave $U\text{-}O_{yl}$ /Å	Ave $U\text{-}O_{eq}$ /Å	*U-O-O-U* dihedral angle
Isolated Polyhedra					
$Na_4\ [UO_2(O_2)_3]$[162]	n/a	1.49	1.85	2.31	n/a
$Ca_4\ [UO_2(O_2)_3]$[162]	n/a	1.51	1.84	2.30	n/a
Dimeric Polyhedra					
$Na_2Rb_4[(UO_2)_2(O_2)_5]$[162]	1.50	1.49	1.83	2.32	153.1 °
2D plane					
$Na_5[(UO_2)_3(O_2)_4(OH)_3](H_2O)_{13}{}^2$	1.49	1.47	1.82	2.35	134.8 °
Ring shaped Clusters					
$K_{10}[(UO_2)(O_2)(C_2O_4)]_5(H_2O)_{13}$[163]	1.49	n/a	1.79	2.35	142.5 ° -158.4 °
$Na_{12}[(UO_2)(O_2)(C_2O_4)]_6(H_2O)_{29}$[163]	1.46	n/a	1.79	2.35	137.5 ° -144.5 °
Spherical Clusters[163]		*U-O-O-U* dihedral angles			
U_{20}		138.5 ° -142.1 °			
U_{24}		135.5 °			
U_{60}		144.8 °			

It is clear from **Table 2** that many of these structures contain similar characteristics, for example all of the peroxide ligand bond lengths lie within the range of 1.46 Å – 1.51 Å and the length of the coordinate bond between the peroxide anions and the uranium atom are all within a range of 1.79 Å – 1.85 Å. Kubatko et al.[162] compared these ranges to the mean equatorial bond lengths calculated for a set of pentagonal bipyrimidal uranyl complexes where the equatorially donating species were oxygen donors of any type apart from peroxide. In this set, the mean $U\text{-}O_{eq}$ was calculated to be 2.46 ± 0.11 Å. Kubatko et al. concluded that the shorter mean coordinate bond length suggested that the peroxide anion was able to form stronger interactions with the uranyl ion than is typical of an oxygen donor. This led to the group examining the bond formed between the peroxide anion and the uranyl cation using electronic structure methods in order to elucidate possible reasons for this difference. Using a DFT based energy decomposition analysis the uranyl-peroxide bonds were found to have a small, but significant covalent character being 77 % ionic in nature. It was argued that it

was this covalent component of the bonding, due to a favourable orbital interaction between the metal ion and the peroxide anti-bonding π-MO along with the reduced bite angle of the peroxide anion, that results in peroxide having a smaller steric footprint than most other bidentate ligands thereby favouring the short equatorial contacts.

In addition to the characteristically short equatorial contacts between the uranium atom and the peroxide ligand, Kubatko et al.[162] noted that all of the peroxide bridged species observed were bent about the peroxide axis. i.e. the dihedral angle that ran from the first uranium atom through both of the peroxide oxygen atoms to the second uranium atom was consistently non-linear (see **Table 2**). This prompted the group to undertake a study into the origin of this bend, in particular if it was electronic or steric in nature.

Vlaisavljevich et al.[170] modelled the bisuranyl pentaperoxide anion, $[(UO_2)_2(O_2)_5]^{6-}$ using DFT (PBE) in conjunction with a SC-ECP on the *U* atom to optimise the structures of the complexes in the gas phase and then used these geometries to carry out CASSCF SP calculations followed by a second order perturbative treatment to reclaim a proportion of electron correlation (CASPT2). The active space defined in these models was limited to the bonding and anti-bonding σ_u orbitals of the uranium atoms and the MOs describing the interaction between the uranium atoms and the peroxide ligand, resulting in the active space consisting of eight electrons in eight orbitals. On optimisation of the geometry of the anionic complex $[(UO_2)_2(O_2)_5]^{6-}$ using the XRD structure as an initial guess, Vlaisavljevich et al.[170] found that the peroxide bridge tended towards linearity during the optimisation procedure. This was therefore in contrast to the crystallographic structure that suggested an optimum dihedral angle about the peroxide bridge of 153.1°. On optimisation of the structure of the anion in the presence of the counterions observed crystallographically in the structure $Na_6[(UO_2)_2(O_2)_5]$, Vlaisavljevich et al.[170] found that the optimised structure of the complex was instead bent about the peroxide bridge with a dihedral angle of 144.7°, representative of the experimentally observed angle. The predominant cause for bending of the bisuranyl peroxide bridged complexes was therefore assigned as a templating effect of the cations present in the crystal structure.

In contrast to this work, Miro et al.[171] utilised DFT (BP86) in conjunction with the zeroth order regular approximation (ZORA) to optimise the geometry of a dicationic bisuranyl(VI)-peroxide bridged complex, $[(UO_2)_2(O_2)(H_2O)_4]$, in a continuum solvent model and found that the peroxide bridge in this complex was inherently bent at an angle of 143.9°. In contrast to Vlaisavljevich et al., this led Miro et al. to conclude that the *U-O-O-U* dihedral angle in bisuranyl peroxide complexes was inherently bent. Furthermore, using

geometry constraints, Miro et al. were able to quantify the linear bridged structure as 0.5 kcal mol^{-1} higher in energy than the bent analogue, demonstrating a slight energetic preference for the latter. Studying the electron localisation function (ELF) of the complex, Miro et al. were able to rationalise this energetic preference for a bend as an electronic reorganisation of the peroxide moiety from sp^2 to sp^3 hybridisation, in which the latter favours a slightly more covalent interaction with the uranyl ions thereby resulting in a minor energetic preference.

At first glance, the studies by Vlaisavljevich et al.[170] and Miro et al.[171] appear to be in contradiction, as both were designed to probe the electronic nature of the peroxide bridge and in particular the relative stability of the bent and linear geometries, but the findings of the former suggested that a linear structure was the lowest energy configuration whilst the latter suggested the lowest energy conformation was bent. Despite this, the difference between the findings may be solely due to the fact that both studies employed deceptively different peroxide models; Vlaisavljevich et al.[170] opted to study the hexaanionic $[(UO_2(O_2)_2)_2O_2]^{6-}$ uranyl dimer whereas Miro et al.[171] modelled the dicationic aquated uranyl peroxide species $[(UO_2(H_2O)_2)_2O_2]^{2+}$. As stated in the study by Vlaisavljevich et al., the energetic preference for a linear structure in this model may be down to the excessive anionic charge in this complex and the ability of the peroxide anion to bind the uranyl cation strongly in the equatorial plane. These strong equatorial interactions compete more effectively with the axial O_{yl} ligands to bind to the metal ion then conventional σ-donor water ligands and hence lead to a weakening of the axial uranyl bonds. As found by multiple previous studies of such systems, elongation of the uranyl bonds tends to increase the negative charge localised on the axial oxygen atoms, which in turn leads to a greater mutual electrostatic repulsion between these groups on the adjacent uranyl ions. Hence, it is reasonable to conclude that the model in this study,[170] in which the entire primary coordination sphere of both uranyl ions consisted of peroxide anions, the observed preference for this complex to form of a linear structure is not due to an innate preference for this geometry by the peroxide bridge, but instead is a result of the increased electrostatic interaction between the uranyl oxygen atoms. This repulsion would naturally favour a linear geometry that maximises the separation between these species and thus is likely to be able to overcome the ~0.5 kcal mol^{-1} preference of the bridging peroxide unit to adopt a bent sp^3 hybridised configuration, as defined by Miro et al.[171]

This rationalisation may also be applied to the strong alkali metal templating effect discussed by Vlaisavljevich et al.[170] as the electrostatic interaction between the interstitial cation and

the O_{yl} atoms will be maximised in complexes where the equatorial ligand field binds the uranium atom most strongly. Hence it would be expected that the trisperoxide bound uranyl(VI) structures studied by Vlaisavljevich et al.[170] will interact more strongly with axially located alkali metal cations than the corresponding aquated monoperoxide uranyl(VI) structure studied by Miro et al.[171]

Considering the relative ease with which quantum chemical models suggest the torsional angle about the peroxide bridge may be tuned by secondary interactions between the bisuranyl-peroxide complex and other species in the solid state, it may be considered surprising that more variation in the peroxide torsional angle is not observed experimentally. Specifically, why have no linear peroxide bridges been identified by crystallographic means? The next chapter seeks to address this question firmly dispelling the myth continually proffered by authors in the mainstream literature that the *U-O-O-U* dihedral angle is <u>*always*</u> bent[163,171,172] by conducting a brief meta-analysis of the data published in the CSD.

4.1.5.3 A Meta-Analysis of Secondary and Tertiary Structural Features that may Direct the Bending or Linearity of the Bisuranyl Peroxide Bridged Systems in the Solid State

At the time of writing, performing a search in the CSD for a *U-O-O-U* moiety provides 34 hits. Combining these results with similar structures presented elsewhere provides a sample size of 39. Of these, 11 studies describe structures with a linear *U-O-O-U* dihedral angle, whilst the remaining 28 describe bent peroxide bridged complexes. As it is preferable to remove as many complicating factors as possible when studying systems with such intricate structural chemistry, if the sample of structures is limited to those that only contain a single bisuranyl-peroxide bridged dimer (thereby discarding any extended uranyl peroxide POMs that may be forced to bend by steric means) then the number of bent *U-O-O-U* structures drops to 14. Hence, far from the bent geometry being the only geometry observed for the peroxide bridge, there is a readily characterised relative wealth of linear structures already published in the literature. A table describing selected structural parameters and appropriate references for the 25 dimer structures discussed is presented in **Table 3**.

As identified on comparison of the structures identified by the group of Burns at the University of Notre Dame, there is relatively little variance in the mean peroxide bond length and the separation between the peroxide oxygen atoms and the uranium atom in any of these structures, bent or linear. These values range from 1.43 Å to 1.51 Å and 2.28 Å to 2.37 Å, respectively. Note that in calculating these differences the bond length of the complex AQACIZ has been excluded, this is because there is considerable disorder in this structure,

as will be discussed in Chapter 4.1.5.3.3 (note that it appears in both bent and linear lists) and hence this system represents a somewhat non-typical case. **Table 3** therefore clearly demonstrates that the torsional angle across the peroxide bridge in bisuranyl complexes are definitively not *always* bent and furthermore that on considering only dimeric structures 44 % of the known structures are in fact linear in geometry! The fact that such an oversight has pervaded the authors and editors of even recent reviews[172] on this subject suggests that a basic structural study as to the type of inter- and intra-molecular interactions that promote the bending of the peroxide bridging unit away from or towards linearity is clearly warranted.

4.1.5.3.1 Types of Intra- and Inter-molecular Interactions that Direct Bent or Linear U-O-O-U Torsions

Studying the structures of the peroxide bridged dimers deposited in the CSD on an individual basis, it becomes apparent that the observed preference for a *U-O-O-U* dihedral angle to take on a linear or bent geometry is likely to be due to a complex interplay of different intermolecular interactions and not to a single driving force alone. This possible pliability of the torsional angle across the peroxide bridge is corroborated by the small energetic penalty of 0.5 kcal mol^{-1} calculated by Miro et al.[171] when distorting the aquated bisuranyl-peroxide complex to linearity.

4.1.5.3.2 Interactions that Favour a Bent Torsional Angle

The first driving force of note is that proposed by Vlaisavljevich and Burns et al. in their QM study; that a favourable electrostatic interaction between the O_{yl} atoms on adjacent uranyl ions and a suitably placed cation is able to reduce the repulsion between the δ- O_{yl} groups and promote a degree of bending across the peroxide unit. As stated in their paper, such an electrostatic interaction is also likely to weaken the axial uranyl bond and thus make the central uranium atom more available for interactions with the equatorial ligand field, thereby promoting the uranium-peroxo interaction. An example of such an interaction is depicted in **Figure 30**. A bounding figure for the strength of this interaction was gauged by Vlaisavljevich et al. in their computational study as the energetic penalty required to bend the torsional angle of the $[(UO_2)_2(O_2)_5]^{6-}$ complex. In this model, the linear geometry was found to lie 2 kcal mol^{-1} lower in energy than a structure in which the dihedral angle across the peroxide bridge was 160° and 6 kcal mol^{-1} lower in energy than the structure in which the dihedral angle was 140°. Therefore, as concluded by Vlaisavljevich et al., the stabilisation afforded by an appropriately located alkali metal cation is a significant driving force behind the bending of certain bisuranyl-peroxide complexes, specifically those that

have an excess of anionic charge and multiple strong equatorial donors binding the uranyl(VI) ions.

Table 3: Table of selected structural parameters describing bisuranyl(VI)-peroxide complexes grouped into structures in which the dihedral angle across the peroxide bridge is linear and those in which this dihedral is non-linear. The unique identifier presented for each structure is that designated by the CCDC and the appropriate publication reference for each structure is also provided. Where a particular structure has not been committed to the CSD, it has been assigned the name given to the structure in the appropriate reference.

Structure	Mean Peroxide *O-O* Bond length /Å	Ave $U\text{-}O_{eq}$ Bond Length /Å	*U-O-O-U* dihedral angle / °
Linear U-O-O-U Torsions			
AQUCAR[173]	1.51	2.33	180.0
AQUCIZ[173]	1.75	2.33	180.0
AZEDEO[174]	1.48	2.31	180.0
BZAPXU10[175]	1.49	2.29	180.0
CIFYUN[176]	1.48	2.30	180.0
IVAKIZ[177]	1.49	2.32	180.0
MUWXEH[178]	1.47	2.32	180.0
NUNYUR[179]	1.49	2.32	180.0
OFAZIG[180]	1.48	2.33	180.0
OKOCEW[181]	1.43	2.28	180.0
YEMFAX[152]	1.46	2.32	180.0
Bent U-O-O-U Torsions			
AQUCIZ[173]	1.49	2.32	151.1
CUJDER[163]	1.47	2.35	153.0
DEDCEU [182]	1.48	2.34	144.5
GOPVUC[183]	1.48	2.32	140.9
NAKNOD[184]	1.46	2.30	135.8
NERWIS[151]	1.43	2.36	125.3
TEGSIJ[185]	1.48	2.31	148.0
WESPAL[153]	1.47	2.33	138.4
YEGQOS[155]	1.48	2.34	147.8
YEMFEB[152]	1.47	2.36	141.0
NaRbUT[162]	1.51	2.37	153.1
Studtite[158]	1.46	2.36	140.2
$[UO_2(py)_2(NO_3)]_2O_2.py$[157]	1.46	2.32	139.1
$[UO_2(py)_2(OAc)]_2O_2.py$[157]	1.48	2.32	138.29

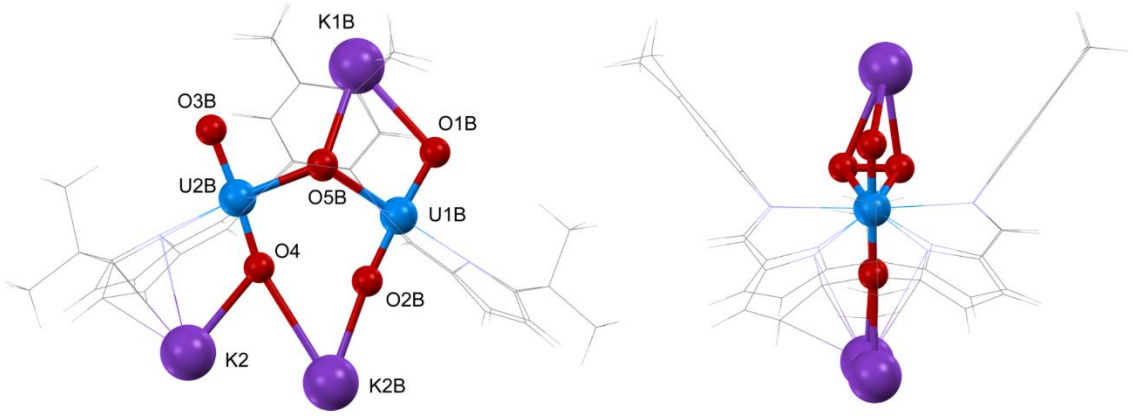

Figure 30: Geometry of the bisuranyl(VI)-peroxide complex characterised by Arnold et al.[151] as designated in the CSD as 'NERWIS'. This structure is an example of electrostatic stabilisation of the δ- charge on the O_{yl} atoms and on the bridging peroxide by coordination of appropriately placed alkali metal cations. Both images were generated using the CIF deposited in the CSD by Arnold et al.[151] using the CCDC Mercury visualisation package.[165–168]

In **Figure 30** it is clear that there is a strong interaction between the uranyl oxygen atoms and the potassium cations located below the uranyl ions in the image. In this structure the potassium atom K2B lies 2.64 Å from O2B, whilst K2 lies 2.72 Å from O4. It also displays relatively short contacts between K1B and O1B which are separated by 2.88 Å as well as K1B and the bridging peroxide group (O5B), to which the shortest contact is 2.78 Å. This short contact hints at a second secondary structural trait that may act to direct the bending of the peroxide bridges in these bisuranyl complexes, namely a disproportionate stabilisation of the sp^3 hybridised electronic structure of the peroxide bridge over the sp^2 hybridised analogue.

On comparison of the small dataset of structures available, it is apparent that the complexes that display the most acutely bent torsional angles have a metal cation or a hydrogen bond donating species located directly above the peroxide bridge. There are only two examples of this secondary interaction that may be firmly assigned in the dataset at present, however these two species, NERWIS and NAKNOD, are the two most bent structures identified. As can be seen in **Figure 30** above, NERWIS, the most bent structure with a *U-O-O-U* dihedral of 125.3 °, benefits from both a short contact between the peroxide bridge and a potassium ion as well as short contacts between the uranyl O_{yl} atoms and two potassium cations. This is in contrast to the less acutely bent structure of NAKNOD (*U-O-O-U* = 135.8 °), which only displays the former interaction, **Figure 31**, below. Nevertheless, NAKNOD arguably better serves as an example of the interaction between the sp^3 hybridised peroxide bridge and a Lewis acid owing to the innate directionality of the hydrogen bonding interaction observed in this structure that clearly demonstrates the trigonal nature of the donor lone pairs on the bridging peroxide in these complexes. This observation thereby provides some

experimental verification of sp^3 hybridisation in the peroxide bridge as predicted by the ELF study conducted by Miro et al.[171]

In the NAKNOD structure characterised by Masci et al.,[184] the shortest distance between the peroxide bridge (O16) and the nitrogen atom of the triethylamine hydrogen bond donor (N4) is 2.73 Å. This is therefore a relatively well formed hydrogen bonding interaction.

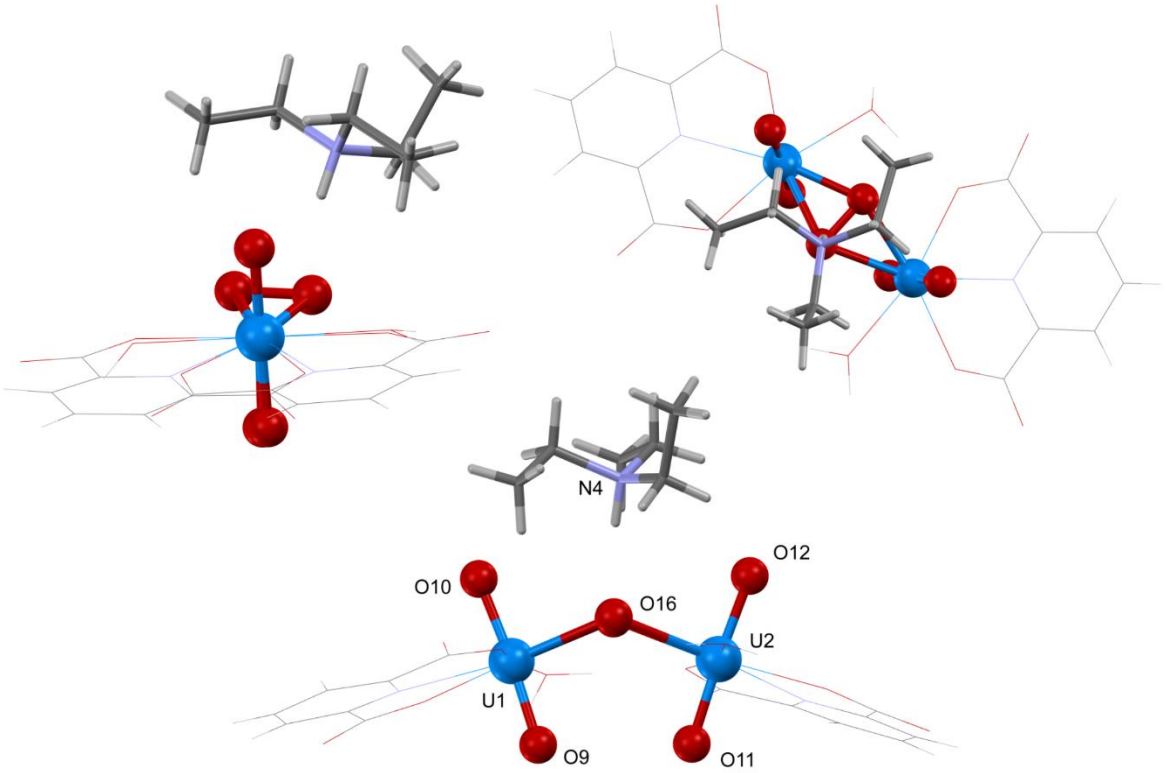

Figure 31: Three orthogonal views of the bisuranyl(VI)-peroxide bridged complex characterised by Masci et al.[184] as designated in the CSD as NAKNOD. This structure is an example of the stabilisation of the *δ*- charge on the bridging peroxide anion through the formation of a hydrogen bond with an appropriately located protonated triethylamine molecule. All images were generated using the CIF deposited in the CSD by Masci et al.[184] using the CCDC Mercury visualisation package.[165–168]

Thus, from the limited data available, it is possible to state that bent *U-O-O-U* angles are favoured in the solid state not only due to electrostatic interactions between the uranyl oxygen atoms and metal cations, as proposed by Vlaisavljevich et al.,[170] but also due to direct interaction of cationic and hydrogen bond donor species with the peroxide bridge. In addition, both effects act in the same direction, resulting in the most acutely bent *U-O-O-U* bridge observed exhibiting both interactions.

4.1.5.3.3 Interactions that Favour a Linear Torsional Angle

On conduction of the contrasting search for similarities between models that exhibit a linear peroxide bridge, it is notable that such complexes tend to be structurally strained or sterically crowded. One reoccurring feature that conveys this strain is exhibited by complexes in which a second coordinated ligand is able to bridge the two uranyl centres, in addition to the

peroxide anion. Thus, the *U-O-O-U* angle in these complexes is subject not only to the electronic will of the peroxide bridge, but also to that of the secondary bridging system that, owing to its own internal strain, may have a vested interest in maintaining the linearity of the torsion about the peroxide bridge in order to maximise its own interaction with both uranyl centres. An example of such a complex is provided in **Figure 32**, which displays the structure, characterised by Aladzheva et al.,[173] of a bisuranyl(VI)-peroxide bridged complex in which the uranyl ions are also bridged by a bidentate *O-P-N-P-O* type ligand.

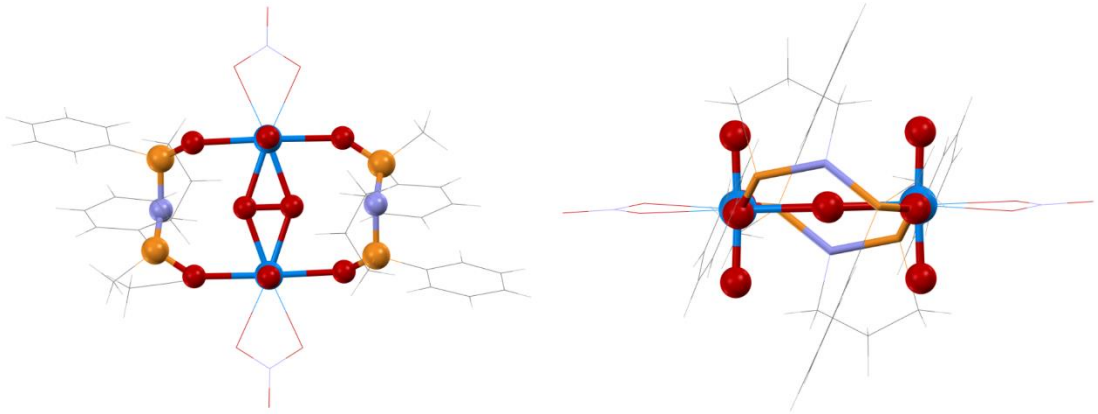

Figure 32: Two orthogonal views of the linear bisuranyl(VI)-peroxide bridged complex characterised by Aladzheva et al.[173] as designated in the CSD as AQUCAR. Both images were generated using the CIF deposited in the CSD by Aladzheva et al.[173] using the CCDC Mercury visualisation package.[165–168] Uranium atoms are turquoise; Oxygen atoms are red; Nitrogen atoms are blue and Phosphorus atoms are orange.

This particular imidophosphorus derived ligand, displaying the popular *(X)P-N-P(Y)* backbone, was designed specifically by Aladzheva et al.[173] as rigid alternative to its traditionally flexible *P-N-P* relatives. This rigidity was achieved by cyclising the ligand, thereby providing an internal penalty to rotation about the cyclised *N-P* bond. This barrier is reflected in the observation that the angle across the *P-N-P* backbone in the free ligand crystal structure and that of its uranium complex are exactly the same, 130.3°.[173] This ligand is able to bind two separate uranyl ions, thus providing a strained secondary bridge in in this structure that promotes the *U-O-O-U* angle to become planar.

By way of contrast, on substituting the phenyl substituents in this ligand for ethoxide groups, a new ligand was characterised by Aladzheva et al.[173] which displayed a *P-N-P* angle of 127.5° in the uranyl complex, AQUCIZ. Despite this complex having the same broad structural features as its phenyl-substituted analogue, it exhibited a large degree of disorder about one of the atoms in the central peroxide bridge and on both of the oxygen atoms of one of the uranyl units. The major constituent of this disorder was refined as a bisuranyl complex with a linear *U-O-O-U* bridge analogous in structure to that of the phenyl-substituted complex. However, the minor component of the disorder hinted at the

presence of a species with a bent *U-O-O-U* bridge, **Figure 33**. This suggests that on relaxing the *P-N-P* angle slightly, the energetic driving force provided by the *P-N-P* ligand to direct the planarity of the *U-O-O-U* bridge is reduced to the point that the formation of the bent peroxide bridged geometry is favourable once again. Thus allowing the bent product to be observed as a minority component of the crystal structure. The coexistence of both the bent and the linear *U-O-O-U* torsion angle geometries in a single crystal provides *de facto* experimental evidence of the small energetic difference between these two structures, in line with the small 0.5 kcal mol^{-1} energy difference predicted by Miro et al.[171]

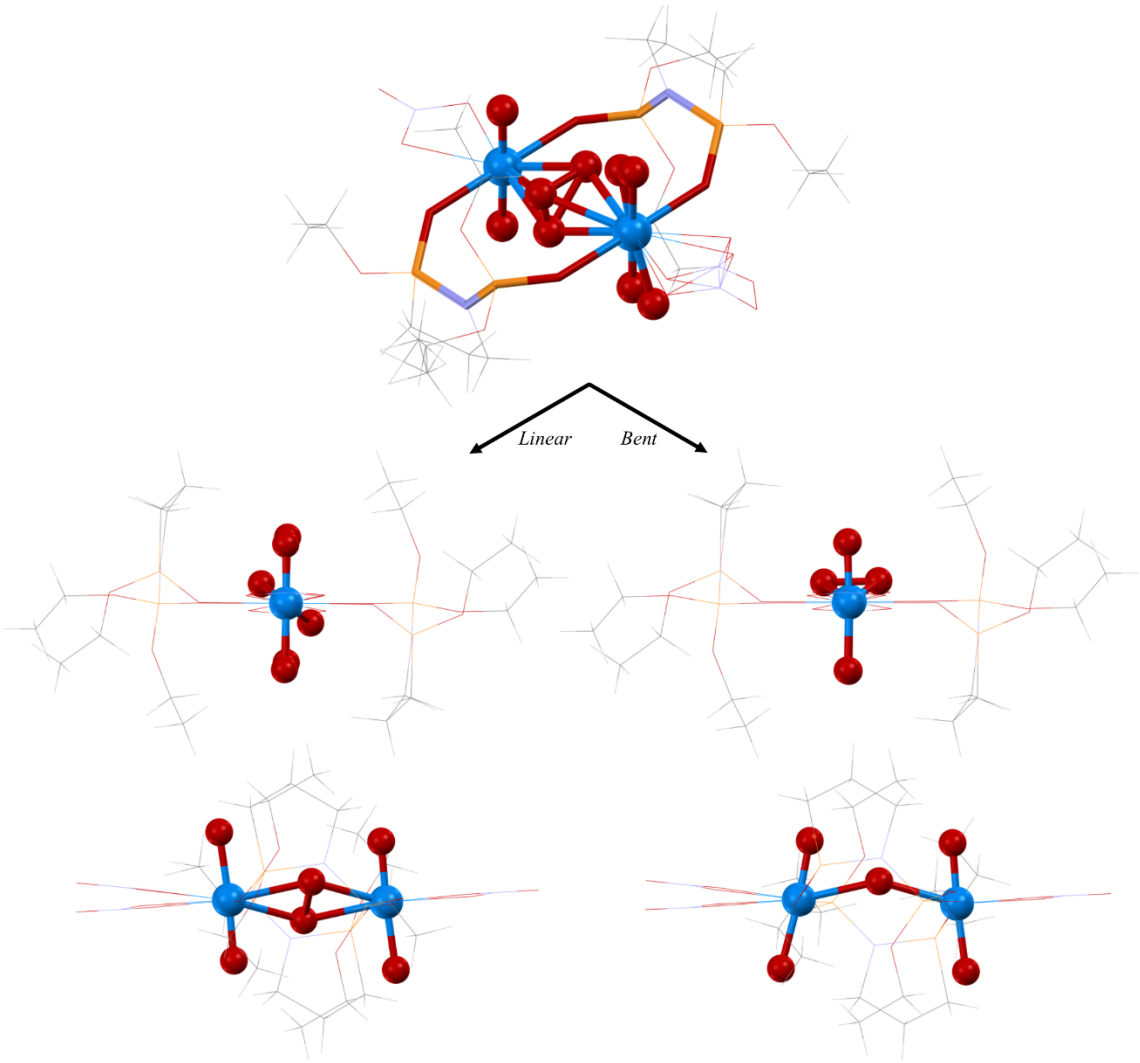

Figure 33: Top: Disordered structure of the bisuranyl(VI)-peroxide and *P-N-P* ligand bridged complex characterised by Aladzheva et al.[173] as designated in the CSD as AQUCIZ. Aladzheva et al.[173] solved this structure in a manner that identified the two disordered components. The majority component is described by the two orthogonal views of the linear complexes on the left, whilst the minority component is described by the two views of the bent structure on the right. All images were generated using the CIFs deposited in the CSD by Aladzheva et al.[173] using the CCDC Mercury visualisation package.[165–168] Uranium atoms are turquoise; Oxygen atoms are red; Nitrogen atoms are blue and Phosphorus atoms are orange.

Taking this study of *P-N-P* bridged uranyl-peroxide-uranyl complexes to its logical conclusion, on comparing the structure of the rigid cyclic *P-N-P* ligands with the more

flexible N,N'-Ethylenebis(2-pyrrolidone) bridged complex characterised by Doyle et al.[153] (WESPAL), **Figure 34**, it is clear that the uranium complex formed once again displays a bent *U-O-O-U* dihedral angle across the peroxide bridge with a value of 138.4°.

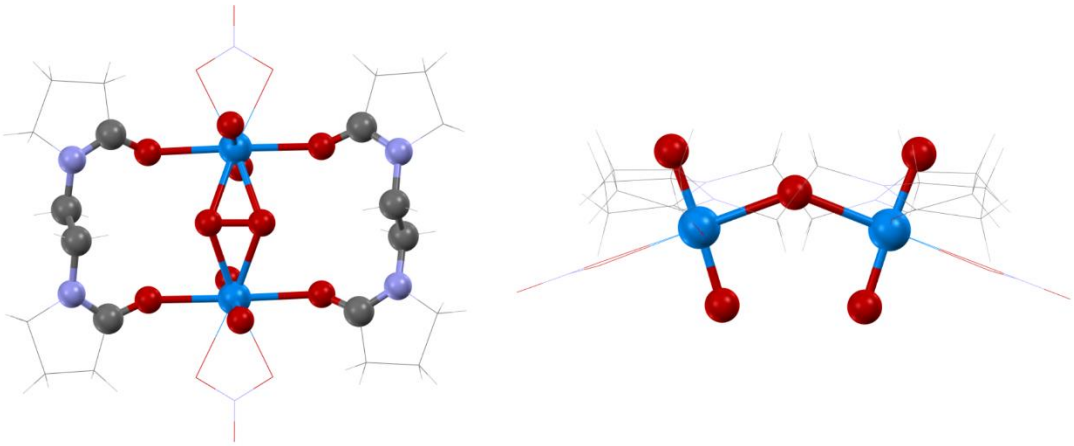

Figure 34: Two orthogonal views of the bent bisuranyl(VI)-peroxide bridged complex characterised by Doyle et al.[153] as designated in the CSD as WESPAL. Both images were generated using the CIF deposited in the CSD by Doyle et al.[153] using the CCDC Mercury visualisation package.[165–168] Uranium atoms are turquoise; Oxygen atoms are red; Nitrogen atoms are blue and Carbon atoms are grey.

From this point onwards, it becomes more complicated to identify firm trends from the structural data available owing to the limited size of the data set. Despite this, it is possible to hypothesise about some further generalities based on the structures available. For example, it is reasonable to assume that heavily sterically crowded bisuranyl peroxide bridged complexes are planar since planarity about the peroxide bridge will most effectively minimise the steric repulsion between the bulky groups of the ligand system. An example of such a complex is the substituted triphenylphosphine oxide complexes of the bisuranyl(VI)-peroxide moiety characterised independently by John et al.[154] (IVAKIZ) and Charushnikova et al.[181] (OKOCEW), **Figure 35**.

Finally, across some series of complexes it is possible to observe the influence of crystal packing effects on the torsion angle of the *U-O-O-U* group, *cf* the collection of bipyridine uranyl peroxide structures presented in **Figure 36**, below. When the secondary ligand in these complexes is the simple nitrate anion, the bisuranyl(VI)-peroxide complexes remain discrete species in the crystal structure, which seemingly promotes a parallel packing motif that favours planar *U-O-O-U* angles, as inferred from the bipyridine and methylbipyridine complexes characterised with simple ligands by Sokolova et al.[180] and Akbarzadeh et al.,[176] respectively. Conversely, substitution of the nitrate anion in the bipyridine structure for a succinate anion, which is able to bridge between two discrete bisuranyl-peroxide complexes in order to form a 1D chain, acts to break the regularity imposed by the near parallel secondary packing motif and permits the peroxide bridge to bend. The fact the equatorial

coordination environment of the uranyl ions in each of these structures in terms of the immediate donor atoms is conserved, but that there is still a change in the preference for a bent *U-O-O-U* dihedral in one complex as opposed to a planar structure in the others, suggests that more subtle forces are directing this trend than direct electronic interactions. Such a difference is echoed by other structures in the set, for example the bent and linear thiolatomethylpyrimadine complexes characterised by Rose et al.[152]

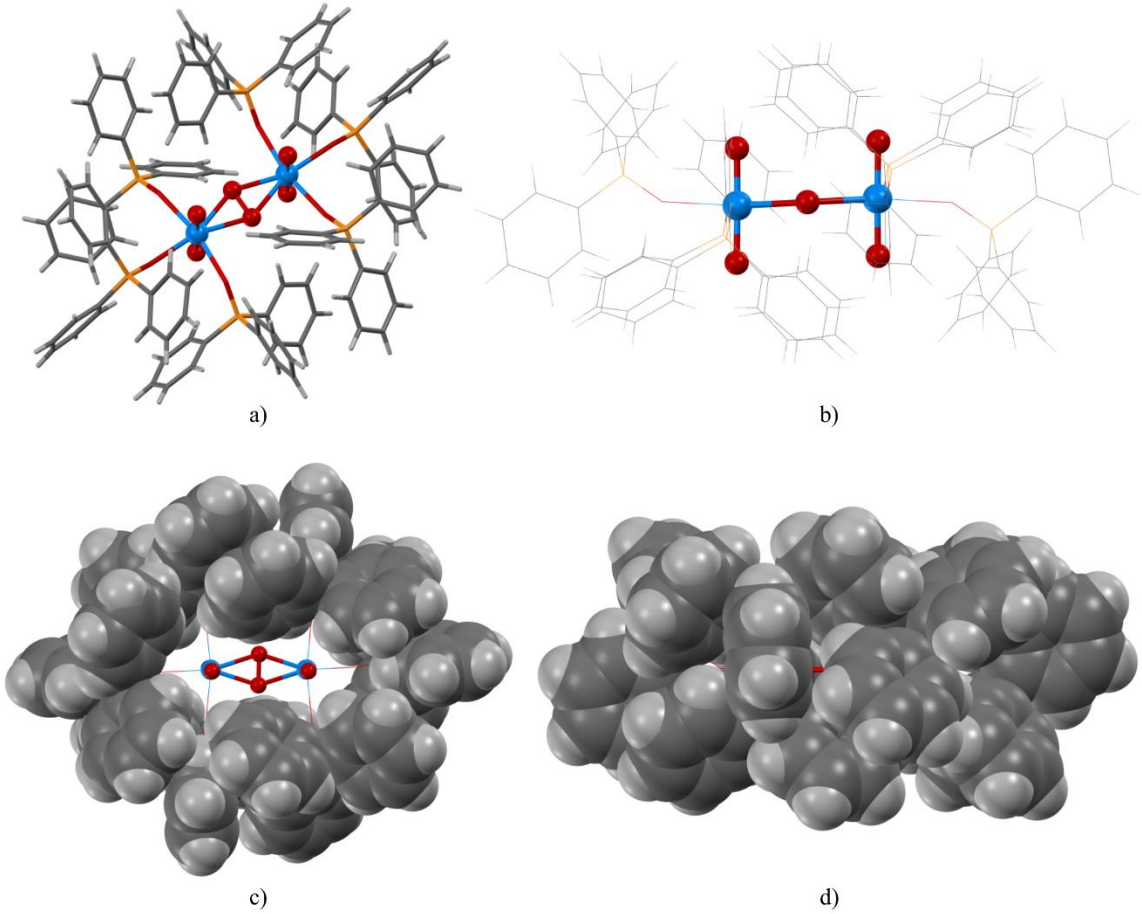

Figure 35: Multiple representations of the planar bisuranyl(VI)-peroxide bridged TPPO complex characterised by John et al.[154] as designated in the CSD as IVAKIZ. a) an image of the structure using a capped stick representation, b) a side-on view of the structure clearly showing the linear nature of the peroxide bridge, c) a plan view of the complex using a space-filling representation for the peripheral phenyl groups in order to visualise the steric crowding around the bisuranyl-peroxide moiety, d) a side on view of the space-filling representation of the complex. All images were generated using the CIF deposited in the CSD by John et al.[154] using the CCDC Mercury visualisation package.[165–168] Uranium atoms are turquoise; Oxygen atoms are red; Nitrogen atoms are blue; Phosphorus atoms are orange; Carbon atoms are grey and Hydrogen atoms are pale grey.

Conclusions

Following a review of the available literature, it has been demonstrated that the dihedral angle across the bridging peroxide anion in bisuranyl(VI)-peroxide complexes is by no means limited to a solely bent geometry as discussed in a recent review of the chemistry in this field.[172] Instead it is likely that multiple secondary and tertiary structural interactions subtly affect the geometry of this bridge in the solid state leading to the diverse range of

angles observed. This diversity is well reflected by the QM calculations of Vlaisavljevich et al.[170] and Miro et al.[171] who suggest that the peroxide bond is ultimately pliable and only requires a minor energetic input to be disfigured.

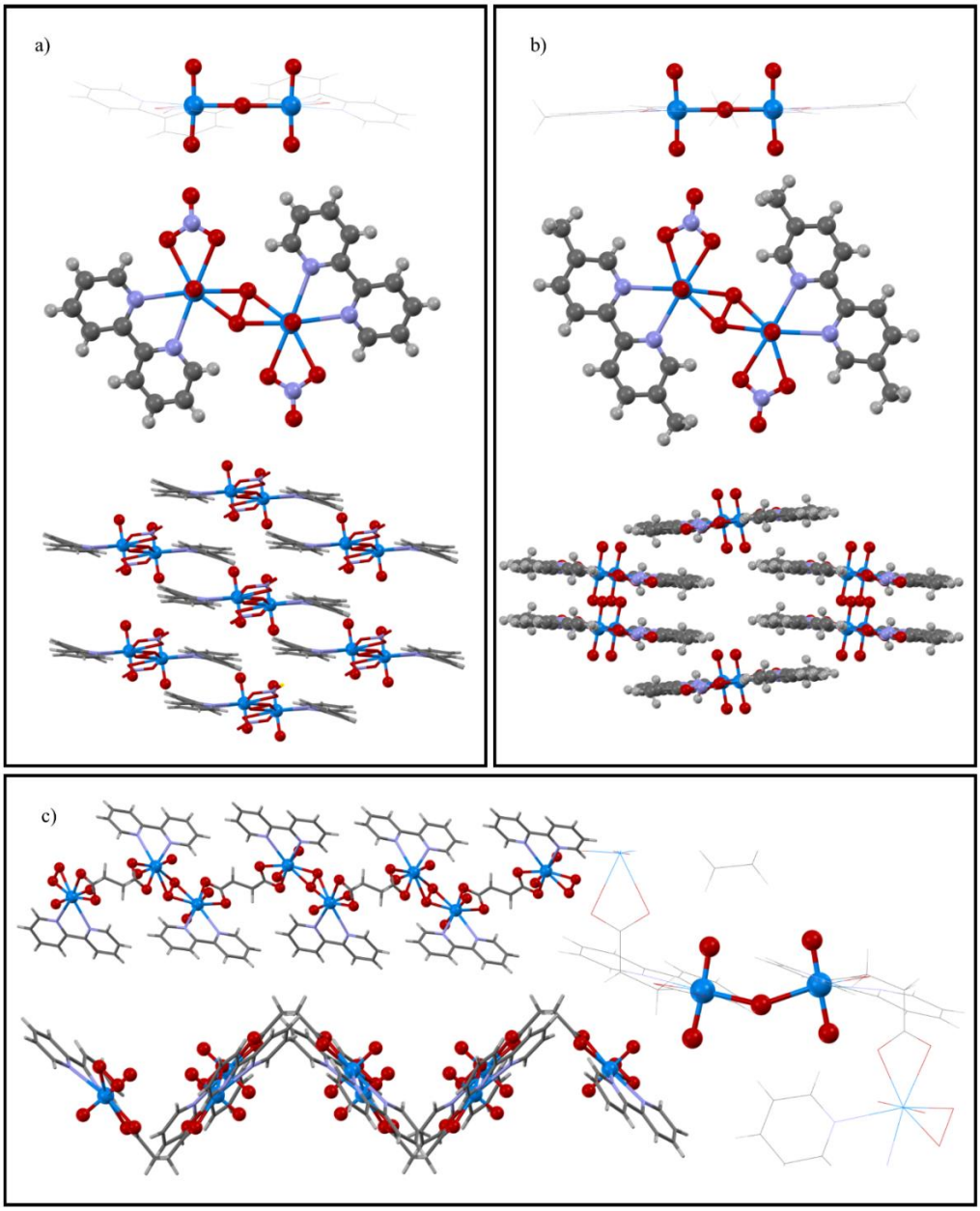

Figure 36: a) Representation of the linearity of the peroxide bridge in the bisuranyl(VI)-peroxide bridged bisbipyridine nitrate complex characterised by Sokolova et al.[180] (OFAZIG) and a plan view of the primary structure of the complex as a whole (middle). (bottom) A representation of the crystal packing in this structure displaying the isolated and near planar nature of the secondary structure in this crystal. b) Representation of the linearity of the peroxide bridge in the bisuranyl(VI)-peroxide bridged bismethylbipyridine nitrate complex characterised by Akbarzadeh-T et al.[176] (CIFYUN) and a plan view of the primary structure of the complex as a whole (middle). (bottom) A representation of the crystal packing in this structure displaying the isolated and near planar nature of the secondary structure in this crystal. c) (right) Representation of the bent torsional angle about the peroxide bridge in the bisuranyl(VI)-peroxide bridged bisbipyridine succinate complex characterised by Wang et al.[155] (YEGQOS) and a plan view of the primary structure of the complex as a whole and the 1D polymer form of the complex (top). (bottom) A view along the b axis of the unit cell that demonstrates the zig-zag pattern that the 1D polymer takes due to the flexibility of the succinate ligand that bridges the bisuranyl complexes. All images were generated using the CIF deposited in the CSD by Sokolova et al.,[180] Akbarzadeh-T et al.[176] and Wang et al.[155] using the CCDC Mercury visualisation package.[165–168] Uranium atoms are turquoise; Oxygen atoms are red; Nitrogen atoms are blue and Carbon atoms are grey.

4.2 Structural Determination of the Bisuranyl(VI)-Peroxide Complex of *CyMe$_4$*-BTPhen by D.M. Whittaker[3]

4.2.1 Some Background about *CyMe$_4$*-BTPhen

CyMe$_4$-BTPhen is a quadridentate nitrogen donor ligand that has been designed for use in advanced nuclear fuel separation technologies that seek to separate trivalent actinide cations from trivalent lanthanide ions. One proposed use of this ligand would be as part of a GANEX process which would aim to separate all of the actinides from the FPs and remaining activation products present in dissolved spent nuclear fuel using a one pot process. When used in this way, the BTPhen ligand will come into contact with uranic and early transuranic elements in relatively large quantities, specifically uranium, neptunium and plutonium, hence it is important to understand how the ligand binds to these species in order to infer if such a process would be feasible using this ligand system. To this end, in 2011 D.M.Whittaker (DMW) a fellow Ph.D. student at the University of Manchester was studying the speciation of uranyl(VI) complexes formed with the BTPhen ligand.[3]

4.2.2 The NMR Complexation Experiment

In early 2011, DMW[3] was carrying out solution phase proton NMR studies of the complexes formed on dissolution of BTPhen and uranyl(VI) nitrate in aqueous methanol. The study sought to identify the stoichiometry of the complex formed. To this end, DMW titrated a methanolic solution of uranyl(VI) nitrate into a methanolic solution of the BTPhen ligand in order to increment the relative concentrations of the species present and determine the proportions of the BTPhen ligand that were complexed and unbound at different concentrations by integrating the proton resonances in the spectrum recorded. In this manner, DMW was able to identify that the maximum stoichiometry of the species formed in solution under these conditions was a 1:1 UO_2^{2+}:BTPhen complex. At the end of the experiment, DMW took the NMR tube containing the experimental solution and placed it in his fume cupboard in the hope that the slow evaporation of the solvent would generate crystals of the 1:1 complex suitable for XRD structural determination. After two days the NMR solution did indeed yield crystalline material and DMW presently determined the structure of the material present. However, as immortalised by Burns "*the best laid schemes o' mice an' men, gang aft agley"*[186] and to his astonishment the complex formed was a bisuranyl(VI)-complex of BTPhen. The crystal structure characterised is depicted in **Figure 37** in which the ORTEP representation of the crystal structure identified by DMW[3] is presented (image replicated directly with DMW's[3] permission).

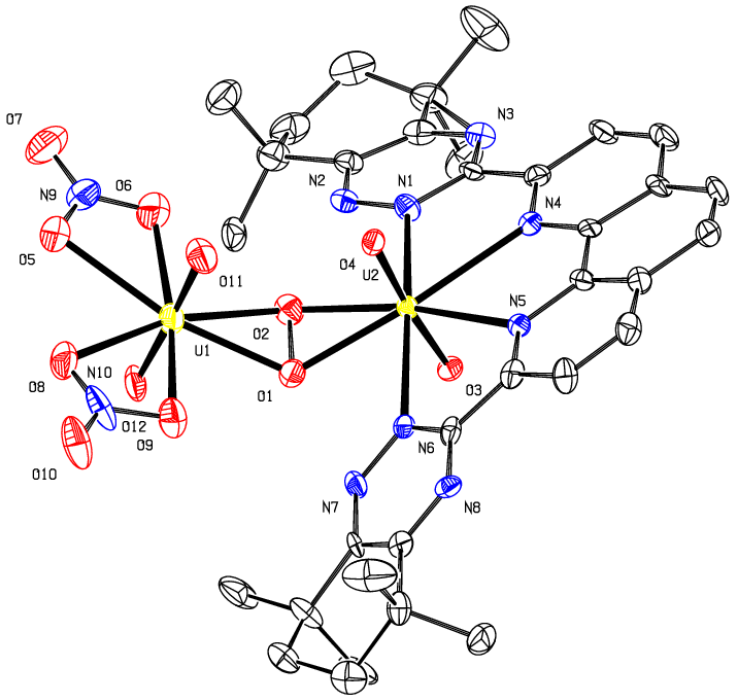

Figure 37: ORTEP representation (50 % probability ellipsoids displayed) of *[UO_2(CyMe$_4$-BTPhen)(O_2)(UO_2)(NO_3)$_2$]*. Yellow = uranium; blue = nitrogen; red = oxygen; black = carbon. CyMe$_4$ disorder and hydrogen atoms have been removed for clarity. Image and figure reference used with permission from the thesis of DMW.[3]

The structure identified by DMW depicts two uranyl ions each with a different set of equatorial ligands, in which the first is bound by the BTPhen ligand and two oxygen donor atoms and the second is bound by two nitrate anions and two oxygen donor atoms. The two oxygen atoms thereby bridge between the two uranyl cations permitting the 2:1 UO_2^{2+}:BTPhen complex stoichiometry. When it was first isolated, it was assumed that the chemical identity of the bisoxygen bridge was two adjacent bridging hydroxide anions owing to the relative prevalence of hydroxide bridged structures in the literature and the fact two hydroxide anions were appropriate on charge balancing grounds. However, on examination of the proximity of these two oxygen species (*O(1)-O(2)* = 1.455(1) Å) it was likely that they were bonded and this led to the suggestion that the bridging species could be a peroxide dianion.

4.2.3 Employing DFT to Identify the Nature of the Bridging Species

Electronic structure methods are well suited to determine the root of such geometric problems and hence it was decided to use the computational chemist's toolkit to analyse the bonding in this system. Two models of the system were constructed, one in which the bridging unit described a peroxide anion,*[UO_2(BTPhen)(O_2)(UO_2)(NO_3)$_2$]*, and one in which the bridging unit described two hydroxide anions, *[UO_2(BTPhen)(OH)$_2$(UO_2)(NO_3)$_2$]*.

Computational Details

All models were optimised in the gas phase using a range of DFT functionals including B3LYP, MO6 and M06L. These functionals employ differing amounts of HF exchange; from their formalism it would be expected that B3LYP and M06 perform similarly as they both represent hybrid functionals that incorporate on the order of 25 % HF exchange. Conversely, M06L is a pure GGA functional in that it does not incorporate any HF exchange directly and is therefore provided in order to act as a control to allow comparison between the structures generated by a pure GGA approach and a hybrid approach. The basis set employed to describe the electronic structure of the ligand was varied between calculations in order to assess the dependence of the structure on the basis set. As described in **Table 4**, the basis set used to describe the *C, H, O* and *N* atoms in the system was varied between Pople's double-zeta 6-31G(s,p) basis and the much more flexible triple-zeta def2-TZVP basis set. The electronic structure of the uranium atom was described using the Stuttgart-Dresden SC-ECP for uranium along with the recommended basis set, including *g*-functions. The description of the uranium atom was not varied between calculations. Following optimisation, the converged structures were confirmed to lie at potential minima by the absence of negative modes in the second derivative spectrum of the energy with respect to the nuclear coordinates. SP calculations were subsequently carried out at these gas phase optimised structures using the larger def2-TZVP basis set in order to generate absolute energies of the species, population analyses and MO diagrams.

Results and Discussion

Figure 38 presents the gas phase optimised geometry of the peroxide bridged complex, *[UO_2(BTPhen)(O_2)(UO_2)(NO_3)$_2$]*, and its bishydroxide bridged analogue *[UO_2($CyMe_4$-BTPhen)(OH)$_2$(UO_2)(NO_3)$_2$]* as determined using the uM06/B1 functional-basis set combination (as defined in Chapter 2).

On comparison of these structures it is apparent that the separation of the oxygen atoms in the bishydroxide bridge (2.57 Å) is much larger than the separation in the peroxide bridged analogue (1.43 Å). These compare to a separation of 1.46 Å as identified crystallographically and hence immediately it is clear that the bridging species is likely a peroxide anion. There are further differences between the models that also suggest that the bridge is a peroxide moiety and not two adjacent hydroxide anions. The first of which is that there is a great degree of strain in the hydroxide bridged complex, as demonstrated by the fact that the torsional angle between the phenanthroline backbone of the ligand and one of the triazinayl groups (i.e. the torsional angle between *N5* and *N6* in **Figure 37**, above) is distorted 23.7°

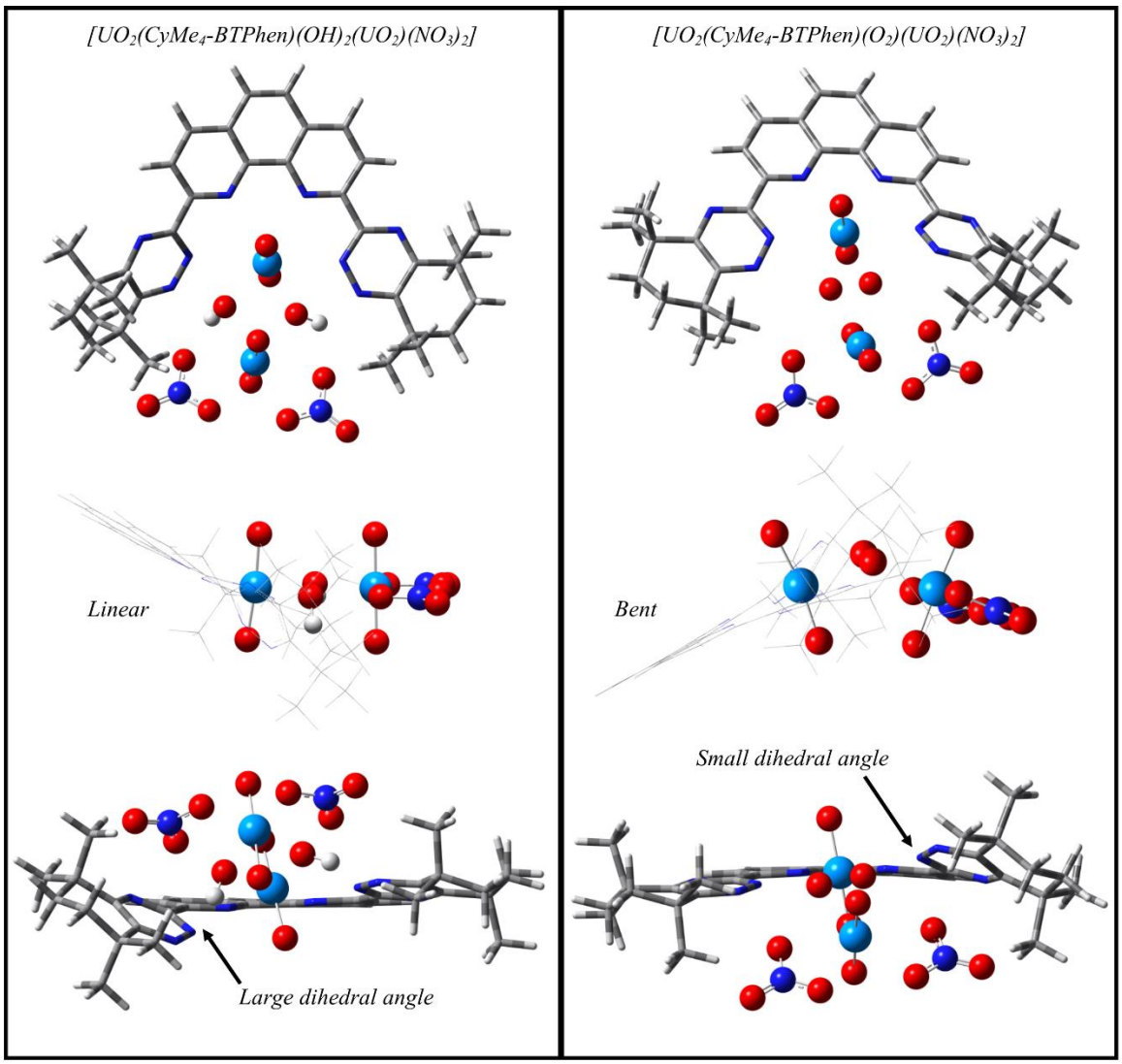

Figure 38: Three orthogonal views of the gas phase optimised structures of the bishydroxide bridged and peroxide bridged bisuranyl-BTPhen complexes as determined using uM06/6-31G(d,p).

out of plane, hence concomitantly decreasing the strength of the interaction between this triazinyl group and the uranyl(VI) ion in the ligand cavity. This torsion corresponds to an angle of 11.7° in the gas phase optimised peroxide bridged complex and a torsion of 8.4° in the XRD structure. A further major difference between the bishydroxide bridged model and the peroxide bridged analogue is that in the former, the dihedral angle across the bishydroxide bridge (*U1-O1-O2-U2* in **Figure 37**, above) is 175.2° as opposed to 133.2° in the latter. The 133.2° bend across the peroxide unit is in line with the bend observed in the structure derived by XRD which was found to be 137.7°. Comparison of these structural parameters in conjunction with the structural characteristics described for peroxide complexes described in Chapter 4.1.5.3 thereby allows firm assignment of the complex characterised by DMW[3] as a bisuranyl(VI)-peroxide bridged complex of the formula *[UO_2(BTPhen)(O_2)(UO_2)(NO_3)$_2$]*.

Following on from this preliminary structural study it was prudent to characterise the dependence of the structure identified on the DFT functional used and the basis set employed to describe the electronic structure of the BTPhen ligand. **Table 4** presents the structural parameters determined by gas phase optimisation of the *[UO_2(BTPhen)(O_2)(UO_2)(NO_3)$_2$]* complex using a range of functionals (two hybrid functionals – M06 and B3LYP, and a meta-GGA functional, M06L) when employing two differently sized basis sets to represent the *C, H, O* and *N* atoms in the system; a double-ζ Pople type basis set, 6-31G(d,p) and a more flexible triple-ζ def2-TZVP basis set.

From this set of data it is clear that the B3LYP/6-31G(d,p) gas phase optimised model most closely resembled the crystallographically determined structure. **Table 4** presents the differences between the significant structural parameters in the bisuranyl-peroxide bridged complex in order to highlight the excellent agreement between the B3LYP/6-31G(d,p) optimised structure and the empirical data.

Despite the structure optimised using B3LYP/6-31G(d,p) providing the closest agreement with the empirical data, the structures identified by the M06 family of functionals are by no means poor. Indeed all of the functional-basis set combinations tested generated structural parameters that typically corresponded to within ~0.05 Å of the crystallographically derived structure. However, as a general trend the M06 family of functionals tended to provide shorter interatomic distances than the corresponding B3LYP or XRD derived structures indicating a possible tendency for this family of functionals to over-bind. The effect of increasing the size of the basis set was observed to lead to a greater degree of over-binding in the system, although the effect of changing the basis set on the structure identified was not as great as changing the functional employed.

Empirical Structural Analysis of the Peroxide Bridged Complex Identified by DMW[3]

As shown in **Table 6**, the structural parameters of the peroxide bridged complex as identified by DMW[3] are all within the range of parameters identified during the literature survey of known bisuranyl-peroxide bridged species that are bent about the peroxide axis.

Furthermore, analysis of the secondary structure of the *[UO_2(BTPhen)(O_2)(UO_2)(NO_3)$_2$]* system indicates that the bend in this particular complex is not favoured by any direct interaction between the peroxide bridge or the uranyl oxygen atoms and a Lewis acidic species, as described in Chapter 4.1.5.3. It is therefore likely that the bend across the peroxide bridge in this system is either due to an inherent electronic preference of the system or due to the fact that bending may minimise a steric interaction. On examination of the structure

Table 4: Table of structural data for models of *[UO_2(BTPhen)(O_2)(UO_2)(NO_3)$_2$]* optimised in using different functional and basis set combinations.[a]

Model Employed	Peroxide *O-O* length / Å	Range. *U-O_{yl}* lengths / Å	Ave. *U-O_{yl}* length / Å	Range *U-O_{eq}* lengths / Å	Ave. *U-O_{eq}* length / Å	*O_{yl}-O_{yl}* (on adjacent ions) / Å	*U-O-O-U* dihedral angle / °
XRD Structure	1.455(1)	1.763 - 1.781	1.7725	2.309 – 2.335	2.318	2.992	-137.66
Peroxide bridged DFT optimised models							
B3LYP/6-31G(d,p)	1.452	1.770 - 1.783	1.775	2.263 - 2.419	2.337	3.044	-138.09
MO6/6-31G(d)	1.429	1.743 - 1.756	1.749	2.257 - 2.405	2.332	2.899	-133.35
MO6L/6-31G(d)	1.439	1.767 - 1.782	1.773	2.283 – 2.426	2.355	2.941	-133.31
MO6/def2-TZVP	1.418	1.738 - 1.751	1.743	2.252 - 2.405	2.329	2.899	-133.22
Hydroxide bridged DFT optimised model							
MO6/6-31G(d)	2.573	1.744 - 1.750	1.748	2.245 - 2.429	2.335	3.748	-175.18

[a] In order to facilitate comparison the crystallographically determined structural parameters for this complex (as characterised by DMW[3]) and the parameters optimised for the bishydroxide bridged dimer are also presented.

Table 5: Table of the differences in significant structural parameters between the crystallographically identified structure of *[UO_2(BTPhen)(O_2)(UO_2)(NO_3)$_2$]* (as determined by DMW[3]) and the structure of this complex as determined by gas phase optimisation of using a B3LYP/6-31G(d,p) functional-basis set combination.

Peroxide *O-O* length / Å	Range *U-O_{yl}* lengths / Å	Ave. *U-O_{yl}* length / Å	Range *U-O_{eq}* length / Å	Ave. *U-O_{eq}* length / Å	*O_{yl}-O_{yl}* (on adjacent ions) / Å	*U-O-O-U* dihedral angle / °
+0.003	-0.007– -0.003	-0.003	0.046 – -0.084	-0.019	-0.052	-0.43

Table 6: Comparison of the structural parameters for the *[UO_2(BTPhen)(O_2)(UO_2)(NO_3)$_2$]* complex characterised by DMW[3] to the mean and the range structural parameters determined from interrogation of the literature published in the CSD in Chapter 4.1.5.3.

Structure	Mean Peroxide *O-O* Bond length /Å	Ave *U-O_{eq}* Bond Length /Å	*U-O-O-U* dihedral angle / °
Mean Published Values (CSD)	1.48	2.35	141.0
Range of Published Values (CSD)	1.43 – 1.54	2.30 – 2.44	125.3 – 153.1
Mean Characterised by DMW[3]	1.46	2.32	137.7
Range Characterised by DMW[3]		2.31 – 2.34	

of the peroxide bridged complex in **Figure 38** it is clear that there is some degree of steric interaction in the complex as a whole that promotes bending of the torsional angle between the phenanthroline backbone of the ligand and one of the triazinyl groups. It is likely that this interaction is an embodiment of the steric strain in this system due to the proximity of the uranyl(VI)-bisnitrate species to the bulky tetramethylcyclohexane groups of the BTPhen ligand.

In order to probe the nature of the bend about the peroxide bridge in this system, a range of 'deannulated' models were constructed in which the *$CyMe_4$* groups on each arm of the BTPhen ligand had been removed in order to minimise the steric interaction in this system. These *DA*-BTPhen models were then optimised using the uB3LYP/B1 functional-basis set combination identified by the previous study to best replicate the empirical structure of this system. The models generated differed only in the symmetry constraints applied. The initial model optimised was completely unconstrained. The optimised structure of this unconstrained model is presented in **Figure 39**. As can be seen, even in the absence of the *$CyMe_4$* groups the dihedral angle across the peroxide bridge in this system remains bent. In this deannulated model, the torsional angle is calculated to be 139.6° as compared to a dihedral of 138.1° in the structure optimised at the same level of theory including the *$CyMe_4$* groups and a value of 137.7° in structure determined using XRD by DMW.[3]

In order to gauge the energetic penalty to deform the bent torsional angle in this complex to linearity, a second calculation was constructed in which the torsional angle across the peroxide bridge was constrained to 180° whilst all other coordinates were allowed to relax. This constrained optimisation gave rise to an energy for the system that was 1.78 kcal mol^{-1} higher than that for the bent state of the system. This difference in energy between the bent and linear states of the peroxide bridge is therefore of a similar magnitude as that calculated for the dicationic aquated analogue of this system modelled by Miro et al.,[171] in which the

linear state of the complex was found to lie 0.5 kcal mol^{-1} higher in energy than the bent state. Since removing the bulky *CyMe₄* groups from the model did not lead to a significant change the torsion angle about the peroxide bridge, it is reasonable to conclude that the driving force behind the bend in this structure is not steric in nature. Considering that no secondary structural effects were identified in the experimentally determined crystal structure[3] that could promote the bending of the peroxide bridge and the fact that the quantum chemical models of the peroxide bridged complex consistently converged upon a bent state of this system leads this study to suggest that in the BTPhen complex studied here has an inherent electronic preference for the dihedral angle about the peroxide bridge system to bend.

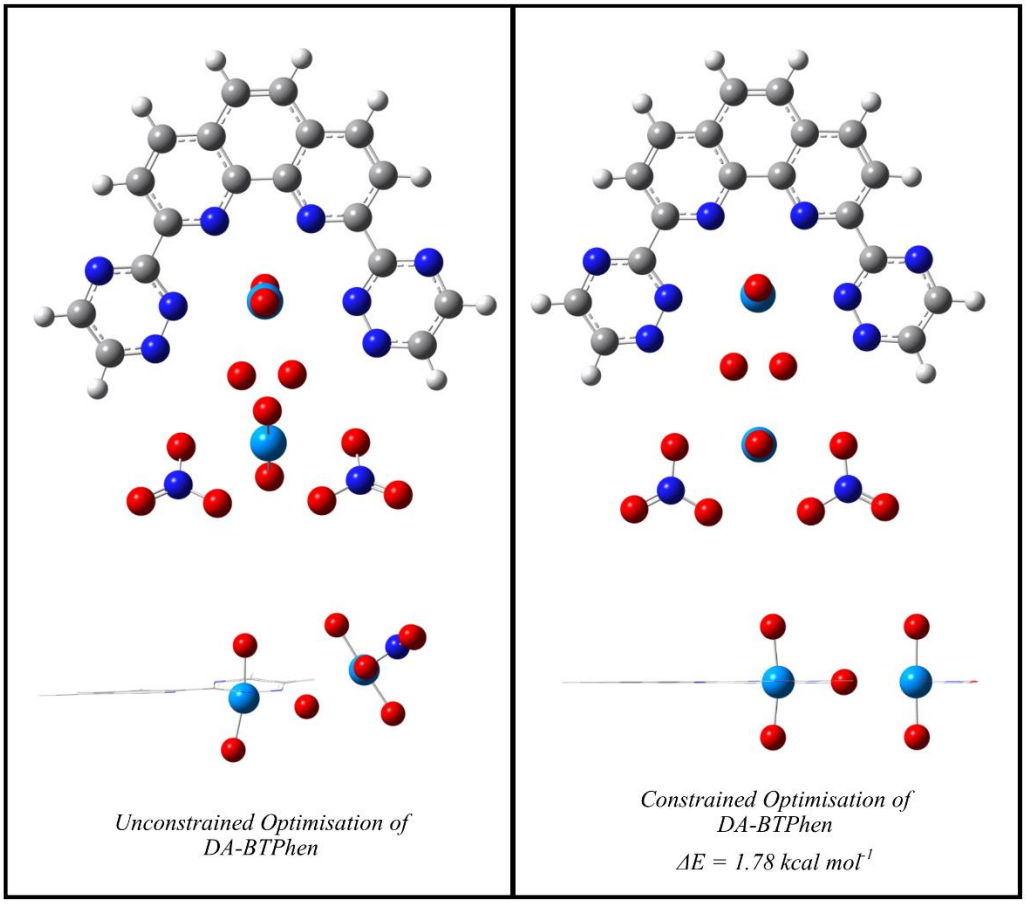

Figure 39: Optimised structures of the deannulated bisuranyl-peroxide bridged models. (left) the model has been optimised in the absence of geometric constraints generating a bent structure. (right) the optimised structure of a model in which the dihedral angle across the peroxide bridge has been constrained to 180°. The energetic difference between this constrained structure and the ground state bent structure is presented.

Conclusions

A preliminary quantum chemical study of the peroxide bridged bisuranyl-BTPhen system characterised by DMW has been carried out. Using structural constraints it has been shown that the bend in the torsional angle across the peroxide moiety in this complex is due to an inherent electronic effect and not due to a steric interaction or crystal packing effect. The

energetic penalty to deform the bent structure to linearity was calculated to be 1.78 kcal mol^{-1}. This small energetic difference is in agreement with the findings of a similar computational study conducted by Miro et al.[171] A survey of the available literature has been carried out that has identified a range of primary and secondary structural features of complexes that are able to promote either a bent or linear geometry across the peroxide bridge. Many of these structural effects are relatively weak interactions thereby providing some empirical evidence that the angle across the peroxide bridge is somewhat pliable. The relatively small energetic difference between the bent and linear states was compounded by the characterisation of a crystal structure by Aladzheva et al.[173] in which both the linear and bent geometries were coincident. The structure of the peroxide bridged bisuranyl(VI)-BTPhen complex characterised by DMW^3 to which this body of work predominantly pertains has been introduced and compared to the body of published literature. Replication of the crystallographically observed structure was attempted using DFT methods. Two hybrid functionals (B3LYP and M06) and a meta-GGA functional (M06L) were employed along with two basis sets of differing flexibility. The combination of an unrestricted formalism of B3LYP and the 6-31G(d,p) basis set to represent the ligand orbitals was found to reproduce the crystallographically determined structure excellently when optimised in the gas phase.

As a final note, although a selection of structural observations have been made and correlated with the angle of the *U-O-O-U* dihedral in this chapter, one should bear in mind that the list provided does not constitute a set of rules, merely a collection of observations of structural motifs. This is important, as currently the data set is too small to make any firm correlations, especially considering the delicacy of the interaction in question. As a result it is only possible to speculate as to the origin of the driving force behind many of the linear or bent structures known that do not display the directional bonding motifs outlined above. Thus, for the purposes of understanding the general chemistry of uranyl-peroxide-uranyl bridges, the dihedral angle should not be considered inherently bent, but merely as pliable and able to assume a dihedral ranging from 125° to 180° as directed by the ligand field. Should a more detailed description of the energy landscape of the *U-O-O-U* dihedral angle for a particular complex be desired, then bespoke computational models will likely be required in order to elucidate the inter- and intra-molecular driving forces in the system that give rise to the observed structure.

4.2.4 Elucidating the Mechanism of Formation of the Peroxide Bridged Complex

As stated previously, the crystals of *[UO_2(BTPhen)(O_2)(UO_2)(NO_3)$_2$]* characterised by DMW[3] were grown from an methanolic solution of uranyl(VI) nitrate and BTPhen. None of the reagents used during the NMR titration experiment had been dried, hence the solution would have contained a significant amount of water. At no point during the experimental process was the atmosphere in contact with the sample controlled.

In light of the fact that the preceding computational study had indicated that the bridging species present in the crystallographically identified structure was likely to be a peroxide ligand, it was decided to launch a further collaboration with DMW in order to identify the probable mechanism of formation of the peroxide bridged complex in the experimental solution. As discussed previously, there is a wealth of information in the scientific literature concerning the formation of peroxide in solution as detailed by Bakac et al.,[4,125,132] Burrows et al,[5,128,187] Formosinho et al.[127,188,189] and Tsushima et al.,[105,106] to mention a few. Prior to launching a computational assessment of the thermodynamic feasibility of the vast number of differing paths the system could take to form peroxide, it was decided to narrow down the possibility space of relevance to this particular mechanism by suggesting a set of reactions in which the access of key reagents would be restricted in order to assess if the peroxide was being formed in a manner as laid out by Bakac et al.[4]

As discussed in Chapter 4.1.2, the mechanism proposed by Bakac et al.[4] proceeds via absorption of a blue or UV photon of light by the uranyl ion, UO_2^{2+}, to generate the lowest lying excited state of the uranyl ion, $^*UO_2^{2+}$. This species is known to have a high oxidising potential (E^0 = +2.6 V[5,122,190]) and in alcoholic solutions it has been shown to quench by hydrogen atom abstraction from the solvent to form a uranyl(V) species, UO_2^{+}. Subsequently, in solutions with access to an oxidative atmosphere the reactive uranyl(V) species has been shown to reduce molecular oxygen to superoxide and regenerate the uranyl(VI) catalyst. Following this point, Bakac et al.[4] suggest that a second photon absorption occurs leading to the formation of a second molecule of uranyl(V) which is able to reduce the superoxide formed by the initial cycle to peroxide. This scheme therefore necessitates the presence of multiple reagents in order for the mechanism to proceed as described. The first quantity required is light of the correct wavelength to excite the uranyl(VI) ion. The uranyl(VI) absorbs strongly ultra-violet (UV) as well as the blue wavelengths, the λ_{max} for UO_2^{2+} is 414 nm.[4,5,126] The second quantity required for this mechanism to proceed is that the excited state uranyl ion formed must be quenched in a manner that generates a uranyl(V) ion. The studies of excited state quenching discussed

previously suggest that there are two methods of quenching the uranyl(V) excited state that lead to the generation of a uranyl(V) species. The first is via hydrogen atom abstraction and the second is via ET. The third quantity required in order for the mechanism to proceed as described is for the uranyl(V) species formed to be oxidised by molecular oxygen. In light of these limiting variables an array of experiments were laid out that would act to confirm or deny if the mechanism being followed in DMW's NMR sample[3] to the peroxide bridged product shared any similarities with the route proposed by Bakac et al.[4] The experiments proposed were:

1) Limit the access of light to the reaction mixture.
2) Perform the reaction in a solvent with relatively high *C-H* bond energies and high ionisation energy in order to limit the quenching of the uranyl excited state via formation of a uranyl(V) species.
3) Perform the reaction under an inert atmosphere and thereby limit the access of molecular oxygen to the reaction mixture.

DMW acted on these suggestions and set up the following reaction mixtures:

1) A methanolic solution of uranyl(VI) nitrate and BTPhen with access to the atmosphere in a transparent reaction vessel.
2) A methanolic solution of uranyl(VI) nitrate and BTPhen with access to the atmosphere in a reaction vessel coated in tinfoil.
3) A dichloromethane solution of uranyl(VI) nitrate and BTPhen with access to the atmosphere in a transparent reaction vessel.
4) A dichloromethane solution of uranyl(VI) nitrate and BTPhen with access to the atmosphere in a reaction vessel coated in tinfoil.
5) A methanolic solution of uranyl(VI) nitrate and BTPhen stored under the inert nitrogen atmosphere of a glove box in a transparent reaction vessel.
6) A methanolic solution of uranyl(VI) nitrate and BTPhen stored under the inert nitrogen atmosphere of a glove box in a reaction vessel coated in tinfoil.

Of these six experiments, the four that were not stored in the glovebox were analysed following a month of storage. The samples were allowed to reduce to dryness prior to analysis by the natural evaporation of the solvent. The solids formed were subsequently dissolved in deuterated solvent and immediately analysed by proton NMR. A stacked plot of the NMR spectra generated by DMW[3] is reproduced with permission in **Figure 40**.

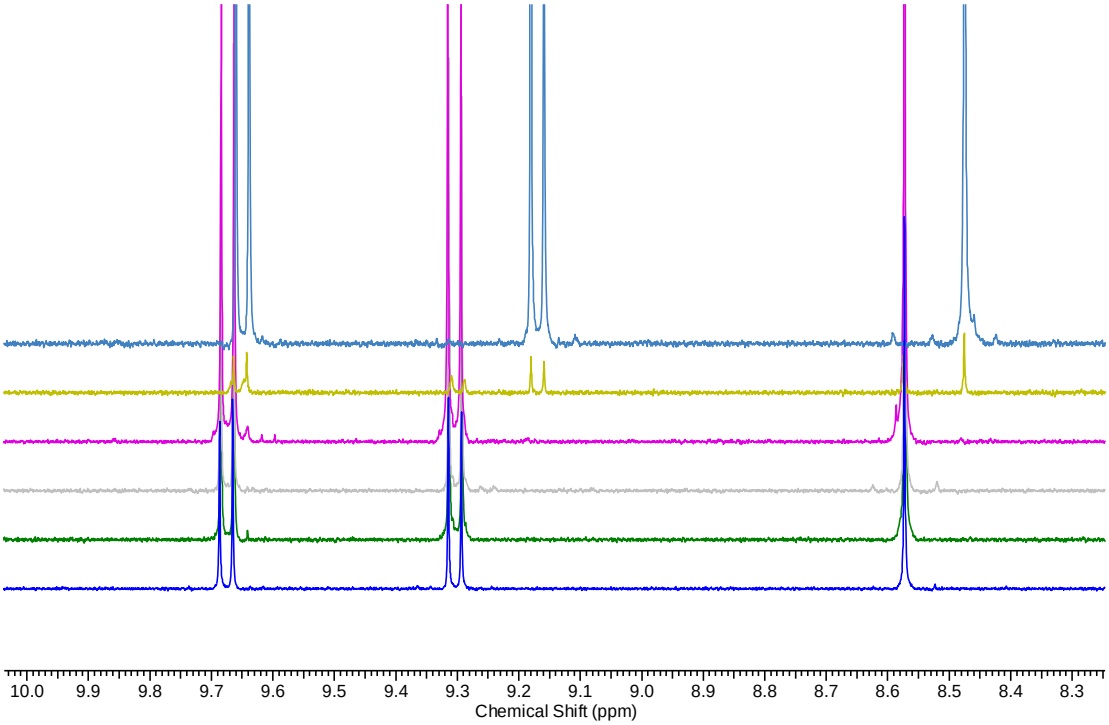

Figure 40: Stacked, zoomed in (8.2-10 ppm – aromatic region), ^{1}H NMR spectra of the samples used to investigate the effect of light/dark and hydrogen atom donor solvents on the formation of *[UO_2(CyMe$_4$-BTPhen)(O_2)(UO_2)(NO_3)$_2$]*. DCM dark, DCM light, MeOH dark, MeOH light (amorphous), MeOH crystalline and synthesised *[UO_2(CyMe$_4$-BTPhen)(O_2)(UO_2)(NO_3)$_2$]* from bottom to top, respectively. Figure and caption reproduced with permission from the thesis of DMW.[3]

Shown in **Figure 40** are six overlaid NMR spectra centred about shifts that are typically relevant to aromatic protons. The resonances observed are those attributable to the protons on the phenanthroline backbone of the BTPhen ligand. The blue spectrum at the top of **Figure 40** represents the resonances observed when *[UO_2(BTPhen)(O_2)(UO_2)(NO_3)$_2$]* that has been purposefully synthesised is dissolved and analysed. Whereas, the bottom four traces represent the dissolved material collected from the experimental reaction vessels 1 to 4. As shown in the figure, there aren't any resonances in any of the four lower traces that align with resonances characteristic of the neat *[UO_2(BTPhen)(O_2)(UO_2)(NO_3)$_2$]* sample in the top trace. This thereby suggests that excluding any single one of the variables light or methanol was sufficient to prevent the formation of peroxide. Following on, after three months of storage under an inert atmosphere, DMW[3] reduced experiments 5 and 6 to dryness and removed them from the glovebox. Over the following week, DMW[3] analysed these samples using proton NMR, however very little difference between the NMR signals evolved over this time period. Despite this, crystalline material was observed to form in the reaction vessel. XRD analysis of this material demonstrated the formation of *[UO_2(BTPhen)(O_2)(UO_2)(NO_3)$_2$]* in these reaction mixtures on exposure to air. As this material had not formed during the three months of storage in a glove box, DMW concluded that molecular oxygen was required to form the peroxide bridged complex.[3] An interesting

point to note is that whilst no peroxide bridged complex was observed to form on storage under an inert atmosphere, in the reaction vessel with access to ambient light, brown and pale yellow powders were observed to form in the vessel. Without access to molecular oxygen any uranium(V) formed will likely disproportionate, thereby generating uranyl(VI) and uranium(IV). It is possible that the brown powder observed may be the product of this reaction. Furthermore, when dry the BTPhen ligand is pale yellow in colour. No further analysis was performed on these solids and hence it is not possible to speculate further on their composition.

Conclusion

By eliminating the variables of light, solvents with readily abstractable hydrogen atoms and molecular oxygen from a set of six reaction mixtures in the presence of uranyl(VI) nitrate and the BTPhen ligand, DMW was able to demonstrate that all three of these variables were required in order to form the peroxide bridged complex crystallographically identified previously, *[UO_2(BTPhen)(O_2)(UO_2)(NO_3)$_2$]*. The necessity that all of these quantities were required to form the peroxide bridged complex suggested that the reaction is likely to proceed via a mechanism similar to that proposed by Bakac et al.[4] The empirical confirmation that light, methanol and molecular oxygen play a role in the reaction considerably reduces the number of variables associated with the process and paves the way for a quantum chemical study of the mechanism of peroxide formation in solutions containing uranyl(VI) nitrate and BTPhen.

4.3 A Mechanistic Study of the two Electron Reduction of Dioxygen in Solutions Containing the Uranyl(VI) Ion and *CyMe$_4$*-BTPhen

As discussed previously, this study was born from the crystallographic identification of peroxide in solutions to which no peroxide had been added. On turning to the literature, this led to a dawning realisation that the uranyl ion is not an inert species as is often claimed, but is instead a gateway allowing access to a diverse collection of photochemically created curiosities. Based on studies of the mechanism probing the quenching of the excited state of the uranyl(VI) ion conducted by the likes of Burrows[5] and Bakac[132] beginning in the 1970s, it was possible to confirm the route to peroxide taken in the uranyl(VI) nitrate and BTPhen solution required the presence of light, methanol and dioxygen. This suggested that the reaction proceeded via a photoinitiated hydrogen atom abstraction from the alcohol solvent to form a reactive uranium(V) species that was able to reduce solvated dioxygen to peroxide over two successive catalytic cycles. The broad strokes of this reaction have been the subject of multiple kinetic studies over the past 40 years, leading to much speculation over the optimum course such a reaction would follow. However, to date there have been no mechanistic studies of this complicated redox system and in particular the complex interplay between the redox potentials and states of protonation that drive this reaction in solution.

4.3.1 A Brief Summary of the Study to Follow

The following study is concerned with modelling the photo-initiated two electron reduction of dioxygen by the uranyl ion via a mechanism similar to that outlined by Bakac et al.[125] By exploiting the flexibility of computational chemistry it is possible to shed light on the feasibility of individual reaction processes that are not amenable to kinetic investigations and thereby compliment previous kinetic studies by elucidating the mechanism most conservative of energy. The following study is separated into three broad sections;

1) The electron transfer reactions;
2) The protonation, deprotonation and proton transfer reactions;
3) The approach of a second uranyl ion in order to form a bisperoxide bridged complex.

The first section is concerned with modelling the two individual electron transfer (ET) reactions that occur during this mechanism; the ET from a uranyl(V) ion to an equatorially bound dioxygen molecule to form a uranyl(VI)-superoxide complex and the subsequent electron transfer that sees an electron jump within a uranyl(V)-superoxide complex to form a uranyl(VI)-peroxide complex. This section is also concerned with the formation of the initial catalyst-substrate complex and the effect of protonation of the uranyl ion and the dioxygen species on the feasibility of the ET.

The second section turns the spotlight on to the acid-base reactions that connect the two ET processes and seeks to determine if the ET reactions modelled in the first section could occur *in vitro* or whether they are precluded by the infeasibility of the reactions that form the precursor state of each ET process. This section quantifies the proton affinities of the uranyl(V) and (VI) ions in various complexes and uses the observed trends to infer the likely protonation state of these species at various points in the ET mechanism. In addition, the dissociation of the superoxide and peroxide uranyl complexes is modelled in this section in order to study the validity of the mechanism proposed by Bakac et al.[4] This section also probes the effect of including solvation in the computational model in various forms in order to determine the sensitivity of the study to the solvation model employed. Finally, this section probes the possibility that a proton transfer reaction could occur between a protonated uranyl ion and an equatorially coordinated dioxygen ligand and the impact this might have on the proposed mechanism.

The final section is concerned with modelling the approach of a second uranyl ion in order to form the peroxide bridged bisuranyl ion complex observed experimentally by DMW.[3]

4.3.2 The Electron Transfer Reactions

At the heart of the proposed mechanism are the ET reactions integral to this process. Specifically, these are the transfer of an electron from a formally *U(V)* $[U^{V}O_2(BTPhen)]^{+}$ species to an equatorially bound dioxygen molecule and the analogous second step of this cycle that sees a regenerated uranyl(V) species reduce an equatorially-bound superoxide anion to form a uranyl peroxide complex.

4.3.2.1 Formation of the Catalyst-Substrate Precursor Complex and ET from Uranyl(V) to Dioxygen

Prior to each ET reaction, the excited state uranyl ion, $*UO_2^{2+}$, must be formed on absorption of a photon of light by a ground state species, UO_2^{2+}. This oxidising species is then able to abstract a hydrogen atom from a methanol molecule, thereby protonating an apical oxygen atom of the uranyl unit and funnelling the electron abstracted to the uranium atom to form a formally *U(V)* species, UO_2^{+}. At this point, the hypothetical monomeric system is primed to perform the first ET. However, even in this early position in the mechanism, there are a number of variables that can significantly alter the feasibility of the ET reaction. In particular, the effect of protonation on the redox potentials of the species involved is most pronounced, but there are also subtleties in the manner in which the multiplicity and spin coupling of the system plays a role in the mechanism. In this way, the reductive chemistry of the uranyl ion in the presence of dioxygen is reminiscent of the action in biological

systems, such as the oxygen evolving centre in Photosystem II of green plant cells. This is because both systems concern poorly understood catalytic factories that use a combination of sunlight and successive proton transfers to manipulate the redox chemistry of oxygen species.

When considering the starting point of the mechanism, the first point to note is that the ground state of dioxygen is a triplet $^3\Sigma_g^-$ state. This state is 22 kcal mol^{-1} lower in energy than the first excited state of dioxygen, $^1\Delta_g$. However, there is a finite probability that this excited state of molecular oxygen will be present in the experimental solution under study owing to the fact that the excited triplet state of the uranyl ion is sufficiently energetic and long-lived that it could in theory act as a sensitiser towards the formation of singlet oxygen.[191] Such a sensitisation can proceed via the direct transfer of energy from $*UO_2^{2+}$ to $^3\Sigma_g^-$ dioxygen during a collision of the two species, forming the ground state uranyl ion $UO_2^{2+}$and $^1\Delta_g$ oxygen. However, despite the excited state uranyl(VI) meeting the theoretical conditions required of a singlet oxygen sensitiser, no direct interaction between $*UO_2^{2+}$ and molecular oxygen has been observed to date.[5] Alternatively, it could form by direct interaction of triplet oxygen and the CCR generated by the hydrogen atom abstraction from the solvent by $*UO_2^{2+}$, giving rise to reactive oxygen species, such as singlet dioxygen but even superoxide may be formed.[191] Such a pathway would circumvent the requirement for the first ET proposed in this study to occur at all! However, the yield from such a sensitisation under non-optimal conditions is unlikely to yield a crystalline product over the timescale of days as was observed in the experiment conducted by DMW[3], thus the probing of alternative mechanisms is necessary. Despite this, it is reasonable that superoxide formed by reduction of dioxygen by the CCR could disproportionate on approach of a second superoxide species formed in a similar manner generating peroxide. Finally, it is conceivable that this peroxide may encounter two uranyl ions, which will be present in such a solution in a concentration in vast excess to the peroxide concentration, thereby forming the peroxide-bridged product.

The possible presence of both singlet and triplet oxygen species in solution is the first metaphorical fork in the mechanistic path towards the peroxide-bridged bisuranyl product observed experimentally. Both species are able to act as electron acceptors towards UO_2^+, although the excited nature of singlet oxygen results in it having an experimentally determined redox potential ~1 V more positive than triplet oxygen.[191] This suggests that singlet oxygen should be significantly more reactive than triplet dioxygen, but may lose out to the triplet oxygen path kinetically, owing to the relative abundance of the ground state triplet species. Despite this, as stated, this assertion depends on the currently unquantified

quantum yield of singlet oxygen sensitisation of the uranyl ion. Therefore, since the proportion of singlet oxygen in the system that this study is concerned with is unknown, the mechanisms that proceed via both singlet and triplet oxygen reaction pathways are necessarily discussed in the forthcoming analysis. At this point it is worthwhile to note that in the work of Bakac et al. and Burrows et al., the presence of singlet oxygen in the uranyl nitrate solutions is never explicitly referred to, however Burrows does state in an early study that no interaction between the excited state of the uranyl(VI) ion and molecular oxygen is observed hence it is reasonable to assume that the formation of singlet oxygen via such an energy transfer mechanism is precluded in this system.[5] Following on, in the work of Burrows et al. and Bakac et al. all reactions that are proposed concern the association of the reduced state of the metal ion with the triplet ground state of the dioxygen species.[5,132,139,190]

The first step in any catalytic cycle is the association of the substrate with the active site, in this case it is the association of a dioxygen species and the uranyl ion. As for any ET reaction, the transfer could occur via an inner sphere or outer sphere process. An inner sphere (IS) process proceeds via the formation of a discrete complex between the species involved in the ET, whereas on outer sphere (OS) process occurs via a weakly coupled state in which the redox active species are separated by their respective solvation spheres. Due to the weakly interacting nature of the OS-ET model, it is possible to gauge the feasibility of such reactions using the standard reduction potentials of the species involved. Therefore, knowing that for the redox couple UO_2^{2+}/UO_2^{+} E^0 = +0.16 V[125,192] and that for $^3O_2, H^+/\cdot O_2H$ E^0 ranges from -0.05 V to +0.12 V in acidic solution[150,192,193] the standard redox potentials suggest that the OS-ET that occurs to reduce triplet dioxygen and oxidise the uranyl(V) ion is a thermodynamically unfeasible process. This indicates that the experimentally inferred reaction is likely to proceed via an IS-ET process, in which, on coordination of the dioxygen species to the uranyl(V) ion, there is a partial reduction of the former, which modifies the redox potentials of the species involved and facilitates the latter ET process.[193]

4.3.2.1.1 Competition between Water and Dioxygen for the Labile Uranyl Coordination Site

Owing to the greater affinity of water for uranyl coordination than methanol and based on solution phase studies of the behaviour of actinyl ions and BTPhen detailed in the thesis of DMW[3] and Chapter 3 it is reasonable to assume that the majority complex in the experimental solution is $[U^{VI}O_2(BTPhen)(H_2O)]^{2+}$. Hence, in order to form an inner sphere complex with the uranyl ion, the dioxygen species must compete with water for access to the most labile coordination site in this system. Following a first glance, this appears to be

by no means a facile substitution, kinetically or thermodynamically, owing to the strong ionic interaction between this particular metal-ligand pair and the relative abundance of water in solution as compared to dioxygen. Nevertheless, in order to probe such a hypothesis, models were constructed to simulate this substitution reaction by quantifying the thermodynamic feasibility of the substitution of a molecule of water bound to a protonated uranyl(V) ion or a uranyl(VI) ion for a molecule of singlet or triplet dioxygen in solution.

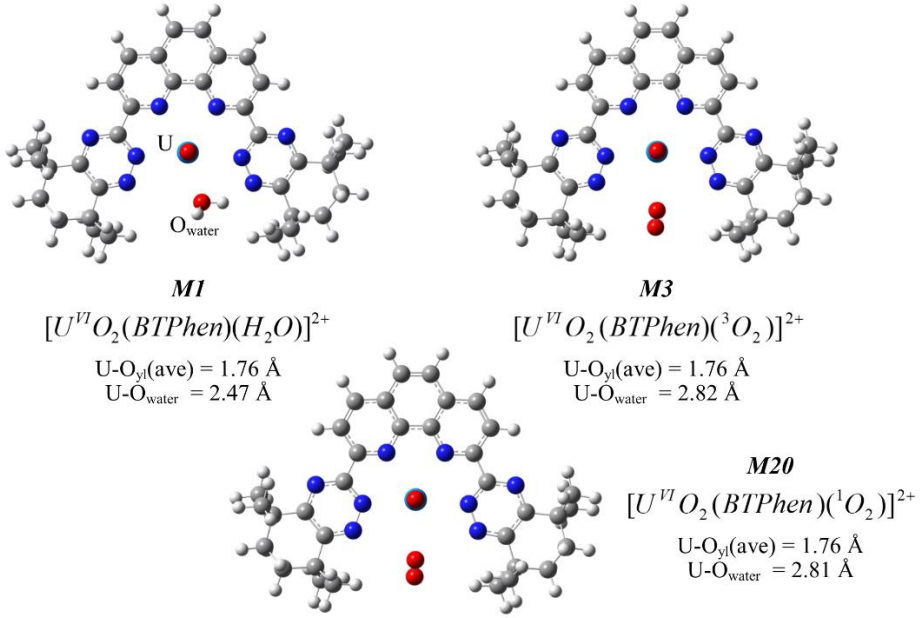

Figure 41: Optimised geometries of the aquated (***M1***), singlet oxygen (***M20***), and triplet oxygen (***M3***) bound complexes of the uranyl(VI) ion and BTPhen. The model number used to refer to these species, an empirical equation and significant structural parameters have been supplied for each model. The uranium atom is coloured green, oxygen is red, nitrogen is blue, carbon is grey and hydrogen is white.

Computational Details

In order to model this displacement, the structure of $[U^{VI}O_2(BTPhen)(H_2O)]^{2+}$, ***M1***, and its protonated uranyl(V) analogue, $[U^{V}OHO(BTPhen)(H_2O)]^{2+}$, ***M2***, were determined in the gas phase using the uB3LYP/B1 functional and basis set combination as described in Chapter 2. Following optimisation, thermodynamic and solvation corrections to the absolute energies of these species were calculated at the uB3LYP/B1 and uB3LYP/B2 levels, respectively. In addition to treating the aquated uranyl species, models of the dioxygen bound analogues were also optimised in a manner that constrained their spin multiplicities to represent the triplet and singlet electronic states of the bound dioxygen molecules. The optimised structures calculated for the aquated, singlet dioxygen bound and triplet dioxygen bound uranyl(VI) models are presented in **Figure 41** and the electronic energies and the thermodynamic corrections applied to both uranyl(VI) and protonated uranyl(V) complexes are presented **Table 7** along with the energies of the secondary species required to complete this reaction scheme. The optimised geometries of the protonated uranyl(V) complexes

themselves are not presented at this point due to the fact they are essentially identical to the uranyl(VI) analogues, excepting presence of an additional proton on the uranyl ion and the corresponding elongation of this bond. The details surrounding the optimisation of the uranyl(V) models and their energies will be outlined in greater detail in the following chapter.

Results and Discussion

Table 7: Table of the internal energies and thermodynamic, solvation and BSSE corrections to the energies[a] calculated for species involved in the substitution of a ligated water molecule in the complexes $[U^{VI}O_2(BTPhen)(H_2O)]^{2+}$ and $[U^{V}OHO(BTPhen)(H_2O)]^{2+}$ for singlet or triplet dioxygen.

Model	E	ZPE_{corr}	G_{corr} (H_{corr})	ΔE_{solv}	$BSSE_{corr}$
M1- $[U^{VI}O_2(L)(H_2O)]^{2+}$	-1,544,260.3	+442.0	+397.7 (+472.5)	-113.1	+2.8
M3- $[U^{VI}O_2(L)(^3O_2)]^{2+}$	-1,590,626.2	+428.9	+379.6 (+459.1)	-111.6	+1.4
M20- $[U^{VI}O_2(L)(^1O_2)]^{2+}$	-1,590,616.4	+428.9	+380.3 (+459.1)	-111.5	+1.4
M2- $[U^{V}OHO(L)(H_2O)]^{2+}$	-1,544,633.4	+447.0	+398.4 (+475.8)	-113.6	+2.8
M4.1- $[U^{V}OHO(L)(^3O_2)]^{2+}$ **H.S.**[c]	-1,591,000.1	+434.2	+382.5 (+463.9)	-112.3	+1.4
M21- $[U^{V}OHO(L)(^1O_2)]^{2+}$	N/A[b]	N/A	N/A	N/A	N/A
$(H_2O)_6$	-287,936.5	+94.1	+67.2 (+104.0)	-10.1	+5.2
$^3O_2(H_2O)_5$	-334,315.6	+81.7	+53.0 (+92.2)	-9.5	+7.7
$^1O_2(H_2O)_5$	-334,276.0	+82.2	+56.0 (+92.2)	-9.2	+7.8

[a] All energies are presented in kcal mol^{-1}.
[b] N/A denotes models for which it was not possible to converge a reliable solution.
[c] H.S. denotes that this model was optimised with a high spin multiplicity imposed, for example in the case of ***M4*** the spin multiplicity was constrained as a quartet. (L) represents the BTPhen ligand. As described in Appendix 2 a cluster model has been used to incorporate some explicit effects of solvation on the stability of the dioxygen and water species.

Using **Equation 50**, the free energy changes for the ligand substitution reactions that occur on approach of singlet and triplet states of dioxygen on the $[U^{VI}O_2(BTPhen)(H_2O)]^{2+}$ complex were calculated.

$$\Delta E = E(\text{prod}) + E(H_2O)_6 - E(\text{react}) - E(^SO_2(H_2O)_5) \qquad \textbf{(50)}$$

Where, E(prod) represents the energy of the dioxygen bound complex, $[U^{VI}O_2(BTPhen)(^3O_2)]^{2+}$ or $[U^{VI}O_2(BTPhen)(^1O_2)]^{2+}$ as appropriate, and E(react) represents

the energies of the aquated complex, $[U^{VI}O_2(BTPhen)(H_2O)]^{2+}$. The internal energies and thermodynamic, solvation and BSSE corrections for all these species are presented in **Table 7**, above. The ligand substitution energies calculated using the data in **Table 7** according to the relationship in **Equation 50** are presented in **Table 8**.

$$[U^{VI}O_2(L)H_2O]^{2+} + {}^3O_2 \longrightarrow [U^{VI}O_2(L){}^3O_2]^{2+} + H_2O \qquad \textbf{(51)}$$

$$[U^{VI}O_2(L)H_2O]^{2+} + {}^1O_2 \longrightarrow [U^{VI}O_2(L){}^1O_2]^{2+} + H_2O \qquad \textbf{(52)}$$

Table 8: Table of the ligand substitution reaction energies[a] calculated for the approach of triplet and singlet dioxygen on an aquated-BTPhen-uranyl(VI) complex.

Reaction	Equation No.	$\Delta E+ZPE$	ΔG_{gas} (ΔH_{gas})	ΔG_{solv} (ΔH_{solv})	$\Delta G_{solv}+BSSE$ $\Delta(H_{solv}+BSSE)$
M1 – M3	51	+12.6	+10.7 (+13.0)	+11.7 (+14.0)	+7.8 (+10.1)
M1 – M20	52	-17.7	-21.3 (-16.8)	-20.5 (-15.9)	-24.4 (-19.9)

[a] All energies are presented in kcal mol^{-1}. The energies of the secondary species that take part in this reaction were calculated using a solvating cluster model, the structures and energies of which are presented in Appendix 2.

It can be seen from the calculated free energies of reaction presented in **Table 8** that the displacement of an equatorially bound water molecule on uranyl is not a spontaneous process when the approaching dioxygen species is in its ground triplet state, for which a ΔG_{solv} of +11.7 kcal mol^{-1} was calculated. However, the substitution of water with a molecule of singlet dioxygen is calculated to have ΔG_{solv} = -20.5 kcal mol^{-1}, thereby suggesting this is a feasible process at RT. To the uninitiated, this may be somewhat surprising, as water is a conventional strong ligand for the uranyl(VI) ion, whereas the coordination chemistry of dioxygen is to this day an emergent field of study. Despite this, with the increased application of laser flash photolysis in conjunction with well-designed competition experiments, multiple recent studies have been able to calculate the stability constants for various transition metal complexes of dioxygen. A couple of examples of particular importance are the stability constants of rhodium(II) and cobalt(II) *meso*-Me_6-cyclam complexes with dioxygen. These have recently been identified as 3.7 x 10^{11} M^{-1} and 300 M^{-1} respectively,[193] thus despite these species having the same valence electronic structure they exhibit drastically different stabilities with respect to the binding of dioxygen. It has been suggested that this difference in stability is due to the differing reduction potentials of the metal ions, where Rh^{3+}/Rh^{2+} = +0.13 V and Co^{3+}/Co^{2+} = +0.49 V,[193] which results in the metal ion with the less oxidising potential delocalising a greater degree of electronic charge onto the dioxygen ligand and thus stabilising the interaction between the two weakly interacting

species. At this point it is worthwhile to note that whilst no direct empirical study of the formation of uranyl-dioxygen complexes has been carried out to date, the redox potential of the uranyl redox couple, UO_2^{2+}/UO_2^{+} is +0.16 V[192] and thus it is very close to the potential of the rhodium(III/II) couple that was observed to form the more stable complex with dioxygen. The corollary of this argument is that it would be expected that the uranyl(V) ion would be able to form more stable complexes with dioxygen than the uranyl(VI) ion. In line with this hypothesis, on repeating the calculation of the ligand substitution energies described above to identify the feasibility of the analogous reactions occurring on the protonated uranyl(V) analogue, the substitution energy for triplet dioxygen on uranyl(V) is calculated to be slightly less endergonic than the corresponding ligand exchange on uranyl(VI), see Table 9. However, despite this, the difference is rather small, amounting to only 0.2 kcal mol^{-1}. Nevertheless, it could be argued that the variation is due to the increased ability of uranyl(V) to donate electron density to the incoming dioxygen ligand. However, considering the errors inherent of such models it would be foolish to assign considerable weight to this finding in lieu of an in depth study of such trends.

$$[U^{V}OHO(L)H_2O]^{2+} + {}^{3}O_2 \longrightarrow [U^{V}OHO(L){}^{3}O_2]^{2+} + H_2O \qquad (53)$$

Table 9: Table of the thermodynamically corrected reaction energy for the substitution of an equatorially coordinated water ligand for triplet dioxygen in a complex of the protonated uranyl(V) ion.[a]

Reaction	Equation No.	$\Delta E+ZPE$	ΔG_{gas} (ΔH_{gas})	ΔG_{solv} (ΔH_{solv})	$\Delta G_{solv}+BSSE$ $\Delta(H_{solv}+BSSE)$
M2 – M4.1	53	+12.1	+10.8 (+12.4)	+11.5 (+13.1)	+7.7 (+9.3)

[a] All energies are presented in units of kcal mol^{-1}.
[b] (*L*) represents the tetradentate nitrogen donor ligand *CyMe$_4$*-BTPhen.

Returning to the QM models of the uranyl(VI)-dioxygen system, on examination of the individual energies of the component species of this reaction, **Table 7**, it is apparent that the feasibility of the reaction with singlet oxygen is not driven by an increased stability of this complex relative to that of an aquated uranyl(VI) complex or even the triplet dioxygen bound complex for that matter. Rather, there is a favourable change in energy because singlet dioxygen has such a high energy in solution that there is much stabilisation to be gained on forming even a weakly bound coordination complex with uranyl(VI). These energetic considerations are reflected in the geometries of the singlet and triplet dioxygen bound complexes, which as well as being energetically similar are also geometrically similar. In fact, the interatomic distance between the uranium atom and the loosely bound dioxygen species in these models are 2.82 Å and 2.81 Å respectively, and the *O-O-U* angle of the dioxygen species to the uranium atoms are 127.9° and 128.7° as compared to a ligand to

metal bond distance of 2.47 Å in the aquated complex. This similarity suggests that the overall feasibility of the predicted singlet dioxygen substitution reaction is a process driven by differential solvation of the reactants and products and not because of the inherent stability of the uranyl complex formed.

Summary and Implications for the Reaction Mechanism

This study has looked to quantify the ligand substitution energies for uranyl ions coordinated by an essentially non-exchangeable chelating ligand, BTPhen, and a monodentate labile species, water. The substitution reactions on which this initial body of work has focussed play a role in the primary steps of the peroxide forming mechanism under study and represent the ligand substitution that occurs to form the initial substrate bound catalytic system prior to and following its photoactivation. The reaction of two spin states of the dioxygen substrate with the uranyl ion has been considered; that of the ground state triplet multiplicity of dioxygen and its first excited state, singlet dioxygen. It was found that the substitution of a water molecule equatorially coordinating a uranyl(VI) ion for a molecule of singlet oxygen is an exergonic process, whereas the analogous substitution for triplet dioxygen is an endergonic process. The favourability of the singlet dioxygen coordination was found to be a predominantly solvation driven process, resulting from the instability of the singlet dioxygen solvent cluster relative to its 'aqueous' water analogue. In addition, it was found that the ligand substitution energies calculated for the interaction of triplet dioxygen with uranyl(VI) and protonated uranyl(V) ions was similar, the latter process being 0.2 kcal mol^{-1} less endergonic.

In the mechanistic scheme under study, the first step of the process may be the formation of a uranyl(VI)-dioxygen complex, followed by photoexcitation and the subsequent hydrogen atom abstraction that leads to the reductive protonated uranyl(V) oxidation state. However, it is also reasonable to assume that the reactive uranyl(V) state could form whilst coordinated by water forming the aquated uranyl(V) species. This species could then have its water molecule displaced on approach of dioxygen to provide the activated catalyst-substrate complex desired. The latter pathway is conceptually appealing as it would relax kinetic constraints on the lifetime of the weakly bound uranyl-dioxygen complex by providing a route that does not require this species to persist in solution long enough to be excited by an ambient photon and then oxidise solvent, as the following discussion will elaborate.

In order for the ET reaction to occur, two precursor states are required. However, these states may come about in any order. The first precursor state required is that the uranyl ion must be reduced to its +5 oxidation state and second is that there must be a dioxygen molecule

bound equatorially and thereby primed to accept the electron. There are many reactions in solution competing with the formation and destruction of these precursor states that are able to dictate the kinetics of the ET. The competitors of particular importance in this scheme are the oxidation of uranyl(V) by a species other than dioxygen and the possibility of a ligand substitution occurring on the weakly bound dioxygen uranyl(VI) species thereby regenerating an inert complex. Both of these interceptions of the reaction scheme are dependent on the relative lifetimes of the species involved. Whilst it is likely that neither species has an appreciable concentration in solution at any one point, as long as one of the species has a lifetime that permits the coalescence of the two precursor states by diffusion, then the proposed ET could occur with an appreciable yield. Of the two possibilities, it is likely that the most transient species will be the dioxygen complex, as this is a very weakly bound system (*cf.* the long bond lengths of 2.8 Å) and the solvated dioxygen species is heavily outnumbered in solution by better suited ligands for uranyl such as water, methanol and nitrate. On the other hand, the stability of the uranyl(V) species is likely relatively respectable in the solution under study, owing to the fact the BTPhen ligand chelates the metal centre and does not exchange readily in such solutions. This chelation will likely preclude the formation of the uranyl(V) cation-cation interactions that are thought to play a major role in the disproportionation of the uranyl(V) ion[194] and may thus appreciably decrease the rate of quenching of these species. There is also experimental evidence for the proposed greater longevity of the uranyl(V) species relative to the superoxide bound complexes, as a dioxygen complex of uranyl is yet to be characterised spectroscopically as opposed to the peroxide and superoxide complexes of uranyl(VI) and uranyl(V) which are readily observed in solution and solid states under certain conditions.[143,169,156,162] It is therefore conceptually appealing that in the system under study the mechanism is considered to commence via the absorption of an ambient photon by a $[U^{VI}O_2(BTPhen)(H_2O)]^{2+}$complex followed by a hydrogen atom abstraction from the solvent to form the analogous *U(V)* species $[U^{V}OHO(BTPhen)(H_2O)]^{2+}$. This species will then likely have a lifetime long enough to persist in solution until a molecule of dioxygen approaches and displaces the equatorially bound water to form the transient complex $[U^{V}OHO(BTPhen)(O_2)]^{2+}$. Although in terms of the thermodynamic analysis the models propose that this process will be feasible when the approaching species is singlet dioxygen, the fact that the behaviour of the excited state uranyl(VI) ion as a singlet oxygen sensitiser leads this study to suggest that the ET process proceeds via the transient formation of triplet dioxygen uranyl(V) complexes. Following the formation of such a complex, the prerequisites required for an ET to occur have been met, and if it is feasible, one should

occur spontaneously, thereby negating the condition that the dioxygen complex of the uranyl ion is required to have an appreciable lifetime.

4.3.2.1.2 The first ET

In general, the first ET reaction concerns the reduction of a dioxygen molecule equatorially bound to a protonated uranyl(V) species. However, the number of specific pathways that this first ET can follow is deceptively large, leading to different reaction free energy profiles depending on whether the uranyl(V) unit deprotonates prior to or following the ET and whether the bound oxygen species is in its ground state triplet or excited state singlet electronic configuration on approach. The presence of unpaired spins on both the uranyl unit and the dioxygen unit in the triplet oxygen bound complex adds a further complication to this reduction, as the spins on the two species could theoretically be ferromagnetically coupled, i.e. spin aligned to give a quartet state overall, or ferrimagnetically coupled, i.e. spin anti-aligned to give an open shell doublet solution, **Figure 42**.

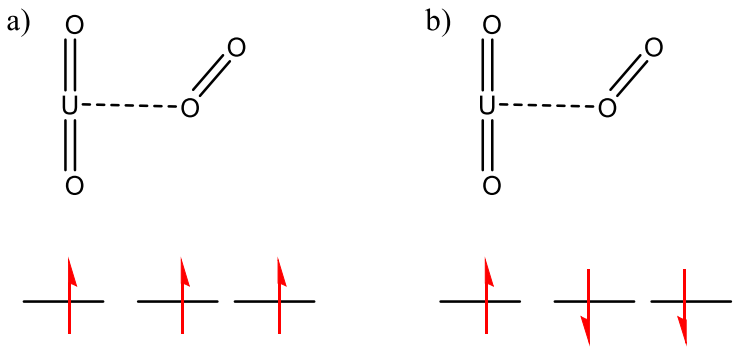

Figure 42: Schematic of the uranyl(V)-triplet dioxygen complex when in a spin aligned ferromagnetically coupled state (a) and a spin opposed anti-ferromagnetically coupled state (b).

Computational Details

When modelling ferromagnetically coupled species, it typically proves relatively facile to converge solutions representing the desired high spin multiplicity states as these configurations typically only describe the state that is sought and this system is no exception. However, when searching for anti-ferromagnetically coupled complexes, one typically runs into problems, especially when studying systems that may undergo ET, as the ferrimagnetically coupled states by necessity have the same multiplicity as the products of the ET. This results in reactant and product species lying on the same PES and necessitates a more careful search of the topology of the PES in attempt to identify a well-defined local minimum representing the precursor state in addition to the global energy minimum representing the product. In certain circumstances, it is possible to persuade the algorithm to converge to such local minima by using a fragment based approach to construct an initial

guess with broken spin symmetry or by using chemical intuition to vary the geometry of the initial guess to a structure that will favour one of the electron configurations over the other. However, as presently described, such an approach proved unsuccessful in some of the cases encountered this study. Unfortunately, one of these cases was the precursor state of the $[U^{V}OHO(BTPhen)(^{1}O_{2})]^{2+}$, ***M21***, complex in which a uranyl(V) species is bound by a singlet dioxygen ligand. Attempts to isolate a stable solution for this system failed, as the algorithm consistently converged on a state that described the electronic structure following ET. Whilst this is unhelpful when trying to quantify the change in free energy for the ET, the sheer fact that there was considerable difficulty in trying to identify the state of the system prior to ET suggests that the initial state of the reaction is unstable relative to the final ET state. In attempt to isolate the uranyl(V)-singlet dioxygen precursor state, multiple geometric and electronic initial guesses were imposed with varying constraints on symmetry. However, all optimisation procedures ultimately collapsed on the uranyl(VI)-superoxide state of the system following ET. This provides tentative *de facto* evidence that the uranyl(VI)-superoxide ET product is more stable than the uranyl(V)-dioxygen precursor. However, in lieu of conducting a complete search of the PES this concept is largely conjecture. For this reason alternative approaches to gauging the energy of this reaction have been pursued. To this end, the reaction energies for the triplet dioxygen ET processes have been studied in order to provide insight into the initial ET process. Furthermore, using the ET free energies calculated in conjunction with the ligand substitution energies for the singlet and triplet dioxygen reactions described previously, it has been possible to construct a thermodynamic cycle able to provide an estimate of the singlet dioxygen reduction free energy as will be shown later.

In addition to the problems inherent of attempting to identify multiple minima on a single PES using algorithms designed to converge only to the global minimum on the PES, any study of open shell compounds is also complicated by the possibility of spin contamination in the resulting wavefunction. As described in Chapter 2.9, spin contamination is the mixing of higher order multiplicity states into the spin state sought. It is not facile to correct the energy of a spin contaminated state to provide an absolute spin pure energy and furthermore within a single computational method it is not necessarily possible to identify a spin pure wavefunction for some systems. For this reason, it is often necessary to use spin projection methods to provide an estimate of a range that bounds the energy of the non-spin contaminated energy. As described in Chapter 2.9, one such method is the Yamaguchi method. This method has been employed in this chapter in order to provide a range of

energies that bound the spin pure energy of the ***M4*** system, assuming the geometry of the spin pure system does not differ significantly from that of the spin contaminated system.

All the models discussed have been optimised in the gas phase using the uB3LYP/B1 functional basis set combination. Frequency calculations were carried out at the same level of theory in order to generate thermochemical correction factors and to confirm that the converged geometries represented an energetic minimum. Gas phase and solution phase SP calculations were carried out using the uB3LYP/B2 level of theory. BSSE corrections were calculated using the CP method in a manner as described in Chapter 2.6. All models were optimised in the absence of any symmetry constraints.

Results and Discussion

The Formation of Protonated Uranyl(V)-Dioxygen Complexes and the Effect of Spin Coupling on Stability

The optimised structure of the anti-ferromagnetically coupled uranyl(V) complex of triplet dioxygen, ***M4.1***, is presented in **Figure 43**. As observed for the analogous uranyl(VI) complexes of singlet and triplet dioxygen discussed previously, there are very few geometrical differences between the anti-ferromagnetically coupled uranyl(V)-triplet dioxygen model and its ferromagnetically coupled counterpart. Furthermore, neglecting the effect of protonation of the axial bond of the uranyl unit, the structures of the *U(V)* species are also very similar to the *U(VI)* species. In particular, regardless of spin multiplicity, all these complexes exhibit the same monodentate binding mode of the dioxygen species and have equatorial *U-O* distances ranging between 2.81 Å and 2.83 Å. In addition, the *U-O-O* angles in these complexes are all within the range 127.3°-130.0°.

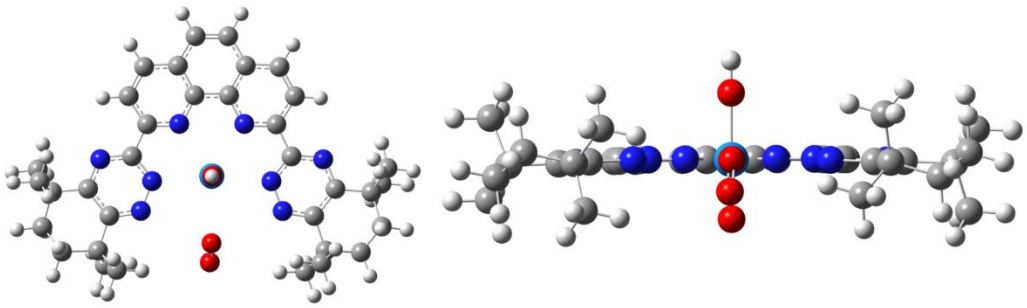

Figure 43: Plan view and side view of a complex of **[**$U^{V}OHO(BTPhen)(^{3}O_{2})]^{2+}$**,** (***M4.1***) an example of a dioxygen complex modelled with the protonated uranyl(V) ion.

Despite, these geometric similarities, the uranyl(V) complexes do differ energetically. The difference in the energy between the open shell doublet and quartet multiplicity states of the

system, ***M4*** and ***M4.1***, is presented in **Table 10**. The difference is necessarily presented as a range because, despite best efforts, the author was not able to identify a spin pure wavefunction for the system in an open shell doublet state. This contamination is exemplified by the fact that the $<\hat{S}^2>$ value for ***M4***, presented in **Table 10**, is not close to the spin pure value of $<\hat{S}^2>$ for a doublet system, as presented in **Table 11**. In order to provide a range of energies that bounds the energy of the spin pure state of ***M4***, the Yamaguchi method has been applied, as described in Chapter 2.9.

As described, a structural comparison of the optimised ***M4*** and ***M4.1*** models suggests that geometric differences between the models are minor, hence, this energetic difference must predominantly be due to a varying degree of the coupling between the unpaired spins on the opposing fragments. The calculated energies of the ferromagnetically and ferrimagnetically coupled uranyl(V)-triplet dioxygen complexes are presented in **Table 10**.

Table 10: Table of the internal energy, thermodynamic, solvation and BSSE errors calculated for the protonated *U(V)*-dioxygen complex in ferromagnetically coupled quartet state and anti-ferromagnetically coupled broken symmetry doublet state.

Model	$<\hat{S}^2>$	***E***	ZPE_{Corr}	G_{Corr} (H_{Corr})	ΔE_{Solv}	$BSSE_{Corr}$
M4- $^2[U^VOHO(BTPhen)(^3O_2)]^{2+}$	1.75	-1,590,999.2 – -1,590,997.8	+434.1	+382.5 (+463.8)	-112.4	+1.4
M4.1- $^4[U^VOHO(BTPhen)(^3O_2)]^{2+}$	3.77	-1,591,000.1	+434.2	+382.5 (+463.9)	-112.3	+1.4
$\Delta E =$ ***M4.1 – M4***		-0.9 – -2.3	+0.1	0.0 (+0.1)	+0.1	0.0

[a] All energies are presented in kcal mol^{-1}.

Table 11: Table presenting the relationship between the number of unpaired electrons in a system, the unpaired spin, S, and the expectation value of the spin operator, $<\hat{S}^2>$.

# Unpaired Electrons	***S***	$<\hat{S}^2>$
1	0.5	0.75
2	1.0	2
3	1.5	3.75

It can be seen that the thermodynamic corrections for both complexes are essentially the same, as would be expected for complexes with similar structures. However, this is offset by a relatively large difference in the internal energy of the system amounting to 0.9 to 2.3 kcal mol^{-1} in favour of the ferromagnetically coupled quartet state. This suggests that the ground state electronic structure of the uranyl(V)-triplet dioxygen complex is the ferromagnetically coupled quartet state. The implications of this result for the overall ET

mechanism will be discussed following a discussion of the superoxide bound product of the ET reaction.

The First ET: From Dioxygen to Superoxide

In the proposed ET mechanism, following the formation of the protonated uranyl(V)-dioxygen complex, it is possible for an intramolecular electron transfer to occur generating a protonated uranyl(VI)-superoxide complex, $[U^{VI}OHO(BTPhen)(^{\bullet}O_2)]^{2+}$, ***M5***. The optimised structure of which is presented in Figure 44.

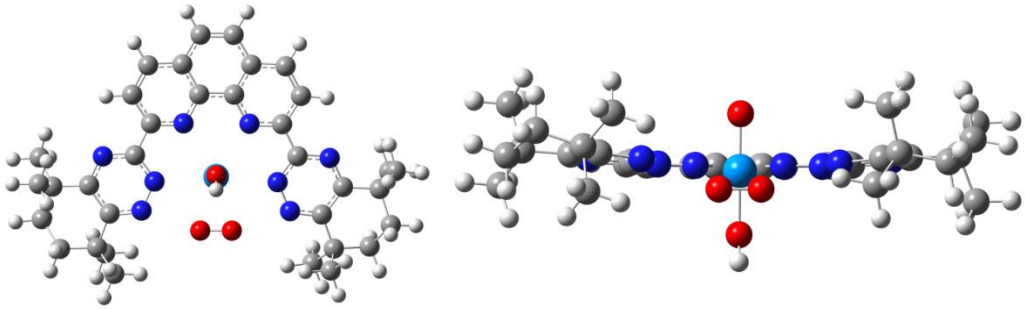

Figure 44: Plan and side depictions of the optimised geometry of the uranyl(VI)-superoxide complex, $[U^{VI}OHO(BTPhen)(^{\bullet}O_2)]^{2+}$, (***M5***).

Comparing the bidentate binding mode of the superoxide species in this complex to the monodentate mode of the dioxygen species in **Figure 43**, it is clear that following the ET the metal-ligand interaction has changed significantly. In particular, it is clear that the superoxide anion favours binding the uranyl ion using a more stable bidentate interaction as opposed to a relatively labile monodentate interaction as observed with dioxygen. This change is succinctly quantified by the much shorter average metal to ligand bond lengths of ***M5***, 2.32 Å, relative to the monodentate interaction with dioxygen in ***M4.1***, 2.81 Å. Probing the Mulliken spin density of the model of the uranyl(VI)-superoxide complex, ***M5***, and the protonated uranyl(V)-dioxygen complex, ***M4.1***, confirms that the electronic structure of the models generated do indeed represent the spin states of the system of interest in this study. As shown in **Table 12**, this means that the ferromagnetically coupled quartet state of ***M4.1*** has three unpaired spins, one centred on the uranium atom and two on the dioxygen ligand; whereas the ferrimagnetically coupled open shell doublet state of ***M4*** has three unpaired spins, one on the uranium atom and two spins aligned anti-parallel to the initial on the dioxygen unit and the superoxide complex in ***M5*** has a single unpaired spin distributed evenly across the superoxide anion.

As shown in **Table 12**, even though the wavefunction of ***M4*** is a spin contaminated solution, the contamination has little impact over the magnitudes of the atomic spins identified by the population analysis when compared to the spin pure triplet analogue of this state. As

expected the predominant difference between the population analyses of the quartet, ***M4.1*** and open shell doublet, ***M4***, solutions is that the unpaired spins are aligned parallel in the former, whilst one spin is opposed in the latter. Such invariance of population analyses to spin contamination has been noted previously.[195]

Table 12: Table of Mulliken spin densities centred on the uranyl and dioxygen species that take part in the first ET process.

Model	*U*	*O(1)*[a]	*O(2)*[a]
M4.1 - $^{4}[U^{V}OHO(BTPhen)(^{3}O_{2})]^{2+}$	+1.15	+0.88	+1.10
M4 - $^{2}[U^{V}OHO(BTPhen)(^{3}O_{2})]^{2+}$	-1.10	+0.88	+1.09
M5 - $[U^{VI}OHO(BTPhen)(^{\bullet}O_{2})]^{2+}$	-0.07	+0.52	+0.53

[a] For the triplet dioxygen bound complexes O(1) and O(2) represent the structurally distinct bound oxygen atom and unbound oxygen atom, respectively.

In order to aid visualisation of these spin densities, **Figure 45** is a plot of the excess spin density of the ferromagnetically coupled $^{4}[U^{V}O_{2}(BTPhen)(^{3}O_{2})]^{2+}$complex, ***M4.1***, and its anti-ferromagnetically coupled analogue, ***M4***, as compared with that of the $[U^{VI}OHO(BTPhen)(^{\bullet}O_{2})]^{2+}$ complex, ***M5***. Using these plots it is clear that in the ***M5*** model the excess spin is predominantly centred about the superoxide unit, whereas in the ***M4*** and ***M4.1*** models it is more uniformly distributed between the atoms in dioxygen unit and the uranium atom.

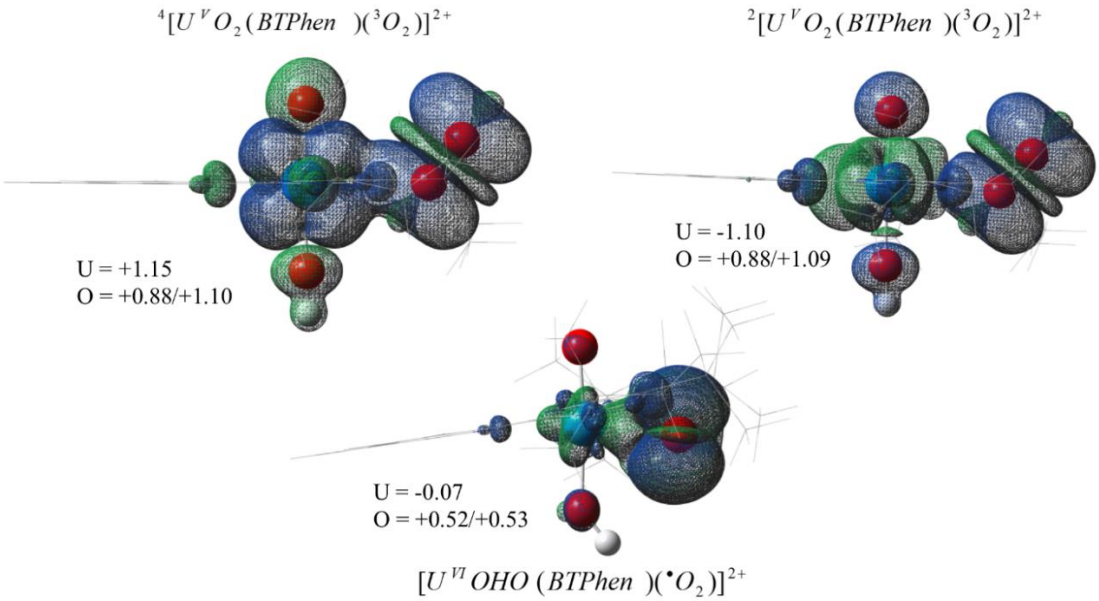

Figure 45: Plot of the unpaired spin density in the ferromagnetically coupled and anti-ferromagnetically coupled uranium(V)-triplet dioxygen complexes and the spin density in the *U(VI)*-superoxide product formed following ET. The Mulliken spin density for each model is also provided. Spin density surfaces are all plotted with an isovalue of 0.0004.

$$^{4}[U^{V}OHO(L)(^{3}O_{2})]^{2+} \longrightarrow [U^{VI}OHO(L)(^{\bullet}O_{2})]^{2+} \qquad \textbf{(54)}$$

$$^{2}[U^{V}OHO(L)(^{3}O_{2})]^{2+} \longrightarrow [U^{VI}OHO(L)(^{\bullet}O_{2})]^{2+} \quad \textbf{(55)}$$

In the above equations, *(L)* represents the BTPhen ligand.

Table 13: Table of calculated reaction energies[a] for the ET from a protonated uranyl(V) species to dioxygen to give a protonated uranyl(VI)-superoxide complex.[b]

Reaction	Equation No.	$\Delta E+ZPE$	ΔG_{gas} (ΔH_{gas})	ΔG_{solv} (ΔH_{solv})	$\Delta G_{solv}+BSSE$ $\Delta(H_{solv}+BSSE)$
M4.1 –M5	54	-1.1	+1.8 (-2.1)	+1.3 (-1.7)	+3.4 (-0.4)
M4 –M5	55	-1.8 to -3.2	+0.8 to -0.6 (-2.9 to -4.3)	+1.3 to -0.1 (-2.4 to -3.8)	+2.6 to +1.2 (-1.2 to -2.6)

[a] All energies are presented in kcal mol^{-1}.
[b] Two initial states are considered, the ferromagnetically coupled complex of the protonated uranyl(V) ion and triplet dioxygen and the ferrimagnetically coupled open shell doublet multiplicity.

Table 13 presents the reaction energy changes calculated for the ET from a uranyl(V) ion to a dioxygen ligand as described by **Equations 54** and **Equation 55**. Considering the values in **Table 13**, it is clear that despite the radical modification of the bonding in the system that accompanies the ET, the change in the reaction energy for the process is relatively small. Nevertheless, as would be expected for a reaction in which a more tightly bound bidentate complex is formed, the ΔH_{solv} for the reaction is marginally exothermic. However, this is offset by the increased order in the system following the reaction, which leads to a negative ΔS for the ET and thus provides a free energy for the transition that is marginally unfavourable at 298.15 K for both of the proposed processes. Despite this, as discussed earlier, the estimation of the entropy of complexes that have many low energy modes, such as those studied here, is often inaccurate owing to the incorrect treatment of hindered internal rotations as vibrations. This leads to some uncertainty in the accuracy of the entropies calculated. Whilst the calculated ΔS term will benefit from a partial cancellation of errors when comparing the reaction energy of two complexes with similar structures, in models such as this where the geometry of the initial and final states are significantly different the errors may be magnified. In this particular model, the error is further compounded by the fact this change in energy is close to zero, the reference point for spontaneity in a free energy calculation. Hence, there is some uncertainty whether this will be a spontaneous process at room temperature, or if this ET requires a modest activation energy input to occur. Despite this uncertainty, the free energies calculated are still a useful metric to compare the relative feasibilities of the processes studied. Thus the fact that the predicted energy of this transition is close to zero does not necessitate the conclusion that this is an unfeasible process, considering the uncertainty inherent in the model, see Chapter 2.

Comparing the energetics calculated for the ET within the ferrimagnetically coupled complex ***M4*** to that of its ferromagnetically coupled counterpart, ***M4.1***, it is clear that the former is the most favourable. The final product of each of these ET reactions is the same species, ***M5***, hence the difference in the reaction energy must solely result from the fact that the high spin quartet state of the reactant complex in ***M4.1*** is more stable than the open shell doublet state of ***M4***, as described previously. This discrepancy introduces an interesting debate over the most likely path the ET mechanism would follow when kinetics are considered. If the most stable configuration of the uranyl(V)-triplet dioxygen complex lies on a quartet surface, then the ET to the doublet product would necessitate a change of spin in the system. Such a process is disallowed by the spin selection rule. Hence, prior to the ET occurring, it is likely that the system will have to access the ferrimagnetically coupled doublet state by a matter of course, which lies ~0.9 to 2.3 kcal mol^{-1} higher in energy than the ground state. An alternate approach would see the spin symmetry of the reactants and products retained if the reaction proceeds via a complex of the uranyl(V) ion and singlet dioxygen as opposed to triplet dioxygen, since by definition, the reactants and products of such a system could only lie on a doublet surface. However, as stated, the presence of appreciable amounts of singlet dioxygen in these solutions is highly uncertain.

As stated previously, it was not possible to isolate a stable solution that described the coveted uranyl(V)-singlet oxygen electronic state, ***M22***. However, owing to the fact that singlet oxygen is an excited state of the species, it is reasonable to propose that any ET to this unstable species will be more favourable than the ET to the ground state. In this way it is possible to assume that the quantified energy range for the ET from ***M4*** to ***M5*** of ΔG_{solv} = +1.3 to -0.1 kcal mol^{-1} represents an upper bound to the free energy change for the singlet dioxygen analogue of this reaction. Furthermore, by invoking Hess's law and the principle of conservation of energy in the form of a thermodynamic cycle, it is possible to estimate the free energy and enthalpy change for the ET from the protonated uranyl(V) species to singlet dioxygen using the ligand substitution reaction energies and the triplet dioxygen ET energy calculated previously. The thermodynamic cycle required is presented in Figure 46. It is composed of two ligand substitution reactions, the exchange of a molecule of water for singlet dioxygen or triplet dioxygen, the energies of which were calculated in Chapter 4.3.2.1.1, and the free energy change calculated for the ET from *U(V)* to superoxide, as quantified in this chapter. Using this information along with the energies of the secondary species involved in each reaction, $^1O_2$, $^3O_2$, and H_2O, it is possible to estimate the free energy and enthalpy change for the unknown ET in order to calculate the free energy and enthalpy change for the reduction of singlet dioxygen by a protonated uranyl(V) ion, also known as

reaction ***M21 – M5***. In this cycle it has been necessary to assume that the energy change for the substitution of a water ligand on uranyl(V) for singlet dioxygen is the same as the substitution energy for the uranyl(VI) analogue. This is a reasonable assumption considering the non-bonding nature of the additional electron that differentiates the two models and the fact that when the same exchange was studied previously for the triplet dioxygen system the energetic difference was marginal at 0.2 kcal mol^{-1}.

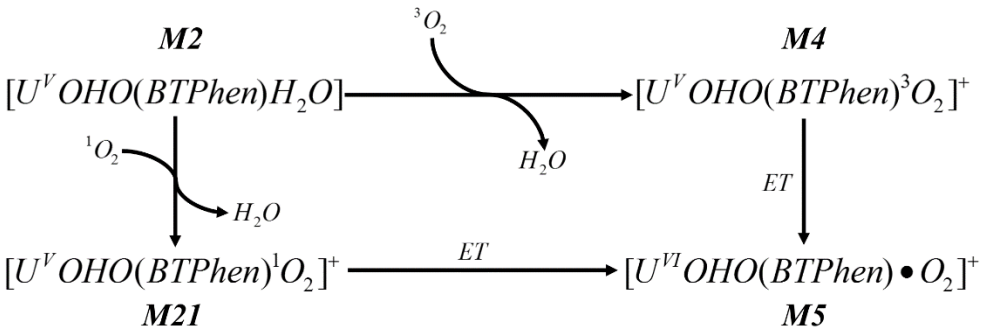

Figure 46: A schematic of the thermodynamic cycle used to estimate the electron transfer energy for the protonated uranyl(V)-singlet dioxygen to protonated uranyl(VI)-superoxide reaction, ***M21*** – ***M5***, which was not possible to model quantum mechanically due to difficulties converging to the electronic state that describes ***M21***.

Using this thermodynamic cycle and the energies of the species presented in **Table 8**, Table **9** and **Table 13**, along with the energies of the water clusters containing singlet dioxygen, triplet dioxygen and water in **Table 7**, a change in free energy of -8.7 kcal mol^{-1} is calculated for the ET reaction ***M21 – M5***. This is ~8-10 kcal mol^{-1} lower in energy than that of the ET to the triplet dioxygen molecule, as modelled by the transition from ***M4*** to ***M5***.

Effect of Changing the Protonation State of the Uranyl(V) Ion on the Feasibility of the ET

The free energy change calculated for the ET from a protonated uranyl(V) species to triplet dioxygen proved to be marginally endergonic, with a ΔG_{solv} of +1.3 to -0.1 kcal mol^{-1}. However, by altering the state of protonation of the species involved in the process it may be possible to significantly alter the feasibility of the ET reaction. In the reaction mechanism as described above, the ET occurs between a protonated uranyl(V) cation and an equatorially bound dioxygen species. Hypothetically, it is possible that the uranyl ion could deprotonate prior to the first ET occurring. It is likely that such a deprotonation would dramatically change the redox potential of the uranyl unit and this in turn would have a knock-on effect on the free energy change for the ET reaction overall. In order to investigate the magnitude of the effect of protonation of the uranyl(V) ion, a model of the deprotonated uranyl(V)-triplet dioxygen complex, ***M15.1***, $[U^V O_2(BTPhen)(^3O_2)]^{2+}$ was prepared. Due to the structural similarity of ***M15.1*** and its protonated analogue, ***M4***, an image of the deprotonated complex is not presented here. The only differences of note are the elongation of the

protonated uranyl *U-O* bond, as would be expected, and an increase in the interatomic separation between the uranium atom and the dioxygen ligand, which is observed to increase from 2.82 Å when the uranyl ion is protonated to 2.97 Å when it is not protonated.

The calculated free energy for the deprotonation of the $^4[U^VOHO(BTPhen)(^3O_2)]^{2+}$ model, ***M4.1***, to give $[U^VO_2(BTPhen)(^3O_2)]^{2+}$, ***M15.1***, is presented in **Table 14**.

$$^4[U^VOHO(L)(^3O_2)]^{2+} + H_2O \longrightarrow {}^4[U^VO_2(L)(^3O_2)]^{+} + H_3O^{+} \qquad \textbf{(56)}$$

In the above equation, *(L)* represents the BTPhen ligand.

Table 14: Reaction energies for the deprotonation of ***M4***, leading to ***M15.1***.[a,b]

Reaction	Equation No.	$\Delta E+ZPE$	ΔG_{gas} (ΔH_{gas})	ΔG_{solv} (ΔH_{solv})	$\Delta G_{solv}+BSSE$ $\Delta(H_{solv}+BSSE)$
M4.1- M15.1	56	-50.1	-51.2 (-50.3)	-17.2 (-19.0)	-20.0 (-19.1)

[a] All energies are in kcal mol^{-1}.
[b] The energies of the secondary species involved in this reaction were calculated using a solvating cluster model, the structures and energies of which are presented in Appendix 2.

The deprotonation is strongly exothermic and thus it is conceivable that the ET process could indeed occur via a deprotonated uranyl(V) species. However, it should be noted that these calculations consider only the thermodynamic driving forces behind the reaction and ultimately it is the rate of reaction that will define the path most travelled in solution. The free energy calculated for the ET from the non-protonated uranyl(V) ion in ***M15.1*** to the equatorially bound dioxygen ligand to generate the complex $[U^{VI}O_2(BTPhen)(^{\bullet}O_2)]^{2+}$, ***M6,*** is presented in **Table 15**.

$$^4[U^VO_2(L)(^3O_2)]^{+} \longrightarrow [U^{VI}O_2(L)(^{\bullet}O_2)]^{+} \qquad \textbf{(57)}$$

In the above equation, *(L)* represents the BTPhen ligand.

Table 15: Reaction energies for the electron transfer within ***M15*** leading to the *U(VI)*-superoxide product, ***M6***.[a]

Reaction	Equation No.	$\Delta E+ZPE$	ΔG_{gas} (ΔH_{gas})	ΔG_{solv} (ΔH_{solv})	$\Delta G_{solv}+BSSE$ $\Delta(H_{solv}+BSSE)$
M15.1 - M6	57	-25.5	-22.0 (-26.6)	-17.0 (-21.6)	-15.3 (-19.9)

[a] All energies are in kcal mol^{-1}.

With ΔG_{solv} = -17.0 kcal mol^{-1}, this ET is considerably more exergonic than the ET of the protonated analogue for which ΔG_{solv} = +1.3 to 0.1 kcal mol^{-1} was predicted. The large difference between these free energy changes highlights the influence of protonation on the redox potentials of inorganic species, and mirrors contemporary theories about the mode of

operation of the oxygen evolving centre of Photosystem II, the manganese cluster used by green plants to oxidise water via photosynthesis.[196,197]

Calculating the ΔG for the Spin Allowed ET from $U^{V}O_2$ to O_2

It should be noted that the models used to calculate the energies presented in **Table 15** formally represent a spin disallowed quartet to doublet transition, as ***M15.1*** was constrained to a quartet multiplicity. As discussed previously, this is not the desired state to model. However, on attempting to optimise the geometry of the desired broken symmetry doublet solution for this complex, similar convergence problems as described previously for ***M21*** were experienced. In essence, this meant that any attempt to identify the local potential minimum that represented the broken symmetry doublet solution ultimately converged to the closed shell global minimum that represents the product of the ET, ***M6***. Despite not being able to identify the ground state geometry of the ferrimagnetically coupled doublet state, it was possible to converge an SCF SP electronic solution representing the open shell doublet state at the ground state geometry of the quartet. In this way it has been possible to estimate the energy of the open shell doublet state of this system, albeit in thermally excited state. As identified during the study of the open shell analogues of ***M4***, the ferromagnetically coupled state converged upon in this study incorporated a degree of spin contamination. Hence, the Yamaguchi spin projection method has been applied in order to provide a range of energies that bound the energy of the spin pure state.

The energy of the open shell doublet electronic state calculated using the geometry optimised for the quartet state, ***M15.1sf***, was calculated to lie 3.4 to 8.2 kcal mol^{-1} lower in energy than the ground state quartet, ***M15.1***. Despite being an estimate, the uncertainty in this correction can be gauged by calculating the 'spin flipped' energy of the protonated uranyl(V)-dioxygen analogue, for which both the anti- and ferromagnetically coupled optimised geometries are known, ***M4*** and ***M4.1,*** respectively. The ground state energies of the optimised ***M4*** and ***M4.1*** complexes are presented in **Table 16**, along with the spin corrected energy range of the open shell doublet state calculated using the nuclear coordinates optimised for the quartet state, dubbed the '***M4.1*** spin flipped state', or ***M4.1sf***. The difference between the energy of ***M4.1sf*** and the energy of the open shell doublet solution in its ground state geometry, ***M4***, is found to be +0.03 to +1.4 kcal mol^{-1}. This is a negligible difference considering the other sources of error in the model applied. Despite this, caution should be exercised when inferring conclusions using the spin flipped values in place of their optimised analogues, as the error bars on these estimates are larger than the majority and hence it cannot be

guaranteed, even when comparing similarly composed systems, that unexpected chemical differences will not arise.

It is of interest to note that whilst the calculated energies for the quartet multiplicity state of the protonated uranyl(V) dioxygen complexe, ***M4.1***, was found to be lower in energy than the ferrimagnetically coupled doublet state, ***M4***, the trend is reversed for the deprotonated analogues, ***M15.1*** and ***M15.1sf***.

Table 16: Table indicating the difference in energy between the ground state quartet and broken symmetry doublet optimised geometries, ***M4.1*** and ***M4*** respectively and the approximation to the energy of the broken symmetry doublet model calculated as the energy of a converged open doublet electronic solution about geometry optimised for the quartet state, ***M4.1sf***.[a, b]

Model	$\langle \hat{S}^2 \rangle$	E	ZPE_{corr}	G_{corr} (H_{corr})	ΔE_{solv}	$BSSE_{corr}$
M4.1sf - $^2[U^{V}OHO(L)(^3O_2)]^{2+}$	1.75	-1,590,999.2 to -1,590,998.1	+434.2	382.5 (+463.9)	-112.3	+1.4
M4.1 - $^4[U^{V}OHO(L)(^3O_2)]^{2+}$	3.77	-1,591,000.1				
M4 - $^2[U^{V}OHO(L)(^3O_2)]^{2+}$	1.75	-1,590,999.2 to -1,590,997.8	+434.1	+382.5 (+463.8)	-112.4	+1.4
$\Delta E =$ ***M4 - M4.1sf***		*0.0 to +1.4*	*-0.1*	*0.0 (-0.1)*	*+0.1*	*0.0*

[a] All energies are reported in kcal mol^{-1}.
[b] The difference in energy is shown to be negligible. The states ***M4.1sf*** and ***M4.1*** share a set of thermodynamic, solvation and BSSE parameters as they share a geometry, hence it was assumed that any differences arising due to changing the change in electronic coupling would lead to energetically insignificant differences.

The reaction energies calculated for the ET using the spin flip corrected ***M15.1sf*** model and the *U(VI)*-superoxide model ***M6*** are presented in **Table 17**, along with the reaction energies calculated using the quartet state model ***M15.1*** as the initial state for comparison. Both models predict a strongly exergonic process, in blatant contrast with the mildly endergonic processes calculated for the protonated analogues.

$$^2[U^{V}O_2(L)(^3O_2)]^{+} \longrightarrow [U^{VI}O_2(L)(^{\bullet}O_2)]^{+} \qquad \textbf{(58)}$$

In the above equation, *(L)* represents the BTPhen ligand.

Table 17: Reaction energies for two different models of the electron transfer that describe the transition from a deprotonated *U(V)*-dioxygen complex, ***M15.1sf*** or ***M15.1***, to the *U(VI)*-superoxide product, ***M6***.[a]

Reaction	Equation No.	$\Delta E+ZPE$	ΔG_{gas} (ΔH_{gas})	ΔG_{solv} (ΔH_{solv})	$\Delta G_{solv}+BSSE$ $\Delta(H_{solv}+BSSE)$
M15.1sf – M6	58	-22.1 to -17.4	-18.5 to -13.8 (-23.2 to -18.5)	-13.6 to -8.9 (-18.2 to -13.5)	-11.9 to -7.2 (-16.5 to -11.8)
M15.1-M6	57	-25.5	-22.0 (-26.6)	-17.0 (-21.6)	-15.3 (-19.9)

[a] All energies are in kcal mol^{-1}.

Effect of Changing the Protonation State of Dioxygen on the Feasibility of the ET

Deprotonation of the uranyl unit is not the only method by which the protonation environment of the constituent species can be manipulated. Theoretically, it is also possible that the dioxygen unit could exist in a protonated state. Despite this hypothetical feasibility, chemical intuition suggests that this would not be a viable species. Nevertheless, the beauty of computational chemistry is that the feasibility of such processes can be quantified, hence a model in which a protonated triplet dioxygen ligand bound equatorially to uranyl(V) was optimised, generated ***M17***. The optimised geometry of ***M17***, is presented in **Figure 47**. As expected this system is rather strained since the protonated dioxygen ligand seeks to interact more closely with an oxygen atom of the uranyl unit than the metal ion itself, thereby forming a hydrogen bond with the uranyl axial oxygen atom and only a weak interaction bond with the uranium atom. The *U-O* distance in this complex is 2.65 Å, representing the closest interaction between uranium and dioxygen observed in any of the complexes described to this point. However, this complex lies 40.3 kcal mol^{-1} higher in energy than the model in which the proton is located on the uranyl ion, ***M4.1***, and hence it is unlikely that this species plays a significant role in the ET process.

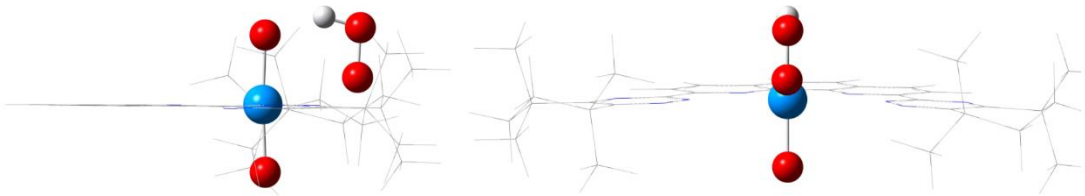

M17

$[U^{V}O_2(BTPhen)(^3O_2H)]^{2+}$

Figure 47: Images of the optimised model of a protonated triplet dioxygen species binding to a uranyl(V)-BTPhen complex.

A Summary of the Chemistry Surrounding the First ET

The discussion to this point has centred around a single redox cycle of the uranyl catalyst, which has acted to reduce one molecule of dioxygen into a superoxide anion. The most likely order of the initial steps that lead to the primed catalytic system has been inferred from published kinetic evidence and theoretical models as photoexcitation of an aquated uranyl(VI) complex, hydrogen atom abstraction from solvent and then by ligand substitution of water for dioxygen. It has been shown that the reduction of singlet dioxygen by a protonated uranyl(V) species is a feasible reaction. However, even in the absence of singlet dioxygen if the uranyl(V) ion is deprotonated the ET to triplet dioxygen is also predicted to be feasible at RT. Thermodynamic studies of the deprotonation of uranyl ions has indicated that the process is energetically feasible, however as discussed in Chapter 4.3.3 these

processes may not be comprehensively kinetically feasible. These initial studies of the protonated uranyl ion foreshadow a study detailed in Chapter 4.3.3 of this report in which the height of the potential barrier to these deprotonation processes is discussed. A different route of deprotonation for the protonated uranyl(V) ion was examined, a proton transfer (PT) from the uranyl ion directly to the bound dioxygen molecule, but the process was found to be strongly opposed energetically.

In order to aid the reader's visualisation of where the reaction energies quantified up to this point fit within the proposed reaction mechanism as a whole, a flowchart, hereby known as the reaction web schematic, has been generated and is presented in **Figure 48**. In this chart, the lines represent reaction paths (the free energy and enthalpy changes occurring during which are presented adjacent) and the boxes at the intersections of the lines designate the names of the appropriate uranyl centred chemical models used to calculate the reaction energies (as referred to by the appropriate '***Mx***' code). The flowchart is essentially a string of coupled thermodynamic cycles, against which the solvated free energy and enthalpy changes of the reactions discussed to this point have been included in kcal mol^{-1}.

4.3.2.1.3 The Second ET Process

The purpose of the present chapter is to discuss the feasibility of the second ET process that transforms superoxide into peroxide. The starting point for this process is a uranyl(VI)-superoxide complex in some, as of yet, unknown state of protonation. By this point, all of the energy put into the system by the initial photoexcitation has been quenched as the system tumbled through a cascade of chemical reactions that have ultimately led to the formation of a uranyl(VI)-superoxide complex. A point of differentiation between this complex and its dioxygen analogue prior to the first ET is that previously there were concerns over the stability and hence longevity of the catalyst-bound substrate species. However, for the superoxide complex these worries are abated as empirical kinetic studies have quantified the stability constant of the uranyl(VI)-superoxide complex as a reasonably stable 1,500 M^{-1}.[142,143]

Outer Sphere ET

The most simple route that the second ET could follow to generate a molecule of peroxide is via an outer sphere reduction of a free solvated superoxide species by a free solvated uranyl(V) ion. The standard reduction potentials of the O^{2-}/O_2^{2-} and UO_2^{2+}/UO_2^{+} redox couples are +0.2 V And +0.16 V respectively.[4,141,192,144,150] Therefore, unlike the reduction of dioxygen by the uranyl(V) ion, these standard reduction potentials suggest that the OS-ET from a solvated uranyl(V) species to a solvated superoxide anion is a feasible process.

Furthermore, considering that the pK_a of the conjugate acid of the superoxide anion is 4.86,[142,144,145] it is reasonable to assume that in an aqueous-methanol solution the anion would exist in its monoprotonated form as the hydroperoxyl radical, $^{\bullet}O_2H$. The hydroperoxyl radical has a standard reduction potential of +1.44 V,[192] hence the OS-ET reduction of this species by uranyl(V) is also predicted to be a feasible process.

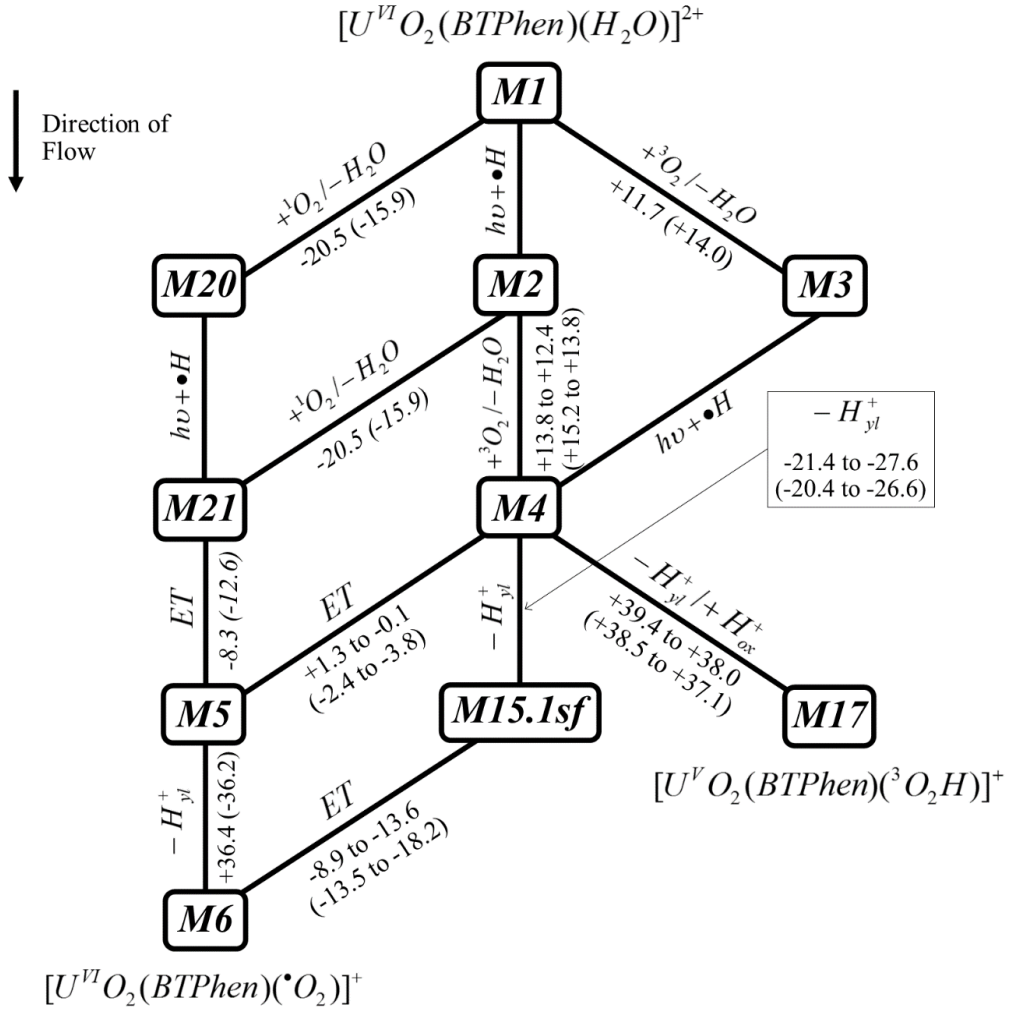

Figure 48. Mechanistic web schematic of the reactions relevant to the initial IS-ET process in which a molecule of dioxygen equatorially binds to a uranyl ion then is subsequently reduced to superoxide. The boxed numbers refer to the model representative of that state, as detailed in the text. The models selected for inclusion in this schematic are those that do not violate the spin selection rule. Hence, as opposed to the lowest energy quartet multiplicity model ***M4.1*** being selected to model the protonated uranyl(V)-triplet dioxygen system at ***M4***, the doublet multiplicity state that lies 1 kcal mol^{-1} higher in energy has been used as an ET from this species to generate the doublet uranyl(VI)-superoxide product does not necessitate a change in the overall spin of the system. Each line connecting two models represents a reaction occurring. These lines are labelled with the calculated free energy (and enthalpy in parentheses) change for that process and a description of the reaction that has occurred. *ET* represents an electron transfer; *+/-H_{ox}* represents the addition or abstraction of a proton from the dioxygen unit; *+/-H_{yl}* represents the addition or abstraction of a proton from the uranyl ion; *+^{n}O_2/-H_2O* represents the substitution of an equatorial water ligand for a molecule of dioxygen and '*hν+·H*' represents the photoexcitation of the uranyl(VI) ion in the corresponding complex and the quenching of this excited state via hydrogen atom abstraction from the solvent to generate a protonated uranyl(V) species. Reaction energies that it was not possible to model and have been inferred using the other energies presented in the thermodynamic cycles have been italicised. All energies are reported in kcal mol^{-1} and solvation corrections have been applied in all cases. No BSSE or '*sf*' corrections have been applied to the values presented. The sign of the energy changes presented applies for reactions as they flow from the top of the schematic at ***M1*** to the bottom at ***M6***.

Inner Sphere ET

Despite the likelihood that the OS-ET between the solvated uranyl(V) and superoxide species is a feasible process without the involvement of any novel inner sphere complexes, it is reasonable to explore the feasibility of the corresponding IS-ET reactions for the following reasons.

1) The first ET results in the formation of the required precursor complex in solution.
2) Uranyl-superoxide complexes are known to be relatively stable.
3) The crystalline product that initiated this study was an inner sphere bisuranyl peroxide bridged complex.

The simplest route that an IS-ET reaction could follow to generate a peroxide bound product is via the direct photoexcitation of the uranyl(VI)-superoxide complex, ***M6***, formed following the first ET process. This excited state species would subsequently quench its excess energy on abstraction of a hydrogen atom from the solvent to generate the reactive protonated uranyl(V)-superoxide complex, $[U^{V}OHO(BTPhen)(^{\bullet}O_2)]^{+}$, ***M7***. This complex would subsequently undergo an intramolecular ET between the uranium and superoxide species, generating a protonated *U(VI)*-peroxide bound product, $[U^{VI}OHO(BTPhen)(O_2)]^{+}$, ***M8***, which would lose the uranyl bound proton to yield the neutral peroxide bound product, ***M9***. This reaction scheme is laid out in **Equations 59-64** in **Scheme 1**, below, in which the presence of BTPhen in the models has been ignored in order to facilitate interpretation.

Scheme 1

$$[U^{V}OHO(L)(O_2)]^{2+} \xrightarrow{ET} [U^{VI}OHO(L)(^{\bullet}O_2)]^{2+} \quad \textbf{(59)}$$

$$[U^{VI}OHO(L)(^{\bullet}O_2)]^{2+} + H_2O \longrightarrow [U^{VI}O_2(L)(^{\bullet}O_2)]^{+} + H_3O^{+} \quad \textbf{(60)}$$

$$[U^{VI}O_2(L)(^{\bullet}O_2)]^{+} \xrightarrow{hv} {}^{*}[U^{VI}O_2(L)(^{\bullet}O_2)]^{+} \quad \textbf{(61)}$$

$${}^{*}[U^{VI}O_2(L)(^{\bullet}O_2)]^{+} + H_3COH \longrightarrow [U^{V}OHO(L)(^{\bullet}O_2)]^{+} + H_2\dot{C}OH \quad \textbf{(62)}$$

$$[U^{V}OHO(L)(^{\bullet}O_2)]^{+} \xrightarrow{ET} [U^{VI}OHO(L)(O_2)]^{+} \quad \textbf{(63)}$$

$$[U^{VI}OHO(L)(O_2)]^{+} + H_2O \longrightarrow [U^{VI}O_2(L)(O_2)] + H_3O^{+} \quad \textbf{(64)}$$

Computational Details

All models studied in this section have been optimised using DFT at the uB3LYP/B1 level as described in Chapter 2.2. Following optimisation, each model was confirmed to lie at a minimum on its PES from the absence of any negative frequency modes in its predicted vibrational spectrum, which was calculated using the same basis set. SP energies were

computed at these optimised geometries using the uB3LYP/B2 functional and basis set combination. Thermodynamic correction factors, as calculated during the SHO frequency analysis, were subsequently applied to these energies in order to calculate the quantities presented in this chapter. Solvation energies were modelled using the implicit CPCM method parameterised for methanol solvent. The solvent cavity was generated using the UA0 that typically assumes that protons in a system do not require explicit consideration. As the systems of interest in this study typically contained hydrogen bonding interactions as well as other relatively long hydrogen to main atom separations, in all systems in this work any proton bound to a typical hydrogen bond donor atom, e.g. *O* and *N*, was described by an explicit sphere during cavity generation. As described in Chapter 2, such protons were also represented using a larger basis set than that for the typical hydrogen atoms in the system, 6-311++G(d,p). When converging solutions for the anti-ferromagnetically coupled states of ***M7*** the resulting unrestricted set of orbitals typically suffered from a degree of spin contamination. As described previously, an estimate of the spin pure energy of these systems can be estimated using the Yamaguchi spin projection method. As stated in Chapter 2.9, this method typically overestimates the energy of the spin pure state and hence is unable to provide an absolute spin corrected energy. However, using the procedure it is possible to identify a range of energies that bound the absolute energy of the spin pure state. Such an application has been employed in the following discussion.

Results and Discussion

ET from a Protonated Uranyl(V) ion to an Equatorially Bound Superoxide Anion

The optimised geometries required to calculate the feasibility of the second ET as described in **Scheme 1**, ***M6*** through to ***M9***, are presented in **Figure 49**.

Compared with the first ET process, in which there was a stark change in the coordination mode of the dioxygen ligand on reduction, the change observed following the second ET process is less pronounced. However, there are subtle changes in the bond lengths of the species involved that hint at slight modifications in the electronic structure. The most obvious manifestation of the two single electron reductions on the structure of the dioxygen unit is the elongation of the internal *O-O* bond. This elongation is evidence of the increased occupation of the two degenerate antibonding π_g^* HOMOs of dioxygen as the moiety is reduced to superoxide and subsequently to peroxide. As shown in **Table 18**, the *O-O* bond length increases by around 0.1 Å following each ET. As the dioxygen ligand is reduced it forms a stronger interaction with the uranyl ion; from an initial monodentate $U\text{-}O_{eq}$ interaction of length 2.82 Å in the dioxygen complex to a bidentate interaction of length 2.16

Å in the peroxide complex. Furthermore, this increased affinity of the reduced dioxygen species for the equatorial binding of the uranyl ion adversely affects the internal bonding within the uranyl ion, leading to a small, but significant elongation in the *U-O*$_{ax}$ bonds as the equatorial and axial oxygen ligands compete for influence over the uranium ion.

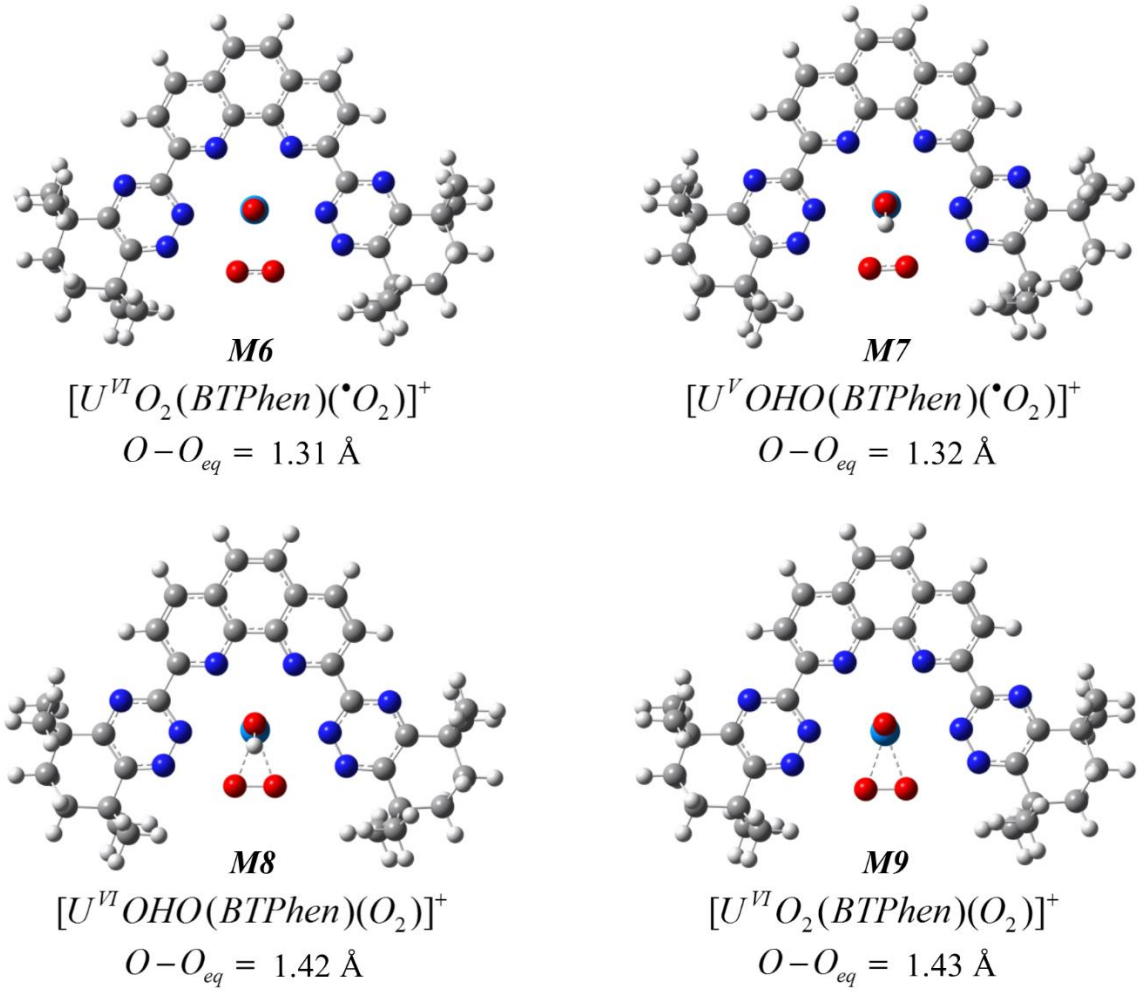

Figure 49: Optimised structures of the models ***M6*** through to ***M9***. In addition to each structure's designation and formula, the distance between the oxygen atoms in the equatorially bound dioxygen species is presented in order to highlight the change in bonding in the system.

Table 18: Table detailing the trend in bond lengths on reduction of the dioxygen species from triplet dioxygen to superoxide and finally peroxide, as modelled by ***M3***, ***M6*** and ***M9***.[a]

Model	*O-O*	*U-O*$_{eq}$	*U-O*$_{ax}$
M3 - $[U^{VI}O_2(BTPhen)(^3O_2)]^{2+}$	1.21	2.82	1.75/1.75
M6 - $[U^{VI}O_2(BTPhen)(^{\bullet}O_2)]^{+}$	1.31	2.35/2.35	1.77/1.77
M9 - $[U^{VI}O_2(BTPhen)(O_2)]^{0}$	1.43	2.16/2.16	1.81/1.81

[a] All distances are in Å and for the cases where there are two equivalent bonds in the complex, both values have been presented separated by a forward slash.

In order to confirm that the electronic structure of the computational models of the dioxygen and superoxide complexes studied, the excess spin density distribution and atomic spin population differences of the complexes were analysed. Whilst this was a viable method of assessment for the open shell dioxygen and superoxide complexes, the peroxide anion is a closed shell species and so spin population could not be used as the test of the applicability of the computational model. However, there are various methods of population analysis available that attempt to localise electrons on atoms in order to calculate effective atomic charges and populations that often prove useful in such situations. The NBO approach is one of such methods. The NBO procedure strives to reduce the orthonormal 1-electron MO description of bonding into a Lewis type description by diagonalising the density matrix to generate bonding orbitals of maximum density (i.e. as close to 2.0 as possible). In this way, the NBO procedure provides a method to describe the electron density in terms of the chemically familiar core, valence bonding and lone pairs of electrons. This often greatly simplifies the interpretation of the bonding in complex systems. **Table 19** shows the outcome of the NBO analysis of the ***M3***, ***M6*** and ***M9*** complexes. The analysis indicates a firm trend of increasing negative charge on the dioxygen atoms as the species is reduced, as would be expected. **Table 19** also quantifies the electron population of the *p*-orbitals of the oxygen atoms as the species is reduced, which indicates that the majority of the additional charge present on the dioxygen unit due to the reduction is housed in the 2*p*-orbitals, as one would expect for a successive reduction of dioxygen to superoxide followed by peroxide.

Table 19: Table detailing the electronic population of the dioxygen ligand on reduction from triplet dioxygen, to superoxide and finally, peroxide, as represented by the models ***M3***, ***M6*** and ***M9*** respectively.

Model	O_1-O_2 Charges	O_1 $2p^x$ Population	O_2 $2p^x$ Population
M3 - $[U^{VI}O_2(BTPhen)(^3O_2)]^{2+}$	+0.01 /+ 0.12	4.20	4.05
M6 - $[U^{VI}O_2(BTPhen)(^{\bullet}O_2)]^{+}$	-0.11 / -0.11	4.34	4.34
M9 - $[U^{VI}O_2(BTPhen)(O_2)]^{0}$	-0.35 / -0.35	4.57	4.57

The models ***M7*** to ***M9*** have been used to calculate the solvated free energy and enthalpy changes for the reduction of an equatorially bound superoxide anion by a protonated uranyl(V) species. The energies calculated for the reactions described by Equations **63** and **64** are presented in **Table 20**, in which ***M7*** represents the protonated uranyl(V)-superoxide complex, ***M8*** the protonated uranyl(VI)-peroxide complex and ***M9*** the non-protonated uranyl(VI)-peroxide complex.

$$[U^{V}OHO(^{\bullet}O_2)]^{+} \xrightarrow{ET} [U^{VI}OHO(O_2)]^{+} \quad \textbf{(63)}$$

$$[U^{VI}OHO(O_2)]^{+} + H_2O \longrightarrow [U^{VI}O_2(O_2)] + H_3O^{+} \quad \textbf{(64)}$$

Table 20: Table of reaction energies calculated for the excitation of the ***M6*** complex, followed by intramolecular ET modelled by ***M7*** and ***M8*** and finally deprotonation to yield the uranyl-peroxide product, ***M9***.[a]

Reaction	Equation No.	$\Delta E+ZPE$	ΔG_{gas} (ΔH_{gas})	ΔG_{solv} (ΔH_{solv})	$\Delta G_{solv}+BSSE$ $\Delta(H_{solv}+BSSE)$
M7 – M8	63	+1.0 to +4.1	+1.6 to +4.7 (+0.6 to +3.7)	+0.5 to +3.6 (-0.6 to +2.5)	+3.2 to +6.3 (+2.2 to +5.3)
M8 – M9	64	+26.9	+26.3 (+26.8)	-7.1 (-6.6)	-11.5 (-10.9)

[a] All energies are quoted in kcal mol^{-1}.

As explained in Chapter 4.3.2.1.2, in systems containing unpaired electrons centred on different atoms, the electronic spins can either align or anti-align. The corresponding ferromagnetic and anti-ferromagnetic spin states represent systems with different energies and hence it is most rigourous to converge models of both states in order that the lowest energy solution can be identified and carried forward. ***M7*** is an example of such a problematic state since it contains a protonated uranyl(V) ion and an equatorially bound superoxide anion, both of which have open shell doublet electronic configurations. The model used in the free energy calculation presented in **Table 20** above, represents the ground state geometry of the anti-ferromagnetically coupled state of the system. Thus, the unpaired electrons on the uranyl(V) ion and the superoxide anion are spin anti-aligned, as confirmed by an analysis of their excess spin populations. Similarly to the triplet dioxygen analogue of this system described previously, ***M4***, it was also possible to identify the ground state geometry of the ferromagnetically coupled triplet state of this complex, ***M7.1***. As encountered when studying the first ET process, it is not always possible to identify the ground state geometry corresponding to the anti-ferromagnetically coupled states of interest to this study. By definition, these states lie on the same PES as the products of the ET reaction and hence the optimised geometries of the anti-ferromagnetically coupled states lie in local minima in the PES that may not be characterised by a well-defined stationary point. In these cases one must approximate the spin anti-aligned state of the system to have the same geometry as the ferromagnetically coupled state. It is, therefore, necessary to assess the error associated with this assumption in the ***M7*** and ***M7.1*** systems for which the ground state geometry of both spin states of the model are known.

The thermodynamically corrected SP energies of the ferromagnetically and anti-ferromagnetically coupled electronic states of the protonated uranyl(V)-superoxide

complex at its ferromagnetically, ***M7.1,*** coupled optimised geometry, ***M7.1*** and ***M7.1sf***, respectively, and the energy of the ground state of the anti-ferromagnetically coupled complex, ***M7***, are presented in **Table 21**. As stated previously, open shell states are typically prone to spin contamination and these models are no exception. To account for the effect of this contamination on the energy of the system the Yamaguchi spin projection method has been applied in order to provide a range of energies for each of the models in **Table 21** that bounds the energy of the spin pure state.

Table 21: Table of the SP energies and thermodynamic corrections calculated for the ground state optimised ***M7*** and ***M7.1*** models that represent the anti-ferromagnetically coupled and ferromagnetically coupled protonated uranyl(V)-superoxide complexes, respectively.[a]

Model	$\langle \hat{S}^2 \rangle$	E	ZPE_{corr}	G_{corr} (H_{corr})	ΔE_{solv}	$BSSE_{corr}$
M7.1 - $^3[U^V OHO(L)(^\bullet O_2)]^+$	2.01	-1,591,208.01	+434.77	+385.05 (+463.57)	-36.72	+1.87
M7.1sf - $^1[U^V OHO(L)(^\bullet O_2)]^+$	1.02	-1,591,208.03 to -1,591,210.66				
M7 - $^1[U^V OHO(L)(^\bullet O_2)]^+$	0.84	-1,591,210.64 to -1,591,213.79	+434.72	+385.67 (+463.49)	-36.77	+2.41
$\Delta E =$ ***M7 – M7.1sf***		*-2.61 to -5.76*	*-0.05*	*+0.62 (-0.08)*	*-0.05*	*+0.54*

[a] For comparison, the energy of the anti-ferromagnetically coupled electronic state at the nuclear coordinates optimised for the ferromagnetically coupled state is presented in order to gauge the error associated with the assumption that these geometries may be considered equivalent.

The data in **Table 21** show that that the error introduced into the superoxide bound model by the assumption that the ferromagnetically coupled optimised geometry of the superoxide complexes is the same as their anti-ferromagnetically coupled analogues amounts to an underestimation of the absolute free energy of the spin anti-aligned complexes by 2.6 to 5.8 kcal mol^{-1}. This discrepancy compares to a difference of +0.03 to +1.4 kcal mol^{-1} when testing this assumption on the more weakly bound dioxygen analogue of this system as described by ***M4*** and ***M4.1***. On comparison of the geometries optimised for ***M7*** and ***M7.1***, it is found that the main difference between the two is that in the symmetry broken ***M7*** model the superoxide is able to form a closer interaction with the uranyl ion than in its ferromagnetically coupled analogue, represented by an average $U\text{-}O_{eq}$ of 2.28 Å and 2.35 Å in ***M7*** and ***M7.1***, respectively. The closer approach of superoxide on the uranyl ion also results in a slight lengthening of the superoxide bond length from 1.32 Å to 1.33 Å. This change in the bonding motif, based on spin symmetry, suggests that the error associated with the approximation is greater for the relatively tightly bound superoxide complexes when compared with the weakly coupled dioxygen complexes. However, the difference is of the

order of 5 kcal mol^{-1}, which is tolerable considering other uncertainties in the model and the fact that it has not been possible to otherwise identify the ground state geometry of these complexes.

Redirecting attention back to the reaction free energies presented in **Table 21** above, the ET from a protonated uranyl(V) ion to a superoxide anion, described by models ***M7*** and ***M8***, is calculated to have a near neutral ΔG_{solv} of +0.5 to +3.6 kcal mol^{-1} (ΔH_{solv} = -0.6 to +2.5 kcal mol^{-1}). This compares to a ΔG_{solv} of -0.1 to +1.3 kcal mol^{-1} (ΔH_{solv} = -3.8 to -2.4 kcal mol^{-1}) calculated for the analogous reduction of triplet dioxygen. Considering the known inherent uncertainty in the modelling procedure, these differences are not likely to be significantly different so that one process can be discerned as more favourable than the other. However, it is possible to state that they are of comparable feasibility and that they appear to be essentially thermodynamically neutral, thus neither confirming that these processes likely play a dominant role in the mechanism to form peroxide nor denying it.

The deprotonation reaction described by ***M8*** and ***M9*** is calculated to be exergonic with a ΔG_{solv} of -7.1 kcal mol^{-1}. Whilst this is calculated to be a feasible process at RT, it is found to be considerably less exergonic than deprotonation of the uranyl ion following the initial ET, for which ΔG_{solv} of -36.4 kcal mol^{-1} and ΔH_{solv} = -36.2 kcal mol^{-1} were calculated.

Although the free energy and enthalpy for the reduction of superoxide by a protonated uranyl(V) ion has been found to be essentially energetically neutral when the error is taken into account, it may be that significantly more exergonic transitions are observed when differing states of protonation of the uranyl and superoxide species are considered, as observed for the analogous ET to dioxygen. To this end, the ET reactions for systems containing non-protonated uranyl(V) ions and the protonated analogue of the superoxide anion, the hydroperoxyl radical, is considered in the following section.

ET from a Non-protonated Uranyl(V) ion to an Equatorially Bound Superoxide Anion

The next permutation of the active site to consider with respect to protonation is the ET from a deprotonated uranyl(V) species to an equatorially bound superoxide anion. This ET is described by the models ***M16*** and ***M9***, where ***M16*** is the deprotonated form of ***M7***. The structure and chemical formula of ***M16*** are presented in **Figure 50**.

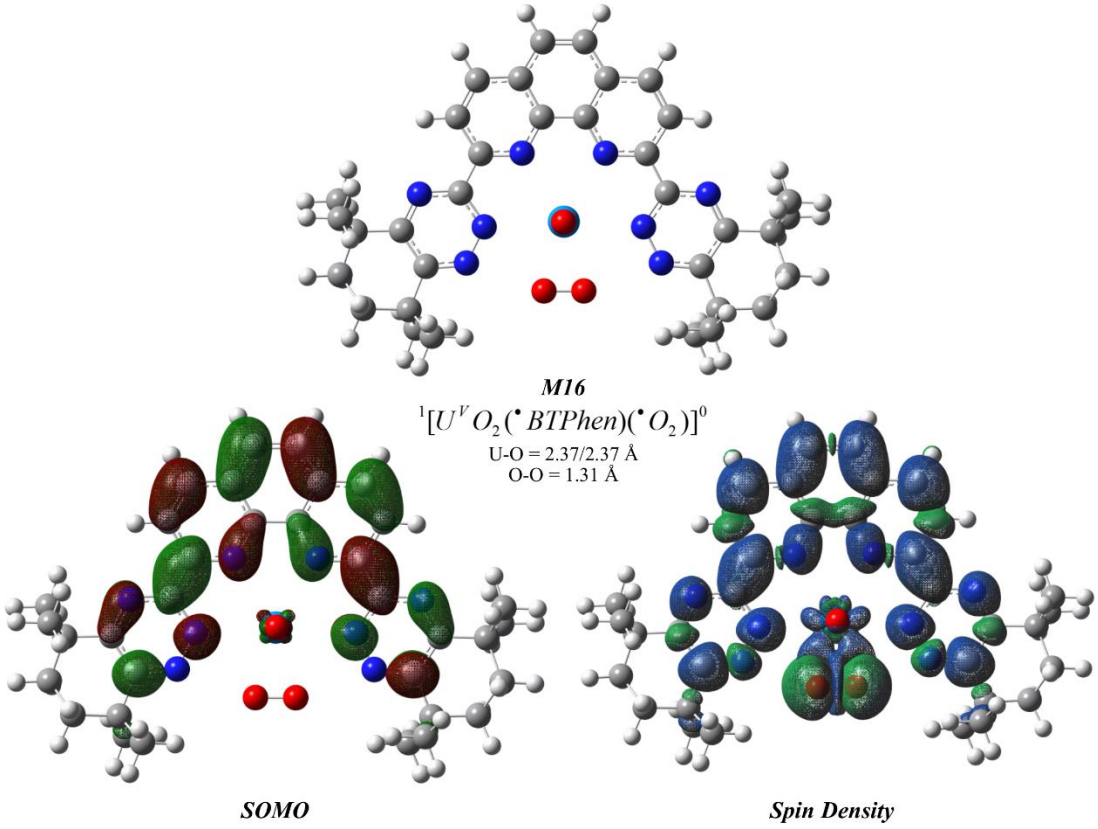

Figure 50: The structure of ***M16***, including the singly-occupied MO and the difference in spin density for this broken symmetry singlet system. on would expect the excess spin to be localised on the uranium and superoxide species in this system, but as the identity of the SOMO and spin density plot show clearly, it is instead shifted onto the BTPhen ligand. Both MO and spin density surfaces were calculated at the 0.004 isosurface.

On inspection of the electronic structure of this model, it appears that the optimisation procedure has not identified the *U(V)*-superoxide complex as desired, but has instead converged upon a uranyl(VI)-superoxide complex in which the BTPhen ligand has been reduced. This reduction is clearly indicated in **Figure 50**, in which the BTPhen based singly-occupied MO (SOMO) of ***M16*** and a plot of the spin density of this system have been provided. Together, these indicate that the excess spin in this system predominantly resides on the BTPhen and superoxide ligands and hence the model represents a reduced BTPhen species and not the reactive uranyl(V) species as desired. The reason why this particular system led to a reduction of BTPhen whereas in the analogous non-protonated uranyl(V)-dioxygen system the uranium atom happily retained the excess electron in is not immediately clear. However, stability tests of the DFT solution for ***M16*** indicate this is a stable density and all subsequent attempts to characterise a state in which the unpaired spin is localised on the metal failed. Thus, it is likely that the reduced BTPhen state identified is the ground state of this particular system.

The reaction energies calculated for the deprotonation of ***M7***, generating ***M16*** and its subsequent electron transfer to give ***M9*** are provided in **Table 22**.

$$^{1}[U^{V}OHO(L)(^{\bullet}O_{2})]^{+} + H_{2}O \longrightarrow {}^{1}[U^{VI}O_{2}(^{\bullet}L)(^{\bullet}O_{2})] + H_{3}O^{+} \quad \textbf{(65)}$$

$$^{1}[U^{VI}O_{2}(^{\bullet}L)(^{\bullet}O_{2})] \longrightarrow {}^{1}[U^{VI}O_{2}(L)(O_{2})] \quad \textbf{(66)}$$

In the above equations, *(L)* represents the chelating BTPhen ligand.

Table 22: Table of the calculated deprotonation energy of ***M7*** leading to the biradical complex ***M16*** and the subsequent ET to form ***M9***.[a]

Reaction	Equation No.	$\Delta E+ZPE$	ΔG_{gas} (ΔH_{gas})	ΔG_{solv} (ΔH_{solv})	$\Delta G_{solv}+BSSE$ $\Delta(H_{solv}+BSSE)$
M7 – M16	65	+24.2 to +27.3	+24.3 to +27.3 (+23.9 to +27.0)	+8.9 to +12.0 (+8.5 to +11.6)	+6.9 to +10.0 (+6.5 to 3.1)
M16 – M9	66	+3.7	+3.7 (+3.6)	-15.5 (-15.6)	-15.1 (-15.2)

[a] All energies are presented in kcal mol^{-1}.

As observed for the ET from a non-protonated uranyl(V) ion to an equatorially bound dioxygen molecule, the predicted ET energy for the deprotonated uranyl species is much more exergonic than the corresponding protonated analogue. However, this statement is not as definitive as the initial dioxygen reduction analogue of this process, since the transition of ***M16*** to ***M9*** actually models a uranyl(VI) inter-ligand redox process in which the superoxide anion is reduced by a reduced BTPhen molecule. Despite the uncertainty in the applicability of these models to the mechanism under study, it is worthwhile to note that the deprotonation of the uranyl(V)-superoxide complex, as modelled by the transition from ***M7*** to ***M16***, is not predicted to be a spontaneous process at room temperature. This is in contrast to all other uranyl deprotonation reactions quantified to this point. Hence, if the mechanistic route were to be considered as a whole then it is very unlikely that the route ***M16*** to ***M9*** would be traversed owing to the uphill energetic struggle inherent in the deprotonation reaction required to form the unstable non-protonated uranyl(VI)-reduced BTPhen-superoxide complex. This finding is in line with the fact that no degradation products of the BTPhen ligand were observed during the empirical synthesis of the peroxide bridged bisuranyl complex.

ET from Uranyl(V) ions to Equatorially Bound Hydroperoxyl Radicals

When studying the various states of protonation of the uranyl-dioxygen system, the feasibility of transferring a proton on a uranyl ion to an equatorially bound dioxygen ligand was quantified. However, owing to the low proton affinity (PA) of dioxygen, the free energy change for this PT was calculated to be +40.3 kcal mol^{-1} and hence the models identified it as grossly endergonic. Despite this finding, owing to the greater nucleophilicity of superoxide relative to dioxygen it may be found that the corresponding PT reaction occurring

within a protonated uranyl(V)-superoxide complex is spontaneous at room temperature. Such a PT would result in the formation of a non-protonated uranyl(V)-hydroperoxyl radical complex that may display drastically modified redox behaviour than its protonated uranyl(V)-superoxide analogue. An alternative state of protonation would see the additional proton provided by the external solvent field leading to the formation of a protonated uranyl(V)-hydroperoxyl radical complex. The feasibility of intramolecular ET reactions occurring within these two complexes is the focus of this section.

ET from a Protonated Uranyl(V) ion to an Equatorially Bound Hydroperoxyl Radical

Should it prove energetically favourable to protonate the superoxide ligand in this system to form a formally uranyl(V)-hydroperoxyl radical complex, $[U^{V}OHO(L)(^{\bullet}O_2H)]^{2+}$, ***M12a***, then the ET within this complex that follows to form the uranyl(VI)-hydroperoxide bound species, $[U^{VI}OHO(L)(O_2H)]^{2+}$, ***M13***, should, theoretically, be more favourable than that of the non-protonated analogue. The basis for this assumption is the more oxidising standard reduction potential of the hydroperoxyl radical as compared to superoxide, +1.44 V And +0.2 V, respectively.[4,141,192,144,150]

In order to calculate the feasibility of such a process, a search of the relevant multiplicity PES was conducted for each case in order to identify the geometries of the species that might arise during the ET from a protonated uranyl(V) ion to an equatorially bound hydroperoxyl radical. Surprisingly, this particular search led to the identification of more local minima than any of the other models studied to this point. This provides insight into the reorganisation of the complex prior to, during and following the ET and the relative feasibilities of these individual processes. The optimised structures of the models identified, ***M12a1***, ***M12a-TS***, ***M12a*** and ***M13,*** are presented in **Figure 51** along with a brief description of the bonding in each complex. In addition to these species, the previously described structures of ***M8*** and ***M9*** have been presented since one termination route of this pathway is deprotonation of ***M13*** to generate ***M8***. All of the geometries discussed in this section were confirmed to be at energetic minima with respect to their nuclear coordinates with the exception of ***M12a.1-TS***. This complex was confirmed to be a TS by the presence of a single imaginary frequency mode in its vibrational spectrum that described the translation of the hydroperoxyl radical from a mode predominantly interaction with the BTPhen ligand, as in ***M12a.1***, to one that more closely resembled the uranyl binding mode of ***M12a***.

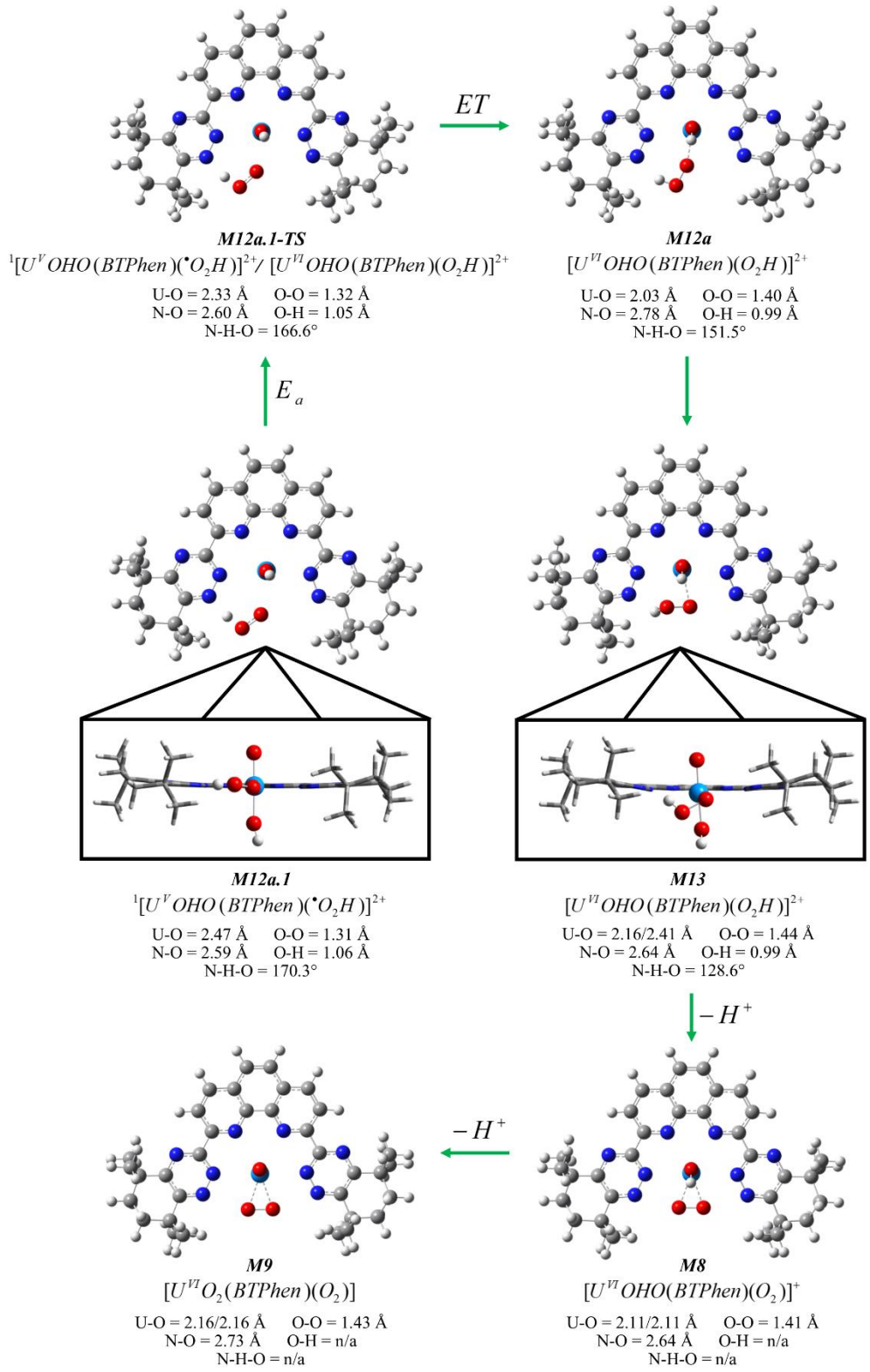

Figure 51: Schematic detailing the structures of the complexes ***M12a.1*** through to ***M13*** along with significant structural parameters to illustrate the competition between the hydrogen bonding interaction with the ligand and the coordinate bond to the uranyl. The structures of the previously presented ***M8*** and ***M9*** complexes have also been included in order to detail the effect of deprotonation of the peroxide and uranyl units, respectively. All of the O-atoms considered in the structural analysis are components of the dioxygen species and not the uranyl ion. Green arrows indicate the order of these models in the proposed reaction mechanism, starting with ***M12a.1***. E_a, *ET* and $-H^+$ represent activation energy, electron transfer and deprotonation reactions, respectively.

The absolute thermodynamically corrected energies for each of these structures were calculated following the procedure described in Chapter 2.5, yielding a set of reaction energies as presented in **Table 23**. Unfortunately, despite the fact that the search of the PES for this ET yielded many more local minima along the reaction coordinate than the other models studied, it was not possible to isolate an optimised geometry for the anti-ferromagnetically coupled analogue of ***M12a.1***. Hence, in line with the discussion earlier in this chapter, it was assumed that the triplet optimised geometry of ***M12a.1*** was a reasonable approximation to the anti-ferromagnetically coupled singlet solution, hence the model ***M12a.1sf*** was generated. As stated previously, this assumption has been shown to underestimate the stability of the similar complexes by between 2.6 and 5.8 kcal mol^{-1}. The effect of including this uncertainty in the energy of the broken spin symmetry model on the calculated reaction energies is included in the figures presented in the final column of **Table 23**, below.

$$^{1}[U^{V}OHO(L)(^{\bullet}O_2H)]^{2+} \longrightarrow \textbf{\textit{M12a-TS}} \qquad \textbf{(67)}$$

$$\textbf{\textit{M12a-TS}} \longrightarrow [U^{VI}OHO(L)(O_2H)]^{2+} \qquad \textbf{(68)}$$

$$[U^{VI}OHO(L)(O_2H)]^{2+} \longrightarrow [U^{VI}OHO(L)(O_2H)]^{2+} \qquad \textbf{(69)}$$

$$[U^{VI}OHO(L)(O_2H)]^{2+} + H_2O \longrightarrow [U^{VI}O_2(L)(O_2H)]^{+} + H_3O^{+} \qquad \textbf{(70)}$$

Table 23: Table of the energies of the sequential reactions that result in the conversion of a protonated *U(V)*-hydroperoxyl radical complex, ***M12a1sf***, into ***M13,*** a protonated *U(VI)*-hydroperoxide complex.[a, b]

Reaction	Equation No.	$\Delta E+ZPE$	ΔG_{gas} (ΔH_{gas})	ΔG_{solv} (ΔH_{solv})	$\Delta G_{solv}+sf_{corr}$ $\Delta(H_{solv}+sf_{corr})$[c]
M12a1sf - M12a-TS	67	+2.4 to +3.5	+3.7 to +4.8 (+2.0 to +3.1)	+4.2 to +5.3 (+2.4 to +3.5)	+6.8 to +11.1 (+5.1 to +9.3)
M12a-TS - M12a	68	-8.2	-7.9 (-8.3)	-9.4 (-9.8)	-9.4 (-9.8)
M12a - M13	69	-2.8	-2.6 (-3.0)	-1.5 (-1.9)	-1.5 (-1.9)
M13 - M8	70	-51.2	-52.2 (-51.0)	-16.1 (-14.8)	-16.1 (-14.8)

[a] All energies are presented in kcal mol^{-1}.
[b] In addition, the change in energy on deprotonating this complex to yield the model ***M8*** presented previously is also included.
[c] sf_{corr} is the correction factor associated with the 'spin flip' approximation, as discussed in the text.

A schematic of the reaction coordinate defined by these models is presented in **Figure 41**. The ET from a protonated uranyl(V)-species to a protonated hydroperoxyl radical has a modest barrier of activation of at least 4.2 kcal mol^{-1} and possibly a barrier as high as 11.1 kcal mol^{-1} accounting for the error in the use of the 'spin flip' model as well as spin

contamination. Despite the fact that a barrier to activation has been identified for this process, the activation energies required may be rather modest, corresponding to Boltzmann populations of 0.083% for a barrier of 4.2 kcal mol^{-1}. Conversely, should the errors due to the two spin projection corrections applied to this model be compounded then the barrier suggests that the Boltzman population of the high energy state may be 0.0000003% at 298.15 K. Despite this seemingly low population, the lifetime of these reactive species is likely to be similar to or exceed the 25 ms longevity of the analogous aquated uranyl(VI)-hydroperoxyl radical complex,[143] hence it is feasible that this mechanism may be travelled some proportion of the time to form the peroxide product. Although, of course, identification of a single process with no activation barrier would ultimately be more defensible. Despite this kinetic consideration, assuming a particular complex has enough energy to access the transition state, then the remaining geometric relaxations and deprotonations following the ET are reasonably exergonic, allowing the molecular system at ***M12a-TS*** to tumble downhill towards the thermodynamically stable uranyl(VI)-peroxide complex, ***M9***.

Despite the presence of an activation barrier for this process, the structures of the local minima and the transition state characterised as part of this reaction coordinate hint at one possible explanation for why this particular ligand system may promote the formation of peroxide. Examining the optimised geometries of models ***M12a.1***, ***12a-TS*** and ***12a***, it is clear that the hydroperoxyl radical ligand is not only bound to the uranium atom, but also by the presence of a hydrogen-bond with the α-nitrogen atom of the triazinyl ring of BTPhen, see **Figure 52**. As the ET reaction coordinate in **Figure 52** is followed through, it is clear that there is competition between the bidentate binding mode of the dioxygen ligand and the stabilisation afforded due to the inter-ligand hydrogen bond. The latter necessitating that the dioxygen ligand only binds the uranyl ion in a monodentate fashion. This competition is best exemplified by the structural parameters of the models ***M12a.1***, ***M12a*** and ***M12a-TS*** that represent the ground state uranyl(V)-hydroperoxyl radical complex, the uranyl(VI)-hydroperoxide product of the ET and the TS between these two species, respectively. The energy required for ***M12a.1*** to access the transition state acts to deform the *N-H-O* angle of the hydrogen bonded system. This deformation allows the closer approach of the hydrogen bonded oxygen atom of the hydroperoxyl radical towards the uranyl ion, thereby facilitating the ET that follows.

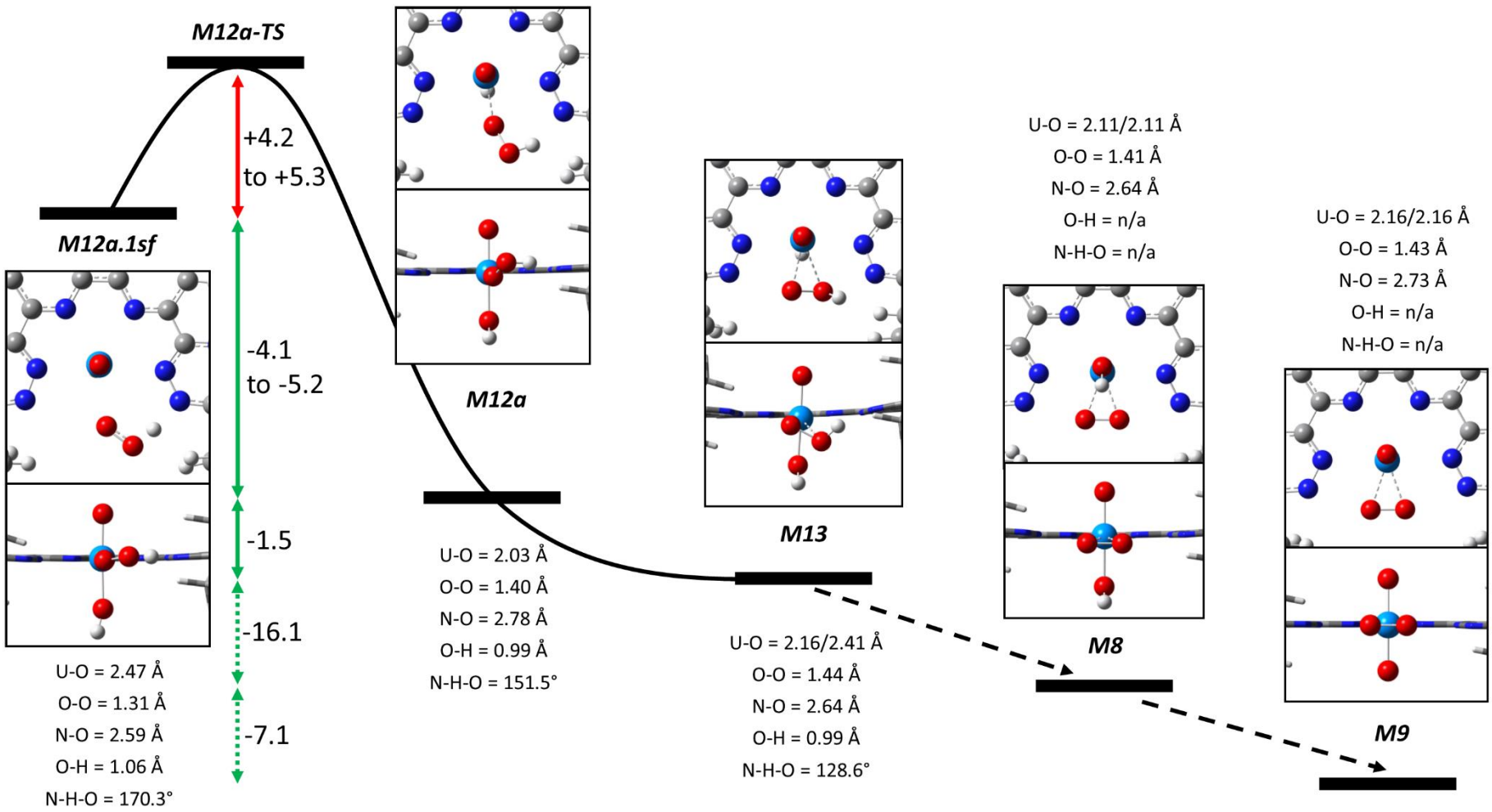

Figure 52: Schematic of the reaction coordinate for the reduction a hydroperoxyl radical by a protonated uranyl(V) species, as described by models ***M12a.1sf***, ***M12a-TS***, ***M12a***, ***M13***, ***M8*** and ***M9***. Along with images of the catalytic site, significant structural parameters are also provided. When quoting these parameters any reference to oxygen refers to the oxygen atoms of the dioxygen unit, not the uranyl oxygen atoms. All ΔG_{solv} reaction energies are presented in kcal mol^{-1}. This schematic is not to scale. No 'spin flip' corrections have been applied to the stated energies, although a correction due to spin contamination has been included.

The transition is best described on viewing the atomic displacements of the single imaginary mode TS. However in place of this, the minimal change of 0.01 Å in all the structural parameters between models ***M12a.1*** and ***M12a-TS,*** except the angle of the hydrogen bond and the *U-O*$_{eq}$ separation, describes the transition adequately, as quantified in **Figure 52**. Following the ET, the strength of the interaction between the uranyl unit and the dioxygen unit increases sharply, as indicated by the very short interatomic separation of the uranium atom and the hydroperoxide unit of 2.03 Å. Such a short interaction necessitates that the hydrogen bond with the ligand is weakened somewhat, as indicated by the tighter *N-H-O* angle, 151.5°, and increased separation of the *N* and *O* hydrogen bonding species, from 2.60 Å to 2.78 Å, as well as the resulting stronger influence of the hydroperoxide anion over the hydrogen atom, as shown by the *O-H* separation decreasing from 1.05 Å to 0.99 Å. Following the ET, there is an exergonic relaxation of the structure of the complex towards a bidentate binding mode of the hydroperoxide, as shown by ***M13***. However, in this geometry the complex is still somewhat conflicted, as shown by the degree with which the hydroperoxide anion twists out of the equatorial plane of the uranyl ion in attempt to maintain a hydrogen bond with the BTPhen ligand. Ultimately, this conflict is resolved following a very favourable deprotonation of the hydroperoxide unit that yields a strongly bidentate complex with something closer to C_s symmetry than C_1, as described by ***M8***. The final step of this process is the same as that described previously and involves only a deprotonation of ***M8*** leading to ***M9***. As previously stated, this transition is also calculated to be favourable at room temperature.

A very rough model of the strength of this hydrogen bond can be provided by calculating the energy change associated with the transfer of the proton on the uranyl ion to the equatorially bound superoxide anion, as modelled by ***M5*** and ***M11***, respectively, **Figure 53**. Whilst the energy resulting from such a comparison technically provides the PT energy and not the strength of the hydrogen bond alone, it is reasonable to assume that the dominant factor influencing the monodentate binding mode observed in ***M11*** over the bidentate mode observed in ***M5*** is the formation of an inter-ligand hydrogen bond.

The data in **Table 24** indicate that unlike the analogous transfer of a proton to dioxygen, the PT from a protonated uranyl(VI) ion to an equatorially bound superoxide anion is a thermodynamically feasible process. Furthermore, the solvated free energy change for the process is reasonably exergonic with a ΔG_{solv} = -9.4 kcal mol^{-1}. Therefore, despite the protonation of the superoxide anion apparently weakening the interaction between the uranyl

ion and the dioxygen species via disruption of the bidentate binding mode, overall the complex is stabilised owing to the formation of a hydrogen bond with the chelating ligand leading to a more stable complex. Such cooperation between ligands surrounding a metal centre is reminiscent of the action of the active sites of enzymes, in which the barrier to proton and electron transfer reactions is often substantially lowered by preorganization of the ligand field in order to favour specific reactions.[107] Furthermore, the observed increased stability of the ***M11*** system relative to ***M5*** suggests that the ET mechanism under study may utilise such proton transfer at some point in the mechanism in order to generate such a protonated dioxygen species. The feasibility of such a process is investigated in Chapter 4.3.2.1.2.

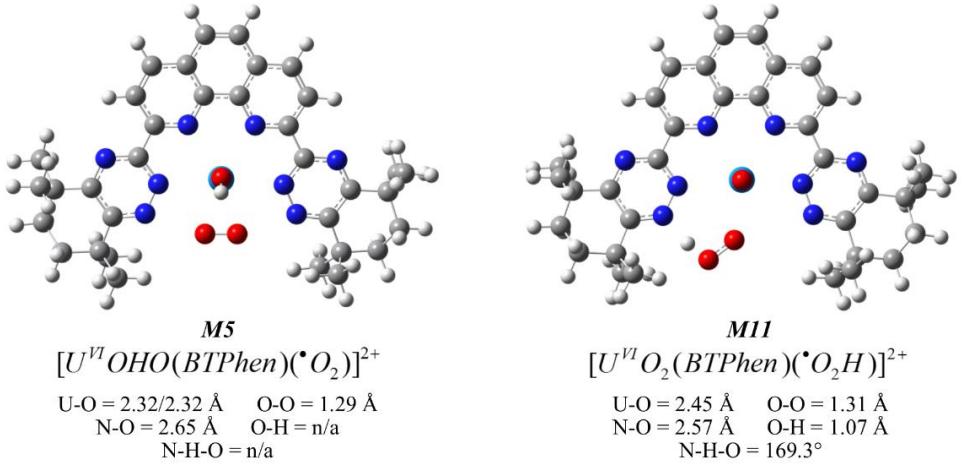

Figure 53: Images, formulae and selected structural parameters of the ***M5*** and ***M11*** optimised complexes. These two structures differ only by the position of the proton, hence their energies can be used to estimate the stabilisation afforded to the system on forming a hydrogen bond between the superoxide species and the BTPhen ligand.

ET from a Non-protonated Uranyl(V) ion to an Equatorially Bound Hydroperoxyl Radical

As observed when modelling previous ET reactions in this study, it is likely that deprotonating the uranyl ion prior to ET would result in a process that is significantly more exergonic than when this species is protonated. To this point, all of the variations in protonation environment have been modelled except the system in which the uranyl ion is not protonated and the bound superoxide species is protonated. This arrangement is likely to be the most energetically favourable owing to the fact that it would benefit from both an increased reduction potential of the uranyl ion and an increased oxidation potential of the superoxide species. In order to verify this, models have been constructed and optimised that represent the ET from a non-protonated uranyl ion to an equatorially bound hydroperoxyl radical.

Table 24: Table of the absolute and calculated reaction energies for the displacement of a proton from an axial oxygen atom of the uranyl ion to the bound superoxide species.[a, b]

Model	E **a**	ZPE_{corr} ***b***	G_{corr} (H_{corr}) ***c***	ΔE_{solv} ***d***	$BSSE_{corr}$ ***e***
M5 -$[U^{VI}OHO(L)(^{\bullet}O_2)]^{2+}$	-1,591,002.0	+435.1	+386.2 (+463.7)	-111.9	+2.7
M11 -$[U^{VI}O_2(L)(^{\bullet}O_2H)]^{2+}$	-1,591,013.9	+436.2	+387.6 (+464.4)	-110.8	+1.6
	ΔE *a*	$\Delta E+ZPE$ *a + b*	ΔG_{gas} (ΔH_{gas}) *a + c*	ΔG_{solv} (ΔH_{solv}) *a + c + d*	$\Delta G_{solv}+BSSE$ $\Delta(H_{solv}+BSSE)$ *a + c + d + e*
$\Delta E =$ ***M11 – M5***	*-11.9*	*-10.8*	*-10.5* *(-11.2)*	*-9.4* *(-10.1)*	*-10.4* *(-11.1)*

[a] All energies are reported in kcal mol^{-1}.
[b] This transition results in a change in the binding mode of the dioxygen species; from a bidentate to a monodentate mode with respect to the uranyl ion, driven by the fact the monodentate mode facilitates the formation of a hydrogen bond between the dioxygen species and the BTPhen ligand.

Prior to ET, this system is best described as a non-protonated uranyl(V)-hydroperoxyl complex, $^{3}[U^{V}O_2(BTPhen)(^{\bullet}O_2H)]^{+}$, ***M12b.1***, and following ET it is best described as a non-protonated uranyl(VI)-hydroperoxide product, $[U^{VI}O_2(BTPhen)(O_2H)]^{+}$, ***M14***. The optimised structures of these models are presented in **Figure 54**.

As in the previous study, it has also been possible to isolate multiple energetic minima on the PES in this study that correspond to different structural states along the reaction coordinate. These structures describe the complex prior to and following ET as well as the geometry of the complex at varying points of structural relaxation and protonation. A schematic of the reaction coordinate followed during this ET is presented in **Figure 55**.

In line with the previous study of the ET from a protonated uranyl(V) ion to a hydroperoxyl radical, many of the geometries optimised as part of this study also exhibited hydrogen bonding interactions within the ligand field, see **Figure 54** for examples. The presence of such interactions thereby suggests that intramolecular hydrogen bonding is also an important stabilising force in the formation of peroxide via this mechanistic route.

As before, it was not possible to identify an optimised geometry of the anti-ferromagnetically coupled ET precursor complex so it has been assumed that the optimised geometry of the ferromagnetically coupled triplet state is a good model of the geometry of the broken symmetry singlet state. As stated previously, such a ‘spin flip’ approximation has been shown to an underestimate the stability of a similar complex by approximately 2.6 to 5.8 kcal mol^{-1}. Therefore, this uncertainty must be considered when calculating the

energetics of the transitions. Following the convention defined previously, the broken spin symmetry energy calculated in this way will be designated ***M12b.1sf***, representing the $^{1}[U^{V}O_2(BTPhen)(^{\bullet}O_2H)]^{+}$ complex.

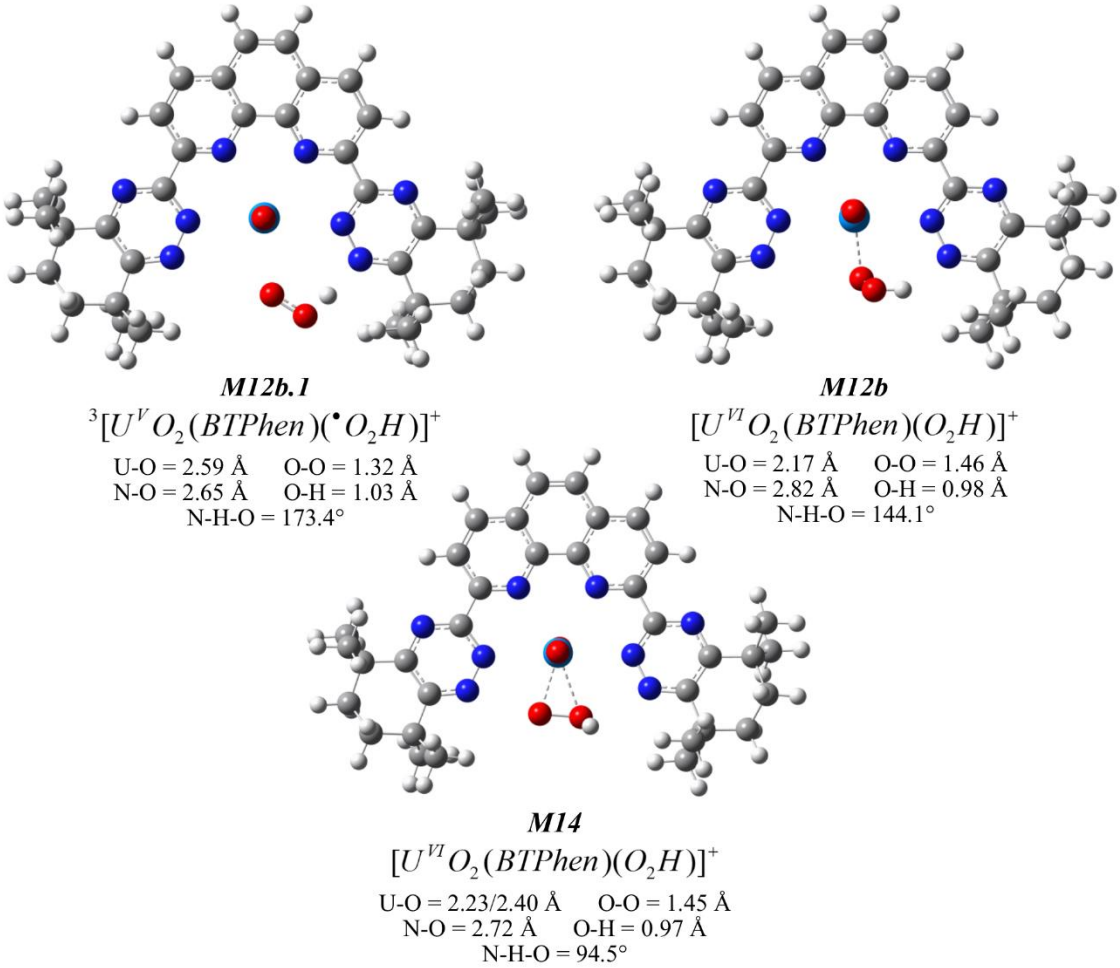

Figure 54: Images, formulae and selected structural parameters of the ***M12b.1***, ***M12b*** and ***M14*** optimised complexes. These models describe the ET from a deprotonated *U(V)* complex to a hydroperoxyl radical.

The energetics calculated for the ET from a non-protonated uranyl(V) ion to an equatorially bound hydroperoxyl radical and the deprotonation reactions that precede and follow it are presented in **Table 25** as well as in the reaction schematic in **Figure 55**.

$$^{1}[U^{V}OHO(L)(^{\bullet}O_2H)]^{2+} + H_2O \longrightarrow {}^{1}[U^{V}O_2(L)(^{\bullet}O_2H)]^{+} + H_3O^{+} \quad \textbf{(71)}$$

$$^{1}[U^{V}O_2(L)(^{\bullet}O_2H)]^{+} \longrightarrow [U^{VI}O_2(L)(O_2H)]^{+} \quad \textbf{(72)}$$

$$[U^{VI}O_2(L)(O_2H)]^{+} \xrightarrow{reorg} [U^{VI}O_2(L)(O_2H)]^{+} \quad \textbf{(73)}$$

$$[U^{VI}O_2(L)(O_2H)]^{+} + H_2O \longrightarrow [U^{VI}O_2(L)(O_2)] + H_3O^{+} \quad \textbf{(74)}$$

Table 25: Table of the reaction energies calculated for the ET from a deprotonated uranyl(V) ion to a hydroperoxyl radical and the surrounding deprotonation reactions.[a]

Reaction	Equation No.	ΔG_{gas} (ΔH_{gas})	ΔG_{solv} (ΔH_{solv})	ΔG_{solv}+ sf_{corr} $\Delta(H_{solv}+sf_{corr})$ +*BSSE*
M12a.1sf - M12b.1sf	71	-48.8 to -54.1 (-48.9 to -54.2)	-15.0 to -20.3 (-15.1 to -20.4)	-12.5 to -24.1 (-12.6 to -24.2)
M12b.1sf - M12b	72	-17.1 to -21.3 (-22.5 to -18.3)	-16.3 to -20.5 (-17.6 to -21.8)	-8.0 to -11.2 (-9.3 to -12.5)
M12b - M14	73	-3.7 (-4.3)	-2.2 (-2.7)	-3.2 (-3.7)
M14 - M9	74	+42.2 (+43.3)	+8.8 (+9.9)	+8.7 (+9.8)

[a] All energies are presented in kcal mol^{-1}.

On comparing the energies presented in **Figure 55** and **Table 25**, it can be seen that, as predicted, deprotonating the uranyl unit prior to ET results in a process that is much more exergonic than those quantified previously. Furthermore, despite best efforts testing multiple starting geometries, it was not possible to identify a TS for this ET. This lack of evidence, whilst not positive affirmation that there is no barrier for this ET, is the best confirmation of such achievable without mapping the whole PES at great computational cost.

The reaction coordinate in **Figure 55** is broadly described by **Equations 71-74**, above. The starting point of this reaction is ***M12a.1sf***, which represents the open shell singlet state of the protonated uranyl(V)-hydroperoxyl complex. Described by **Equation 71**, traversing this reaction coordinate, the uranyl ion is initially deprotonated on approach of a molecule of solvent to generate ***M12b.1sf***. This has been calculated to be an exergonic process with ΔG_{solv} = -15.0 to -20.3 kcal mol^{-1}. Following generation of the ET precursor complex, ***M12b.1sf***, ET occurs generating ***M12b***, a structurally excited state of the uranyl(VI)-hydroperoxide complex. This reaction, described by **Equation 72**, is found to be strongly exergonic with ΔG_{solv} = -16.3 to -20.5 kcal mol^{-1}. At this point in the mechanism, the hydroperoxide anion formed binds the uranyl ion in a monodentate fashion. However, the bidentate binding mode is predicted to be 2.2 kcal mol^{-1} lower in energy than the monodentate mode and hence it is reasonable to assume that structural reorganisation occurs to generate the ground state structure of this complex, ***M14***. The final step in this mechanism to generate the non-protonated uranyl(VI)-superoxide complex, ***M9***, is the deprotonation of the hydroperoxide anion.

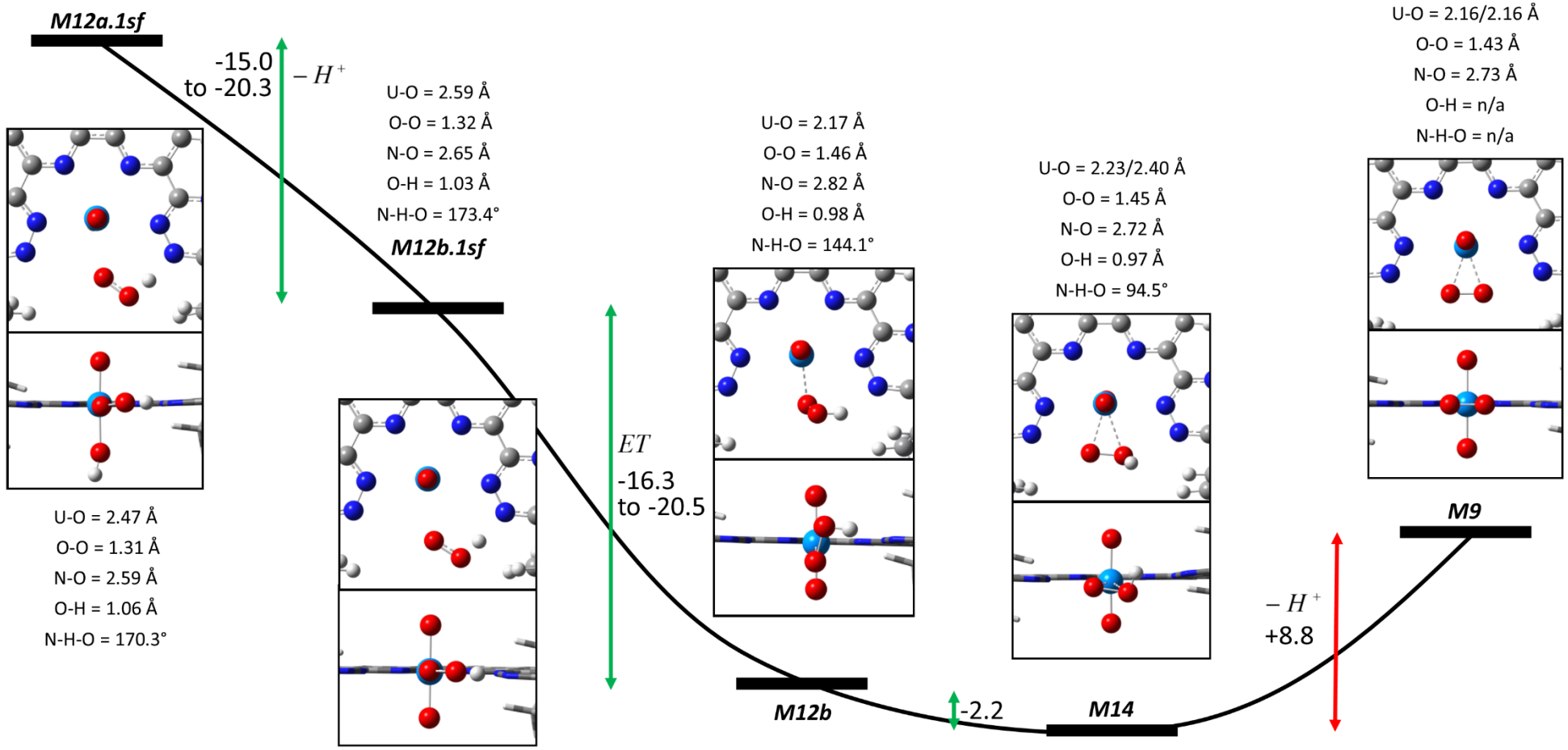

Figure 55: Schematic of the reaction coordinate for the reduction a hydroperoxyl radical by a deprotonated uranyl(V) species, as described by models ***M12a.1sf***, ***M12b.1sf***, ***M12b***, ***M14*** and ***M9***. Along with images of the active catalytic site, significant structural parameters are also provided. When quoting these parameters, any reference to oxygen refers to the oxygen atoms of the dioxygen unit, not the uranyl oxygen atoms. All ΔG_{solv} reaction energies are presented in kcal mol^{-1}. This schematic is not to scale.

However, in contrast to the corresponding hydroperoxide deprotonation occurring once bound to a protonated uranyl(VI) ion, as modelled previously by the transition from ***M13*** to ***M8***, the deprotonation when bound to a non-protonated uranyl(VI) ion is calculated to be an unspontaneous process at RT with ΔG_{solv} = +8.8 kcal mol^{-1}. This suggests that should the mechanism follow this route towards the deprotonated bisuranyl peroxide bridged complex observed crystallographically, then an additional stimulus may be required to displace the proton. Such a stimulus may be provided by the approach of the second uranyl ion on the uranyl(VI)-hydroperoxide complex. The feasibility of such processes are considered in Chapter 4.3.5.

A Summary of the Chemistry Surrounding the Second ET

Following a study of how the feasibility of the ET reaction is affected by the state of protonation of the uranyl(V) ion and the equatorially bound superoxide species, it has been possible to construct a hierarchy of protonation states that are conducive, or not, to ET. The most exergonic process with ΔG_{solv} = -16.3 to -20.5 kcal mol^{-1} was observed when an electron was transferred from a non-protonated uranyl(V) ion to an equatorially bound hydroperoxyl radical. This process was found to be over 10 kcal mol^{-1} more exergonic than the next most energetic process: the ET from a protonated uranyl(V) species to a hydroperoxyl radical, for which a ΔG_{solv} = -4.1 to -5.2 kcal mol^{-1} was predicted. This process was found to have a minimum barrier to activation of +4.4 kcal mol^{-1}, which assuming Boltzmann statistics, suggests that only 0.08% of the species present at RT possess enough energy to overcome this barrier. Despite being a proportion of less than 1/1000, this barrier does not represent a significant constraint to the proposed mechanistic scheme considering that the experimental timescale required to elapse before a uranyl peroxide complex could be observed in solution was a period of days as opposed to minutes. The next state of protonation in the feasibility hierarchy is represented by the ET from a protonated uranyl(V) ion to an equatorially bound superoxide anion. This process was found to be essentially thermodynamically neutral, with ΔG_{solv} = +0.5 to +3.6 kcal mol^{-1}. The ΔH_{solv} for this reaction was marginally negative with a value of -0.6 to +2.5 kcal mol^{-1}. Thereby suggesting that whilst this ET may be a mildly exothermic process leading to a more stable complex, entropic factors, resulting from the fact that the bidentate system formed is more ordered than the monodentate bound precursor, may be great enough to make this process mildly endergonic.

The final ET studied in this section was from a non-protonated uranyl(V) ion to an equatorially bound superoxide anion. Despite the ΔG_{solv} for this reaction being calculated to

be exergonic (ΔG_{solv} = -15.5 kcal mol^{-1}), the applicability of this model to fit within the mechanism proposed was discounted owing to the fact that in the ground energy state identified for the ET precursor complex, ***M16***, the BTPhen ligand was reduced as opposed to the uranyl ion. Should such a reduction occur empirically then it is likely that ligand degradation products would be observed as the reaction progressed. This was not the case when analysing the solutions using proton NMR over the course of months. In order to probe the accessibility of this state computationally, the feasibility of the deprotonation reaction that generates the complex ***M16*** from the protonated uranyl(V)-superoxide complex, ***M7***, was quantified. The theoretical model indicated that this deprotonation reaction was unfeasible with ΔG_{solv} = +8.9 to +12.04 kcal mol^{-1}, therefore it is reasonable to assume that in the proposed mechanism very little of the energy associated with the reductive uranyl(V) species is dissipated by reduction of the BTPhen ligand.

Thus, three of the four candidate reactions studied in this chapter have been identified as reasonable routes that the mechanism could follow from a singly reduced dioxygen species, superoxide, to the doubly reduced product, peroxide. A strong dependence of the feasibility of the ET reaction on the state of protonation of the uranyl and dioxygen species was observed. This dependence favoured ET from a deprotonated uranyl unit to a protonated dioxygen species. In this way, the proton can be seen as a device to stabilise the excess charge on a reduced species. The greatest effect was observed when the proton was localised on the dioxygen unit. Considering this observation, it is likely that any intramolecular interaction that acts to promote protonation of the dioxygen unit would likely lead to a more thermodynamically and possibly also kinetically feasible process of forming peroxide from dioxygen due to the increase in effective concentration of the electron acceptor at the active site. One such interaction was observed in the $[UO_2(BTPhen)(^{\bullet}O_2H)]^{n+}$ type complexes studied in this chapter. Within these species, a hydrogen bond was seen to form between the protonated dioxygen unit and an appropriately located α-nitrogen atom on the triazinyl ring of BTPhen. It is proposed that the formation of such intramolecular hydrogen bonds may act to stabilise the uranyl-hydroperoxyl radical complex and thus significantly hinder the rate of disproportionation of reactive dioxygen species, which would otherwise detrimentally impact the kinetic feasibility of the proposed mechanism.

A schematic of the ET and selected deprotonation reactions and their corresponding reaction free energy and enthalpy changes as modelled in this chapter is presented in **Figure 56**. As with the mechanistic web presented that relates to the initial ET, the sign of the energies presented in this diagram relate to the directions of the reactions as read from top to bottom.

The starting point in this flow chart may be either ***M6*** or ***M11***. The models are the non-protonated uranyl(VI)-superoxide and non-protonated uranyl(VI)-hydroperoxyl radical complexes, respectively. The end point of this mechanistic web is the non-protonated uranyl(VI)-peroxide dianion complex, ***M9***. Between these points all of the reactions discussed in this chapter have been included with the exception of one. This is the deprotonation of the hydroperoxide anion in the protonated uranyl(VI)-hydroperoxide complex, ***M13***, to give ***M14***. This transition has not been discussed in the main body of text as it provides no information to the study in excess of that already discussed. It has been included in **Figure 56**, below, for the sake of completeness.

4.3.3 Deprotonation, Dissociation and Proton Transfers

As detailed in the previous chapter, the effect of protonation on the redox potentials of the species involved in the ET is huge. However, until now, this study has given little consideration to the feasibility of the acid-base reactions that lead to these protonated species. Such is the purpose of this chapter.

When modelling acid-base reactions, consideration of the effects of solvation are imperative. In the study of the water clusters described in Appendix 2, it was confirmed that, provided a minimum number of water molecules have been described explicitly, the solvation energy of the proton could be replicated with < 3 kcal mol^{-1} accuracy using the same level of theory as applied to study the larger uranyl complexes. This methodology was subsequently extended to calculate the solvated enthalpies and free energies of the remaining small molecules of consequence to this study, such as H_2O, $^{\bullet}O_2^-$ and $HO_2^{\bullet}$.

During discussion of the initial ET to triplet dioxygen in Chapter 4.3.2.1.2, the prospect of protonating the dioxygen species in order to promote ET was considered. However, on optimising such a complex (***M17*** as detailed in **Figure 47**, Chapter 4.3.2.1.2) it was found that rather than forming an intramolecular hydrogen bond with the ligand, as observed when a hydroperoxyl radical was the hydrogen donor, the protonated dioxygen species favoured forming a hydrogen bond with an oxygen atom on the uranyl ion. Furthermore, the energy of this complex was calculated to be 43 kcal mol^{-1} higher in energy than the ground state protonated uranyl complex, modelled by ***M4.1***. This thereby suggested that the proton transfer between these species was thermodynamically unfavourable, thus any hypothetical increase in the favourability of the ET reaction that followed would be precluded since it is not likely that the system would be able to access the required precursor state. A similar constraint was also observed for the reduction of the BTPhen ligand by a deprotonated uranyl(V)-superoxide complex, as modelled by ***M16***.

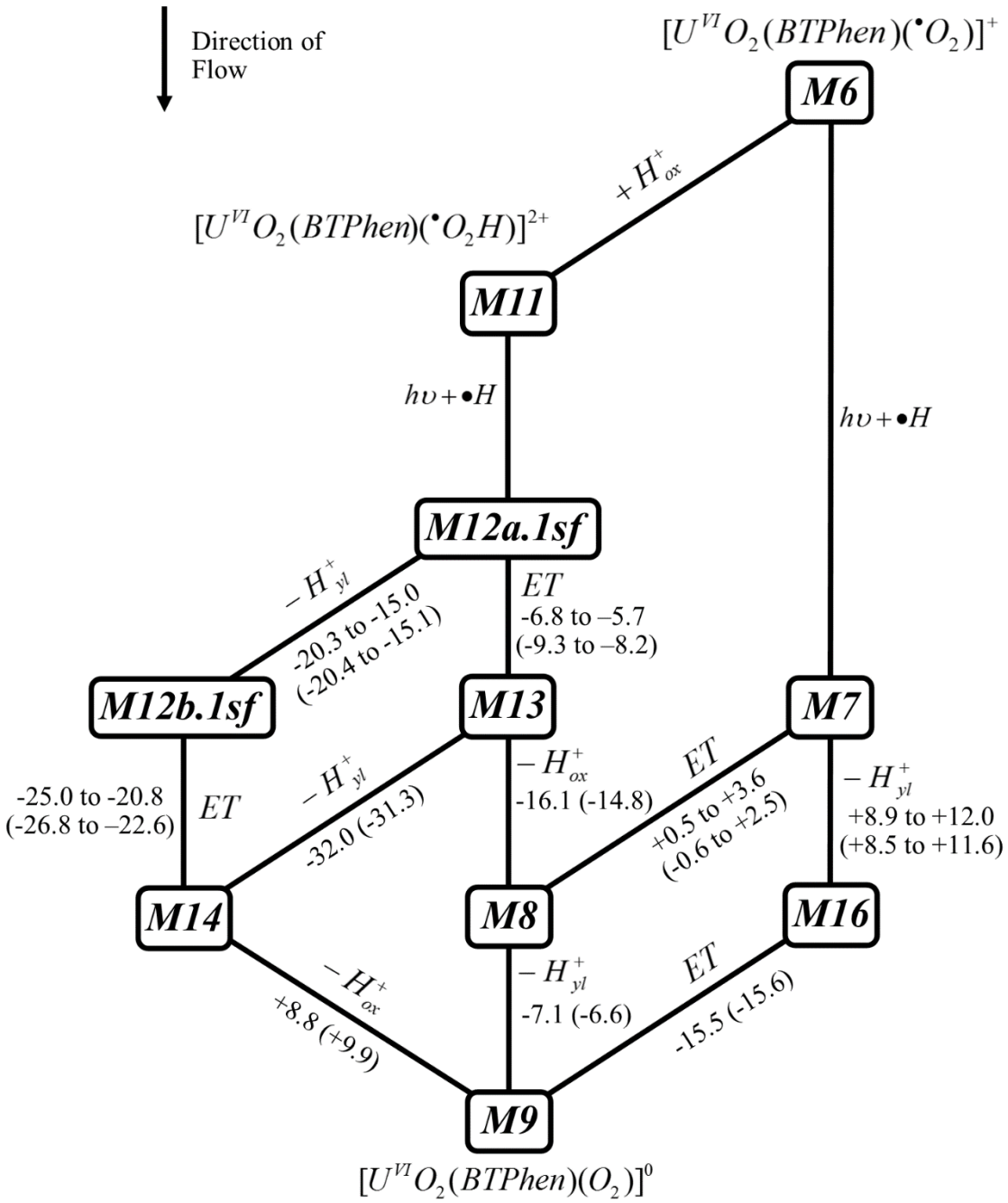

Figure 56: Mechanistic web schematic of the reactions relevant to the second IS-ET process in which superoxide is reduced to peroxide. The boxed numbers refer to the model representative of that state, which is detailed in the text. The models selected for inclusion in this schematic are those that do not violate the spin selection rule. Hence, the energies of the ***M12a.1sf*** and ***M12b.1sf*** have been used in this schematic since they are the best estimates of the ground state anti-ferromagnetically coupled complexes identified in this study. Each line connecting two models represents a reaction occurring. These lines are labelled with the calculated free energy (and enthalpy in parentheses) change for that process and a description of the reaction that has occurred. Where *ET* represents an electron transfer; *+/-H_{ox}* represents the addition or abstraction of a proton from the dioxygen unit; *+/-H_{yl}* represents the addition or abstraction of a proton from the uranyl ion and '*hν+·H*' represents the photoexcitation of the uranyl(VI) ion in the corresponding complex and the quenching of this excited state via hydrogen atom abstraction from the solvent to generate a protonated uranyl(V) species. All energies are reported in kcal mol^{-1} and solvation corrections have been applied in all cases. No BSSE or '*sf*' corrections have been applied to the values presented. The sign of the energy changes presented applies for reactions as they flow from the top of the schematic at ***M6*** to the bottom at ***M9***.

In order to confirm whether the most exergonic ET reactions described in Chapter 4.3.2 are similarly precluded from a role in the mechanism as a whole, it is essential to model the protonation and deprotonation reactions that generate the precursor species. The importance of the following study is given considerable weight when it is considered that the only two strongly exergonic processes identified by this study for the second ET step require an equatorially bound hydroperoxyl radical species. Hence, should either of these electron transfers play a role in the mechanism to form peroxide then it must first be shown that it is thermodynamically favourable to form a hydroperoxyl radical in this system.

4.3.3.1 Concerning the Effect of Explicit Solvation on the Acidity of the Uranyl Ion

In general, the dipolar and hydrogen bonding nature of protonated oxygen species allows them to interact strongly with polar solvents in a directional manner that stabilises them more than would be possible through a purely electrostatic screening of charge. Such interactions are able to significantly alter the stability of a complex. Hence, in order to construct computational models that are comparable with solution phase empirical studies, it is often necessary to include explicit water molecules in the model in order to account for these specific solute-solvent interactions with vulnerable residues. In this study, two such moieties are present in the models; the uranyl ion itself and the equatorially bound dioxygen species. Both these species exist in various oxidation and protonation states throughout the mechanism, thus it is reasonable to suspect that each of these states may interact differently with the surrounding solvent. Such differences may be non-trivial and could subvert the course of the reaction mechanism from that determined using only gas phase models, thereby possibly providing results that are largely incomparable with experiment. To this end, it is important to gauge the impact of explicit solvation on the most susceptible residues of the models presented. This is conducted in order to model the change in energy and structure associated with these specific solvent-solute interactions and subsequently infer the effect that solvation has on the reaction mechanism beyond the CPCM model.

Of the two problematic residues present in the models studied, it is fortunate that the dioxygen species in each inherently benefits from a considerable degree of explicit solvation by the presence of the BTPhen ligand. This ligand is not only able to preclude the approach of additional solvent molecules that might interact with the dioxygen ligand via steric means, but, as observed in ***M11***, it is also able to act as a hydrogen bond acceptor to a protonated bound dioxygen species. In this way, the chelating BTPhen ligand is able to account for many of the possible explicit interactions between the dioxygen species and the external solvent field intrinsically. Unfortunately, the oxygen atoms of the uranyl ion do not benefit

from such an effect, as they lie perpendicular to the equatorial ligand plane and are thus exposed and available to interact with solvent.

As discussed in Chapter 2, multiple previous computational studies of the hydration of the uranyl ion have shown that the degree of interaction between the uranyl ion and the solvent depends largely on the oxidation state of the metal ion. Specifically, these studies suggest that the oxygen atoms of the uranyl(VI) ion are essentially inert with respect to forming hydrogen bonds with the solvent.[79,198] However, this is in contrast to the uranyl(V) ion, which favours forming three such interactions split across the two uranyl oxygen atoms.[25,79] The increased propensity for the uranyl(V) ion to interact with the solvent in this way is consistently attributed to the increased negative charge localised on the oxygen atoms in this species relative to the *U(VI)* analogue.[25] Despite this interest in the naked uranyl ions, the analogous solvation of the protonated species has yet to be studied by the scientific community at large. This is likely to be due to the fact that the oxygen atoms of the uranyl ion have, until recently, been considered essentially inert. However, interest in axial functionalisation of uranyl ions has peaked over the past few years, driven by the identification of the stable *U(V)* 'Pacman' complex by Arnold et al.[156] and the relative ease with which this species undergoes reaction at the axial oxygen atom. As part of their studies, Arnold et al. have characterised a protonated uranyl(V) species using IR and proton NMR spectroscopies. The differing electronic structure of the protonated uranyl(V) ion relative to its non-protonated *U(VI)* analogue is exemplified by the large difference between the asymmetric stretching frequencies of the Pacman bound species, found to be ν_3 = 765 cm^{-1} and ν_3 = 908 cm^{-1}, for the protonated *U(V)* and non-protonated *U(VI)* complexes respectively.[156] It is of interest to note at this point that no such protonated *U(VI)* species have been characterised to date. In addition to this recent empirical interest, the protonated uranyl ion has also been implemented in multiple computational mechanistic studies over the last decade. Often it is invoked in order to explain some of the poorly understood chemistry of the uranyl ion, including the disproportionation of *U(V)*[194] and the mechanism of exchange of equatorial and axial –yl oxygen atoms in basic aqueous media.[199,200] Such an awakening to the importance of the protonated uranyl ion as a pivotal intermediate species in many emerging areas of uranium chemistry suggests that it is a species that certainly warrants further enquiry.

In the mechanism under study, the protonated uranyl ion is formed by a hydrogen atom abstraction from the methanol solvent. This leads initially to a protonated *U(V)* species, but there is a finite probability that this species could be oxidised by an equatorially bound

dioxygen species, generating a protonated *U(VI)* species in the process. In Chapter 4.3.2.1.2, the free energy change for the ET from a protonated uranyl(V) ion to an equatorially bound dioxygen ligand was modelled, along with the non-protonated analogue of this process. The latter was calculated to be a much more exergonic process than the former. Hence, in order to infer which path the peroxide forming mechanism is most likely to follow, it is pertinent at this point to attempt to elucidate the proton affinity (PA) of the uranyl ion when in the accessible +5 and +6 oxidation states and thus whether in the global mechanistic scheme to form peroxide the uranyl ions are likely to deprotonate prior to or following ET.

Computational Details

In order to gauge the affinity of the uranyl(V) and (VI) ions to bind protons, two models based around the structure of the $[UOHO(BTPhen)H_2O]^{n+}$ complex were constructed: the first contained the uranyl ion in its +6 oxidation state and the second, the +5 oxidation state. These models were treated in the gas phase using the uB3LYP/B1 level of theory described in Chapter 2.2 for geometry optimisations and subsequent frequency calculations. Gas phase and CPCM solvated SP calculations were carried out at the gas phase optimised geometries using the uB3LYP/B2 level in order to generate the desired energetic and population analyses. The optimised geometries of the protonated *U(V)* and *U(VI)* states of the $[UOHO(BTPhen)H_2O]^{n+}$ structures, ***M2*** and ***M1b*** are presented in **Figure 57**, along with the deprotonated analogues of these structures, ***M2b*** and ***M1***, respectively. The SP energies calculated for these models were corrected for the effects of temperature and pressure using the thermochemical analysis performed during the frequency calculation, as described in Chapter 2.5. The appropriately corrected energies were then used in conjunction with the free energy of the solvated proton, calculated as described in Appendix 2, to calculate the free energy of deprotonation for each of the *U(V)* and *U(VI)* species.

Results and Discussion

Implicitly Solvated Models

Analysis of B2 energies for the models ***M1b*** and ***M1*** allowed the free energy of deprotonation of the uranyl(VI) species, $[UOHO(BTPhen)H_2O]^{3+}$, to be calculated. The ΔG_{solv} for this reaction is found to be -52.7 kcal mol^{-1}. Utilising models ***M2*** and ***M2b***, the analogous process for the uranyl(V) analogue, $[UOHO(BTPhen)H_2O]^{2+}$, was also be calculated. The ΔG_{solv} for this deprotonation is also found to be favourable, albeit considerably less exergonic than the analogous deprotonation of the uranyl(VI) ion, with a

ΔG_{solv} of -9.3 kcal mol^{-1}. This difference suggests that the affinity of the uranyl(V) ion for the axially bound proton is considerably greater than that of the uranyl(VI) ion.

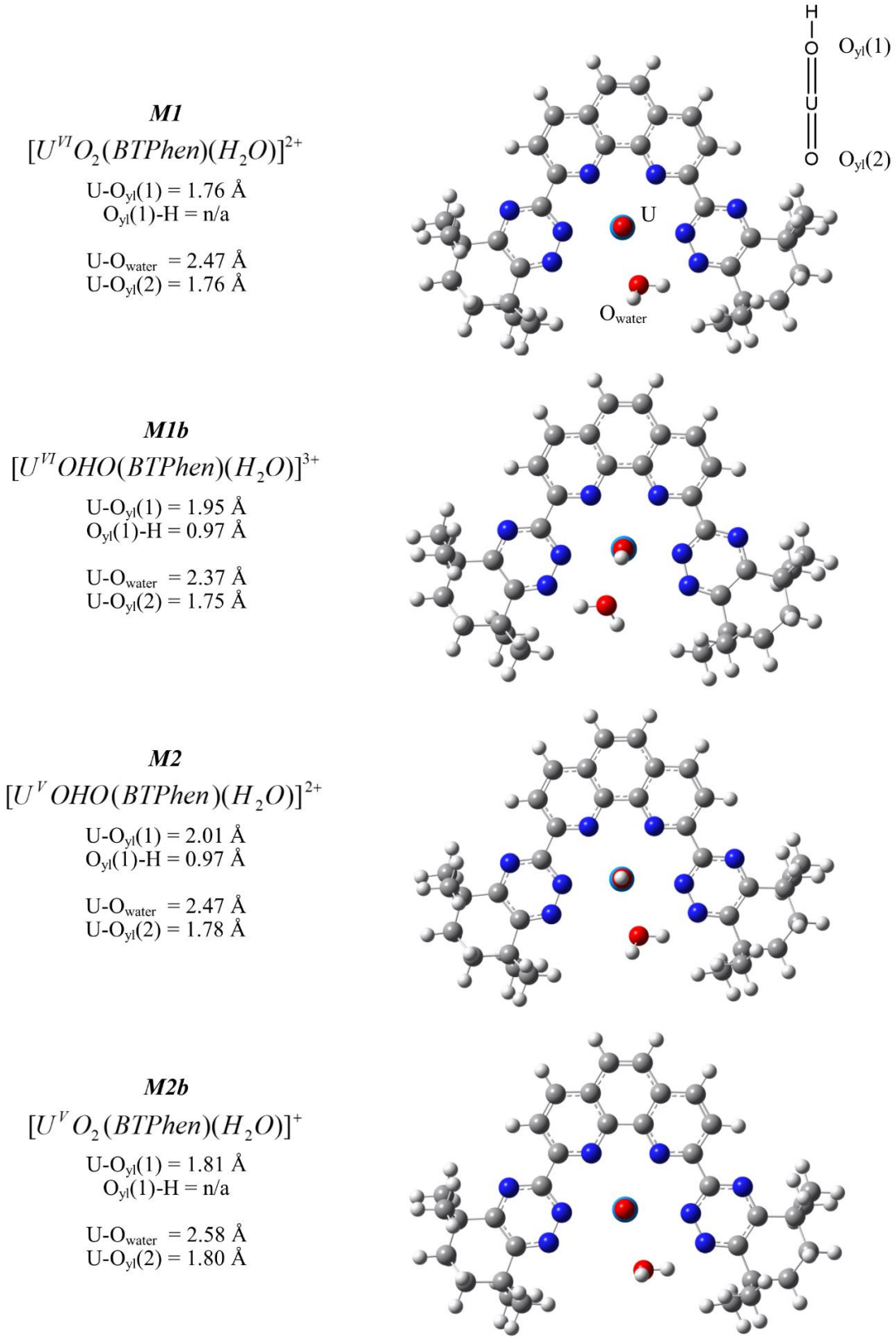

Figure 57: Gas phase optimised structures of models with the generic formula *[UO$_2$(BTPhen)H$_2$O]$^{n+}$* and its protonated analogue *[UOHO(BTPhen)H$_2$O]$^{x+}$*, where *n* = 1, 2 and *x* = 2, 3 representing the +5 and +6 oxidation states of the uranium atom, respectively. Selected structural parameters are presented alongside an elemental formula and the designation of each model.

This observation compares well with studies conducted by others on the solvation of uranyl(V) and uranyl(VI) ions,[79,201] in which the uranyl(V) ion has been found to form stronger hydrogen bonding interactions with the surrounding solvent than the uranyl(VI) ion. This difference is typically attributed to the increased negative charge localised on the *–yl* oxygen atoms (O_{yl}) of the uranyl(V) species resulting in a greater electrostatic interaction with the solvent. This trend of greater localised charge on the O_{yl} atoms in the *U(V)* species relative to *U(VI)* is echoed by the NBO charges presented in **Table 26**. Despite this similarity, whereas a greater O_{yl} based negative charge increases the degree of interaction between naked uranyl ions and the solvent, when the uranyl ion is protonated a greater charge on O_{yl} results in the deprotonation energy of the species becomes significantly less exergonic. This trend corresponds to an increased PA of the uranyl(V) ion relative to its uranyl(VI) analogue due to the stronger electrostatic interaction between O_{yl} and the proton when the uranium atom is in its +5 state.

Table 26: Electronic charges (NBO) centred on the uranium and O_{yl} atoms of the protonated and naked uranyl(V) and (VI) species when bound by BTPhen and water.[a]

Uranyl Species	Model	*An*	O_{yl}[b]	O_{yl}*-(H)*
$U^{V}O_2^{+}$	***M2b***	1.46	-0.71	
$U^{VI}O_2^{2+}$	***M1***	1.66	-0.52	
$U^{V}OHO^{2+}$	***M2***	1.63	-0.63	-0.81
$U^{VI}OHO^{3+}$	***M1b***	1.65	-0.42	-0.66

[a] Optimised structures of the models can be found in **Figure 57**.
[b] The charges presented are the mean charges calculated for models ***M2b*** and ***M1*** in which the O_{yl} atoms are equivalent. For models ***M2*** and ***M1b***, the O_{yl} atoms are not equivalent due to the fact one is protonated. Thus, the charge on the non-protonated oxygen is presented in the column O_{yl}, whilst the charge on the protonated oxygen is presented in column O_{yl}*-(H)*.

Accounting for the Effects of Explicit Solvation

As discussed earlier, when modelling such acid-base reactions appropriate treatment of solvation is essential in order to generate a reasonable model of a system. Typically, such a treatment requires explicit consideration of certain specific solvent-solute interactions. In order to gauge the effect of including explicit solvation on the deprotonation reactions of the uranyl ions, two additional models were generated. These were the *U(V)* and *U(VI)* analogues of a $[UOHO(BTPhen)H_2O]^{n+}$ (where n = 1, 2) complex, to which an additional molecule of water was added in a position suitable to accept a hydrogen bond from the proton on the uranyl ion. The optimised geometries of these '***M2*** + H_2O' and '***M1b*** + H_2O' complexes are presented in **Figure 58**. As described in the computational details section (Chapter 2.2), these optimisations were also carried out at the uB3LYP/B1 level of theory.

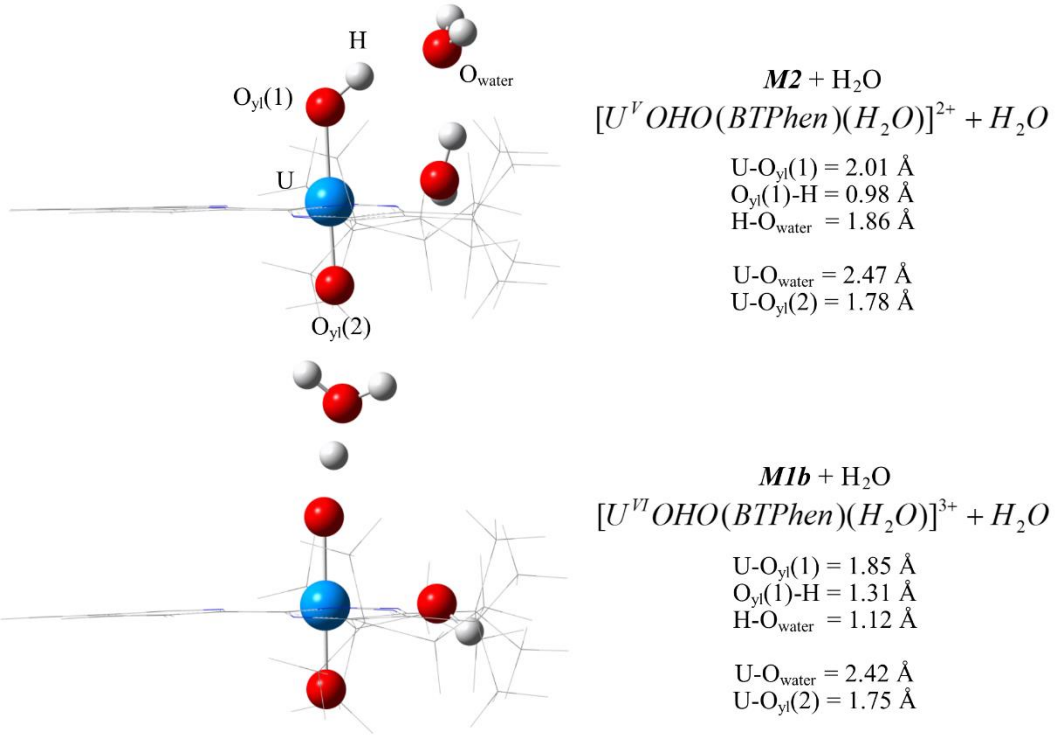

Figure 58: Gas phase optimised structures of the *[UOHO(BTPhen)H₂O]$^{n+}$ + H₂O* models, where *n*=2 represents the uranyl(V) model, ***M2 + H₂O***, and *n*=3 represents the uranyl(VI) model, ***M1b + H₂O***. Selected geometric parameters describing the hydrogen bonding interactions are provided in order to allow comparison to the corresponding structural parameters in the absence of the explicit water molecule presented in **Figure 57**.

Studying these gas phase optimised geometries, it is apparent that the *UOHO*$^{2+}$ and *UOHO*$^{3+}$ ions behave very differently in the presence of the additional molecule of water. Analysing the '***M2*** + *H₂O*' complex first, which represents the *U(V)* state, it is clear that the optimised geometry of the complex is relatively unaffected by the introduction of an additional water molecule. The only significant difference lies in the angle of the *U-O$_{yl}$-H* unit, which favours bending in the '***M2*** + *H₂O*' model due to the formation of a hydrogen bond between the protonated uranyl ion and the solvating *H₂O*. This is in contrast to the *U(VI)* analogue, modelled by '***M1b*** + *H₂O*', in which the minimum energy structure describes the water molecule acting as a Brønsted base, deprotonating the uranyl(VI) ion and generating a hydroxonium ion without a barrier to activation.

4.3.3.1.1 Uranyl Deprotonation: Relaxed PES Scan

In order to observe whether the uranyl(VI) deprotonation reaction is indeed a barrierless process as implied by the unconstrained geometry optimisations, a relaxed PES scan was carried out in which the distance between the disputed hydrogen atom and the oxygen atom of the approaching water molecule was constrained and incremented in order to provide a cross section of the PES for this reaction coordinate.

Computational Details

The following scans were conducted between constrained *H-O*$_{water}$ distances of 4.28 Å and 1.08 Å, in steps of 0.2 Å or 0.1 Å when greater detail was required. The relaxed PES scans were carried out at the uB3LYP/B1 level of theory. As described previously, acidic protons (i.e. those bound to oxygen atoms) or those involved in specific hydrogen bonding interactions were treated using a 6-311++G(d,p) basis. The energies obtained from this scan are presented without thermodynamic corrections. Hence, these energies are not directly comparable to the thermodynamically corrected energies for the deprotonation reactions calculated at the B2 level, presented in Chapter 4.3.3.1.2. The scan was carried out in order to determine whether there exists a barrier to the deprotonation process and not the accurate height of such a barrier, hence this incomparability between the energies is of little concern. Despite this, these energetics are comparable to calculations conducted at the same level of theory. Unless stated otherwise, this means that the electronic energy changes calculated in the PES scan are comparable to all other PES scans presented in this work.

Results and Discussion

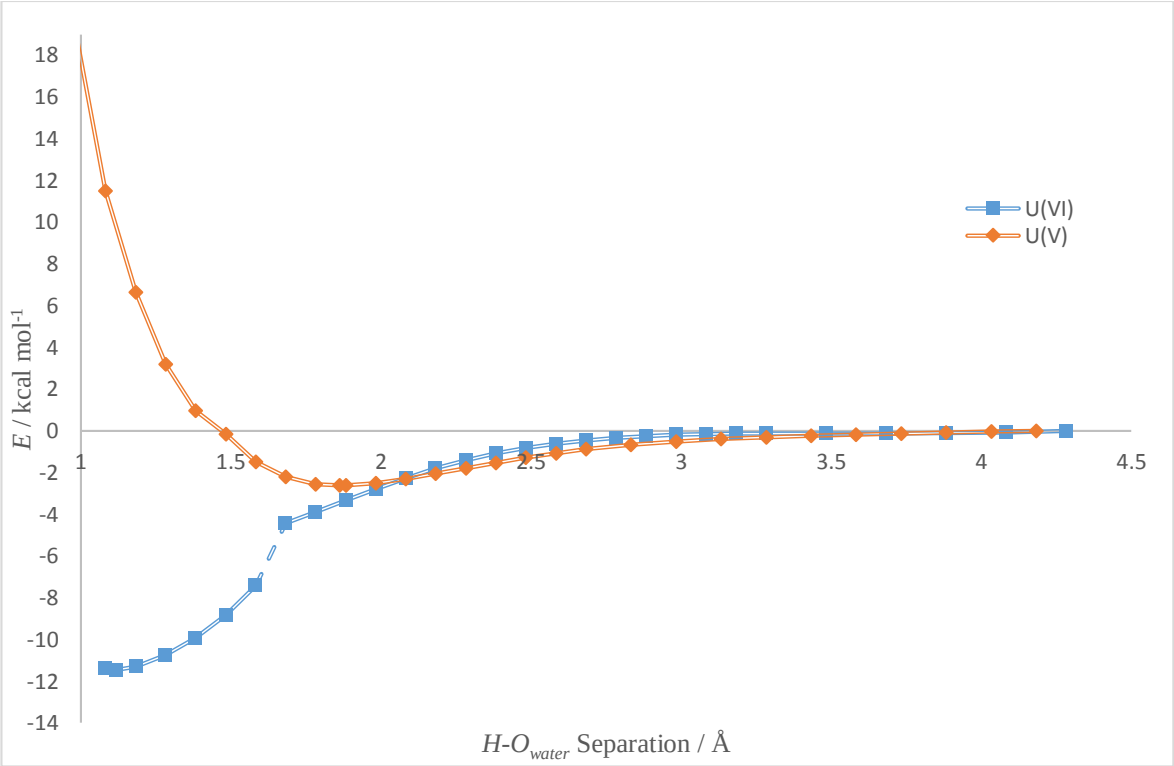

Figure 59: Overlaid PES cross-sections describing the deprotonation of the uranyl(V) and uranyl(VI) ions in complexes of the type *[UOHO(BTPhen)H$_2$O]$^{n+}$*, where n = +2/+3, by a solvating water molecule.

Figure 59 details the result of the relaxed PES scan for the deprotonation of the protonated uranyl(V) and uranyl(VI) species. First of all, examining the cross-section of the uranyl(V) PES, as the water molecule approaches the protonated uranyl(V) from a distance of over 4 Å to a distance of 1.86 Å, there is a gradual decrease in the total energy of the system. This

stabilisation is afforded via the formation of a hydrogen bond between the protonated uranyl(V) ion and the solvating water molecule. At a separation of 1.86 Å the PES reaches a stationary point that corresponds to the equilibrium geometry of the complex as identified by the unconstrained geometry optimisation of the '***M2*** + H_2O' complex, see **Figure 58**, above. However, at shorter separations between the proton and the solvating water molecule there is a sharp increase in the energy of the system, indicating a substantial barrier to the deprotonation of the $U^{V}OHO^{2+}$ ion.

Analysing the second PES cross-section identified for the uranyl(VI) ion, at distances > 2.08 Å the two surfaces behave similarly, exhibiting a gradual decrease in the total energy of the system with decreasing separation due to the formation of a stabilising hydrogen bonding interaction. However, this is where the similarity ends, since following the formation of this hydrogen bonded species the system undergoes a sharp barrierless transition to a deprotonated UO_2^{2+} and hydroxonium ion system that lies 11.5 kcal mol^{-1} lower in energy than the hydrogen bonded system. A small discontinuity in the relaxed PES surface is observed between constrained bond distances of 1.58 Å and 1.68 Å. This discontinuity corresponds to the most stable geometry of the system transitioning from an arrangement in which the solvating water molecule is hydrogen bonded to both the O_{yl} atom and the water molecule in the primary coordination sphere, into a system in which the solvating species only interacts with the uranyl ion, see the differences in **Figure 58**, above.

Summary

Despite previous thermodynamic models of the deprotonation of protonated uranyl(VI) and uranyl(V) ions suggesting that both are thermodynamically favourable processes, following a PES scan for these reactions the two species have been observed to behave very differently on approach of a molecule of solvent. In the presence of an explicitly defined solvent molecule, the protonated uranyl(VI) ion has been observed to deprotonate spontaneously without a barrier to activation, whereas the protonated uranyl(V) ion has been observed to preferentially retain its proton following the approach of solvent, instead favouring the formation of a stabilising hydrogen bond in which it acts as the donor. Despite the standard stoichiometric thermodynamic approach to calculating the feasibility of the reactions suggesting that both processes are exergonic, there is a large difference between the calculated energy changes for the uranyl(V) and uranyl(VI) species of -9.3 kcal mol^{-1} and -52.7 kcal mol^{-1}, respectively. This vast difference clearly suggests that the deprotonation of the protonated uranyl(VI) ion is a much more feasible process than the deprotonation of the uranyl(V) analogue, in line with the results of the PES scan. On comparison of the proton

affinities calculated for the uranyl(V) and uranyl(VI) analogues of other complexes when bound by different equatorial ligands in a similar manner, it may be possible to assess the effect of the equatorial ligand field on the PA of the uranyl ion. Such a dependence may be of use to direct design of ligands that are suited to stabilise this exotic state of uranium in a beaker, in addition to helping to direct the study of the reduction of dioxygen to peroxide.

4.3.3.1.2 Effect of Equatorial Binding on the Free Energy of Deprotonation

The models of the $U^{V}OHO^{2+}$ and $U^{VI}OHO^{3+}$ complexes optimised without consideration of an additional explicit solvent molecule have been shown to be unable to describe whether the uranyl deprotonation reactions would occur spontaneously or with a barrier to activation. Despite this setback, it may be possible to use the relative free energy changes for the deprotonation processes calculated by these models as a gauge of the relative feasibility of each proton abstraction. In this way, the strength of the interaction between the uranyl ion and the proton may be quantified, which, on observation of the variation in energy when the equatorial ligand field is changed, may allow conclusions to be drawn about how the strength of equatorial coordination affects the uranyl deprotonation energies. Knowledge of such trends may be of use when deducing the optimum reaction mechanism, as described in Chapter 4.3.4.1.

Computational Details

All the subsequently described free energy calculations were carried out using the uB3LYP/B2 level of theory, utilising the appropriate gas phase uB3LYP/B1 optimised geometry of each structure of type $[UOHO(BTPhen)X]^{n+}$, where *X* is a simple mono- or bidentate ligand. The electronic uB3LYP/B2 SP energies calculated were corrected for the effects of enthalpy and entropy using the thermochemical corrections identified by frequency calculations carried out at the uB3LYP/B1 level. The effects of solvation were taken into account implicitly by conducting SP calculations for the gas phase optimised geometries embedded in a CPCM solvent field, parameterised for methanol as described in Chapter 2.7. NBO charges were calculated using the NBO 3.1 program integrated into Gaussian 09 and the MO diagrams were constructed using the gas phase DFT orbital eigenvalues calculated at the uB3LYP/B2 level.

Results and Discussion

The free energy of deprotonation calculated for each of the protonated uranyl complexes that play a role in the proposed mechanistic web, plus the aquated analogues described in Chapter 4.3.3.1, are presented in **Table 27**. In this table, the free energies calculated for the

deprotonation reactions have been split into two columns, the first represents deprotonation reactions of the $U^{VI}OHO^{3+}$ ion and the second, deprotonations of $U^{V}OHO^{2+}$.

Table 27: Table of the free energy changes calculated for the deprotonation of the uranyl species in optimised gaseous complexes of the form $[UOHO(BTPhen)X]^{n+}$, where *X* corresponds to one of the species listed in the first column.[a, b,d]

***X* =**	**Model Labels for Reaction – *U(VI)* : [*U(V)*] [c]**	***U(VI)***	***U(V)***
Dioxygen, $^3O_2$	***N/A*** : [***M4*** – ***M15***]	N/A	-27.6 to -21.4
Water, H_2O	***M1b*** – ***M1*** : [***M2*** – ***M2b***]	-52.7	-9.3
Hydroperoxyl Radical, $HO_2^{\bullet}$	***M10*** – ***M11 :*** [***M12a.1***- ***M12b.1***]	-47.5	-20.3 to -15.0
Superoxide Anion, $O_2^{\bullet-}$	***M5*** – ***M6 :*** [***M7***- ***M16***]	-36.4	+8.9 to +12.0
Hydroperoxide Anion, HO_2^-	***M13*** – ***M14 :*** [***N/A***]	-32.0	N/A
Peroxide Anion, O_2^{2-}	***M8*** – ***M9 :*** [***N/A***]	-7.1	N/A

[a] All energies are presented in kcal mol^{-1}.
[b] The deprotonation energies for these species are presented for both *U(VI)* and *U(V)* analogues where applicable.
[c] This column describes the QM models that were used to calculate the energy changes. Note that identity of the models used to calculate both the *U(VI)* and *U(V)* deprotonation energies are provided in this column, the latter is presented in parentheses.
[d] The table is organised following a general trend that the strength of the ligand *X* for the uranyl ion increases as the table is descended. Thus, the peroxide anion is a stronger ligand for uranyl than water.

The table is ordered in such a way that the strength of the interaction between the uranyl ion and the oxygen ligand increases as the table is descended. In order to achieve this ranking, the length of the bond between the uranium atom and the equatorial ligand ($U\text{-}O_{eq}$) and magnitude of the charge localised on the uranium atom have been used as descriptors of the strength of the bond. It has been assumed that shorter interactions represent stronger bonds and that a less positive charge localised on the metal ion is indicative of greater delocalisation with the equatorial ligand field, thus also indicating a stronger bond. The expected correlation between these two descriptors is clear in **Table 28**, below, thereby providing confidence that these parameters are useful descriptors of the bond strength across this range of similarly composed systems.

The first point to note when comparing the calculated deprotonation energies in **Table 27** is that where information is available for both oxidation states of the metal, the *U(VI)* deprotonation energy is consistently much more exergonic than the *U(V)* analogue. The second point to note is that as the strength of the equatorial interaction between the ligand and the uranyl ion increases, there is a steady decrease in the free energy change for the deprotonation reaction i.e. it becomes less exergonic. This suggests that the affinity of the uranyl ion for the axially bound proton may be tuned by varying the equatorial ligand field. Such a finding may be of some use to synthetic chemists who work to functionalise the

uranyl oxygen atoms and who may, therefore, benefit from using harder equatorial donor ligands to stabilise the axially substituted uranyl species.

Table 28: Table of the localised NBO charges on the uranium atom and the mean charge of the O_{yl} atoms in the gas phase optimised $[UO_2(BTPhen)X]^{n+}$ complexes as calculated using a SP calculation using the B2 basis set and CPCM solvation.[a]

***X* = [b]**	**Model**	***U*-O_{eq} /Å**	***U* [c]**	**O_{yl} [c]**
Dioxygen, $^3O_2$	***M3*** [***M15***]	2.82 [2.97]	+1.68 [+1.54]	-0.51 [-0.65]
Water, H_2O	***M1*** **[*M2b*]**	2.47 [2.58]	+1.66 [+1.46]	-0.52 [-0.71]
Hydroperoxyl Radical, $HO_2^{\bullet}$	***M11*** **[*M12b.1*]**	2.45 [2.59]	+1.60 [+1.40]	-0.51 [-0.69]
Superoxide Anion, $O_2^{\bullet-}$	***M6***	2.37/2.37	+1.35	-0.54
Hydroperoxide Anion, HO_2^-	***M14***	2.24/2.40	+1.34	-0.54
Peroxide Anion, O_2^{2-}	***M9***	2.16/2.16	+1.20	-0.60

[a] The interatomic distance between the uranium atom and the equatorial ligand, *X*, is also presented for each model.
[b] The ligand *X* corresponds to the species listed in the first column.
[c] In the final two columns, the first quantity corresponds to the charge of the *U(VI)* model of the complex, whereas the number in parentheses represents the charge of the *U(V)* analogue.

The correlation between the affinity of the equatorial ligand field for the metal ion and the PA of the uranyl ion can be rationalised using arguments similar to those used to justify why the uranyl(V) ion readily forms hydrogen bonds with solvating water whereas the uranyl(VI) analogue does not. As stated previously, this effect is often attributed to an increased charge localised on the O_{yl} atoms in the uranyl(V) ion relative to the uranyl(VI) analogue.[79,201] The observed equatorial ligand field-dependent proton affinity of the uranyl ion may also be rationalised using this logic, as increasing the strength of the interaction between the uranium atom and its equatorial ligand field results in competition between the equatorial and axial proponents to bind the metal. This in turn acts to disrupt the bonding within the uranyl ion leading to an increased localisation of charge on the O_{yl} atoms. The severity of this disruption and hence the size of the charge on the O_{yl} atoms depends on the affinity of the equatorial ligand field for the *U* atom. When the uranyl ion is not protonated, this excess charge is efficiently stabilised on formation of hydrogen bonding interactions with the solvent. When the uranyl ion is protonated, the increased charge leads to a stronger electrostatic interaction between the O_{yl} atom and the bound hydrogen, resulting in an increased PA of strongly equatorially bound uranyl ions relative to those with weak equatorial ligand fields. This inverse proportionality between the strength of the equatorial ligand field interaction and the charge localised on the O_{yl} oxygen atoms is demonstrated in **Table 28**, above, which shows that the negative charge localised on the O_{yl} atoms increases as both the *U*-O_{eq} separation and charge on the uranium atom decreases. This gradual weakening of the axial bonds of the uranyl ion on increasing the strength of the equatorial interaction is also corroborated by a MO description of these systems, **Figure 41**. On examination of the MOs, it is clear that as

the strength of the equatorial ligand interaction increases, the strength of the axial uranyl bonds decrease, as exemplified by the gradual shift of eigenvalues of the uranyl MOs away from what could be described as an 'inverted scheme' in which the highest lying orbitals are predominantly ligand based, towards a normal level scheme, in which the HOMOs are increasingly metal in character.[202,203]

Summary and Implications for the Reaction Mechanism

The acidity of the protonated uranyl ion has been found to be heavily dependent on the oxidation state of the metal ion. Calculations suggest that whilst all deprotonation reactions of the uranyl complexes studied are thermodynamically feasible (with the exception of the *U(V)* superoxide complex), there is a kinetic barrier to the deprotonation of $U^{V}OHO^{2+}$ ions. Conversely, the corresponding *U(VI)* analogues are predicted to deprotonate spontaneously in aqueous solution. A pronounced dependence of the acidity of the protonated uranyl species on the strength of the equatorial coordination has also been observed. This trend suggests that uranyl ions engrossed in strong equatorial bonding interactions are likely to be less acidic than their weakly coordinated counterparts.

Using these findings it is possible to propose that in the peroxide forming mechanism under study, the route most conservative of energy is that which involves an ET from a protonated uranyl(V) species followed by deprotonation, since the deprotonation of the uranyl ion occurs without a barrier to activation. Owing to the fact that the strength of the equatorial coordination of the uranyl species increases as the mechanism progresses, it is likely that this assertion holds more favourably for the second ET process than the first. Nevertheless, both routes via protonated and non-protonated uranyl(V) ions were found to be thermodynamically feasible and so it is probable that in reality both routes are utilised concurrently.

Despite the success of this initial study in narrowing down the mechanistic routes available to the ET process, it has not been possible using the current models to rule out the possibility that the ET and deprotonation reactions may be more closely linked. As stated previously, in biological systems proton transfers between redox active sites are often used to modify the redox potentials of the species involved ergo facilitating the ET in a proton-coupled electron transfer (PC-ET) type process.[197] Thus, the possibility of an intramolecular PT occurring following the first ET is examined in the forthcoming chapters. Such a process may lead the uranyl hydroperoxyl radical complex that was shown in Chapter 4.3.2.1.3 to undergo a much more exergonic ET to form peroxide than the superoxide analogue.

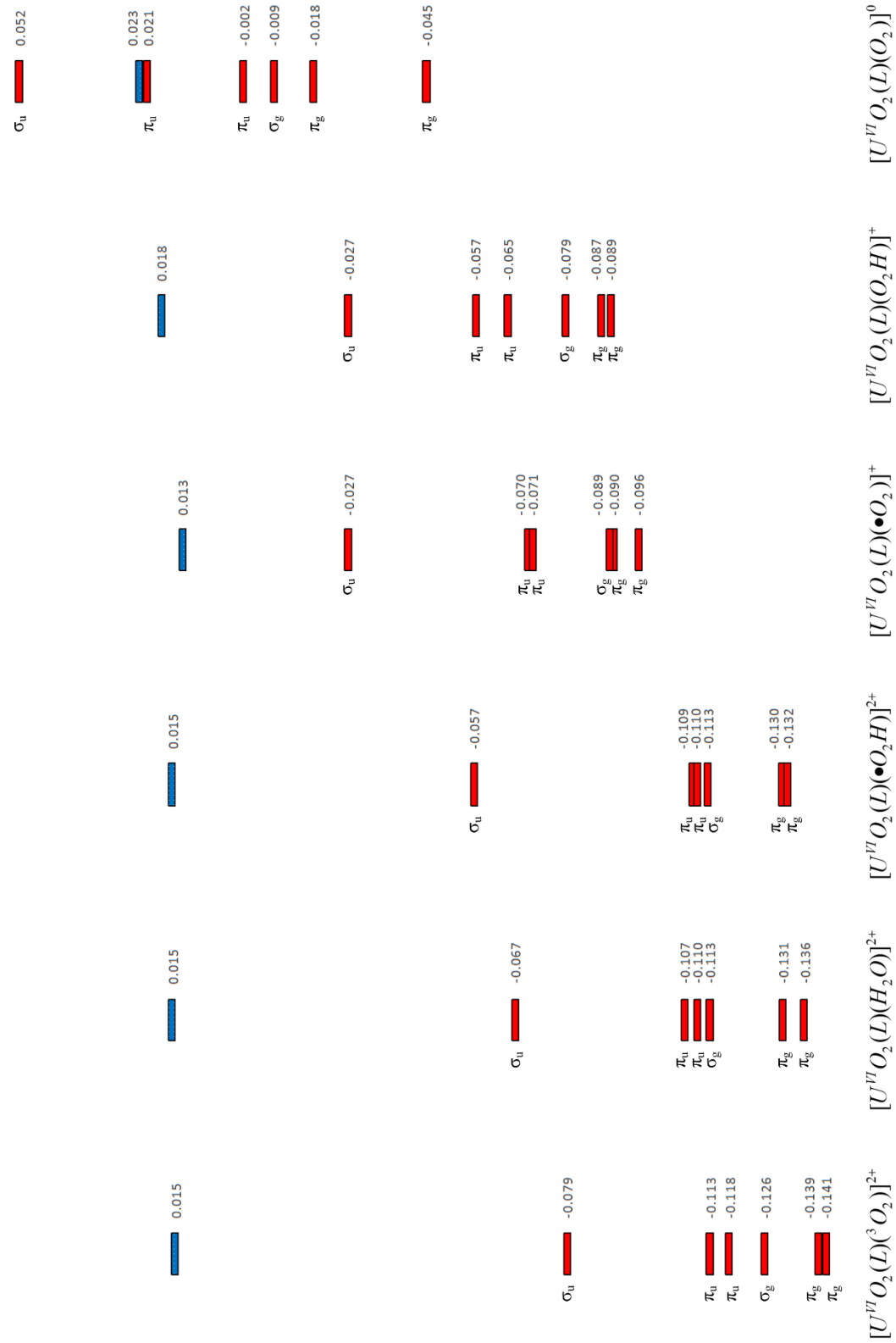

Figure 60: MO diagrams for the uranul(VI)-BTPhen complexes of $^3O_2$, H_2O, $\cdot O_2H$, O_2^-, O_2H and O_2^{2-}. Blue boxes represent the BTPhen ligand based HOMO in each complex, denoted by an *L* in the chemical formula. Red boxes represent the six uranyl based orbitals in each complex. The uranyl MOs have been labelled assuming a $D_{\infty h}$ ligand field to aid interpretation. Where the C_1 symmetry of the molecular model led to splitting of these $D_{\infty h}$ MOs into lower symmetry equivalents, the eigenvalues of all MOs displaying the appropriate obital interaction were averaged to provide the eigenvalues presented. All eigenvalues have been referenced relative to the eigenvalue of a BTPhen ligand MO that varied minimally between the models. In this way, it is assumed that this MO does not take part in any bonding interactions within the complex and is thus independent of the model described, unlike the HOMO in certain cases, and therefore represents the most suitable reference orbital to allow comparison of the different models.

4.3.3.2 The Identity of the Solvated Superoxide Complex of the Uranyl Ion: A Superoxide Anion or Hydroperoxyl Radical Bound Species?

Recap of Previous Work in the Area – The Mechanism Favoured by Bakac et al.

When conducting their kinetic study into the autoxidation of UO_2^+ in the presence of dioxygen, Bakac and Espenson were able to draw several reasonable conclusions about the mechanism of the reaction. First of all, they determined that two equivalents of UO_2^+ were required in order to form one mole of H_2O_2 from O_2. Secondly, they suggested that the first ET to dioxygen is likely to occur within a directly coordinated complex. They go on to suggest that the identity of the 'intermediate species' formed by the reduction of O_2 by a coordinated UO_2^+ could either be a uranyl complex of the superoxide anion, $\cdot O_2^-$, or a complex of its conjugate acid, $\cdot O_2H$. Owing to the nature of their kinetic experiments, they state that the exact identity of this species is unknowable, although considering that their reactions were conducted in acidic solvent, they propose the hydroperoxyl radical complex as the most conceptually appealing.

Schematics of the reactions that lead to the formation of this 'intermediate species', $[U^{VI}O_2(HO_2\cdot)]^{3+}$, are presented in **Equations 75-78**. In line with the mechanism proposed by Bakac et al., **Equations 75-82** are presented in a manner that assumes the protonated uranyl(V) ion releases its bound proton immediately following its formation and thus prior to the ET step. As concluded in the previous chapter, the QM models studied here suggest that this path is not likely to be the most economical of energy, and hence the mechanism proposed by this study will undoubtedly proceed via the protonated uranyl ion analogues dismissed by Bakac et al. Despite this difference of opinion, at this point the scheme favoured by Bakac et al. will be considered in the name of consistency.

$$U^{VI}O_2^{2+} + MeOH \xrightarrow{h\nu} U^{V}O_2^{+} + {}^{\bullet}CH_2OH + H^+ \quad \textbf{(75)}$$

$$U^{V}O_2^{+} + O_2 \longleftrightarrow [U^{V}O_2(O_2)]^+ \quad \textbf{(76)}$$

$$[U^{V}O_2(O_2)]^+ \xrightarrow{ET} [U^{VI}O_2(O_2^{\bullet})]^+ \quad \textbf{(77)}$$

$$[U^{VI}O_2(O_2^{\bullet})]^+ + H_3O^+ \longleftrightarrow [U^{VI}O_2(HO_2^{\bullet})]^{2+} + H_2O \quad \textbf{(78)}$$

$$[U^{VI}O_2(HO_2^{\bullet})]^{2+} + U^{V}O_2^{+} \longleftrightarrow [(U^{VI}O_2)_2(O_2)]^{2+} + H^+ \quad \textbf{(79)}$$

$$[U^{VI}O_2(HO_2^{\bullet})]^{2+} \longleftrightarrow U^{VI}O_2^{2+} + HO_2^{\bullet} \quad \textbf{(80)}$$

$$U^{V}O_2^{+} + HO_2^{\bullet} \xrightarrow{OS-ET} U^{VI}O_2^{2+} + HO_2^{-} \quad \textbf{(81)}$$

$$2U^{VI}O_2^{2+} + HO_2^{-} \longleftrightarrow [(U^{VI}O_2)_2(O_2)]^{2+} + H^+ \quad \textbf{(82)}$$

An 'intermediate species', $[U^{VI}O_2(HO_2^{\bullet})]^{2+}$ in **Equation 78**, is proposed by Bakac et al. that may either oxidise a further mole of UO_2^{+} directly, which leads to the formation of a peroxide bridged bisuranyl(VI) complex, **Equation 79**, or dissociate, **Equation 80**. Following dissociation, as predicted by the standard redox potentials of these species (E^0 = +0.16 V for UO_2^{2+} and E^0 = +1.44 V for $HO_2^{\bullet}$),[4,141,192,144,150] it should be feasible for a mole of free $HO_2^{\bullet}$ to oxidise UO_2^{+} via an OS-ET mechanism. This mechanism promotes the formation of free peroxide, **Equation 81**, regenerating the second mole of free UO_2^{2+} required by the catalytic process. It is constructive to note that the analogous OS-ET to the free $^{\bullet}O_2^{-}$ anion is also predicted to be a thermodynamically feasible process by the standard redox potentials of the species involved (E^0 = +0.2 V for $^{\bullet}O_2^{-}$)[150], albeit one much less exergonic. In the final step in the scheme proposed by Bakac et al., the free peroxide formed in **Equation 81** is bound by two moles of free UO_2^{2+} in solution, leading to the formation of the peroxide bridged uranyl dimer of interest, see **Equation 82**.

$$\Delta G = -RT \ln K \qquad \textbf{(83)}$$

$$pH = pK_a - \log\left(\frac{[O_2^{\bullet -}]}{[HO_2^{\bullet}]}\right) \qquad \textbf{(84)}$$

Despite the impact of their early work, Bakac and Espenson were not the sole pioneers of this field. In the mid-1970s, Meisel et al.[143] were working to measure the stability constant of a paramagnetic UO_2^{2+} complex formed in solutions containing the uranyl(VI) ion and $HO_2^{\bullet}$ i.e. the reverse reaction of **Equation 79**. Using a combination of EPR and UV-vis (ultraviolet-visible) spectroscopy, they calculated a formation constant of K = 1.5 $\times 10^3$ M^{-1} for the the U(VI) complex. Substituting this constant into **Equation 83**, we find this corresponds to a ΔG of complexation of -4.3 kcal mol^{-1}. Similarly to Bakac et al.,[4] Meisel et al.[143] assumed the identity of the complex formed to be $[U^{VI}O_2(HO_2^{\bullet})]^{2+}$, based on the p$K_a$ of free $HO_2^{\bullet}$ (pK_a = 4.86)[143] and the fact the experiments were conducted in 0. 1 M $HClO_4$. Despite this agreement, this conclusion was not an accepted consensus, since at a similar time Berdnikov et al.[147–149] concluded that such metal bound species are likely to take the form of the superoxide analogue of the complexes, i.e. $[U^{VI}O_2\ (O_2^{\bullet})]^{+}$. Since these initial studies, interest in the superoxide chemistry of the uranyl ion has died down, only to be revived relatively recently. Thus, there is still considerable dispute in the literature over the nature of the 'intermediate species' as defined by Bakac et al. and in particular whether it is a uranyl(VI) complex of the hydroperoxyl radical or a complex of the superoxide anion. The timely nature of this study is reflected by a related recent publication by Bühl, Sieffert and Wipff that focusses on the nature of the complex that persists in basic solutions containing

the uranyl(VI) ion and hydrogen peroxide.[35] In their paper, Bühl et al. use a combination of DFT, QM/MM and CPMD to conclude that, in solution, the polarising nature of the solvent favours the formation of the deprotonated uranyl(VI) peroxide complex as opposed to the hydroperoxide analogue, thus contributing to the debate over the nature of the dominant species in basic uranyl hydroperoxide solutions that empirical studies have, to date, failed to determine.

Computational Details

As stated in Appendix 2, the free energy of protonation of the solvated superoxide anion is calculated to be a favourable process by the computational model employed. This is in line with the experimentally determined pK_a of the hydroperoxyl radical of 4.86.[145] Despite this agreement, the model overestimates the basicity of $O_2^{\bullet-}$, resulting in a free energy for the *association* of a superoxide anion and a proton of -12.6 kcal mol^{-1}.This is compared to the empirical free energy for this reaction of -6.6 kcal mol^{-1}. This discrepancy between the empirical and computed free energies is echoed when the solvation energy of the superoxide anion is calculated. In this case the model underestimates the solvation energy of the superoxide anion by between 5.4 kcal mol^{-1} and 13.4 kcal mol^{-1}, depending on the experimental value selected.[144] This underestimation of the solvation energy has a direct impact on the calculated free energy of protonation and thus will also skew the solvated free energies of the acid-base reactions it is used to model. In order to correct for this, whenever the model of the solvated superoxide species is used in the following discussion to calculate a reaction free energy change, two values will be presented; one in which ΔG_{solv} has been computed using the unmodified 'computationally pure' model, and a second in which the ΔG_{solv} for the superoxide anion has been brought into agreement with empirical results on inclusion of a correction factor of -6.0 kcal mol^{-1}.

In order to gauge the thermodynamic feasibility of the mechanism proposed by Bakac et al.,[4] the reactions described by **Equations 78** and **80** were modelled. As stated, these reaction schemes describe the protonation of a superoxide anion equatorially bound to a uranyl(VI) ion and the dissociation of a uranyl(VI) hydroperoxyl radical complex. In addition to modelling these reactions with the remainder of the equatorial ligand field chelated by the BTPhen ligand, they were also modelled as the totally aquated analogues of these species i.e. complexes of the type $[UO_2(H_2O)_x(^{\bullet}O_2)]^+$. These calculations were carried out in order to elucidate any possible differences between the behaviour of the BTPhen model system and the species studied by Meisel et al.[142,143]

The equatorially hexacoordinate species *'$[UO_2(H_2O)_4(^{\bullet}O_2)]^+ + H_2O$'* and its hydroperoxyl analogue were used to represent the majority species present in the aqueous solutions studied. These models contained four water molecules in the primary coordination sphere of the uranium atom and one present in the secondary solvation sphere in a position primed to accept a hydrogen bond from the primary ligand field. Such an *'n+1'* class model was chosen to represent the aquated hydroperoxyl and superoxide species as it was deemed likely that the hydroperoxyl radical species in particular would be stabilised greatly by such specific interactions with the secondary hydration sphere. In line with the findings of Bühl et al., who have recently studied the equatorial coordination geometry of the analogous peroxide and hydroperoxide analogues of these complexes, a hexacoordinate equatorial coordination motif was assumed for the superoxide complex and a pentacoordinate motif was assumed for the hydroperoxyl analogue.[35] The gas phase optimised geometries of these models are presented in **Figure 61**.

The similarly hexacoordinate and pentacoordinate BTPhen complexes of the superoxide and hydroperoxyl radical, ***M6*** and ***M11***, presented previously, were used to represent the majority species present in solutions containing the chelating BTPhen ligand. The gas phase optimised structures of these complexes are also presented in **Figure 61**, below, for convenience of reference. Tables presenting the calculated free energies for the protonation of the superoxide anion complexed with *U(VI)* in the presence of the two ligand fields, as described by **Equation 78**, and the energetics of the subsequent dissociation of the hydroperoxyl complexes formed, **Equation 80**, are presented in **Table 29** and **Table 30**.

As in previous models, the geometries of these complexes were optimised using the uB3LYP/B1 functional-basis set combination. SP calculations were carried out on the gas phase optimised geometries at the uB3LYP/B2 level, with and without CPCM solvation, in order to calculate the energies presented below. All geometries were confirmed to be at local minima by calculating the second derivative of the energy of the structure with respect to the nuclear coordinates using a frequency calculation in Gaussian 09.[6]

Results and Discussion

Comparing the optimised geometries presented in **Figure 61**, it is clear there are similarities between the aquated and the BTPhen chelated uranyl(VI) species. As expected, in both complexes of the superoxide anion, the $^{\bullet}O_2^-$ ligand binds the uranium ion in a bidentate manner and in both of the hydroperoxyl complexes the radical binds in a monodentate manner. On comparison of the *'n+1'* models of the aquated complexes, it is apparent that the water molecule explicitly included to probe interactions between the primary and

secondary solvation spheres, plays a different role in the hydroperoxyl radical complex than in the superoxide complex. In the former, this water species acts as a hydrogen bond acceptor to the hydroperoxyl ion, thereby stabilising the interaction of $^{\bullet}O_2H$ with the uranyl ion, whereas in the latter no such interaction is observed, the additional water molecule instead favours interaction with a water molecule in the primary hydration sphere of the metal ion. The additional stabilisation afforded to the hydroperoxyl complex manifests itself as a shorter bond length between the uranium atom and the hydroperoxyl radical in the *'n+1'* model compared to the model in which the additional water molecule is not explicitly included (the image of which is not presented due to its broad similarity to the n+1 model).

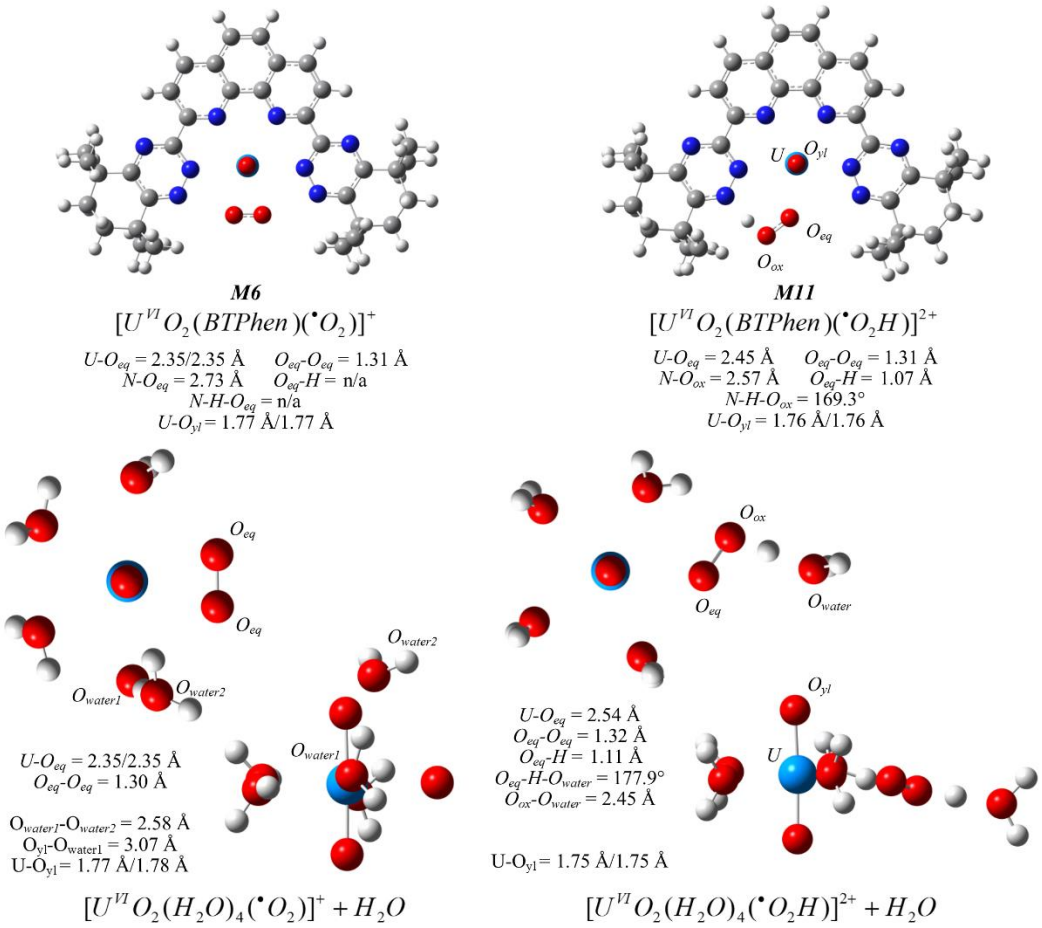

Figure 61: Optimised geometries and selected structural parameters of models representing the aquated and BTPhen chelated uranyl(VI) complexes of $^{\bullet}O_2^-$ and $^{\bullet}O_2H$. Selected residues referred to in the description of the structural parameters are labelled on the diagrams. Uranium atoms are presented in turquoise, oxygen atoms in red, nitrogen atoms in blue, carbon atoms in grey and hydrogen atoms in white.

The parameters for the non-explicitly solvated model are not presented in detail here, however for comparative purposes, the change in this bond length ($U\text{-}O_{eq}$) amounts to -0.07 Å on providing explicit solvation. In contrast, when the superoxide complex is treated using an *'n+1'* model, the most stable geometry identified does not describe a hydrogen bond to the superoxide anion, but rather a hydrogen bond to a water molecule in the primary solvation sphere or the uranyl ion. This results in the geometry of the *'n+1'* and

'n' complexes of the superoxide bound species remaining essentially unchanged on inclusion of the additional molecule of explicit solvent (the change in the $U\text{-}O_{eq}$ = 0.002 Å). In order to confirm this geometry as the global minimum (in addition to performing a frequency analysis) the optimisation procedure was restarted several times employing different initial guess structures that attempted to provoke the formation of hydrogen bonds between the secondary water molecule and the superoxide anion or the uranyl ion. However, in each case the PES was observed to direct the secondary water molecule to interact with the primary solvation sphere, thereby reinforcing previous conclusions drawn about the relatively low propensity for the uranyl(VI) O_{yl} atoms and the bound superoxide anion to form explicit interactions with solvent.

Comparing the interatomic distances between the hydrogen bonding species in the BTPhen model, ***M11***, and its aquated analogue, $[U^{VI}O_2(H_2O)_4(^{\bullet}O_2H)]^{2+}$, the optimised models suggest that the latter is a stronger interaction. This suggestion may be inferred from the shorter distance between the hydrogen bond donor and acceptor atoms in the aquated complex, 2.45 Å, than in the BTPhen complex, 2.57 Å and the fact that the separation between the donor atom and the hydrogen atom itself is also greater in the aquated species; 1.11 Å compared with 1.07 Å in the BTPhen model. The greater stability of the hydrogen bond in the aquated complex may be attributed to the nature of the hydrogen bond acceptor atoms in these species. Hydrogen bonding is a primarily dipolar interaction, thus the larger dipole of the water molecule relative to that of the nitrogen based triazinyl ring inherently permits the water molecule to form stronger hydrogen bonding interactions. Despite this enthalpic preference for hydrogen bonding to water, the effects of entropy and the inaccuracy of the static model employed to quantify these effects cannot be discounted. Hence, it is possible that because the BTPhen complex is essentially pre-organised to accept a hydrogen bond, it may act to stabilise the hydroperoxyl complex more effectively than the aquated analogue owing to the increased effective concentration of the hydrogen bond acceptor in this species. Despite this speculation, without turning to a time resolved study of these species, such entropic effects on their rate of dissociation cannot be confirmed.

When studying solutions containing uranyl(VI) ions and hydroperoxyl radicals, Meisel et al. calculated the free energy of association of the complex formed to be -4.3 kcal mol^{-1} and hence the free energy of *dissociation* of the complex to be +4.3 kcal mol^{-1}. Meisel et al. proposed that this dissociation constant describes the process occurring in **Equation 80**, i.e. the dissociation of the hydroperoxyl bound uranyl complex.

$$[U^{VI}O_2(HO_2^{\bullet})]^{2+} \longleftrightarrow U^{VI}O_2^{2+} + HO_2^{\bullet} \qquad \textbf{(80)}$$

Table 29 presents the energetics calculated for this dissociation process using the *'n+1'* model of the hydroperoxyl complex and that of the pentaaqua uranyl(VI) ion, along with the related dissociation energy of the uranyl(VI) superoxide complex. The free energy of dissociation calculated for the process described by **Equation 80** is -3.9 kcal mol^{-1}, see **Table 29**. Hence, whilst this value is of a similar magnitude to that determined experimentally, +4.3 kcal mol^{-1}, the computational model employed incorrectly suggests that the dissociation of the aquated uranyl hydroperoxyl radical complex is spontaneous at room temperature. Although disconcerting, this difference is not unexpected owing to the previously discussed difficulty of accurately describing the effects of solvation. The errors inherent of the finite cluster model utilised here to account for solvation effects are large when compared to energetics of subtle reactions such as the single ligand substitution of a water molecule for a hydroperoxyl radical. The conclusions are, however, more reliable when used to study reactions that inherently involve larger changes in free energy.

$$[U^{VI}O_2(L)(O_2^{\bullet})]^{+} + H_2O \rightarrow [U^{VI}O_2(L)(H_2O)]^{2+} + O_2^{\bullet -} \qquad \textbf{(85)}$$

$$O_2^{\bullet -} + H_3O^{+} \longrightarrow HO_2^{\bullet} + H_2O \qquad \textbf{(86)}$$

In the equation, above, *(L)* represents *$(H_2O)_4$*.

Table 29: Calculated reaction energies for the protonation and dissociation of *$[U^{VI}O_2(L)(X)]^{2+}$* superoxide and hydroperoxyl radical complexes, in which *$L=(H_2O)_4$* and *$X= O_2^{\bullet -}$* or *$^{\bullet}O_2H$*.[a, b]

Equation No.	ΔG_{gas} (ΔH_{gas})	ΔG_{solv} (ΔH_{solv})	ΔG_{solv} (ΔH_{solv}) $+\Delta G_{corr}$
78	+96.9	+26.7	+26.7
	(+98.4)	(+28.2)	(+28.2)
80	+10.0	-3.9	-3.9
	(+10.7)	(-3.3)	(-3.3)
85	+193.7	+35.4	+29.4
	(+197.0)	(+38.7)	(+32.7)
86	-86.7	-12.6	-6.6
	(-87.9)	(-13.8)	(-7.8)

[a] All energies are presented in kcal mol^{-1}.
[b] The uncorrected gaseous and solution phase ΔG and ΔH values are presented along with the corresponding values including an empirical correction to account for the fact the computational model employed underestimates the solvation energy of the superoxide anion. ΔG_{corr}.

In contrast to the marginal instability of the aquated uranyl(VI) hydroperoxyl complex with respect to ligand exchange, the dissociation of the corresponding superoxide complex is predicted to be an unfavourable process by the computational model, with ΔG_{solv} = +29.4 kcal mol^{-1}. This result is therefore in line with the observed stability of a

paramagnetic uranyl complex studied by Meisel et al.[142,143] as well as the results of a recent study by Bühl et al.[35] that found the peroxide complex of the aquated uranyl(VI) ion to be more stable than the hydroperoxide analogue. Regardless of the apparent failing of the computational model employed to replicate the empirical free energy change for the dissociation of the hydroperoxyl complex, there is a great enough difference in energies predicted between the superoxide and hydroperoxyl complexes to state with confidence that the superoxide bound species is the most stable of the two in solution. The greater stability of the superoxide compared with the hydroperoxyl radical complex is most succinctly manifested in the free energy of protonation of the uranyl(VI) bound superoxide anion, **Equation 78**, which is calculated to be strongly endergonic with ΔG = +26.7 kcal mol^{-1}.

The above calculated reaction free energy changes can be rationalised with respect to the empirical findings as follows. The experimentally determined pK_a of the hydroperoxyl radical is 4.8.[145] Hence in a 0.1 M acidic solution, 99.975% of the free superoxide will exist as $^{\bullet}O_2H$.[142,143] Therefore, as proposed by Meisel et al.,[142,143] the first step of the association mechanism will undoubtedly involve the interaction of the hydroperoxyl radical and the uranyl ion, as per **Equation 80**. Since this association is an equilibrium process, the complex formed could feasibly dissociate before any further reaction continues. However, should it remain together, then the QM calculations suggest that there is a significant thermodynamic driving force for the bound hydroperoxyl radical to deprotonate, thereby generating the uranyl(VI)-superoxide complex.

There is a reasonable degree of uncertainty in the identity of the uranyl species probed experimentally due to the intrinsically similar electronic structure of the superoxide and hydroperoxyl radical species. These similarities are likely to result in the UV absorption and EPR spectra of the superoxide and hydrosuperoxide complexes of the uranyl(VI) ion formed displaying similar characteristics, *cf* the broad and essentially coincident UV-vis absorption spectra of the unbound superoxide anion and hydroperoxyl radical that exhibit absorption maxima at 245 nm and 225 nm, respectively.[144] Nevertheless, if the similar studies of Bakac et al.[4] and Meisel et al.[142,143] had been conducted at differing solution pH then it may have been possible to infer some aspect of the solution speciation from a difference spectrum. Despite this lack of empirical information, considering the overwhelming stability of the superoxide complex over the hydroperoxyl complex calculated using the QM models employed, it is the conclusion of this study that the 'intermediate species' as defined by Bakac et al.[4] is most likely the uranyl superoxide complex, $[U^{VI}O_2(H_2O)_4(O_2^{\bullet})]^+$, and not its hydroperoxyl analogue.

In agreement with the experimentally observed kinetics, the formation of this complex as two step wise reactions; 1) the formation of $[U^{VI}O_2(H_2O)_4(HO_2^{\bullet})]^{2+}$ via **Equation 80**, and 2) the deprotonation of this complex to form $[U^{VI}O_2(H_2O)_4(O_2^{\bullet})]^{+}$ (the reverse of **Equation 78**) would still be observed empirically as a pseudo first order reaction with respect to the concentration of the metal ion, described by Bakac et al.[4] Hence, the mechanism proposed by the QM models detailed agrees with the experimental evidence and provides molecular insight not available from kinetic studies alone.

Using the data presented in **Table 30** to extend this study of the aquated uranyl(VI)-superoxide and hydroperoxyl complexes to examine the species formed in the presence of BTPhen ligand, it is clear that similar energetic trends are predicted. Of particular importance is that the free energy of protonation of $[U^{VI}O_2(BTPhen)(O_2^{\bullet})]^{+}$ to form $[U^{VI}O_2(BTPhen)(^{\bullet}O_2H)]^{2+}$ is calculated to be of a similar magnitude to the aquated analogue with ΔG = +27.0 kcal mol^{-1}. Hence, similar to the aquated complex, in the presence of the BTPhen ligand the superoxide bound complex is predicted to be more stable than the hydroperoxyl radical bound analogue.

$$[U^{VI}O_2(L)(O_2^{\bullet})]^{+} + H_3O^{+} \longrightarrow [U^{VI}O_2(L)(HO_2^{\bullet})]^{2+} + H_2O \qquad \textbf{(87)}$$

$$[U^{VI}O_2(L)(HO_2^{\bullet})]^{2+} + H_2O \longrightarrow [U^{VI}O_2(L)(H_2O)]^{2+} + HO_2^{\bullet} \qquad \textbf{(88)}$$

$$[U^{VI}O_2(L)(O_2^{\bullet})]^{+} + H_2O \longrightarrow [U^{VI}O_2(L)(H_2O)]^{2+} + O_2^{\bullet -} \qquad \textbf{(89)}$$

In the above equations, *(L)* represents the BTPhen ligand.

Table 30: Calculated reaction energies for the protonation and dissociation of $[U^{VI}O_2(L)(X)]^{2+}$, in which *L*=BTPhen and *X*= $^{\bullet}O_2^{-}$ or $^{\bullet}O_2H$.[a,b]

Reaction	Equation No.	ΔG_{gas} (ΔH_{gas})	ΔG_{solv} (ΔH_{solv})	ΔG_{solv} (ΔH_{solv}) $+\Delta G_{corr}$
M6 → M11	87	+64.5 (+63.7)	+27.0 (+26.2)	+27.0 (+26.2)
M11 → M1	88	-4.7 (-6.1)	-7.4 (-8.9)	-7.4 (-8.9)
M6 → M11	87	+146.5 (+145.5)	+32.2 (+31.1)	+26.2 (+25.1)
N/A	86	-86.7 (-87.9)	-12.6 (-13.8)	-6.6 (-7.8)

a All energies are presented in kcal mol-1.
b The uncorrected gaseous and solution phase ΔG and ΔH values are presented along with the corresponding values including an empirical correction, ΔGcorr, to account for the fact the computational model employed underestimates the solvation energy of the superoxide anion.

The identification of the 'intermediate species' as the uranyl(VI)-superoxide complex not only has implications for the mechanism proposed by Meisel et al.,[143] but also for the feasibility of the mechanism proposed by Bakac et al.[4] Bakac et al. theorised that following the ET from the non-protonated *U(V)* species to the equatorially bound dioxygen molecule, **Equation 77**, the superoxide complex formed would be rapidly protonated, generating the hydroperoxyl analogue of the complex, **Equation 78**. Finally, they proposed that this protonation would stimulate the dissociation of the uranyl hydroperoxyl species, releasing free hydroperoxyl radical into solution, **Equation 80**, which would subsequently undergo a further OS-ET reduction with the uranyl(V) ion in order to generate peroxide, **Equation 81**.

$$[U^{V}O_2(O_2)]^{+} \xrightarrow{ET} [U^{VI}O_2(O_2^{\bullet})]^{+} \quad \textbf{(77)}$$

$$[U^{VI}O_2(O_2^{\bullet})]^{+} + H_3O^{+} \longleftrightarrow [U^{VI}O_2(HO_2^{\bullet})]^{2+} + H_2O \quad \textbf{(78)}$$

$$[U^{VI}O_2(HO_2^{\bullet})]^{2+} \longleftrightarrow U^{VI}O_2^{2+} + HO_2^{\bullet} \quad \textbf{(80)}$$

$$U^{V}O_2^{+} + HO_2^{\bullet} \xrightarrow{OS-ET} U^{VI}O_2^{2+} + HO_2^{-} \quad \textbf{(81)}$$

Considering first the feasibility of the dissociation of $[U^{VI}O_2(\cdot O_2H)]^{2+}$, **Equation 80**, the QM models suggest that this is a mildly exergonic process, in agreement with the conclusions of Bakac et al.[4] However, this is in contrast with the empirical findings of Meisel et al.[143] which suggest this dissociation to be a mildly endergonic process. Regardless of the reasons for these differing results, it is clear that this dissociation is an equilibrium process. As such, this equilibrium represents a branching point in the mechanism to form peroxide, following which, the species could dissociate and follow an outer sphere ET pathway to the peroxide anion, as suggested by Bakac et al, or the complex could remain intact and follow an inner sphere ET pathway to the product, as modelled Chapter 4.3.2.1.3. The mechanistic path is complicated further by the fact that, should the complex remain intact, the bound hydroperoxyl radical could feasibly deprotonate once more regenerating a uranyl-superoxide complex. Since all three of these pathways are predicted to be feasible, it is likely that they all occur concurrently in a vessel at room temperature and thus the only question that may be answered further on this topic concerns the relative yields of each process. Such an in depth study of these reaction rates is beyond the ability of the methods applied in this study. However, assuming only a limited number of hydroperoxyl radicals are generated initially, the relative yields of these reaction routes may be estimated simply using the lifetimes of the uranyl bound and free hydroperoxyl species in solution as a guide. The rate of disproportionation of hydroperoxyl/superoxide species in solution is known to be faster than the rate of disproportionation of these species when bound to metal ions.

Hence, such a dependency leads to the conclusion that the inner sphere mechanism proposed may generate the majority of the peroxide bridged product observed as free solvated hydroperoxyl radicals that are more likely to be destroyed in solution than their bound analogues.[143] Despite this, it should be considered that even the disproportionation of hydroperoxyl (and analogously, superoxide) species generates peroxide via **Equation 90**. Hence, ultimately this seemingly disruptive route may provide an important source of the peroxide that bridges the two uranyl ions observed in the crystalline product, as formed via **Equation 82**.

$$2HO_2^{\bullet} \longrightarrow H_2O_2 + O_2 \qquad \textbf{(90)}$$

$$2U^{VI}O_2^{2+} + HO_2^{-} \longleftrightarrow [(U^{VI}O_2)_2(O_2)]^{2+} + H^{+} \qquad \textbf{(82)}$$

The proposal of Bakac et al. that the uranyl superoxide complex is favourably protonated following its formation, **Equation 78**, appears to disagree with the recommendations made by the modelled mechanism. Despite this apparent contradiction, the process modelled assumes that the acidic proton is supplied by the external solvent field and hence there is a barrier to reaction considering the large solvation energy of a proton in water. Despite this limitation, the external solvent field is not the only proton source in the system. As discussed in Chapter 4.3.3.1, the proton affinity of the uranyl(V) ion is greater than that of the uranyl(VI) ion. This has previously led to the conclusion that the protonated uranyl species formed following the hydrogen atom abstraction will likely persist until after the ET has occurred. Hence, it is reasonable to propose that a protonated uranyl(VI) ion itself may act as the proton donor to an equatorially bound superoxide anion. In this way, it may be possible to offset the strong favourability of the uranyl(VI) deprotonation against the disfavoured superoxide protonation in order to generate a concerted proton transfer process that is moderately thermodynamically feasible overall. The scope of the next section is to investigate such a possibility.

Summary

Meisel et al.[143] and Bakac et al.[4] proposed that the intermediate species formed in solutions containing the uranyl(VI) ion and the hydroperoxyl radical is a uranyl(VI)-hydroperoxyl radical complex of the type, $[U^{VI}O_2(^{\bullet}O_2H)]^{2+}$. The present study is in agreement with these authors that the most stable form of superoxide in solution is the hydroperoxyl radical. However, when complexed, this study has shown that there is a significant driving force for the bound hydroperoxyl radical to deprotonate in order to yield the superoxide bound complex, $[U^{VI}O_2(^{\bullet}O_2)]^{+}$. The preponderance of this species in solution has previously been

suggested by Berdnikov et al.[147–149] In this respect, both the aquated and BTPhen chelated complexes have been shown to behave similarly. Due to the greater stability of the metal bound superoxide complex over the hydroperoxyl analogue, the protonation of $[U^{VI}O_2(BTPhen)(^{\bullet}O_2)]^+$ by acidic species in the bulk solvent has been shown to be an unfavourable process. This reaction is modelled by the transition from ***M6*** to ***M11*** in the updated first ET mechanistic web in **Figure 62**. Despite the unfavourable nature of this reaction, it may be feasible for the uranyl(VI) deprotonation reaction, ***M5*** to ***M6***, and the superoxide protonation, ***M6*** to ***M11***, to occur *via* concerted PT reaction step, i.e. a direct transition from ***M5*** to ***M11***, should it prove to be a thermodynamically viable process.

4.3.3.3 The Concerted Proton Transfer

The thermodynamic feasibility of a concerted proton transfer step can be easily assessed as the difference in energy between the modelled protonated *U(VI)*-superoxide complex, ***M5***, and the corresponding non-protonated *U(VI)*-hydroperoxyl complex, ***M11***. This comparison has been made previously in Chapter 4.3.2.1.3, in order to gauge the stability conferred to the system on forming an intramolecular hydrogen bond. The ΔG_{solv} for this proton transfer was found to be -9.4 kcal mol^{-1}. Thus, unlike the previously modelled sequential acid-base reactions leading to the protonation of the superoxide anion, the protonation of $^{\bullet}O_2^-$ in a concerted PT step from the nearby protonated uranyl(VI) ion is calculated to be a thermodynamically feasible process. However, despite the suggested thermodynamic feasibility of this process, the PT may not prove to be kinetically feasible if it has a particularly high barrier to activation. Probing the kinetic feasibility of this process is the focus of this chapter.

4.3.3.3.1 Direct PT Between Uranyl and Superoxide

Computational Details

In order to model the height of the barrier for the transfer of a proton directly from a uranyl(VI) ion to an equatorially bound superoxide anion, a relaxed PES scan was carried out using the gas phase optimised geometry of the uranyl(VI)-superoxide complex, ***M5***, as the starting point. In this optimised geometry, the distance between the proton on the uranyl ion and one of the superoxide oxygen atoms was constrained and subsequently shortened in 0.05 Å increments. Following each incremental change, all other atoms in the structure were allowed to relax to their minimum energy arrangement about the constrained bond. This process was repeated until the stationary point corresponding to the apex of the activation barrier for the PT had been identified. The PES scans were carried out at the uB3LYP/B1 level of theory in the absence of symmetry constraints. As described for previous examples,

acidic protons, i.e. those attached to or involved in hydrogen bonding interactions with oxygen atoms, were represented using a 6-311++G(d,p) basis. The energies calculated are presented without applying any thermodynamic or solvation corrections, thus the activation energy calculated cannot be considered a true activation barrier. However, it can be compared with confidence to the other PES scans carried out at the same level of theory in order to infer the relative feasibilities of the reactions modelled.

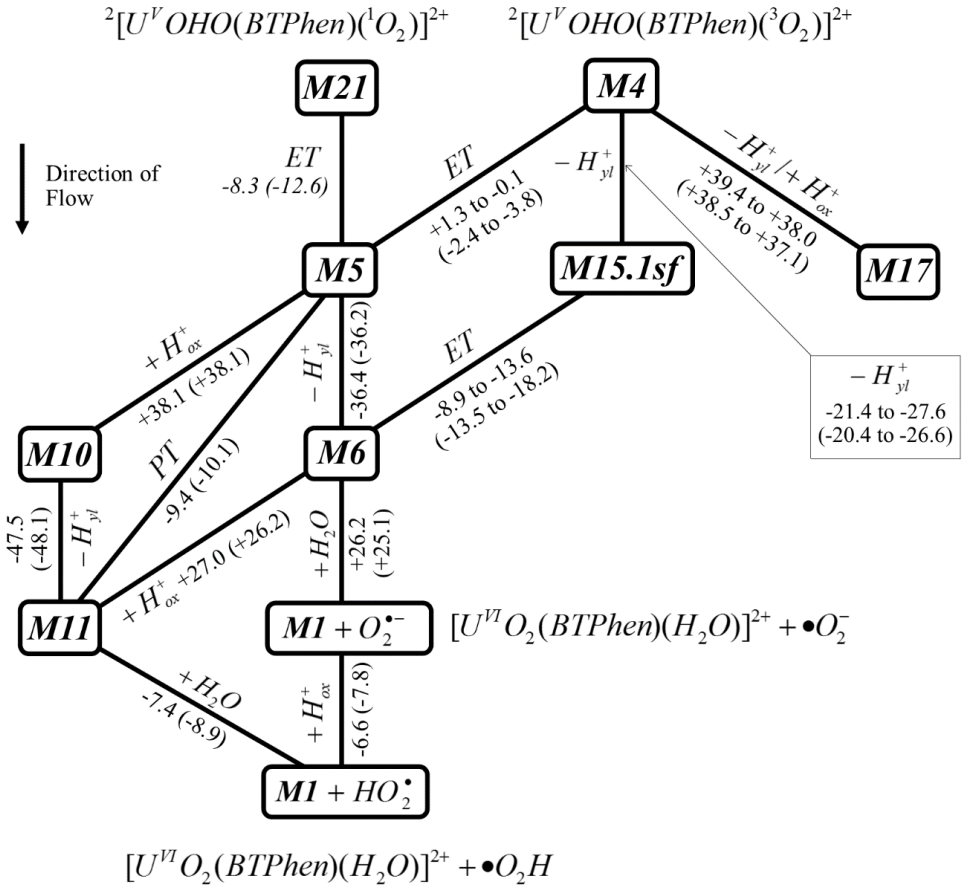

Figure 62: Mechanistic web schematic of the reactions relevant to the tail end of the initial IS-ET process and in particular the acid-base reactions that lead to the protonation and deprotonation of the uranyl and superoxide moieties and the ligand substitution reactions that may occur to regenerate the aquated uranyl catalyst. The boxed numbers refer to the model representative of that state, as detailed in the text. The models selected for inclusion in this schematic are those that do not violate the spin selection rule. Hence, as opposed to the lowest energy quartet multiplicity model ***M4.1*** being selected to model the protonated uranyl(V)-triplet dioxygen system at ***M4***, the doublet multiplicity state that lies 1 kcal mol^{-1} higher in energy has been used since an ET from this species to generate the doublet uranyl(VI)-superoxide product does not necessitate a change in the overall spin of the system. Each line connecting two models represents a reaction occurring. These lines are labelled with the calculated free energy (and enthalpy in parentheses) change for that process and a description of the reaction that has occurred. Where *ET* represents an electron transfer; *+/-H_{ox}* represents the addition or abstraction of a proton from the dioxygen unit; *+/-H_{yl}* represents the addition or abstraction of a proton from the uranyl ion; *+H_2O* represents the substitution of an equatorial hydroperoxyl radical or superoxide ligand for a molecule of water and '*hν+·H*' represents the photoexcitation of the uranyl(VI) ion in the corresponding complex and the quenching of this excited state via hydrogen atom abstraction from the solvent to generate a protonated uranyl(V) species. Reaction energies that could not be modelled, and thus have been inferred using the other energies presented in the thermodynamic cycles, have been italicised. All energies are reported in kcal mol^{-1} and solvation corrections have been applied in all cases. No BSSE or '*sf*' corrections have been applied to the values presented. The sign of the energy changes presented applies for reactions as they flow from the top of the schematic to the bottom.

The topography of the activation barrier, its height and a schematic indicating the changes in the relaxed structure of the complex as the PT reaction coordinate is traversed are presented in **Figure 63**.

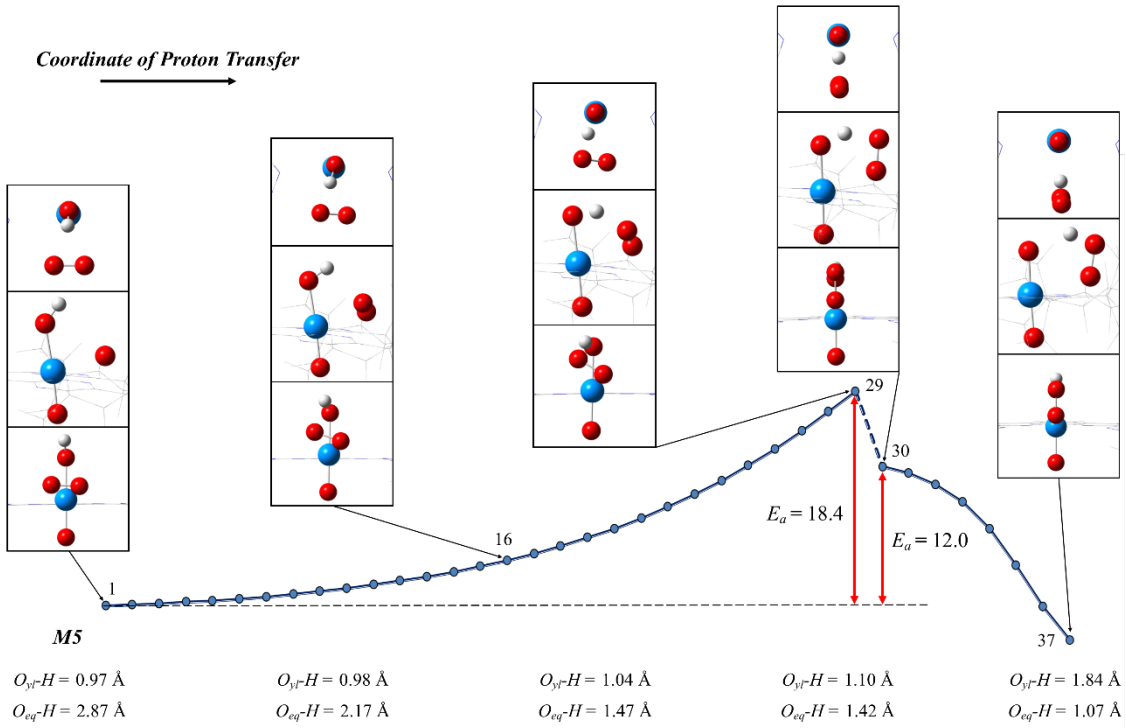

Figure 63: Schematic of a relaxed PES scan modelling the transfer of a proton directly from a uranyl(VI) O_{yl} atom to a bound superoxide. The discontinuities observed correspond to changes in the binding mode of the superoxide. The non-thermodynamically corrected activation energy for the proton transfer is included in the schematic. All energies are presented in kcal mol^{-1}

Considering **Figure 63**, it is clear that in order access the TS for the transfer of the proton on the uranyl ion directly to the equatorially bound superoxide ligand, the stabilisation energy associated with the bidentate binding mode of $^{\bullet}O_2^-$ must first be overcome. A gradual deformation of the bidentate binding mode of the equatorial ligand is observed between points 1 and 29 of the scan, i.e. between the ***M5*** starting geometry and the geometry in which the proton is 1.42 Å away from the superoxide. Following this point there is a sharp -6.4 kcal mol^{-1} discontinuity in the relaxed energy of the structure that corresponds with the breaking of the bidentate binding mode of the superoxide anion. This discontinuity is an artefact of the reaction coordinate followed to probe this process, thus, the true energy of the TS would be somewhere between the limiting values of 12.0 kcal mol^{-1} and 18.4 kcal mol^{-1}, but is likely to be significantly closer to the former than the latter. Following the formation of the monodentate complex, the proton transfer between the uranyl ion oxygen atom and the superoxide anion is found to be energetically favourable, leading

sharply downhill towards a structure in which the proton is more closely associated with the superoxide species, as shown by the geometry at point 37.

By way of comparison, a scan of the PES for the dissociation of the uranyl ion and the proton in model ***M5*** was carried out in a manner that attempted to avoid the bound superoxide acting as a proton acceptor. This was achieved by incrementing the uranyl oxygen atom to proton bond distance over a limited range of 0.97 Å to 1.62 Å. Above this range, the stationary point corresponding to the complete dissociation of these species was not identified. However, the massive 71 .8 kcal mol^{-1} energy input required to move the proton just 0.65 Å further from the uranyl ion into the vacuum indicates the stabilising effect that the concerted movement of the superoxide unit has on the feasibility of this PT. Clearly this huge barrier is artificially high, owing to the fact the gaseous model employed does not account for the solvation of the proton, which would be expect to stabilise the dissociated species somewhat in solution. However, it is useful in that it serves as a control model that describes the energetic penalty to the deprotonation of the uranyl ion in the absence of solvation.

4.3.3.3.2 PT between a Uranyl(VI) Ion and a Bound Superoxide Mediated by a Water Molecule

The largest component of the activation barrier to the direct PT reaction was associated with the deformation of the bidentate binding mode of the superoxide ion. However, in solution, such a deformation may not be necessary, as it is conceivable that this PT could be catalysed by an appropriately located solvent molecule able to accept the proton from the uranyl ion and then subsequently donate a second proton to the superoxide ligand. In this section, the action of a molecule of water as a mediator in the PT process is investigated.

Computational Details

In order to model such a process, the structure of ***M5*** was modified on addition of a single molecule of water located between the uranyl and superoxide species. The water molecule in the '***M5*** + H_2O' model created was orientated to act as a hydrogen bond donor to the superoxide anion and a hydrogen bond acceptor to the uranyl ion. The model was optimised in the gas phase using the uB3LYP/B1 level of theory, in the absence of any constraints and the converged geometry is presented in **Figure 64**.

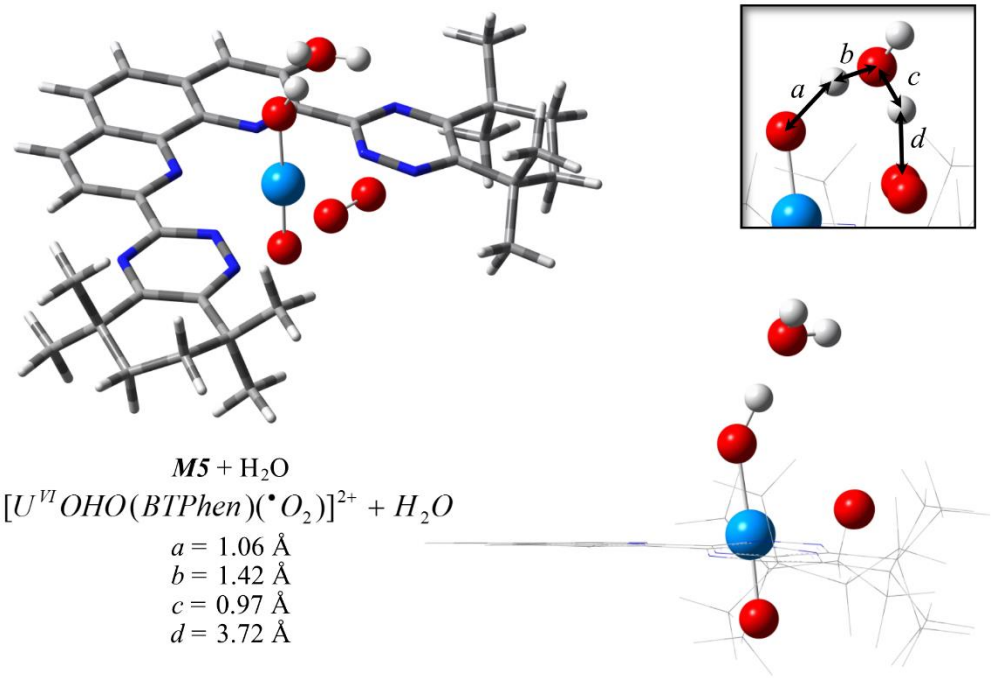

Figure 64: Structure of '***M5***+H_2O'; a model of an explicitly solvated protonated uranyl(VI) complex optimised in the absence of any geometric constraints. Selected geometric parameters are presented to facilitate comparison to other model geometries.

Following identification of this structure, a relaxed PES scan was carried out in which the constrained reaction coordinate described the transfer of the proton from the mediating water molecule to the superoxide anion (coordinate *d* in **Figure 64**). The constrained bond distance was decreased in increments of 0.05 Å until the stationary point corresponding to the transition state for the PT had been successfully traversed. This made it possible to calculate a non-thermodynamically corrected gas phase activation energy for the process, comparable to the direct transfer energy calculated in Chapter 4.3.3.3.1. A schematic of the surface topology traversed by this PES scan is presented in **Figure 65**.

Results and Discussion

The PES in **Figure 65** displays two features, each relating to a separate proton transfer event; one centred around point 5 and a second centred around point 15. On shortening the length of variable *d* between points 1 and 5, there is a gradual transfer of the proton initially bound to the uranyl ion towards the mediating water molecule. The shift results in slight hump in the PES (about point 5) prior to which the proton is predominantly associated with the uranyl ion and following which it is essentially under the influence of the water molecule. As this initial PT occurs, there is very little change in the second bridging *O-H* bond of the mediating water molecule, indicating that this minor energetic feature on the PES almost exclusively describes the first PT reaction. Despite this, it should be noted that there is necessarily some contribution to the total energetic destabilisation of this state due to the increasing strain

within the three membered hydrogen bonded bridge, brought about by the shortening of variable *d*. Following the initial PT, the system can be considered, descriptively, as a formally uranyl(VI)-hydroxonium-superoxide system.

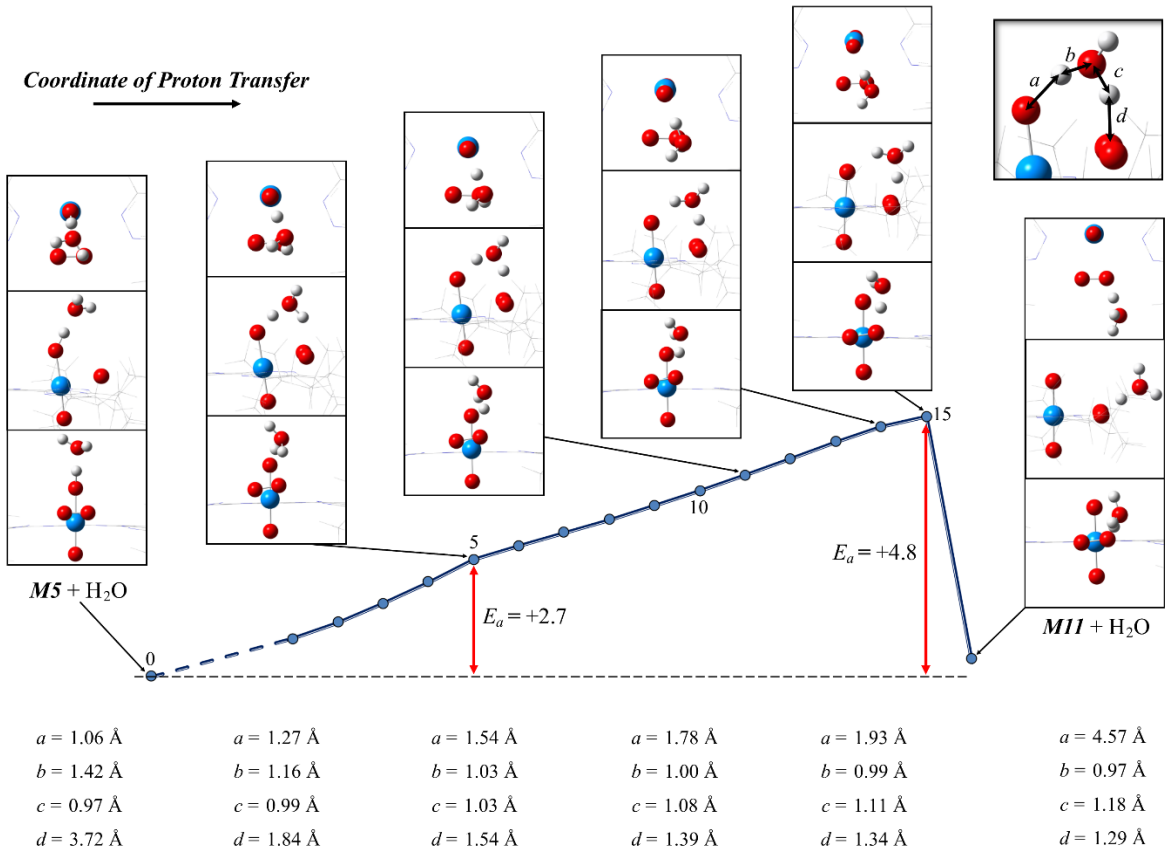

Figure 65: Schematic of the relaxed PES describing the water mediated transfer of a proton from an apical position on the uranyl(VI) ion to an equatorially bound superoxide anion. The points connected by solid lines are to scale and represent the points on the PES calculated by the scan procedure. The point connected to the scanned points by a dashed lines represents the energy of the unconstrained optimised initial geometry of the complex, '***M5***+H_2O' (as presented previously). For the purpose of clarity, this point is not presented using the same scale as the PES scan points and has only been used to calculate the activation energies for the PTs. All energies are presented in units of kcal mol^{-1} and were calculated using the uB3LYP/B1 functional-basis set combination without consideration of the effects of thermochemistry.

As the reaction coordinate is followed further uphill, there is the clear appearance of a second feature, at about point 15, corresponding to the transfer of a proton from the hydroxonium ion to the superoxide anion. Conceptually, the symmetric geometry of the two adjacent hydrogen bonds at point 11 is an appealing candidate for the TS. However, energetically, this is found to be the case, as confirmed by a second derivative test of the energy of the structure at point 15. This TS is henceforth referred to as '***TS-M5*** + H_2O'. The imaginary mode that characterises this TS describes the PT between the mediating hydroxonium ion and the superoxide anion and proceeds with little variation in the length of the two other *O-H* bonds of the hydroxonium ion. This confirms the previous suggestion that the PT coordinate occurs as two subsequent steps and not as one concerted process, although the barrier to the initial PT is dwarfed by that of the second.

Structurally, following point 11, the distance between the hydroxonium ion and the uranyl ion begins to increase swiftly, as the relaxed PES scan shifts to favour the transfer of the acidic proton on the hydroxonium ion to the superoxide anion and concomitantly disfavour the influence of the uranyl ion over its former proton. This second PT is accompanied by a rolling motion of the hydroxonium ion over the superoxide anion and towards empty space, as best exemplified by the difference between the structures depicted for points 15 and 16. The water molecule essentially passes out of the hydrogen bonded cavity between the uranyl ion and the superoxide anion towards the bulk solvent. This suggests that the complex formed following PT has a lower affinity for explicit solvation than that prior to PT. Such a lowered affinity between a solvating water molecule and the uranyl(VI)-superoxide bound species is reflected by the structure of an analogous complex, '***M24*** + *H_2O'*, in which it has been observed that in the absence of geometric constraints there is minimal stabilisation offered to the uranyl(VI)-hydroperoxyl radical complex by a free water molecule. This is demonstrated by the fact that the shortest contacts between the oxygen atom of the water molecule and the O_{yl} atoms and hydroperoxyl moieties are 3.17 Å and 4.23 Å, respectively in the non-protonated '***M24*** + *H_2O'* model, as compared to 2.47 Å and 3.89 Å in the protonated uranyl analogue, '***M5*** + *H_2O'*. Hence, it appears this species is able to provide very little stabilisation to the uranyl(VI)-superoxide complex by the way of hydrogen bonding, even in the gas phase.

It should be noted that ***M24*** differs from ***M11*** in the position of the proton in the hydrogen bond between superoxide and the BTPhen ligand. In the latter, the proton essentially rests on the superoxide, resulting in a model of a monodentate hydroperoxyl radical complex, whereas in the former, the proton resides predominantly on the BTPhen ligand, thereby describing a superoxide bound complex. Despite these structural differences, it is reasonable to assume that the explicit interactions between ***M11*** and the solvent will be bounded by the solvation behaviour observed for the ***M24*** model owing to the greater electrostatic charges on the O_{yl} atoms in the latter (NBO Charges: Average O_{yl} [***M24*** = -0.50] [***M11*** = -0.48]).

All energies calculated for the water mediated PT are presented **Table 31**. The data generated from the PES scan are by necessity raw electronic energy changes and hence no thermodynamic corrections have been taken into account in these quoted data. In order to gauge the effect of increasing the size of the basis set on these calculated energies, SP calculations were carried out on the initial and transition state structures identified by the scan, '***M5*** + *H_2O*' and '***TS-M5*** + *H_2O*' respectively, using the B2 basis set, following which

the appropriate thermodynamic corrections were applied to provide the PT activation energy presented in **Table 31**.

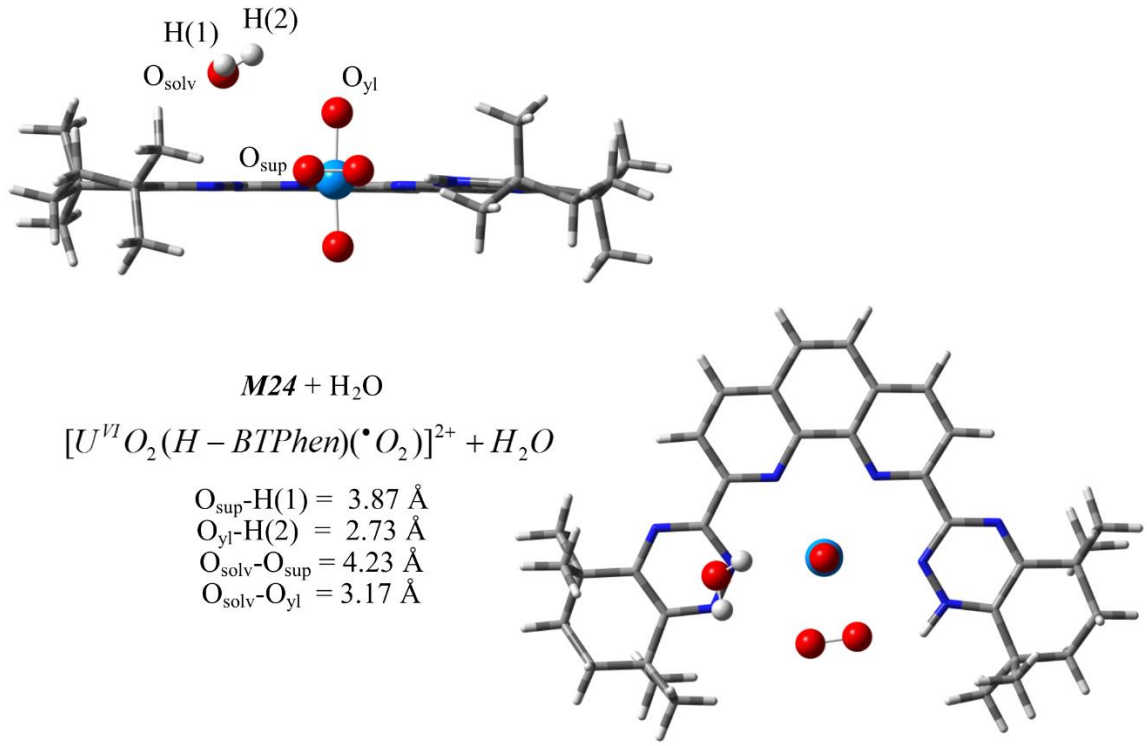

Figure 66: Unconstrained optimised geometry and selected structural parameters of the model '***M24*** + H_2O'.

Table 31: Table of the PT energies for the water mediated process as calculated using different computational parameters and corrections.[a]

	Explicit Only[b]	**Explicit Only[c]**	**Implicit and Explicit[d]**
	E_{elec} only – B1 (B2)	B2 – Δ*G* (Δ*H*)	B2 – Δ*G* (Δ*H*)
***E*$_a$ (1st PT)**	+2.72 (N/A)	N/A[e]	N/A[e]
***E*$_a$ (2nd PT)**	+4.83 (+7.26)	+10.08 (+6.70)	+8.01 (+4.63)

[a] All energies are presented in units of kcal mol^{-1}.
[b] The first column presents the raw electronic energies of the proton transfers calculated using the B1 and B2 basis sets in the presence of the explicitly defined water molecule.
[c] The second column presents the effect of including thermodynamic corrections on the barrier predicted at the B2 level.
[d] In addition to the thermodynamic corrections included in the second column, the final column presents the activation barriers as calculated on including an implicit solvation correction in the model. Comparison of the second and third columns thereby quantifies the stabilisation of the system due to solvation that has not been accounted for by the single explicit molecule defined.
[e] N/A is used to denote quantities not calculated at present.

The energy changes calculated for the PT reactions in **Table 31** are presently used to assess the effect of explicit solvation on the calculated energetics. Comparing initially the electronic energy changes calculated using the B1 and B2 basis sets, it is clear that increasing the size of the basis set from B1 to B2 increases the height of the activation barrier by approximately 2.5 kcal mol^{-1}. Hence, there is a relatively large dependence of the calculated energetics on the size of the basis set employed. Including thermodynamic corrections to the electronic

energies calculated using the B2 basis in the first column of **Table 31**, gives rise to the free energies and enthalpies presented in the second column. These quantities show that relative to the raw electronic energies calculated during the PES scan, accessing the TS is favoured by ~0.5 kcal mol^{-1} enthalpically, but disfavoured entropically by ~3.5 kcal mol^{-1} when corrections are added. As stated previously, in such large systems with multiple low lying modes there is a distinct possibility that the SHO model used to quantify the entropy may introduce significant error into the predicted reaction energies. This principle is particularly pertinent to these systems as they contain relatively weakly bound water molecules. Considering that the entropic correction factors observed here are non-trivial, more confidence may be ascribed to the reaction enthalpies as they are less susceptible to the error introduced by erroneously considering hindered internal rotations as vibrations in the SHO model.

It is clear, from comparison of the explicitly solvated electronic energy changes calculated using the B1 basis set to those calculated using the combined explicit and implicit solvation model, that in this particular example the solvation correction opposes in sign the error introduced by using a smaller basis set and neglecting thermodynamic corrections. This fortuitous cancellation of errors thereby provides solvated reaction enthalpies calculated using the B2 level that are within 0.2 kcal mol^{-1} of the less computationally demanding B1 electronic energies. Whilst it cannot be assumed that such an exact cancellation will have occurred in the other PES scans conducted, it is useful when gauging the relative applicability of the energies quoted for this particular PES scan that have not been modelled at the higher level of theory.

The free energy and free enthalpy of activation calculated for the water mediated PT reaction using the gas phase optimised model are predicted to be +8.01 kcal mol^{-1} and +4.63 kcal mol^{-1}, respectively (see **Table 31**). These values relate to a raw electronic activation energy of +4.83 kcal mol^{-1} for the water mediated PT process. Comparing this barrier to the range of activation energies calculated in Chapter 4.3.3.3.1 for the direct PT between a uranyl ion and an equatorially bound superoxide (ΔG_{solv} = 12.0 kcal mol^{-1} to 18.4 kcal mol^{-1}) it is apparent that the water mediated process is at least 7.17 kcal mol^{-1} more favourable than the direct PT. Hence, it is probable that should a PT occur between these species in the real system, the water mediated process would be favoured kinetically.

4.3.3.3.3 PT between a Uranyl(VI) Ion and a Bound Superoxide Mediated by a Water Molecule in a Bath of Implicit Solvent

Despite the significant reduction in the activation barrier to the PT process when a single explicitly defined mediating water molecule is included in the model, the data in **Table 31** shows that the description of solvation utilised during this PES scan is far from complete. This incompleteness manifested itself as a reduction in the height of the potential barrier of > 2 kcal mol^{-1} on employment of a solvation correction calculated using a SP continuum model at the appropriate gas phase optimised geometry. The magnitude of this solvation correction suggests that there may be a considerable degree of stabilisation accessible to the system during the PT, which has not been accounted for by the single water molecule. Hence, it is possible that repeating the PES scan in a bath of implicit solvent may provide a lower still activation barrier for the PT. This is a reasonable hypothesis from an empirical point of view, as proton transfers by their very nature involve the dissociation of highly charged species and thus any electrostatic screening of this excess charge by a dipolar solvent will act to facilitate the transfer. As discussed previously, the electrostatic screening effect of solvation is reasonably well described by simple continuum models. Thus, in order to test this hypothesis the relaxed PES scan of the '***M5*** + H_2O' system has been repeated in the presence of a continuum solvation model. This implicitly solvated PES scan will henceforth be referred to as the '***M5*** + H_2O + *Solv*' model.

Computational Details

The unconstrained optimised structure of the implicitly solvated model '***M5*** + H_2O + *Solv*' was identified using the gas phase optimised structure of '***M5*** + H_2O' as an initial guess. The geometry was optimised using the uB3LYP/B1 functional and basis set combination in the absence of any geometric or symmetry constraints whilst embedded in a CPCM model of solvation parameterised for bulk methanol. The optimised structure identified using this process is presented in **Figure 67**.

Following the identification of the solution phase optimised structure, a relaxed PES scan was carried out in which the geometric coordinate *d* in **Figure 67** was constrained and incremented in order to describe a reaction coordinate for the transfer of a proton from the mediating water molecule to the superoxide anion. During the PES scan, the length of coordinate *d* was incrementally shortened by 0.1 Å until a maximum in the PES had been identified. Following this point, the PES scan was repeated in the region of said maximum using shorter 0.025 Å increments in order to identify the stationary point in the PES to a greater degree of accuracy. The topology of the PES determined by this scan is presented in

Figure 68, along with informative images of the corresponding relaxed structures identified at certain points.

As detailed previously, due to the nature of relaxed PES scans, the energies presented in **Figure 68** are not corrected for thermodynamic effects.

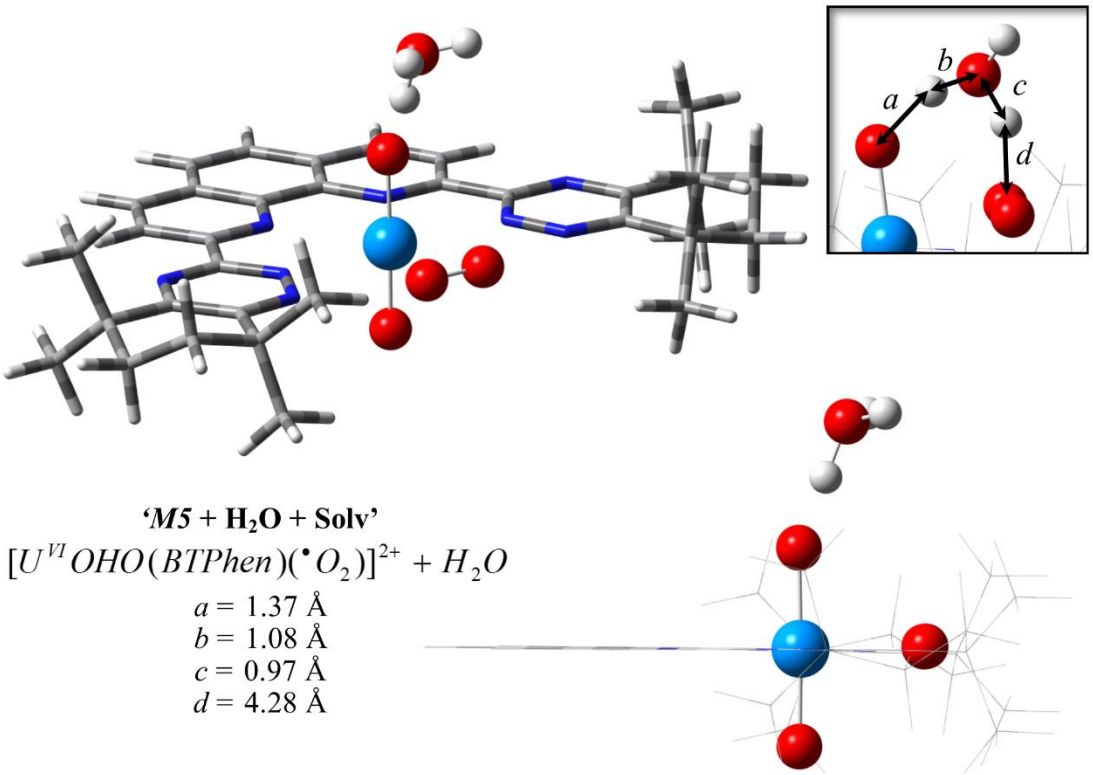

Figure 67: Figure of the optimised structure of 'M5 + H_2O + *Solv'*; a model of the protonated uranyl(VI)-superoxide complex and explicitly defined solvating water molecule optimised employing a continuum model of solvation. Selected geometric parameters are presented in order to facilitate comparison to other models.

Results and Discussion

Comparing the geometry of the '***M5*** + H_2O + *Solv'* model optimised in the presence of an implicit solvent field (**Figure 67**) to that of its gas phase optimised analogue, '***M5*** + H_2O*'* (**Figure 64**), one difference is abundantly clear; the equilibrium geometry of the proton between the uranyl ion and the solvating water molecule has shifted. The lowest energy position of the acidic proton from its initial location on the uranyl ion (*a* = 1.06 Å) shifts a position where it is primarily associated with the water molecule (*a* = 1.37 Å), essentially forming a $U^{VI}O_2$-H_3O^+ species in the process. The implication of this change to the overarching mechanism is that the first proton transfer modelled by the gas phase '***M5*** + H_2O' PES scan has a small 2.7 kcal mol^{-1} barrier to activation. This indicates that if the system were more adequately solvated, it would be likely to be a barrierless process.

Such a finding is not unexpected for this system, since it was found earlier in Chapter 4.3.3.1.1, when gauging the deprotonation energy of the aquated uranyl(VI) complex, $[U^{VI}OHO(BTPhen)H_2O]^{2+}$, that the uranyl(VI) ion spontaneously deprotonates on approach of an explicit molecule of water in the gas phase. Furthermore, subsequent comparison of the proton affinities of protonated uranyl(VI) complexes with different equatorial ligand fields suggested a direct proportionality between the proton affinity of the uranyl(VI) ion and the strength of the equatorial donor. Hence, as the bidentate superoxide ion is a stronger ligand for the uranyl ion than water, it is expected that the former species will have the greatest PA. Following on, the effect of including an implicit solvation model during the optimisation is to favour the separation of charge in the complex due to the electrostatic screening afforded by the model employed. In the gas phase the axial water molecule is exposed with respect to forming stabilising interactions with the other species in the system, hence there is little driving force for the delocalisation of positive charge onto this species. However, on inclusion of a solvation model able to screen such excess charge the energetic balance shifts and the protonation of the axial water molecule becomes increasingly favourable. Coincidently, it appears that the superoxide bound complex represents the tipping point in this energetic seesaw and thus on inclusion of a simple implicit solvation model the lowest energy position of the proton in the superoxide complex is seen to migrate from the uranyl ion towards the axial water molecule. Ultimately, this permits the conclusion that protonated uranyl(VI)-BTPhen complexes that are equatorially bound by a ligand with a similar affinity to or weaker than the superoxide anion will likely undergo a barrierless deprotonation in solution. Conversely, the deprotonation of uranyl(VI) species bound by stronger equatorial ligands than superoxide, such as peroxide, may possess a modest activation barrier to stimulate deprotonation even when solvated.

The PES scan in **Figure 68** represents the reaction coordinate describing the transfer of a proton from the hydroxonium ion to the superoxide anion. Although the first PT from the uranyl ion to the water molecule occurs without a barrier, the second PT does require a modest input of energy, as observed in the gas phase PES scan. However, as expected, the height of the barrier to the PT in solution is marginally lower than in the gas phase due to electrostatic screening of charge provided by the solvation model. Considering the non-thermodynamically corrected internal energy change calculated for the first PT, the height of the barrier is lowered from E_a = 4.83 kcal mol^{-1} when modelled in the gas phase to E_a = 4.25 kcal mol^{-1} when modelled in CPCM solution. This effect of solvation on the barrier is mirrored by the activation free energies ($\Delta G''$) and enthalpies ($\Delta H''$) calculated using the B2 basis set. $\Delta G''$ and $\Delta H''$ calculated using the solution phase optimised models are

5.91 kcal mol^{-1} and 5.69 kcal mol^{-1}, respectively, compared to the barriers to the gas phase transfer of 10.08 kcal mol^{-1} and 6.70 kcal mol^{-1}, respectively.

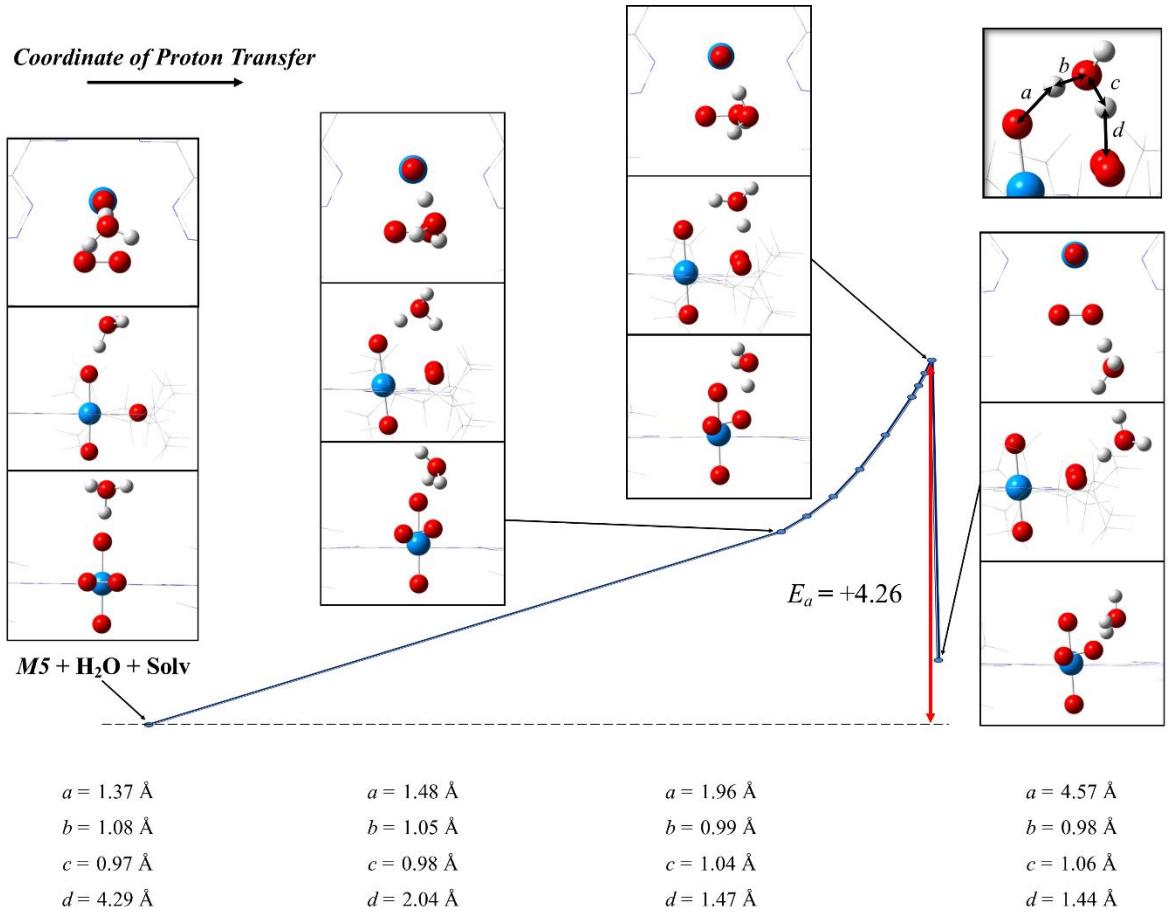

Figure 68: Schematic of the solvated relaxed PES describing the water mediated transfer of a proton from an apical position on the uranyl(VI) ion to an equatorially bound superoxide anion as optimised in the presence of a continuum solvation model. The points connected by solid lines are to scale and represent the geometric points on the PES calculated by the scan procedure. All energies are presented in units of kcal mol-1 and were calculated at the DZ level using the uB3LYP/B1 functional-basis set combination in the presence of a CPCM parameterised for methanol. These energies are raw solvated electronic energies and as such have not been corrected for the effects of thermochemistry.

The thermodynamically corrected barriers to activation for this solvated model were calculated using the B2 basis set at the geometries identified by the relaxed PES scan as the initial and TS structures. The height of the energetic barriers calculated as part of this relaxed CPCM PES scan are presented in **Table 32**, along with information replicated for the gas phase analogues for comparative purposes.

The SP calculations employing the B2 basis set with solvated geometries have higher predicted barriers than those employing the B1 basis set: from 4.26 kcal mol^{-1} calculated at the B1 level to a value of 5.40 kcal mol^{-1} at the B2 level (see **Table 32**). This is the same trend as for the gas phase geometries.

Table 32: Table of the activation free energy and enthalpy barriers calculated for the water mediated transfer of a proton from a protonated uranyl(VI) ion to an equatorially bound superoxide anion.[a]

	CPCM Opt – CPCM SP[b]	**CPCM Opt – CPCM SP[c]**	**Gaseous Opt – Gaseous SP[d]**	**Gaseous Opt – CPCM SP[e]**
	E_{elec} only – B1 (B2)	B2 - $\Delta G''$ ($\Delta H''$)	B2 - $\Delta G''$ ($\Delta H''$)	B2 - $\Delta G''$ ($\Delta H''$)
E_a **(2nd PT)**	4.26 (5.40)	5.91 (5.69)	+10.08 (+6.70)	+8.01 (+4.63)

[a] All energies are presented in kcal mol^{-1}.
[b] The first column gives the raw electronic activation energies calculated using the B1 and B2 basis sets using the geometries optimised in an implicit solvation model.
[c] The second column presents the activation energies calculated including thermodynamic corrections for temperature, pressure and disorder.
[d] For comparison to these new data, the third column presents the corresponding B2 activation energies calculated using a model in which no implicit solvation effects are taken into account
[e] The fourth column presents the corresponding activation energy when implicit solvation is accounted for using a SP solvation correction post optimisation.

These solvent phase optimised models are useful for assessing the validity of the gas phase models that have been applied throughout this study, which are corrected post-optimisation at the CPCM level. The last column in **Table 32** presents the activation energies calculated for the second PT using models optimised in the gas phase, to which a correction to account for the effects of implicit solvation has been applied post optimisation. Using this model, the barriers were calculated to be $\Delta G''$ = +8.01 kcal mol^{-1} and $\Delta H''$ = +4.63 kcal mol^{-1}. In addition, the second column in **Table 32** presents the activation energies calculated when the electrostatic screening effects of solvation were accounted for from the start of the optimisation onwards. These more rigourously solvated barriers were calculated to be $\Delta G''$ = +5.91 kcal mol^{-1} and $\Delta H''$ = +5.69 kcal mol^{-1}. There is therefore a difference of 2.1 kcal mol^{-1} between the free energy barriers calculated using the two solvation models and a 1.06 kcal mol^{-1} difference between the enthalpic barriers predicted. These discrepancies are ultimately tolerable considering the other sources of uncertainty inherent to the model. Hence, this comparison suggests that the fundamental assumption made in this study that the gas phase optimised structures of the uranyl-BTPhen-dioxygen complexes under study are a reasonable representation of their solution phase analogues is valid. As a further point for comparison that is also in support of this conclusion, the uranyl(VI)-hydroperoxyl radical complex, ***M11*** (*[UO_2(BTPhen)·O_2H]$^{2+}$*), was re-optimised in the presence of an implicit solvation model. The solution phase and gas phase optimised geometries of the ***M11*** complex are presented in **Figure 69**, below.

The geometries of the two optimised models are broadly similar with most differences being on the order of 0.01 Å in magnitude. There are a couple of notable changes in the interaction of the uranyl ion with its equatorial ligand field, however. These differences amount to an elongation of the bond between the uranium atom and the hydroperoxyl radical by 0.08 Å

and an elongation between the uranium atom and one of the triazinyl nitrogen atoms also by 0.08 Å (see **Figure 69**). Despite these differences, their combined effect on the absolute free energy and enthalpy of the system is minimal and of the same order of magnitude as observed when calculating the activation energies previously, amounting to 0.83 kcal mol^{-1} and 2.21 kcal mol^{-1}, respectively. Hence, this provides further evidence that the gas phase optimised structures of the uranyl-BTPhen-dioxygen complexes under study are a reasonable representation of their solution phase analogues and that this assumption does not introduce considerable error into the model.

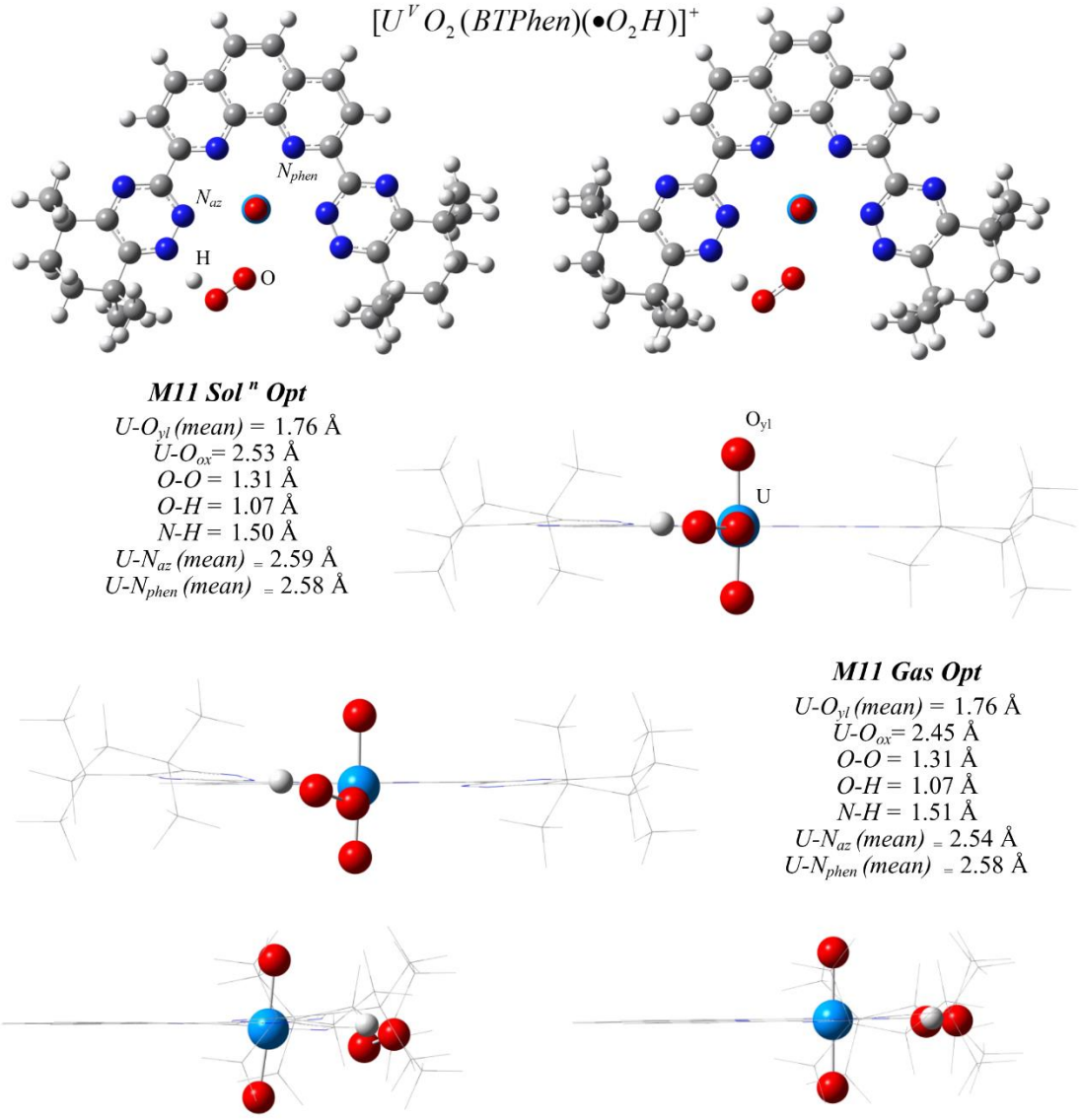

Figure 69: Optimised structures of the ***M11*** uranyl(VI)-hydroperoxyl complex when optimised in the presence of a CPCM parameterised for methanol (left column) and when optimised in the gas phase (right column).

4.3.3.3.4 Estimating the Rate Constant for the Proton Transfer from $UOHO^{3+}$ to $\cdot O_2$

The best estimate of the height of the barrier to PT discussed in this chapter is that calculated using the water mediated PT model optimised in the presence of a CPCM solvent model.

This model incorporates a reasonably complete description of solvation in that it contains an explicit consideration of solvation in the form of the mediating water molecule and an implicit description in the form of the electrostatic screening of charges provided by the CPCM model. The height of the free energy barrier predicted using this model, 5.69 kcal mol^{-1}, is therefore the most suitable value to estimate the rate of such a process occurring at room temperature. This can be achieved using the Eyring equation, expressed in **Equation 91**.

$$k = \frac{k_B T}{h} e^{-\frac{\Delta G''}{RT}} \qquad \textbf{(91)}$$

Where k represents the reaction rate constant, k_B the Boltzmann's constant, T the reaction temperature (298.15 K), h represents Planck's constant, $\Delta G''$ is the activation energy for the process and R is the ideal gas constant. This relationship suggests that, assuming Boltzmann statistics, a reaction temperature of 298.15 K and an activation free energy of 5.69 kcal mol^{-1}, 0.007% of dissolved species in this system have the energy required to overcome the activation threshold. This relates to a rate constant for the transfer of a proton between the protonated uranyl(VI) ion and an equatorially bound superoxide anion of 4.19 $x10^8$ s^{-1}. Whilst this is at the slow end of the range when compared to rate constants of other PT reactions,[204] it should be noted that it is likely to represent a lower bound of the empirical rate, owing to the imperfect nature of the solvation model used in this study.

4.3.3.3.5 Summary of Deprotonation, Dissociation and Proton Transfer Reactions of the Protonated Uranyl unit and Implications for the Overall Mechanism

In this chapter, through the use of thermodynamically corrected and solvated SP energies and relaxed PES scans of protonated and deprotonated uranyl models in the presence and absence of explicit solvent molecules, it has been possible to probe certain aspects of the chemistry of the novel and fleeting intermediate that is the protonated uranyl ion. It has been shown that, when protonated, the uranyl(V) and uranyl(VI) O_{yl} atoms are primed to form stabilising interactions with a polar solvent. Initial studies of protonated uranyl complexes bound equatorially by BTPhen and a single water molecule, i.e. complexes of the type $[UOHO(BTPhen)H_2O]^{2+/3+}$, suggested that the uranyl(V) ion has an inherent greater PA than its uranyl(VI) analogue, owing to the increased charge localised on the O_{yl} atoms of the former. Furthermore, it was found that the PA of the uranyl ion can be fine-tuned by varying the equatorial ligand field. Specifically, PA was found to vary in direct proportion with the strength of the equatorial interaction. Knowledge of this trend may be of use to synthetic chemists working in the expanding field of uranyl oxo-functionalisation. Owing to their

dissimilar proton affinities, the uranyl(V) and uranyl(VI) ions responded differently on approach of a polar solvent molecule. The protonated uranyl(V) ion was observed to form a hydrogen bond with an approaching water molecule of moderate strength, but ultimately retain its proton in the absence of an input of energy, whereas the protonated uranyl(VI) ion was observed to spontaneously deprotonate on approach of a molecule of water.

The chemistry of the equatorially bound superoxide anion was found to be just as dependent on the state of protonation as that of the uranyl ion. The dissociation of uranyl(VI)-superoxide complexes was found to be much less favourable than the dissociation of the corresponding uranyl(VI)-hydroperoxyl radical complexes, which led to the conclusion that the dominant species in solution is likely to be the former, in agreement with conclusions previously drawn by Berdnikov et al.[147–149] In turn, this finding impacted the mechanistic study, since if the protonation of uranyl superoxide complexes in solution is not a spontaneous process at room temperature but is still suspected to play a part in the mechanism, as hypothesised by Bakac et al., then its formation must be coupled to a strongly exergonic process. A suitable exergonic process was identified as the deprotonation of the uranyl(VI) unit. Relaxed PES scans of multiple reaction coordinates suggested that a water mediated transfer of a proton from the uranyl(VI) ion to the equatorially bound superoxide anion was the process with the lowest barrier to activation of 5.69 kcal mol^{-1}. This barrier corresponds to a rate on the order of 4.19 $x10^{8}$ s^{-1} and hence it does not preclude such a PT occurring on kinetic grounds.

In addition to these mechanistic implications, particular calculations encountered during this study allowed the validity of a fundamental assumption made during this study to be gauged. This assumption is that the gas phase optimised geometries of the uranyl species of interest are reasonable approximations of their solution phase optimised analogues. On comparison of reaction energetics calculated using gas phase and solution phase optimised models, it was found that this assumption introduced no more than 2.5 kcal mol^{-1} error into the model, whilst dramatically reducing the computational cost of the study. This was deemed a tolerable discrepancy on the grounds that is comparable to the amount of error associated with other assumptions in the computational methodology employed (see Chapter 2).

4.3.4 Step Back and Take in the View: A Preliminary Analysis of the Mechanism as a Whole

The conclusions of the previous section have various implications for the specific route that the catalytic formation of peroxide might follow. In particular, quantification of the reaction energies associated with acid-base reactions, studied in the last section, allow the individual

mechanistic web schematics presented earlier in this report to be combined to generate a single comprehensive schematic that describes the whole mechanism as identified up to this point **Figure 70**. In the following discussion, the acid-base equilibria are examined in order to identify whether any of the hypothetical ET reactions studied in Chapter 4.3.2 are essentially precluded from playing a significant role in the formation of peroxide. Such a situation may arise if the equilibrium does not lie in favour of the required precursor state.

4.3.4.1 A Chemical Description of the Effects of Acid-Base Equilibria on the ET Mechanistic Route

The following discussion is intended to clarify the different routes the mechanism could take after the first ET that forms superoxide and prior to the second ET that generates peroxide. There are many different pathways that could be taken by the mechanism in this region, since the protonation state of the species has a significant effect on its redox potential. The thermochemical feasibilities of these pathways are ultimately governed by the acid-base reactions that generate the different states. In each scheme broached in the following discussion, it is assumed that the first step in the process is the ET from a uranyl(V) species to an equatorially bound molecule of dioxygen. At this point, no reference will be made to the calculated feasibilities of the reaction schemes presented, as such a discussion will follow presentation of the updated mechanistic web.

In Chapter 4.3.3 it was found that the uranyl(VI) ion possessed a lower PA than the uranyl(V) ion. This difference resulted in the barrierless deprotonation of the former, in contrast with the latter. This suggests that following excitation and hydrogen atom abstraction, the most kinetically favourable mechanistic route to generate a deprotonated uranyl product is for deprotonation to occur via a barrierless process after the ET, as described by **Equations 59** and **60**. This deprotonation could occur via two pathways, both of which start with the approach of a water molecule on the apically bound proton and the subsequent transfer of said proton to the solvent.

In the first possible pathway, outlined in **Scheme 1**, following deprotonation of the protonated uranyl(VI) ion and the concomitant formation of the hydroxonium ion, the latter species migrates away from the reaction site and returns to the bulk solvent. This process thereby generates a uranyl(VI)-superoxide complex and a solvated hydroxonium ion as outlined by **Equation 60**. Since the uranyl(VI)-superoxide complex has been shown to be a persistent species in solution[143] and hence, it is likely that it could exist long enough to be excited by an ambient photon of light, transforming it into an excited state uranyl(VI)-superoxide complex, described by **Equation 61**. Subsequently, this species is

quenched by abstracting a hydrogen atom from an apically located solvent molecule in order to generate a reactive protonated uranyl(V)-superoxide complex as per **Equation 62**. This species then undergoes a rapid intramolecular ET generating the protonated uranyl(VI)-peroxide complex (**Equation 63**), followed by spontaneous deprotonation on approach of a molecule of solvent to give the peroxide bearing product, **Equation 64**.

Scheme 1

$$[U^{V}OHO(O_2)]^{2+} \xrightarrow{ET} [U^{VI}OHO(\bullet O_2)]^{2+} \quad \textbf{(59)}$$

$$[U^{VI}OHO(\bullet O_2)]^{2+} + H_2O \longrightarrow [U^{VI}O_2(\bullet O_2)]^{+} + H_3O^{+} \quad \textbf{(60)}$$

$$[U^{VI}O_2(\bullet O_2)]^{+} \xrightarrow{h\nu} {}^{*}[U^{VI}O_2(\bullet O_2)]^{+} \quad \textbf{(61)}$$

$${}^{*}[U^{VI}O_2(\bullet O_2)]^{+} + H_3COH \longrightarrow [U^{V}OHO(\bullet O_2)]^{+} + H_2\dot{C}OH \quad \textbf{(62)}$$

$$[U^{V}OHO(\bullet O_2)]^{+} \xrightarrow{ET} [U^{VI}OHO(O_2)]^{+} \quad \textbf{(63)}$$

$$[U^{VI}OHO(O_2)]^{+} + H_2O \longrightarrow [U^{VI}O_2(O_2)] + H_3O^{+} \quad \textbf{(64)}$$

In summation, **Scheme 1** represents the baseline scheme in this study as it invokes the minimum number of acid-base equilibria possible in this process; solely the individual deprotonation reactions of the protonated uranyl ions formed by the hydrogen atom abstraction steps. From this point onwards, the models incorporate an additional layer of complexity into the mechanism in the form of protonation of the superoxide species, as described by **Scheme 2** through to **Scheme 7**.

In **Scheme 1**, following the deprotonation of the uranyl ion in **Equation 60**, the hydroxonium ion that was formed returned to the bulk solution. However, as discussed in the previous chapter, it is possible that the system following deprotonation has sufficient energy to immediately undergo a second proton transfer reaction from the hydroxonium ion to the uranyl bound superoxide anion, generating a uranyl(VI)-hydroperoxyl radical complex, as per **Equation 92**. This study has shown that such a species is considerably less stable than its superoxide analogue and it could hence undergo further reaction via different routes. The most simple of which is arguably the scheme that lies at the other end of the spectrum relative to **Scheme 1**, i.e. a scheme in which an ET from a protonated uranyl(V) ion to an equatorially bound hydroperoxyl radical occurs, as described by **Scheme 2**.

Scheme 2

$$[U^{V}OHO(O_2)]^{2+} \xrightarrow{ET} [U^{VI}OHO(\bullet O_2)]^{2+} \quad \textbf{(59)}$$

$$[U^{VI}OHO(\bullet O_2)]^{2+} + H_2O \longrightarrow [U^{VI}O_2(\bullet O_2)]^{+}(H_3O^{+}) \longrightarrow [U^{VI}O_2(\bullet O_2H)]^{2+} + H_2O \quad \textbf{(92)}$$

$$[U^{VI}O_2(\bullet O_2H)]^{2+} \xrightarrow{h\nu} {}^{*}[U^{VI}O_2(\bullet O_2H)]^{2+} \quad \textbf{(93)}$$

$${}^{*}[U^{VI}O_2(\bullet O_2H)]^{2+} + H_3COH \longrightarrow [U^{V}OHO(\bullet O_2H)]^{2+} + H_2\dot{C}OH \quad \textbf{(94)}$$

$$[U^{V}OHO(\bullet O_2H)]^{2+} \xrightarrow{ET} [U^{VI}OHO(O_2H)]^{2+} \quad \textbf{(95)}$$

$$[U^{VI}OHO(O_2H)]^{2+} + H_2O \longrightarrow [U^{VI}O_2(O_2H)]^{+} + H_3O^{+} \quad \textbf{(96)}$$

Scheme 3 outlines a possible mechanism in which the hydroperoxyl ligand (formed in **Equation 92**) undergoes deprotonation, generating a uranyl(VI)-superoxide complex, which was the product of **Scheme 1** though in this case, the hydroperoxyl radical played no part in its synthesis.

Scheme 3

$$[U^{V}OHO(O_2)]^{2+} \xrightarrow{ET} [U^{VI}OHO(\bullet O_2)]^{2+} \quad \textbf{(59)}$$

$$[U^{VI}OHO(\bullet O_2)]^{2+} + H_2O \longrightarrow [U^{VI}O_2(\bullet O_2)]^{+}(H_3O^{+}) \longrightarrow [U^{VI}O_2(\bullet O_2H)]^{2+} + H_2O \quad \textbf{(92)}$$

$$[U^{VI}O_2(\bullet O_2H)]^{2+} + H_2O \longrightarrow [U^{VI}O_2(\bullet O_2)]^{+} + H_3O^{+} \quad \textbf{(97)}$$

$$[U^{VI}O_2(\bullet O_2)]^{+} \xrightarrow{h\nu} {}^{*}[U^{VI}O_2(\bullet O_2)]^{+} \quad \textbf{(61)}$$

$${}^{*}[U^{VI}O_2(\bullet O_2)]^{+} + H_3COH \longrightarrow [U^{V}OHO(\bullet O_2)]^{+} + H_2\dot{C}OH \quad \textbf{(62)}$$

$$[U^{V}OHO(\bullet O_2)]^{+} \xrightarrow{ET} [U^{VI}OHO(O_2)]^{+} \quad \textbf{(63)}$$

$$[U^{VI}OHO(O_2)]^{+} + H_2O \longrightarrow [U^{VI}O_2(O_2)] + H_3O^{+} \quad \textbf{(64)}$$

The potential mechanism in **Scheme 4** highlights the possibility that the uranyl(VI)-hydroperoxyl radical complex may dissociate, generating the first species encountered in this mechanistic cycle, ***M1***, the aquated uranyl complex and a free hydroperoxyl radical (**Equation 98** in **Scheme 4**). The hydroperoxyl radical subsequently disproportionates to generate dioxygen and hydrogen peroxide in equal quantities, as per **Equation 99**. This disproportionation could of course occur between two solvated

hydroperoxyl radicals or between two uranyl-hydroperoxyl complexes or even between a complexed hydroperoxyl radical and a solvated radical. However, based on experimentally determined rate constants,[142,143] it is likely that the disproportionation of the free solvated species occurs most frequently in solution. In mind of earlier findings in this study, it is likely that this difference in rate is due to the large driving force to deprotonate the hydroperoxyl radical once complexed. In addition, once it has lost its proton, the superoxide anion is not only able to form a stronger bidentate with the uranyl ion, but also localises a greater negative charge. These factors contribute to the greater height of the Coulombic barrier associated with the mutual approach of the disproportionating species.

Scheme 4

$$[U^{V}OHO(O_2)]^{2+} \xrightarrow{ET} [U^{VI}OHO(\bullet O_2)]^{2+} \quad \textbf{(59)}$$

$$[U^{VI}OHO(\bullet O_2)]^{2+} + H_2O \longrightarrow [U^{VI}O_2(\bullet O_2)]^{+}(H_3O^{+}) \longrightarrow [U^{VI}O_2(\bullet O_2H)]^{2+} + H_2O \quad \textbf{(92)}$$

$$[U^{VI}O_2(\bullet O_2H)]^{2+} + H_2O \longleftrightarrow [U^{VI}O_2(H_2O)]^{2+} + \bullet O_2H \quad \textbf{(98)}$$

$$\bullet O_2H + \bullet O_2H \longrightarrow O_2 + H_2O_2 \quad \textbf{(99)}$$

Although the solvated hydroperoxyl radical is quite reactive, this species is known to have a finite and measurable lifetime in aqueous solution. Hence, at low concentrations, it could persist long enough either to encounter and bind to a protonated uranyl(V) species (**Equations 100** and **101** in **Scheme 5**) or a uranyl(VI) species (reverse of equilibrium described by **Equation 98** in **Scheme 6**) in solution. Subsequently, the ET and surrounding cascade reactions described in **Scheme 1, Scheme 3** and **Scheme 4** could occur generating a uranyl(VI)-peroxide complex as described by **Scheme 6**.

All of the routes outlined to this point have involved the two subsequent inner sphere ET reactions to generate peroxide. However, as stated previously, the standard reduction potentials for the uranyl(V) and hydroperoxyl ions suggest that the second ET step of interest, the ET from a uranyl(V) ion to a hydroperoxyl radical (or superoxide anion) would be thermodynamically favourable via an outer sphere mechanism. Such a scenario is described in **Scheme 7**, in which a protonated uranyl(V) species is oxidised by a solvated hydroperoxyl radical in a process that does not involve the formation of a discrete complex between the reactants, **Equation 102**.

Scheme 5

$$[U^{V}OHO(O_2)]^{2+} \xrightarrow{ET} [U^{VI}OHO(\bullet O_2)]^{2+} \quad \textbf{(59)}$$

$$[U^{VI}OHO(\bullet O_2)]^{2+} + H_2O \longrightarrow [U^{VI}O_2(\bullet O_2)]^{+}(H_3O^{+}) \longrightarrow [U^{VI}O_2(\bullet O_2H)]^{2+} + H_2O \quad \textbf{(92)}$$

$$[U^{VI}O_2(\bullet O_2H)]^{2+} + H_2O \xleftrightarrow{} [U^{VI}O_2(H_2O)]^{2+} + \bullet O_2H \quad \textbf{(98)}$$

$$[U^{V}OHO(H_2O)]^{2+} + \bullet O_2H \xleftrightarrow{} [U^{V}OHO(\bullet O_2H)]^{2+} + H_2O \quad \textbf{(100)}$$

$$[U^{V}OHO(\bullet O_2H)]^{2+} + H_2O \longrightarrow [U^{V}OHO(\bullet O_2)]^{+} + H_3O^{+} \quad \textbf{(101)}$$

$$[U^{V}OHO(\bullet O_2)]^{+} \xrightarrow{ET} [U^{VI}OHO(O_2)]^{+} \quad \textbf{(63)}$$

$$[U^{VI}OHO(O_2)]^{+} + H_2O \longrightarrow [U^{VI}O_2(O_2)] + H_3O^{+} \quad \textbf{(64)}$$

Scheme 6

$$[U^{V}OHO(O_2)]^{2+} \xrightarrow{ET} [U^{VI}OHO(\bullet O_2)]^{2+} \quad \textbf{(59)}$$

$$[U^{VI}OHO(\bullet O_2)]^{2+} + H_2O \longrightarrow [U^{VI}O_2(\bullet O_2)]^{+}(H_3O^{+}) \longrightarrow [U^{VI}O_2(\bullet O_2H)]^{2+} + H_2O \quad \textbf{(92)}$$

$$[U^{VI}O_2(\bullet O_2H)]^{2+} + H_2O \xleftrightarrow{} [U^{VI}O_2(H_2O)]^{2+} + \bullet O_2H \quad \textbf{(98)}$$

$$[U^{VI}O_2(\bullet O_2H)]^{2+} + H_2O \longrightarrow [U^{VI}O_2(\bullet O_2)]^{+} + H_3O^{+} \quad \textbf{(97)}$$

$$[U^{VI}O_2(\bullet O_2)]^{+} \xrightarrow{h\nu} {}^{*}[U^{VI}O_2(\bullet O_2)]^{+} \quad \textbf{(61)}$$

$${}^{*}[U^{VI}O_2(\bullet O_2)]^{+} + H_3COH \longrightarrow [U^{V}OHO(\bullet O_2)]^{+} + H_2\dot{C}OH \quad \textbf{(62)}$$

$$[U^{V}OHO(\bullet O_2)]^{+} \xrightarrow{ET} [U^{VI}OHO(O_2)]^{+} \quad \textbf{(63)}$$

$$[U^{VI}OHO(O_2)]^{+} + H_2O \longrightarrow [U^{VI}O_2(O_2)] + H_3O^{+} \quad \textbf{(64)}$$

Scheme 7

$$[U^{V}OHO(H_2O)]^{2+} + \bullet O_2H \xrightarrow{ET} [U^{VI}OHO(H_2O)]^{3+} + [O_2H]^{-} \quad \textbf{(102)}$$

$$[U^{VI}OHO(H_2O)]^{3+} + H_2O \longrightarrow [U^{VI}O_2(H_2O)]^{2+} + H_3O^{+} \quad \textbf{(103)}$$

4.3.4.2 All Mechanisms

The individual reaction equations that make up **Scheme 1** – **Scheme 7** are repeated in **Table 33**, along with the other reactions that can be modelled using the structures discussed to this point. This table is intended to act as a Rosetta stone that allows the pictorial representation of the mechanistic web, **Figure 70**, to be translated into chemical terms as well as the nomenclature applied by this paper. As such, it presents the reaction energies and designated equation references alongside the chemical equation specific to each reaction and the names of the corresponding models used to describe it e.g. $[U^{VI}OHO(^{\bullet}O_2)]^{2+}$ = ***M5***. It should be noted that in the chemical equations presented in **Table 33**, the equatorial ligand field of the uranyl ions has been simplified to consider only the interaction at the active site of the uranium photocatalyst, i.e. the uranyl-oxygen bond. This simplification is made purely to increase the readability of the chemical equations by omitting the BTPhen ligand, which is common to all models.

As stated previously, the reaction schematics described by **Scheme 1** to **Scheme 7** are not exhaustive as they merely serve to draw the reader's attention to the competition between the different processes that, theoretically, could be occurring in solution. A more complete description of the different processes modelled can be found in the mechanistic web itself, however even here some connections between models have been ignored in order to preserve interpretability of the diagram. The most complete description of the modelled processes is the list of chemical phenomena in **Table 33**, in which any chemical schemes that are not represented by the web schematic in **Figure 70** have been marked with an asterisk.

Figure 70 presents the reaction web schematic incorporating the majority of the models presented in this study. The schematic provides a visual means to discriminate between the competing reactions in the processes in terms of thermodynamic feasibility. This is achieved using a colour coded convention, whereby the lines representing reactions that have been predicted to be spontaneous at RT and those that have been found to be essentially energetically neutral or within error of the method employed (~2.5 kcal mol^{-1}) are coloured green, whilst those that have been calculated to be non-spontaneous are coloured red. This allows the web schematic to be used to identify whether any of the modelled routes from the aquated uranyl(VI) complex, ***M1***, to the peroxide bound uranyl(VI) complex, ***M9***, are predicted to be spontaneous in their entirety (with the exception of the photoexcitation steps). This is found to be the case for a handful of the possible schemes discussed and these routes will be outlined below.

Table 33: Table listing all of the reactions modelled in this study in order of model designation.[a,b]

Equation #	Chemical Equation	Web Schematic Route	ΔG_{solv} (ΔH_{solv})
104	$[U^{VI}O_2(H_2O)]^{2+} \xrightarrow{h\nu} *[U^{VI}O_2(H_2O)]^{2+}$	***M1*** $\longrightarrow$ ***M2***	N/A
105	$*[U^{VI}O_2(H_2O)]^{2+} + H_3COH \longrightarrow {}^2[U^{V}OHO(H_2O)]^{2+} + H_2\dot{C}OH$		
51	$[U^{VI}O_2(H_2O)]^{2+} + {}^3O_2 \longrightarrow {}^3[U^{VI}O_2(O_2)]^{2+} + H_2O$	***M1*** $\longrightarrow$ ***M3***	+11.7 (+14.0)
52	$[U^{VI}O_2(H_2O)]^{2+} + {}^1O_2 \longrightarrow {}^1[U^{VI}O_2(O_2)]^{2+} + H_2O$	***M1*** $\longrightarrow$ ***M20***	-20.5 (-15.9)
103	$[U^{VI}OHO(H_2O)]^{3+} + H_2O \longrightarrow [U^{VI}O_2(H_2O)]^{2+} + H_3O^+$	***M1b*** $\longrightarrow$ ***M1*** *	-52.7 (-52.9)
123	$[U^{VI}O_2(H_2O)]^{2+} + U^{VI}O_2(NO_3)_2(H_2O) + HO_2^- \longrightarrow [(U^{VI}O_2)_2(O_2)(NO_3)_2] + [H(H_2O)_2]^+$	***M1*** $\longrightarrow$ ***M28***	-29.9 (-48.4)
106	$[U^{V}OHO(H_2O)]^{2+} + H_2O \longrightarrow [U^{V}O_2(H_2O)]^{+} + H_3O^+$	***M2*** $\longrightarrow$ ***M2b***	-9.7 (-9.3)
53	${}^2[U^{V}OHO(H_2O)]^{2+} + {}^3O_2 \longrightarrow {}^2[U^{V}OHO(O_2)]^{2+} + H_2O$	***M2*** $\longrightarrow$ ***M4***	+12.4 to +13.8 (+13.8 to +15.2)
100	${}^2[U^{V}OHO(H_2O)]^{2+} + {}^{\bullet}O_2H \longrightarrow {}^1[U^{V}OHO({}^{\bullet}O_2H)]^{2+} + H_2O$	***M2*** $\longrightarrow$ ***M12a.1sf*** *	N/A
107	${}^1[U^{V}OHO(H_2O)]^{2+} + {}^1O_2 \longrightarrow {}^1[U^{V}OHO(O_2)]^{2+} + H_2O$	***M2*** $\longrightarrow$ ***M21***	*-20.5 (-15.9)*
108	${}^3[U^{VI}O_2(O_2)]^{2+} \xrightarrow{h\nu} *({}^3[U^{VI}O_2(O_2)]^{2+})$	***M3*** $\longrightarrow$ ***M4***	N/A
109	$*({}^3[U^{VI}O_2(O_2)]^{2+}) + H_3COH \longrightarrow *({}^2[U^{V}OHO(O_2)]^{2+}) + H_2\dot{C}OH$		
55	${}^2[U^{V}OHO(O_2)]^{2+} \xrightarrow{ET} {}^2[U^{VI}OHO({}^{\bullet}O_2)]^{2+}$	***M4*** $\xrightarrow{ET}$ ***M5***	-0.1 to +1.3 (-3.8 to -2.4)
110	${}^2[U^{V}OHO(O_2)]^{2+} + H_2O \longrightarrow {}^2[U^{V}O_2(O_2)]^{+} + H_3O^+$	***M4*** $\longrightarrow$ ***M15.1sf***	-27.6 to -21.4 (-26..6 to -20.4)

111	$^2[U^{V}OHO(O_2)]^{2+} \xrightarrow{PT} {}^2[U^{V}O_2(O_2H)]^{2+}$	***M4*** $\longrightarrow$ ***M17***	+38.0 to +39.4 (+37.1 to +38.5)
60	$^2[U^{VI}OHO(^{\bullet}O_2)]^{2+} + H_2O \longrightarrow {}^2[U^{VI}O_2(^{\bullet}O_2)]^{+} + H_3O^{+}$	***M5*** $\longrightarrow$ ***M6***	-36.4 (-36.2)
112	$^2[U^{VI}OHO(^{\bullet}O_2)]^{2+} + H_3O^{+} \longrightarrow {}^2[U^{VI}OHO(^{\bullet}O_2H)]^{3+} + H_2O$	***M5*** $\longrightarrow$ ***M10***	+38.1 (+38.1)
92	$^2[U^{VI}OHO(^{\bullet}O_2)]^{2+} + H_2O \xrightarrow{PT} {}^2[U^{VI}O_2(^{\bullet}O_2H)]^{2+} + H_2O$	***M5*** $\longrightarrow$ ***M11***	-9.4 (-10.1)
89	$^2[U^{VI}O_2(^{\bullet}O_2)]^{+} + H_2O \longrightarrow [U^{VI}O_2(H_2O)]^{2+} + {}^{\bullet}O_2^{-}$	***M6*** $\longrightarrow$ ***M1*** + $^{\bullet}O_2^{-}$	+26.2 (+25.1)
61	$^2[U^{VI}O_2(^{\bullet}O_2)]^{+} \xrightarrow{h\nu} *(^2[U^{VI}O_2(^{\bullet}O_2)]^{+})$	***M6*** $\longrightarrow$ ***M7***	N/A
62	$*(^2[U^{VI}O_2(^{\bullet}O_2)]^{+}) + H_3COH \longrightarrow {}^1[U^{V}OHO(^{\bullet}O_2)]^{+} + H_2\dot{C}OH$		
87	$^2[U^{VI}O_2(^{\bullet}O_2)]^{+} + H_3O^{+} \longrightarrow {}^2[U^{VI}O_2(^{\bullet}O_2H)]^{2+} + H_2O$	***M6*** $\longrightarrow$ ***M11***	+27.0 (+26.2)
63	$^1[U^{V}OHO(^{\bullet}O_2)]^{+} \xrightarrow{ET} [U^{VI}OHO(O_2)]^{+}$	***M7*** $\longrightarrow$ ***M8***	+0.5 to +3.6 (-0.6 to +2.5)
65	$^1[U^{V}OHO(^{\bullet}O_2)]^{+} + H_2O \longrightarrow {}^1[U^{V}O_2(^{\bullet}O_2)] + H_3O^{+}$	***M7*** $\longrightarrow$ ***M16***	+8.9 to +12.0 (+8.5 to +11.6)
127	$^1[U^{V}OHO(^{\bullet}O_2)]^{+} + U^{VI}O_2(NO_3)_2(H_2O) \longrightarrow {}^1[(U^{V}OHO)(U^{VI}O_2)(^{\bullet}O_2)(NO_3)_2]^{+} + H_2O$	***M7*** $\longrightarrow$ ***M18.1sf***	+18.4 to +24.3 (+0.0 to +5.9)
64	$[U^{VI}OHO(O_2)]^{+} + H_2O \longrightarrow [U^{VI}O_2(O_2)] + H_3O^{+}$	***M8*** $\longrightarrow$ ***M9***	-7.1 (-6.6)
124	$[U^{VI}O_2(O_2)] + U^{VI}O_2(NO_3)_2(H_2O) \longrightarrow [(U^{VI}O_2)_2(O_2)(NO_3)_2] + H_2O$	***M9*** $\longrightarrow$ ***M28***	-6.2 (-27.1)
113	$^2[U^{VI}OHO(^{\bullet}O_2H)]^{3+} + H_2O \longrightarrow {}^2[U^{VI}O_2(^{\bullet}O_2H)]^{2+} + H_3O^{+}$	***M10*** $\longrightarrow$ ***M11***	-47.5 (-48.1)
88	$^2[U^{VI}O_2(^{\bullet}O_2H)]^{2+} + H_2O \longrightarrow [U^{VI}O_2(H_2O)]^{2+} + {}^{\bullet}O_2H$	***M11*** $\longrightarrow$ ***M1*** + $\bullet O_2H$	-7.4 (-8.9)

93	$^{2}[U^{VI}O_2(^{\bullet}O_2H)]^{2+} \xrightarrow{h\nu} *(^{2}[U^{VI}O_2(^{\bullet}O_2H)]^{2+})$	***M11* ⟶ *M12a.1sf***	N/A
94	$*(^{2}[U^{VI}O_2(^{\bullet}O_2H)]^{2+}) + H_3COH \longrightarrow {}^{1}[U^{V}OHO(^{\bullet}O_2H)]^{2+} + H_2\dot{C}OH$		
101	$^{1}[U^{V}OHO(^{\bullet}O_2H)]^{2+} + H_2O \longrightarrow {}^{1}[U^{V}OHO(^{\bullet}O_2)]^{2+} + H_3O^{+}$	***M12a.1sf* ⟶ *M7***	-19.2 to -15.0 (-17.9 to -13.7)
71	$^{1}[U^{V}OHO(^{\bullet}O_2H)]^{2+} + H_2O \longrightarrow {}^{1}[U^{V}O_2(^{\bullet}O_2H)]^{+} + H_3O^{+}$	***M12a.1sf* ⟶ *M12b.1sf***	-20.3 to -15.0 (-20.4 to -15.1)
95	$^{1}[U^{V}OHO(^{\bullet}O_2H)]^{2+} \xrightarrow{ET} [U^{VI}OHO(O_2H)]^{2+}$	***M12a.1sf* $\xrightarrow{ET}$ *M13***	-6.8 to -5.7 (-9.3 to -8.2)
72-73	$^{1}[U^{V}O_2(^{\bullet}O_2H)]^{+} \xrightarrow{ET} [U^{VI}O_2(O_2H)]^{+}$	***M12b.1sf* ⟶ *M14***	-25.0 to -20.8 (-26.8 to -22.6)
122	$[U^{VI}OHO(O_2H)]^{2+} + H_2O \longrightarrow [U^{VI}OHO(O_2)]^{+} + H_3O^{+}$	***M13* ⟶ *M8***	-16.1 (-14.8)
96	$[U^{VI}OHO(O_2H)]^{2+} + H_2O \longrightarrow [U^{VI}O_2(O_2H)]^{+} + H_3O^{+}$	***M13* ⟶ *M14***	+32.0 (+31.3)
74	$[U^{VI}O_2(O_2H)]^{+} + H_2O \longrightarrow [U^{VI}O_2(O_2)] + H_3O^{+}$	***M14* ⟶ *M9***	+8.8 (+9.9)
125	$[U^{VI}O_2(O_2H)]^{+} + U^{VI}O_2(NO_3)_2(H_2O) \longrightarrow [(U^{VI}O_2)_2(HO_2)(NO_3)_2]^{+} + H_2O$	***M14* ⟶ *M27***	N/A
58	$^{2}[U^{V}O_2(O_2)]^{+} \xrightarrow{ET} {}^{2}[U^{VI}O_2(^{\bullet}O_2)]^{+}$	***M15.1sf* ⟶ *M6***	-13.6 to -8.9 (-13.5 to -18.2)
66	$^{1}[U^{V}O_2(^{\bullet}O_2)]^{+} \xrightarrow{ET} [U^{VI}O_2(O_2)]$	***M16* ⟶ *M9***	-15.5 (-15.6)
114	$^{2}[U^{V}O_2(O_2H)]^{2+} \xrightarrow{ET} {}^{2}[U^{VI}O_2(^{\bullet}O_2H)]^{2+}$	***M17* ⟶ *M11 ****	-47.5 (-51.0)
128	$^{1}[(U^{V}OHO)(U^{VI}O_2)(^{\bullet}O_2)(NO_3)_2]^{+} \xrightarrow{ET} [(U^{VI}OHO)(U^{VI}O_2)(O_2)(NO_3)_2]^{+}$	***M18.1sf* ⟶ *M19***	-10.7 to -7.9 (-14.8 to -12.0)
129	$[(U^{VI}OHO)(U^{VI}O_2)(O_2)(NO_3)_2]^{+} + H_2O \longrightarrow [(U^{VI}O_2)_2(O_2)(NO_3)_2] + H_3O^{+}$	***M19* ⟶ *M28***	-23.3 (-22.3)

119	$^{1}[U^{VI}O_2(O_2)]^{2+} \xrightarrow{h\nu} *(^{1}[U^{VI}O_2(O_2)]^{2+})$	***M20*** $\longrightarrow$ ***M21***	N/A
120	$*(^{1}[U^{VI}O_2(O_2)]^{2+}) + H_3COH \longrightarrow {}^{2}[U^{V}OHO(O_2)]^{2+} + H_2\dot{C}OH$		
59	$^{2}[U^{V}OHO(O_2)]^{2+} \xrightarrow{ET} {}^{2}[U^{VI}OHO(^{\bullet}O_2)]^{2+}$	***M21*** $\xrightarrow{ET}$ ***M5***	*-8.3 (-12.6)*
126	$[(U^{VI}O_2)_2(HO_2)(NO_3)_2]^{+} + H_2O \longrightarrow [(U^{VI}O_2)_2(O_2)(NO_3)_2] + H_3O^{+}$	***M27*** $\longrightarrow$ ***M28***	-13.4 (-12.3)
115	$U^{V}O_2 + {}^{3}O_2 \xrightarrow{OS-ET} U^{VI}O_2 + {}^{\bullet}O_2^{-}$	OS-ET to $^{3}O_2$ in base	+7.38 to +11.29 [1]
116	$U^{V}O_2 + {}^{3}O_2 + H^{+} \xrightarrow{OS-ET} U^{VI}O_2 + {}^{\bullet}O_2H$	OS-ET to $^{3}O_2$ in acid	+4.84 to +0.92 [2]
117	$U^{V}O_2 + {\bullet}O_2^{-} + H^{+} \xrightarrow{OS-ET} U^{VI}O_2 + HO_2^{-}$	OS-ET to $^{\bullet}O_2^{-}$	-0.92
118	$U^{V}O_2 + {}^{\bullet}O_2H + H^{+} \xrightarrow{OS-ET} U^{VI}O_2 + H_2O_2$	OS-ET to $^{\bullet}O_2H$*	-29.52
90	$2({}^{\bullet}O_2H) \longrightarrow O_2 + H_2O_2$	Disproportionation of $^{\bullet}O_2H$	N/A

[a] All energies are in kcal mol^{-1}.

[b] For each numbered equation, the corresponding model number, free energy and enthalpy change and chemical formula have been presented. For the OS-ET processes presented, the free energy changes have been calculated using the standard reduction potentials of the species as taken from references [4,141,192,193,205]. These potentials were then used to evaluate the free energy change for each ET using the Nernst equation. The standard reduction potentials used were as follows; $E^{0}(UO_2^{2+}/UO_2^{+})$ = +0.16 V; $E^{0}(O_2/{\cdot}O_2^{-})$ = -0.16 V to -0.33 V (see footnote); $E^{0}(O_2, H^{+}/{\cdot}O_2H)$ = -0.05 V to +0.12 V (see footnote); $E^{0}(O_2^{-}, H^{+}/HO_2^{-})$ = +0.20 V; $E^{0}({\cdot}O_2H, H^{+}/HO_2^{-})$ = +1.44 V.

[1] Redox potentials in the literature range from -0.16 V to -0.33 V for reduction of dioxygen in basic conditions i.e. $E^{0}(O_2/{\cdot}O_2^{-})$ [4,150,192,193]

[2] Redox potentials in the literature range from -0.05 V to +0.12 V for reduction of dioxygen in acidic conditions i.e. $E^{0}(O_2, H^{+}/{\cdot}O_2H)$ [4,150,192,193]

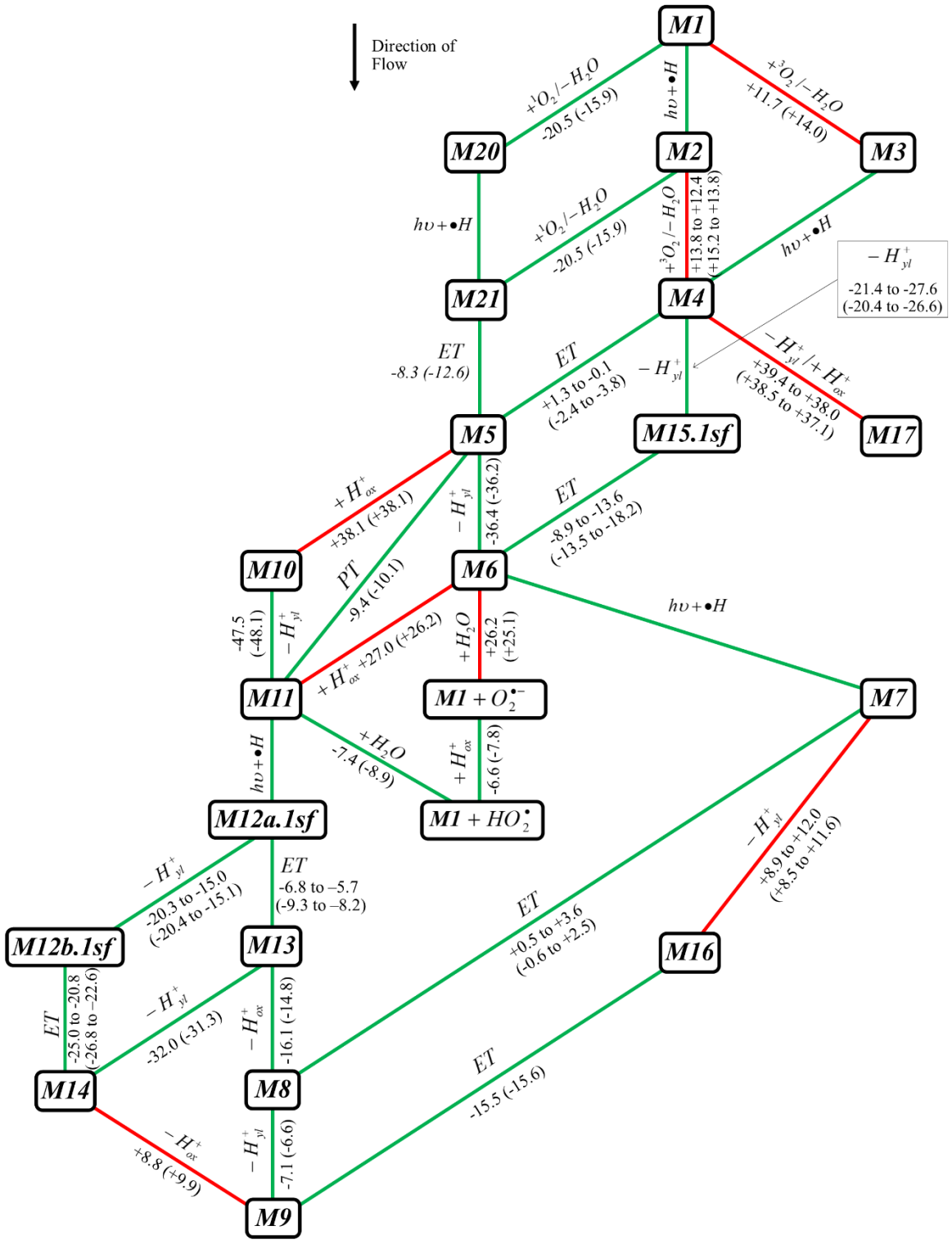

Figure 70: Schematic of the mechanistic web that presents the multiple routes a process to form peroxide could take via an inner-sphere photocatalytic electron transfer process. The boxed ***Mx*** numbers in this schematic represent the names of the computational models used. The lines connecting the boxes represent the reactions occurring to transform one model into the others to which it is linked. Each connection is labelled with a brief description of the process occurring and the ΔG_{solv} (and ΔH_{solv} in parentheses) calculated for the reaction. All energies are quoted in kcal mol^{-1}. The sign of the energy refers to the reactions read as if flowing down the page. i.e. the signs correspond to the reaction occurring that goes from a model higher up the page to one lower on the page. In order to aid interpretation of the schematic, reactions predicted to be spontaneous at room temperature (or have a ΔG_{solv} that is essentially neutral or within the error of the method, i.e. < ~2-5 kcal mol^{-1}) have been coloured green. Reactions that are not predicted to be spontaneous at RT have been coloured red. It is intended that this schematic is used in conjunction with **Table 33**, which provides a labelled list of the chemical equations that describe each of the transformations included in this mechanistic web schematic.

4.3.4.3 The First Wholly Spontaneous Scheme

The first wholly spontaneous scheme of interest is partially described by **Scheme 1** in the previous discussion, only requiring the inclusion of the reactions describing the association of the uranyl ion and dioxygen, which were previously ignored. In this route, the aquated uranyl complex, ***M1***, binds either a molecule of singlet dioxygen before absorption of a photon of light to generate the uranyl(V)-singlet dioxygen complex, ***M21***, or initially undergoes photoactivation as the aquated complex before subsequent equatorial binding of a molecule of singlet dioxygen. Whilst both routes to ***M21*** have been identified as spontaneous processes, largely driven by the effects of solvation, consideration of the kinetic stabilities of the intermediates formed by each route led to the proposal that photoexcitation of ***M1*** is the more favourable pathway. This decision was made considering the relative stabilities of chelated uranyl(V) complexes, which have been observed to exist on spectroscopic timescales as opposed to uranyl(VI)-dioxygen complexes, which have not. This suggests that if a dioxygen complex were to form in these solutions it would form transiently owing to the phenomenal number of competing species in solution. Hence, any mechanistic route to product that does not rely on an extended lifetime of a uranyl(VI)-dioxygen complex is likely to be favoured kinetically. This is compounded by the fact that as no formation of singlet oxygen in such solutions has been definitively observed empirically it is uncertain whether there will be enough singlet oxygen present for the majority of the peroxide species in solution to be formed via a reduction of this species. Therefore it is much more likely that any reduction occurs via the transient formation of a complex with the ground state triplet oxygen as opposed to via the formation of a thermodynamically stable species.

Following formation of ***M21***, a spontaneous ET occurs between the uranyl(V) species and the bound dioxygen molecule to generate the protonated uranyl(VI)-superoxide complex, ***M5***. Conversely, should the process proceed via the formation of a triplet oxygen complex then an essentially energetically neutral ET reaction would occur once the system had the energy required to surmount the 1 kcal mol^{-1} barrier required to access the symmetry broken singlet state of the system. Leading to the formation of the superoxide bound species, ***M5***. At this point in the process, ***M5*** may lose its O_{yl} proton in a barrierless process on approach of a water molecule, losing a hydroxonium ion in the process and leading to the formation of ***M6***. On the other hand, it could have enough energy to pass its proton onto the bound superoxide, forming ***M11*** in a process that is best described overall as a water mediated proton transfer. Considering the path via ***M6*** first, this relatively stable species is likely to

persist in solution for an extended period of time without succumbing to disproportionation. However, one would expect it to absorb an incident photon, abstract a hydrogen atom from the solvent and generate the uranyl(V)-superoxide complex, ***M7***. This species could then undergo an essentially energetically neutral intramolecular ET reaction (ΔG_{solv} = +0.5 to +3.6 kcal mol^{-1}, ΔH_{solv} = -0.6 to +2.5 kcal mol^{-1}) to generate the protonated uranyl(VI)-peroxide complex, ***M8***. The final step in this mechanism is the spontaneous deprotonation of the protonated uranyl(VI) ion to form ***M9***. As stated, this mechanism represents an extended analogue of the mechanism described by **Scheme 1** above, as explicitly presented in totality in **Scheme 8** and **Figure 71**.

Scheme 8

$$[U^{VI}O_2(H_2O)]^{2+} + {}^1O_2 \longrightarrow {}^1[U^{VI}O_2(O_2)]^{2+} + H_2O \quad \textbf{(52)}$$

$${}^1[U^{VI}O_2(O_2)]^{2+} \xrightarrow{h\nu} *({}^1[U^{VI}O_2(O_2)]^{2+}) \quad \textbf{(119)}$$

$$*({}^1[U^{VI}O_2(O_2)]^{2+}) + H_3COH \longrightarrow {}^2[U^{V}OHO(O_2)]^{2+} + H_2\dot{C}OH \quad \textbf{(120)}$$

$${}^2[U^{V}OHO(O_2)]^{2+} \xrightarrow{ET} {}^2[U^{VI}OHO(\bullet O_2)]^{2+} \quad \textbf{(55)}$$

$${}^2[U^{VI}OHO(\bullet O_2)]^{2+} + H_2O \longrightarrow {}^2[U^{VI}O_2(\bullet O_2)]^{+} + H_3O^{+} \quad \textbf{(60)}$$

$${}^2[U^{VI}O_2(\bullet O_2)]^{+} \xrightarrow{h\nu} *({}^2[U^{VI}O_2(\bullet O_2)]^{+}) \quad \textbf{(61)}$$

$$*({}^2[U^{VI}O_2(\bullet O_2)]^{+}) + H_3COH \longrightarrow {}^1[U^{V}OHO(\bullet O_2)]^{+} + H_2\dot{C}OH \quad \textbf{(62)}$$

$${}^1[U^{V}OHO(\bullet O_2)]^{+} \xrightarrow{ET} [U^{VI}OHO(O_2)]^{+} \quad \textbf{(63)}$$

$$[U^{VI}OHO(O_2)]^{+} + H_2O \longrightarrow [U^{VI}O_2(O_2)] + H_3O^{+} \quad \textbf{(64)}$$

As mentioned previously, at point ***M5*** in the mechanism the protonated uranyl(VI)-superoxide complex may undergo spontaneous deprotonation on approach of a molecule of water on the protonated O_{yl} atom. Following deprotonation, the hydroxonium ion formed could emigrate the bulk solvent, as described by the process in **Scheme 8**, or it could have enough energy to pass one of its protons to the equatorially bound superoxide anion in a water mediated PT process, to generate ***M11***. Considering the pathways available to ***M11*** in **Figure 70**, two routes lead downhill in energy; that to '***M1 + •O₂H***' and the route to ***M12a.1sf***. The former describes a ligand substitution reaction to liberate a free hydroperoxyl radical and regenerate the initial state of the uranyl catalyst (***M1***). In the latter process, ***M11*** is photoexcited followed by hydrogen atom abstraction to generate the protonated uranyl(V) analogue (***M12a.1sf***). There is, in fact, a third option predicted to be

feasible: the deprotonation of ***M11*** to regenerate ***M6***. However, as the process that follows this point is indistinguishable from **Scheme 8**, it will not be discussed further at this point.

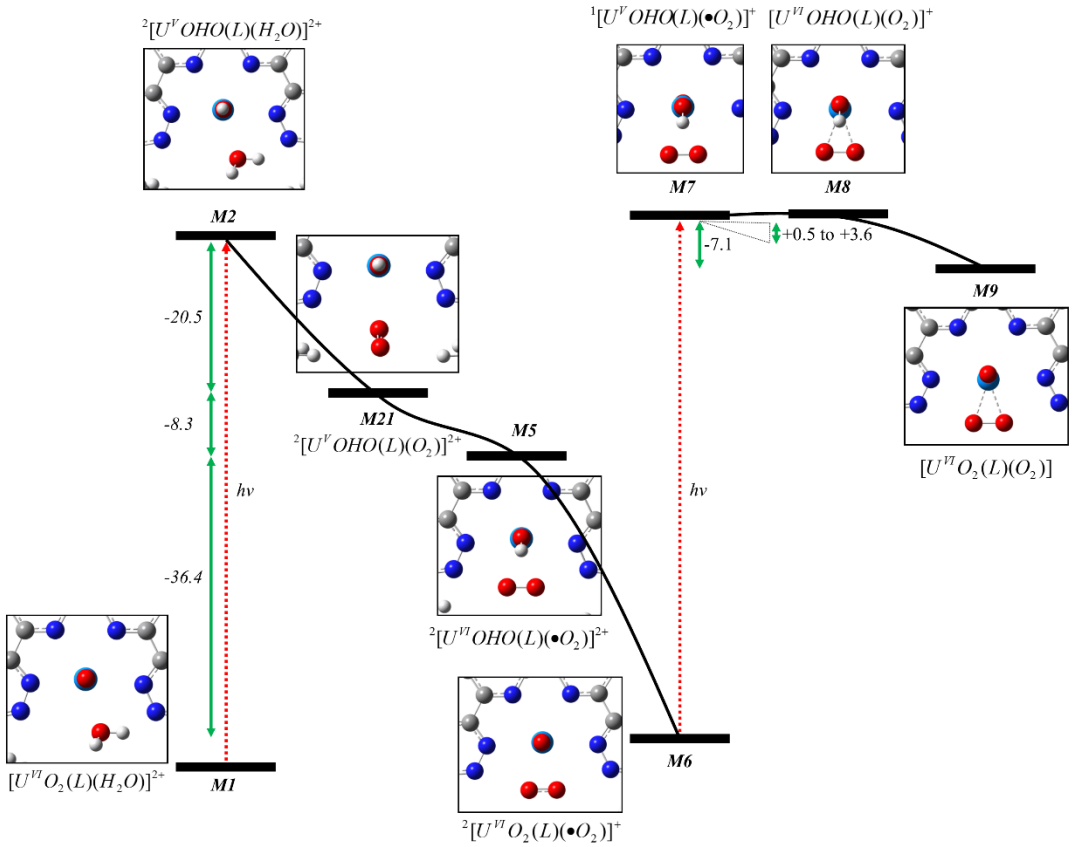

Figure 71: Scaled schematic of the reaction profile calculated for the twice photon activated 2-electron transfer mechanism that converts dioxygen to peroxide. This schematic represents the mechanism described by **Scheme 8**. The red arrows represent photoexcitation steps and the energies used to define them are equivalent to the λ_{max} for UO_2^{2+}, 414 nm. Green double arrows indicate the free energy released for each of the reactions taking place. All energies are quoted in kcal mol^{-1}.

The first route to be considered begins by the ligand substitution of ***M11*** to form '***M1* + $^{\bullet}O_2H$**'. Previous work has shown that this dissociation is a spontaneous process at RT, in contrast with the analogous ligand substitution of the more strongly bound superoxide anion. Following dissociation, the liberated $^{\bullet}O_2H$ radical may disproportionate on interaction with a second $^{\bullet}O_2H$ radical, thereby generating peroxide in a 50 % yield, as per **Equation 90** in **Scheme 9.** Alternatively, it could encounter a solvated uranyl(V) species and undergo an OS-ET process in which the hydroperoxyl radical is reduced to a solvated peroxide anion in a 100 % yield, as per **Equation 102**.

Scheme 9

$$[U^{VI}O_2(H_2O)]^{2+} + {}^1O_2 \longrightarrow {}^1[U^{VI}O_2(O_2)]^{2+} + H_2O \quad \textbf{(52)}$$

$${}^1[U^{VI}O_2(O_2)]^{2+} \xrightarrow{hv} *({}^1[U^{VI}O_2(O_2)]^{2+}) \quad \textbf{(119)}$$

$$*({}^1[U^{VI}O_2(O_2)]^{2+}) + H_3COH \longrightarrow {}^2[U^{V}OHO(O_2)]^{2+} + H_2\dot{C}OH \quad \textbf{(120)}$$

$${}^2[U^{V}OHO(O_2)]^{2+} \xrightarrow{ET} {}^2[U^{VI}OHO(^{\bullet}O_2)]^{2+} \quad \textbf{(55)}$$

$${}^2[U^{VI}OHO(^{\bullet}O_2)]^{2+} \xrightarrow{PT} {}^2[U^{VI}O_2(^{\bullet}O_2H)]^{2+} \quad \textbf{(121)}$$

$${}^2[U^{VI}O_2(^{\bullet}O_2H)]^{2+} + H_2O \longrightarrow [U^{VI}O_2(H_2O)]^{2+} + {}^{\bullet}O_2H \quad \textbf{(97)}$$

THEN:

$${}^{\bullet}O_2H + {}^{\bullet}O_2H \longrightarrow O_2 + H_2O_2 \quad \textbf{(90)}$$

OR:

$$[U^{V}OHO(H_2O)]^{2+} + {}^{\bullet}O_2H \xrightarrow{OS-ET} [U^{VI}OHO(H_2O)]^{3+} + O_2H^- \quad \textbf{(102)}$$

It is therefore reasonable that a viable route to the formation of peroxide in solutions containing the uranyl ion may proceed utilising only one cycle of the photoactiviated catalyst, since formation of the hydroperoxyl radical is in theory sufficient to kick start processes that will naturally yield peroxide. Similarly, as proposed by Bakac et al.,[4] following the first ET the formation of an inner sphere complex between the uranyl(V) ion and superoxide may no longer be required because the standard reduction potentials of these species indicate a spontaneous reduction via an outer sphere mechanism. A reaction profile schematic describing this process is presented in **Figure 72**. Hence, the uranyl catalyst may primarily act as a reducing agent towards dioxygen and then as a facilitator of the dissociation of the superoxide complex formed by shuttling a proton to the dioxygen ligand in order to form a more weakly bound hydroperoxyl radical complex.

It is worth noting that although hypothetically reasonable, the equilibria describing the dissociation of both uranyl(V) and uranyl(VI)-hydroperoxyl complexes has been calculated to lie in favour of dissociation. Hence, liberated hydroperoxyl radicals only re-coordinate solvated uranyl species a minor proportion of the time. Despite this divergence, the reformation of these complexes will not change the proposed mechanistic scheme, though it will reintroduce the complex to the web schematic in the appropriate position for the species formed, i.e if $^{\bullet}O_2H$ binds a uranyl(VI) ion then it re-enters the schematic at ***M11*** and if it binds a uranyl(V) ion it re-enters at ***M12a.1sf***.

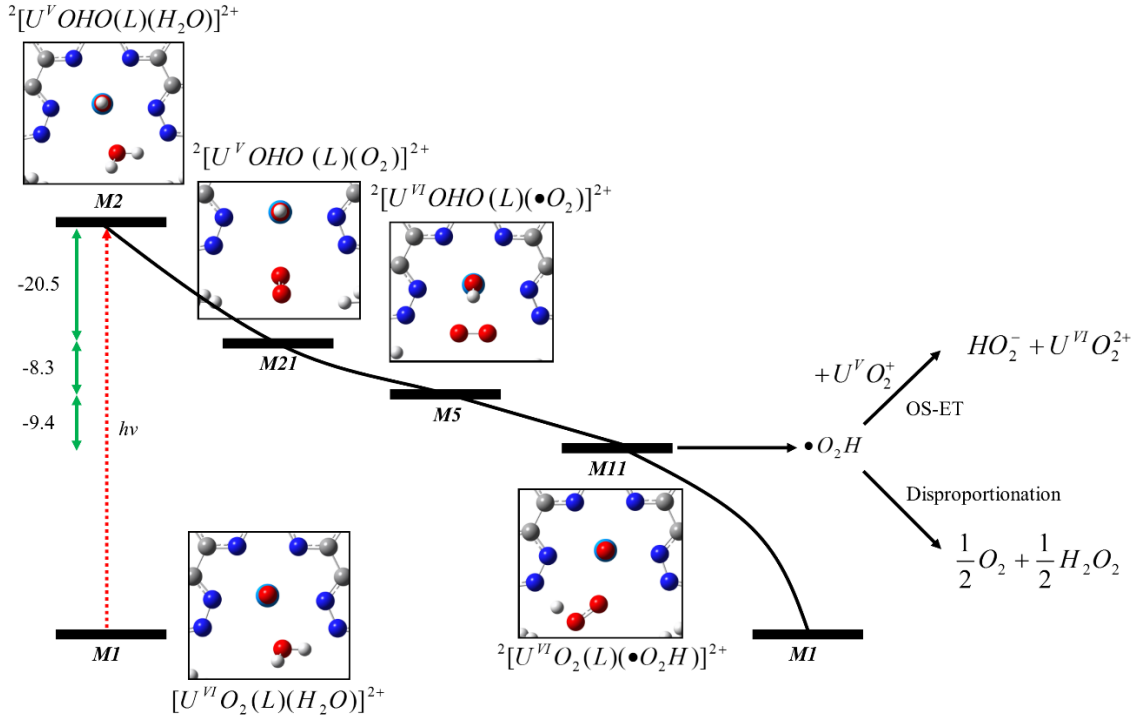

Figure 72: To scale schematic of the reaction profile calculated for the once photon activated single inner sphere ET and single outer sphere ET or disproportionation mechanism that converts dioxygen to peroxide. This schematic represents the mechanism described by **Scheme 9**. The red arrow represents a photoexcitation and the energy used to define it is equivalent to the λ_{max} for UO_2^{2+}, 414 nm. Green double arrows indicate the free energy released for each of the reactions taking place. All energies are quoted in kcal mol^{-1}.

The second route open to the ***M11*** complex, i.e. the route via ***M12a.1sf***, should ***M11*** persist long enough without dissociating that it absorbs an incident photon, is now considered. The excited state analogue of this system may subsequently abstract a hydrogen atom from the nearby solvent, generating the uranyl(V)-hydroperoxyl radical complex, as modelled by ***M12a.1sf***. According to **Figure 70**, there are four reaction routes available to this species that have been identified as thermodynamically feasible. The first two of these routes are analogous to those described for the ***M11*** complex, in that the ***M12a.1sf*** could immediately dissociate releasing a free hydroperoxyl radical along with a protonated uranyl(V)-water complex (***M2***) or ***M12a.1sf*** deprotonate and thereby follow the path previously described via ***M7***. As both of these mechanisms are broadly covered by **Scheme 8** and **Scheme 9,** they will not be presented explicitly for ***M12a.1sf***. For this reason, it should be borne in mind that the individual schemes presented are not the only routes by which this reaction can proceed, but are merely linear representations of exemplar routes. Obviously, one may consult **Figure 70**, for a more general representation.

In addition to these repeated routes, ***M12a.1sf*** has two further unique options, both of which are known to possess barriers to activation. Despite this, it is possible that IS-ET could occur within the ***M12a.1sf*** complex to generate the protonated uranyl(VI)-hydroperoxide complex,

M13, or ***M12a.1sf*** may be deprotonated on approach of solvent in order to generate ***M12b.1sf***. The energetically downhill route that leads from ***M13*** to the peroxide bound product ***M9*** involves initial deprotonation of the bound hydroperoxide species to generate ***M8***, followed by deprotonation of the uranyl ion to generate ***M9***. In contrast, reversing the order of these deprotonation reactions does not constitute a feasible process overall. The mechanism including the ***M12a.1sf*** to ***M13*** step is expressed in **Scheme 10** and a scale diagram of the reaction profile calculated for this reaction is presented in **Figure 73**.

Scheme 10

$$[U^{VI}O_2(H_2O)]^{2+} + {}^1O_2 \longrightarrow {}^1[U^{VI}O_2(O_2)]^{2+} + H_2O \quad \textbf{(52)}$$

$${}^1[U^{VI}O_2(O_2)]^{2+} \xrightarrow{h\nu} *({}^1[U^{VI}O_2(O_2)]^{2+}) \quad \textbf{(119)}$$

$$*({}^1[U^{VI}O_2(O_2)]^{2+}) + H_3COH \longrightarrow {}^2[U^{V}OHO(O_2)]^{2+} + H_2\dot{C}OH \quad \textbf{(120)}$$

$${}^2[U^{V}OHO(O_2)]^{2+} \xrightarrow{ET} {}^2[U^{VI}OHO(^{\bullet}O_2)]^{2+} \quad \textbf{(55)}$$

$${}^2[U^{VI}OHO(^{\bullet}O_2)]^{2+} \xrightarrow{PT} {}^2[U^{VI}O_2(^{\bullet}O_2H)]^{2+} \quad \textbf{(121)}$$

$${}^2[U^{VI}O_2(^{\bullet}O_2H)]^{2+} \xrightarrow{h\nu} *({}^2[U^{VI}O_2(^{\bullet}O_2H)]^{2+}) \quad \textbf{(93)}$$

$$*({}^2[U^{VI}O_2(^{\bullet}O_2H)]^{2+}) + H_3COH \longrightarrow {}^1[U^{V}OHO(^{\bullet}O_2H)]^{2+} + H_2\dot{C}OH \quad \textbf{(94)}$$

$${}^1[U^{V}OHO(^{\bullet}O_2H)]^{2+} \xrightarrow{ET} [U^{VI}OHO(O_2H)]^{2+} \quad \textbf{(95)}$$

$$[U^{VI}OHO(O_2H)]^{2+} + H_2O \longrightarrow [U^{VI}OHO(O_2)]^{+} + H_3O^{+} \quad \textbf{(122)}$$

$$[U^{VI}OHO(O_2)]^{+} + H_2O \longrightarrow [U^{VI}O_2(O_2)] + H_3O^{+} \quad \textbf{(64)}$$

The final route available to ***M12a.1sf***, deprotonation prior to ET in order to generate ***M12b.1sf***, is now examined. The ***M12b.1sf*** complex may subsequently undergo an IS-ET reaction to generate the non-protonated uranyl(VI)-hydroperoxide complex, ***M14***, in a strongly exergonic process. The final step of this reaction required to generate ***M9*** is the deprotonation of the hydroperoxide anion. However, this is not calculated to be a feasible process at RT, and hence as far as the mechanism as modelled to this point is concerned ***M14*** represents the end state for any species that deprotonates at the uranyl ion prior to the hydroperoxide anion. However, the experimental observation of a peroxide bridged bisuranyl complex suggests that this is not the case. Hence, the approach of the second uranyl ion must be considered. It is possible that the approach of this species will provide an additional driving force that may stimulate the deprotonation of the hydroperoxide anion in

M14 and its analogues, generating the crystallographically observed species. The approach of the second uranyl ion on the terminal mono-uranium species is the subject of the final chapter of this study.

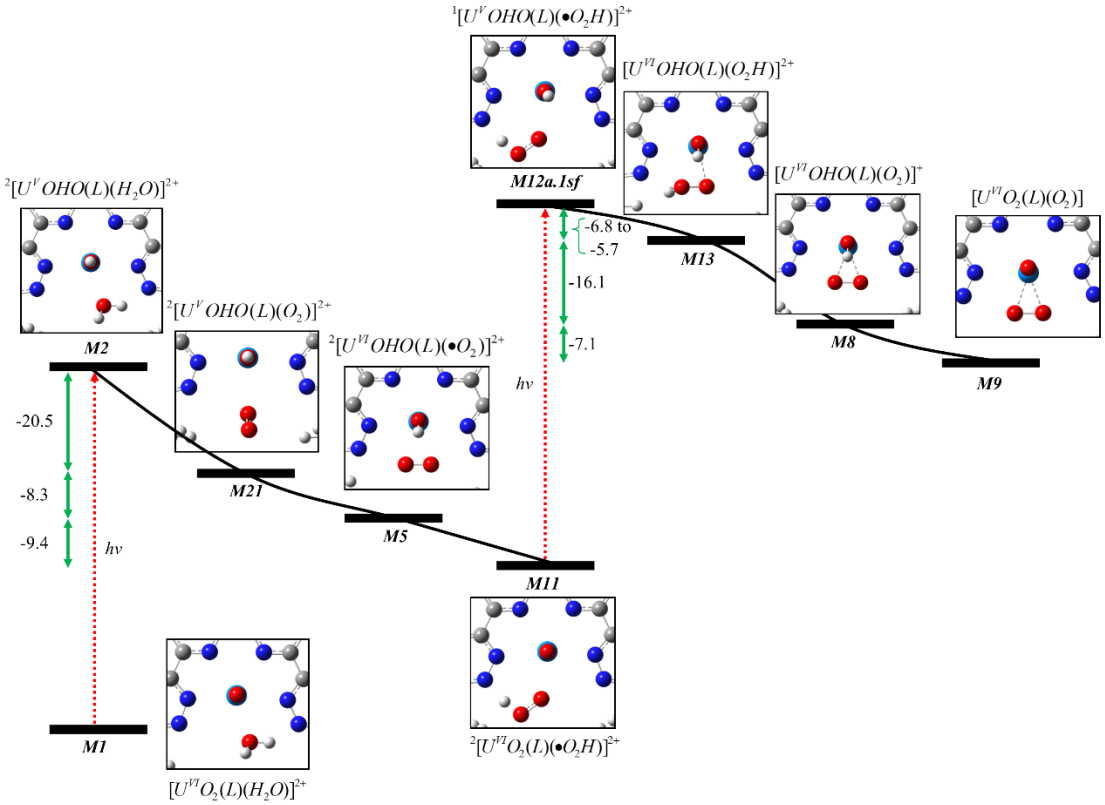

Figure 73: To scale schematic of the reaction profile calculated for the twice photon activated 2-electron transfer mechanism that converts dioxygen to peroxide. This schematic represents the mechanism described by **Scheme 10**. The red arrows represent photoexcitation steps and the energies used to define them are equivalent to the λ_{max} for UO_2^{2+}, 414 nm. Green double arrows indicate the free energy released for each of the reactions taking place. All energies are quoted in kcal mol^{-1}.

Summary

Compilation of all the reaction energies modelled to this point into a single mechanistic web schematic has permitted four thermodynamically favourable mechanisms to be identified that lead downhill from a dioxygen containing complex to a peroxide product. These four mechanisms fall into two broad categories, although all involve the same initial steps. These steps are the formation of a singlet dioxygen complex of the uranyl ion followed by ET to form a uranyl-superoxide complex. Following this point the favoured mechanisms diverge: two represent inner sphere ET processes and two involve dissociation of the uranyl-superoxide complex, followed by steps that convert the solvated hydroperoxyl radical into peroxide without the formation of an explicit coordination complex. The IS-ET processes can generally be described as mechanisms in which the species reduced is a bound superoxide anion and a hydroperoxyl radical, respectively. In contrast, the non-coordinated mechanisms may be categorised as an OS-ET process between a solvated hydroperoxyl

radical and a solvated uranyl(V) ion and the disproportionation of two hydroperoxyl radicals. Unlike all of the other processes identified, the latter mechanism does not make direct use of the uranium species present in order to generate peroxide.

Consideration of the interrelationship of these mechanisms allowed the inner sphere ET via ***M6*** to be identified as the one most likely to be favoured kinetically. All of the other mechanisms discussed involve intermediates that are expected to be unstable with respect to dissociation or deprotonation, or they proceed via intermediates that possess a moderate energetic barrier to formation. The uranyl(V)-superoxide complex, ***M6***, possesses no such caveats and indeed when many of the other higher potential complexes succumb to the energetic gradient they tumble downhill towards ***M6***. The fact that ***M6*** lies in a potential well on the reaction PES therefore suggests that it has the longest lifetime of all other intermediates identified in the feasible mechanisms and hence it is probable that the mechanism that utilises this state will be the one most travelled towards the product.

At this point in the study, the possible routes to form peroxide from dioxygen via two successive photo-initiated ET steps have been explored. Despite this, the peroxide containing product observed in the experimental solution that sparked interest for this study was a peroxide bridged bisuranyl complex. Hence, the final step of the process to be considered is the approach of a second uranyl ion at different points in the mechanism and the effect this approach has on the most favoured course of the reaction.

4.3.5 Feasibility of the Approach of a Second Uranyl Ion

To this point, the majority of the significant mechanistic steps required to generate peroxide from dioxygen have been discussed. In the first part of this study, the feasibility of the formation of a complex between the uranyl ion and triplet and singlet dioxygen were studied. Subsequently, the dependence of the reduction potentials of these redox active species on their state of deprotonation was broached in order to infer which single electron reduction pathways are favoured energetically. Finally, the feasibilities of the acid-base reactions required to generate these species was considered. This approach allowed the disparate islands of the mechanistic web studied in the first two parts to be stitched together in order to generate a holistic mechanism for the 2-electron reduction process as a whole. The final subject to address in order to extrapolate this mechanism to reproduce the experimentally observed bisuranyl peroxide bridged complex is consideration of the approach of the second uranyl ion.

In order to model the formation of the bisuranyl complex, first the nature of the uranyl species that approaches the peroxide bound uranyl complex must be identified. The crystals

of *[$(UO_2)_2(O_2)$(BTPhen)$(NO_3)_2$]* were grown from an aqueous methanolic solution of uranyl nitrate and BTPhen by DMW. In such solutions, it is reasonable that the speciation of uranium is in a state of equilibrium between aquated uranyl complexes and uranyl ions of varying degrees of nitration. The nature of the dominant species present in RT solutions of uranyl nitrate at relatively low nitrate concentration has historically been a source of great debate. Earlier studies tended to conclude that this species was the mono-nitrated product $UO_2NO_3^+$.[206,207] However, recently this view has come under challenge as summarised by a recently published thesis that employed a combined theory and experimental approach making use of UV-Vis and EXAFS spectroscopies along with DFT to conclude that the dominant species under such experimental conditions is the neutral complex, UO_2NO_3.[208] The identification of this neutral complex in such solutions is unsurprising considering the ease with which uranium nitrate complexes are extracted from aqueous solutions into organic solvent. Using this knowledge, along with the previously identified preference for the uranyl(V) and (VI) ions to accept five equatorial coordinate bonds,[209] it is reasonable to assume that the principal species in the experimental solution of interest is an aquated bisnitrate pentacoordiante complex of the uranyl(VI) ion, *[$UO_2(NO_3)_2(H_2O)$]*.

Computational Details

The same computational method applied elsewhere in this study has been used to model the approach of the second uranyl ion in this chapter and is laid out in full in Chapter 2. In summary, all models were optimised in the gas phase using the uB3LYP/B1 level of theory, defined in Chapter 2.2. This basis set treats the majority of the *C, H, O* and *N* atoms in each model using a 6-31G(d,p) basis and uranium atoms are modelled using the Stuttgart quasi-relativistic SC-ECP and the corresponding basis set. The only atoms not represented by this scheme are hydrogen atoms involved in hydrogen bonding interactions, which are treated with the 6-311++G(d,p) basis set. Hydrogen atoms susceptible to forming hydrogen bonds are defined as being directly bound to *N*, *O* and *F* atoms. Following geometry optimisation in the gas phase, frequency calculations were carried out in order to confirm that the geometry identified occupied a potential minimum. Assuming no negative frequency modes are identified by this second derivative test then SP calculations using the TZ B2 basis set are carried out in the presence of a CPCM solvent model. As discussed previously, such an approach to solvation provides a sizable computational saving and has been found to introduce an estimated typical error 2.5 kcal mol^{-1} error into the calculated energies when compared to the corresponding fully solution optimised structures. In addition to the uranyl complexes that make up part of this study there are a range of small molecules implicated in

the process such as the hydroxonium ion, water, nitrate anions and hydroperoxyl radicals. These species have been treated using the same computational method as described for the uranyl complexes, only in order to account for specific interactions between these small molecules and the solvent the geometry optimisations have been carried out using a cluster model as described for the hydroxonium ion in Appendix 2. Using the cluster model to optimise these species in the gas phase followed SP calculations with a CPCM solvent correction in the gas phase, the optimised geometry was found to reproduce the experimentally determined solvation energy of a proton ion to within ~3 kcal mol^{-1}. All calculations were carried out using the Gaussian 09 suite of programs.

Results and Discussion

Establishing a Control Process: The Simultaneous Complexation of the Constituent Species

The most conceptually simple process of formation for the peroxide bridged bisuranyl model in solution is for the constituent species to form separately and then encounter each other simultaneously leading to complexation. Such a process is described by the reaction of $[U^{VI}O_2(L)(H_2O)]^{2+}$ with free HO_2^- and $U^{VI}O_2(NO_3)_2(H_2O)$ to form ***M28*** as per **Equation 123**.

$$[U^{VI}O_2(L)(H_2O)]^{2+} + HO_2^- + U^{VI}O_2(NO_3)_2(H_2O) \longrightarrow [(U^{VI}O_2)_2(O_2)(L)(NO_3)_2] + H_3O^+ + H_2O \quad \textbf{(123)}$$

Using the CPCM solvated energies for these species, this reaction is calculated to be a strongly exergonic process at RT with a free energy of formation of -29.9 kcal mol^{-1} and an enthalpy of formation of -48.4 kcal mol^{-1}. The spontaneous formation of the bisuranyl peroxide unit from its constituent molecular species is therefore determined to be a favourable process, in agreement with the experimental identification of this species. The optimised geometry of the bisuranyl peroxide bridged product, ***M28***, is presented in **Figure 74**, along with selected structural parameters for this complex. As explained previously, when modelling large species with many low frequency modes there is an increased probability that hindered rotations may be considered as vibrations in the thermochemical analysis, which could introduce considerable error into the free energies calculated. In this respect, the enthalpies calculated for the formation of these extended bimetallic species may be a better gauge of the reaction feasibilities than the free energies.

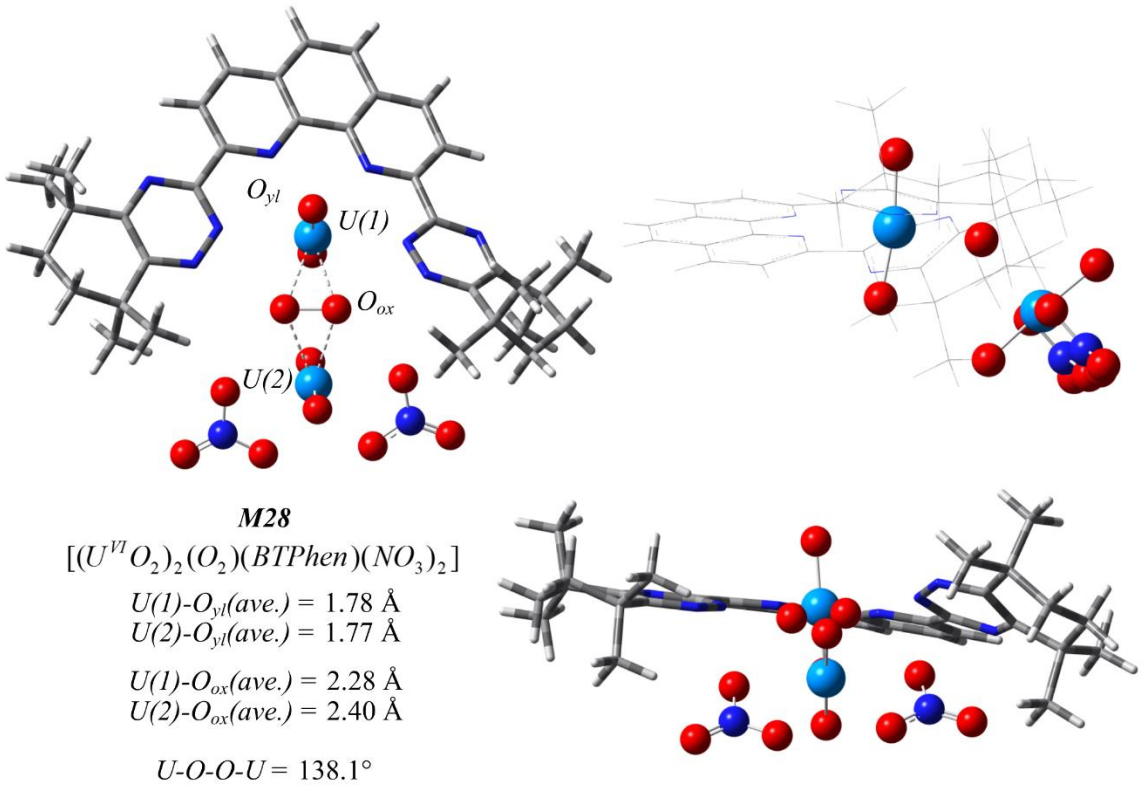

Figure 74: Optimised structure of the bisuranyl peroxide bridged complex as presented earlier.

It was shown earlier in this section that the bisuranyl peroxide bridged unit in the optimised model displays the non-linear bridging *U-O-O-U* dihedral angle, occasionally considered characteristic of these complexes. Furthermore, it is clear that in order to accommodate the second uranyl ion in close proximity to the first, as dictated by the inherently strong bonding between peroxide and uranyl ions, the cyclohexane groups of the BTPhen ligand are forced to distort considerably from the planarity typically observed. As stated in Chapter 4.2, this distortion was also observed in the empirically derived structure and is testament to the strength of interaction between the uranyl species and the peroxide bridge. A final interesting point to note is that the contacts between the peroxide and the BTPhen bound uranyl ion are 0.12 Å shorter than the corresponding interactions with the uranyl ion bound by nitrate anions. It is likely that this is also a manifestation of the steric interaction between BTPhen and nitrate equatorial ligand fields.

*The Approach of Uranyl Nitrate to **M9** and **M14***

Following the identification of the bounding system, discussed above as an exergonic process, the approach of the second uranyl ion to the uranyl peroxide species, ***M9*** and ***M14***, was considered. These species were chosen because they were found to be the end products of many of the mechanistic schemes. Addressing the approach of a uranyl bisnitrate species to the uranyl(VI)-peroxide complex, ***M9***, allows the construction of **Equation 124**. For ease of reference, optimised geometries and selected structural parameters of the ***M9*** and ***M28***

complexes are presented once again in **Figure 75**. In the following equations the BTPhen ligand is represented as *(L)*.

$$[U^{VI}O_2(L)(O_2)] + U^{VI}O_2(NO_3)_2(H_2O) \longrightarrow [(U^{VI}O_2)_2(O_2)(L)(NO_3)_2] + H_2O \quad \textbf{(124)}$$

This reaction is calculated to have a ΔG_{solv} = -6.2 kcal mol^{-1} and ΔH_{solv} = -27.1 kcal mol^{-1}. Therefore, similarly to the spontaneous encounter model described above, the approach of a solvated uranyl nitrate species to an IS complex of uranyl(VI)-peroxide is also calculated to be a spontaneous process at RT.

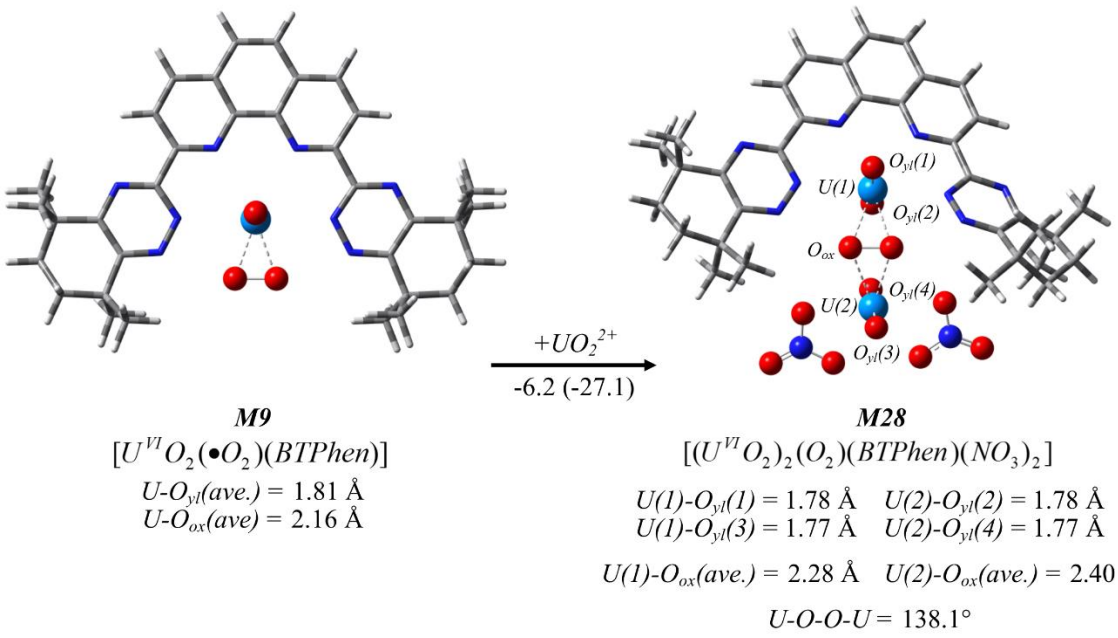

M9
$[U^{VI}O_2(\bullet O_2)(BTPhen)]$
U-O$_{yl}$(ave.) = 1.81 Å
U-O$_{ox}$(ave) = 2.16 Å

M28
$[(U^{VI}O_2)_2(O_2)(BTPhen)(NO_3)_2]$
U(1)-O$_{yl}$(1) = 1.78 Å *U(2)-O$_{yl}$(2)* = 1.78 Å
U(1)-O$_{yl}$(3) = 1.77 Å *U(2)-O$_{yl}$(4)* = 1.77 Å
U(1)-O$_{ox}$(ave.) = 2.28 Å *U(2)-O$_{ox}$(ave.)* = 2.40 Å
U-O-O-U = 138.1°

Figure 75: Optimised structures if the ***M9*** and ***M28*** uranyl peroxide complexes and selected structural parameters. The free energy (and enthalpy in parentheses) calculated for the corresponding reaction described by **Equation 124** is also presented in units of kcal mol^{-1}.

The alternative formation of ***M28*** from ***M14*** is now considered. In the mechanistic study in Chapter 4.3.2.1.3, the uranyl(VI)-hydroperoxyl complex, ***M14***, was found to lie at a potential minimum in the reaction coordinate, which is depicted in **Figure 55**. This meant that the deprotonation of the hydroperoxyl unit to lead to ***M9*** was not predicted to be a spontaneous process. It was hypothesised that the approach of a second uranyl ion on to ***M14*** may stimulate this deprotonation, ultimately leading to the formation of the product ***M28***. Such a reaction is described by **Equations 125** and **126**, in which the approach of the second uranyl ion initially motivates the transfer of the proton on the hydroperoxyl radical to the appropriately placed basic nitrogen atom in a triazinyl ring of BTPhen, which generates a molecule described as BTPhenH$^+$ in model ***M27***. Following this PT, **Equation 126** describes the deprotonation of BTPhen$^+$ in order to generate the end state of the system, ***M28***. Following the convention presented earlier, in these schemes the BTPhen ligand is represented as *(L)*.

$$[U^{VI}O_2(L)(O_2H)]^+ + U^{VI}O_2(NO_3)_2(H_2O) \xrightarrow{PT} [(UO_2)_2(O_2)(LH)(NO_3)_2]^+ + H_2O \quad \textbf{(125)}$$

$$[(UO_2)_2(O_2)(LH)(NO_3)_2]^+ + H_2O \longrightarrow [(UO_2)_2(O_2)(L)(NO_3)_2] + H_3O^+ \quad \textbf{(126)}$$

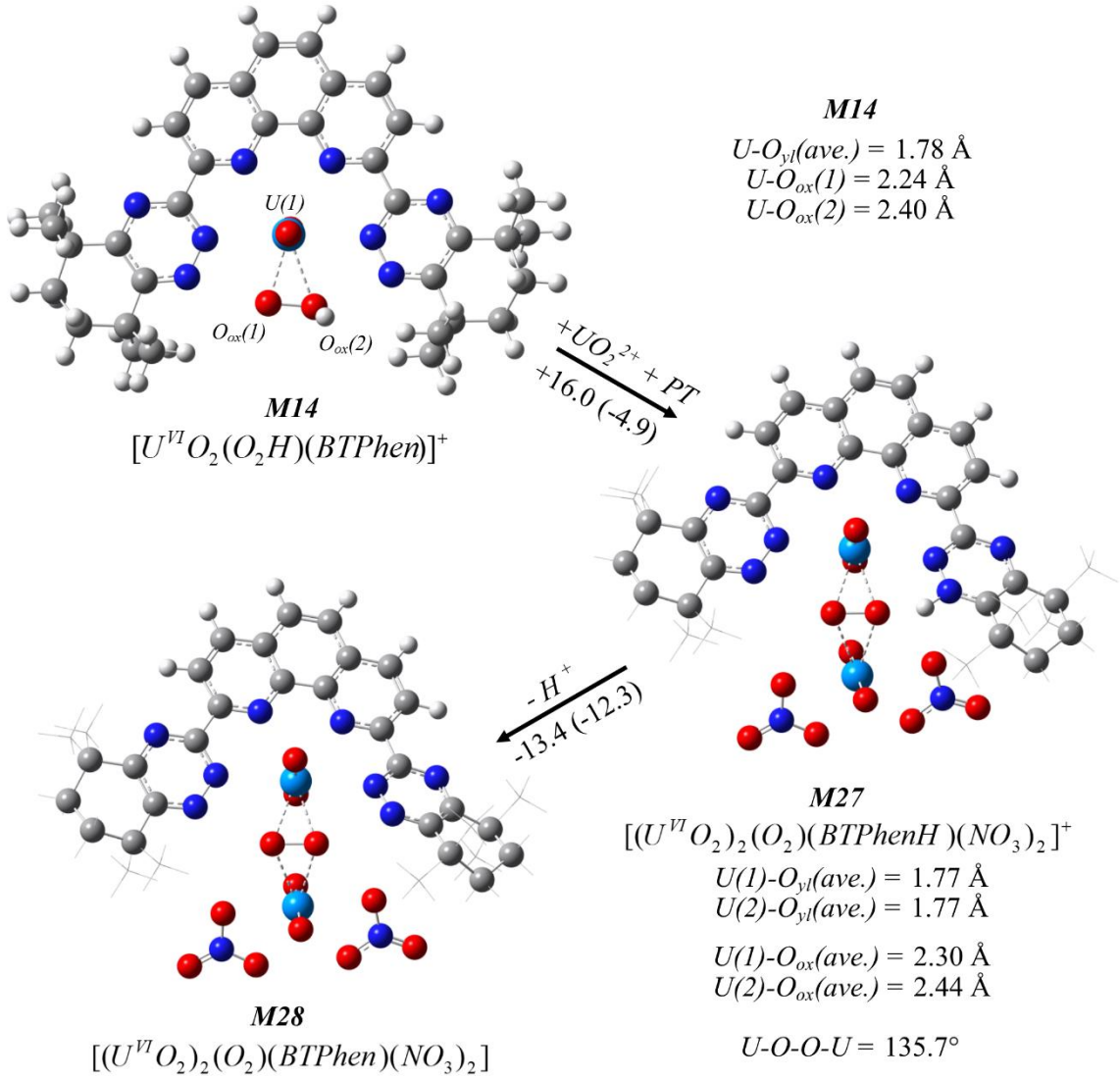

Figure 76: Optimised geometries and selected structural parameters describing the approach of a uranyl nitrate complex to ***M14***. In models ***M27*** and ***M28***, the methyl groups on the tetramethylcyclohexane groups of BTPhen have been represented as a wire frame for clarity. The free energy (and enthalpy in parentheses) calculated are presented in units of kcal mol^{-1}.

The optimised geometries of the species that participate in the PT described by **Equations 125** and **126** are presented in **Figure 76**. Despite the prime position of the basic nitrogen on the BTPhen ligand to accept the proton from the hydroperoxide anion, this process is not calculated to be spontaneous at RT, with ΔG_{solv} = +16.0 kcal mol^{-1} and ΔH_{solv} = -4.9 kcal mol^{-1}. Considering the enthalpy change for the process is calculated to be exergonic it is possible that a large error in the calculated entropy for the bisuranyl complex may have skewed the absolute conclusion about spontaneity for this reaction (note that the ΔG_{solv} has been on the order of 20 kcal mol^{-1} greater than the ΔH_{solv} in all of the reactions involving the bisuranyl complex to this point). Nevertheless, as stated throughout this study,

the relative feasibilities of the processes are the most reliable comparison for the reactions modelled and not their absolute values owing to the presence of such uncertainties in the model applied. Following this logic, it is clear that the association of a second uranyl ion with the ***M14*** complex is a less favourable process than the association of the same species with ***M9***. It is worth noting that following the PT, the deprotonation of the $BTPhenH^+$ molecule formed to generate ***M28*** is calculated to be a feasible process with ΔG_{solv} = -13.4 kcal mol^{-1} and ΔH_{solv} = -12.3 kcal mol^{-1}.

The Feasibility of Formation of Superoxide Bridged Complexes

The scenarios presented to this point describe the approach of a second uranyl ion to the peroxide or hydroperoxide species. However, it is possible that the second uranyl ion could approach on a monouranyl dioxygen complex earlier in the mechanism. Thus, it is conceivable that the effect of coordination of two metal cations to the bridging dioxygen species could alter the redox potential of the system to a greater extent than yet observed, hence it is a process worth exploring.

In order to probe the feasibility that a second uranyl ion could appear earlier the mechanism, the reaction scheme described by **Equations 127-129** was modelled. In this reaction, the second uranyl ion approaches the protonated uranyl(V)-superoxide complex, ***M7***, immediately prior to the second ET step to form a superoxide bridged bis-uranyl complex, $[(U^{V}OHO)(U^{VI}O_2)(\cdot O2)(NO_3)_2]^+$, ***M18***.

$$[U^{V}OHO(L)(\bullet O_2)]^+ + U^{VI}O_2(NO_3)_2(H_2O) \longrightarrow [(U^{V}OHO)(U^{VI}O_2)(^{\bullet}O_2)(L)(NO_3)_2]^+ + H_2O \quad \textbf{(127)}$$

$$[(U^{V}OHO)(U^{VI}O_2)(\bullet O_2)(L)(NO_3)_2]^+ \xrightarrow{ET} [(U^{VI}OHO)(U^{VI}O_2)(O_2)(L)(NO_3)_2]^+ \quad \textbf{(128)}$$

$$[(U^{VI}OHO)(U^{VI}O_2)(O_2)(L)(NO_3)_2]^+ + H_2O \longrightarrow [(UO_2)_2(O_2)(L)(NO_3)_2] + H_3O^+ \quad \textbf{(129)}$$

Following the formation of the superoxide bridged adduct ***M18***, an ET occurs within this species, which generates the protonated analogue of the peroxide bridged product, ***M19***, see **Equation 128**. Finally, as shown in **Equation 129**, this species deprotonates at the uranyl ion in order to generate the product, ***M28***. The optimised structures of the species involved in this reaction scheme are presented in **Figure 77**.

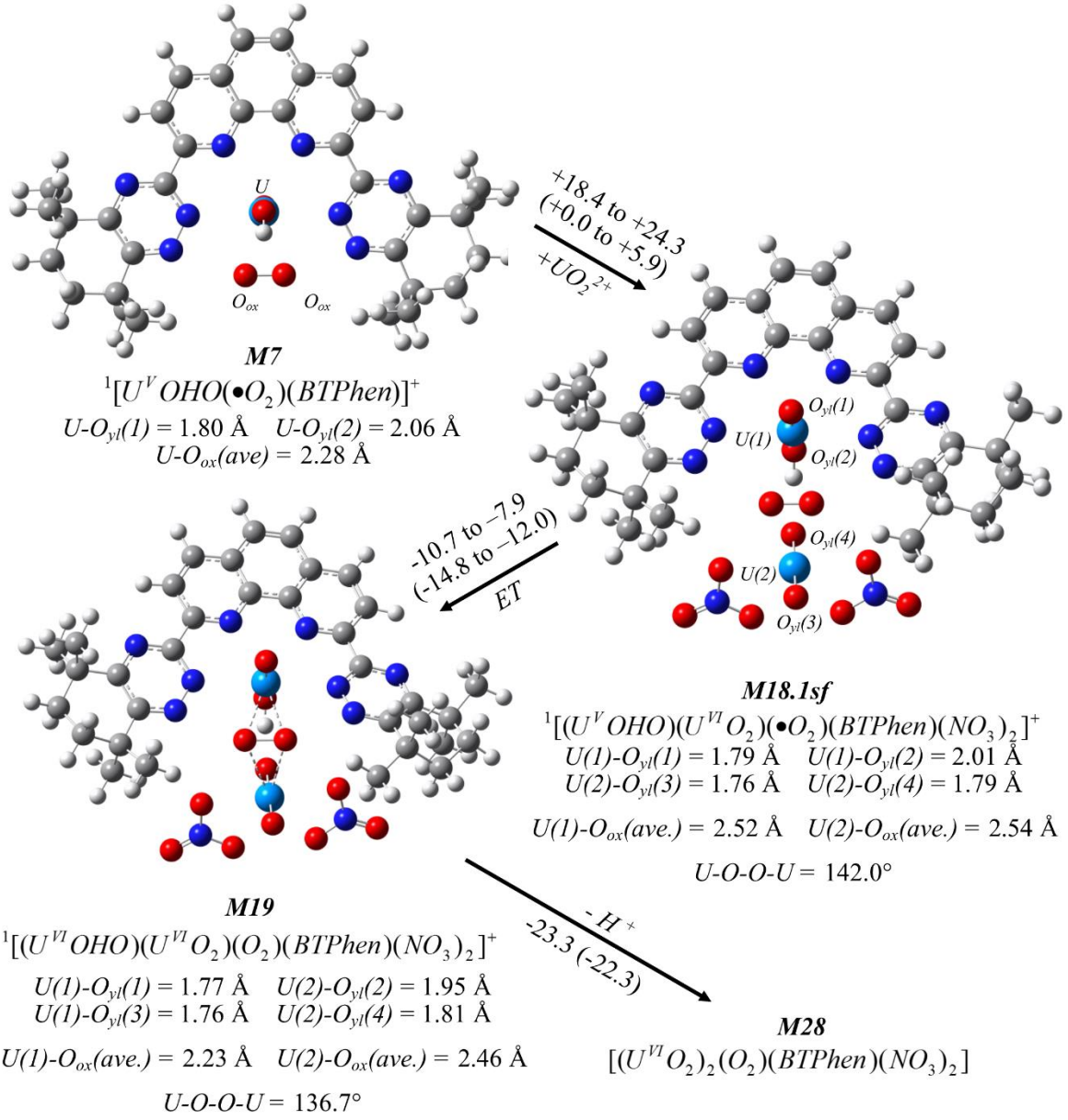

Figure 77: Optimised geometries and significant structural parameters for models that describe the approach of a uranyl nitrate complex onto ***M7***, a superoxide complex.

The range of reaction energy changes for the approach of the nitrated uranyl(VI) ion to ***M7*** are calculated to be ΔG_{solv} = +18.4 to +24.3 kcal mol^{-1} and ΔH_{solv} = +0.0 to +5.9 kcal mol^{-1}. Hence, this is predicted to be the least favourable bridging reaction modelled to this point. It can reasoned that the singly anionic superoxide ion will form inherently weaker ionic interactions with the uranyl ion than its doubly anionic peroxide analogue. In addition, the stabilisation afforded by the slight overlap of π^* MOs in the superoxide anion with the uranyl bonding MOs is not as great as for the peroxide ion.[170,171] This can be attributed to the single occupation of the π^* orbitals in the superoxide anion.

Despite the fact that the initial formation of the bisuranyl superoxide adduct has been shown to be unfavourable, the ET and deprotonation reactions that follow (**Equations 128** and **129**)

are predicted to be favourable processes, with ΔG_{solv} (ΔH_{solv}) calculated to be within the range -7.9 to -10.7 kcal mol^{-1} (-12.0 to -14.8 kcal mol^{-1}) and -23.3 kcal mol^{-1} (-22.3 kcal mol^{-1}), for the ET and deprotonation reactions, respectively.

Since the formation of the superoxide bridged bisuranyl complex was calculated to be unfeasible, the decision was made not to pursue the dioxygen bridged analogue, owing to the inherent lability of the uranium-dioxygen interaction and the transient nature of the species formed. Furthermore, following a similar logic, the analogous approach of a nitrated uranyl(VI) ion to ***M12a.1sf***, the uranyl(V)-hydroperoxyl radical complex, was not modelled since the hydroperoxyl radical was also previously identified as a weaker ligand for the uranyl ion than the superoxide anion.

Summary and Implications for the Mechanism

In this chapter, the final step to turn the monouranyl peroxide complexes, that were identified as likely reaction intermediates in the previous phase of this study, into the bisuranyl peroxide bridged complex observed experimentally have been modelled. It was found that the spontaneous formation of a peroxide bridged bisuranyl complex from a solvated uranyl BTPhen complex, a solvated uranyl bisnitrate complex and a hydroperoxide anion is a thermodynamically feasible process. In addition, the approach and coordination of a uranyl-bisnitrate complex to a preformed uranyl-peroxide species was also found to be a thermodynamically favourable route to the peroxide bridged product. Despite this, the analogous approach of a uranyl nitrate species to a preformed uranyl-hydroperoxide complex was calculated to be non-spontaneous reaction, albeit exothermic. It was suggested that this seeming contradiction may be due to error introduced into the quantified entropy because of the size of the system modelled. Hence it was determined that it was perhaps more appropriate to conclude that the approach of a uranyl ion onto a preformed uranyl-hydroperoxide complex is a process that is less favourable than its peroxide analogue. Finally, it was found that the superoxide ligand did not form sufficiently strong interactions with uranyl cations in order to favourably act as a bridging anion. For this reason, the possibility of a uranyl ion approaching the reactive species an earlier point in the mechanism was discounted.

Ranking the processes describing the approach of the second uranyl ion in order of the most exergonic to the most endergonic suggests that the spontaneous coordination of two uranyl ions and a hydroperoxide anion is the most feasible process, followed by the approach of a uranyl ion to the uranyl-peroxide complex, ***M9***, and finally the approach of a uranyl ion to the uranyl-hydroperoxide complex, ***M14***.

These conclusions have implications for the overall mechanism presented and these implications ultimately permit a complete web schematic describing the whole of the 2-electron reduction of dioxygen studied in this thesis to be presented in **Figure 78**. This web schematic builds upon that in **Figure 70**, by inclusion of the final reaction steps describing the approach of a second uranyl species. These are presented at the bottom of the schematic and lead to the bisuranyl peroxide bridged product of the reaction ***M28***. This schematic is therefore complete; it describes multiple pathways which may lead to the formation of peroxide when irradiated with visible light in a solution containing the uranyl ion, methanol, BTPhen and dioxygen. Using the predicted thermodynamic reaction feasibilities it has been possible to identify three routes to the product that are likely to be feasible. This chapter has addressed the approach of a uranyl to ***M9*** and ***M14*** in order to gauge the applicability of each in the context of the mechanism as a whole. As shown in the updated reaction profiles in **Figure 79** and **Figure 80**, both of the proposed IS processes terminate via model ***M9***. Hence, the identification that the coordination of a second uranyl ion onto ***M9*** is favourable does not eliminate either of these processes as unfeasible. The third mechanism via the OS or disproportionation mechanisms terminates via a spontaneous association of two uranyl ions and a hydroperoxide anion in solution. Hence, as this process was calculated to be strongly favourable, it also does not preclude the OS mechanism from occurring some proportion of the time in a real solution. This process is represented by the reaction profile schematic in **Figure 81**.

Overall, it is likely that the photoactivated catalytic route that leads to the formation of peroxide in solutions containing the uranyl ion, an aliphatic hydrocarbon solvent and exposed to visible light proceeds via multiple routes simultaneously in one pot. All of the three mechanisms proposed by this thermodynamic and kinetic study share the same initial ET process, but diverge following the formation of a uranyl-superoxide complex. The route that is favoured kinetically is that which occurs with the lowest energetic barrier. In order for the OS process, and the IS process that proceeds via the ***M11*** complex, to arise an intramolecular PT must occur that was found to have a modest barrier to activation, on the order of 4.3 kcal mol^{-1}. Conversely, it was not possible to identify any activation barriers for the analogous uranyl-superoxide method that occurred via ***M7***. For this reason, it is possible that the route via ***M7*** is the most conservative of energy and may therefore be the route most travelled by the reactants on the way to the products. This argument is compounded by the relatively poor yields that may be expected for species that have the energy to make it onto the ***M11*** route. This is due to the likely rate of attrition of the species on this path, as judged by the thermodynamic stabilities of these species, and the fact that such attrition typically

leads the mechanism to ultimately follow the route via ***M7***, see **Figure 78**. In addition, as the disproportion rate of free hydroperoxide anions is known to be faster than their coordinated analogues,[4,143] and because this process will only lead to the formation of one molecule of peroxide for every two cycles of the catalytic mechanism, it is reasonable to conclude that kinetically products that form via the relatively stable uranyl-peroxide species, ***M7***, will dominate overall.

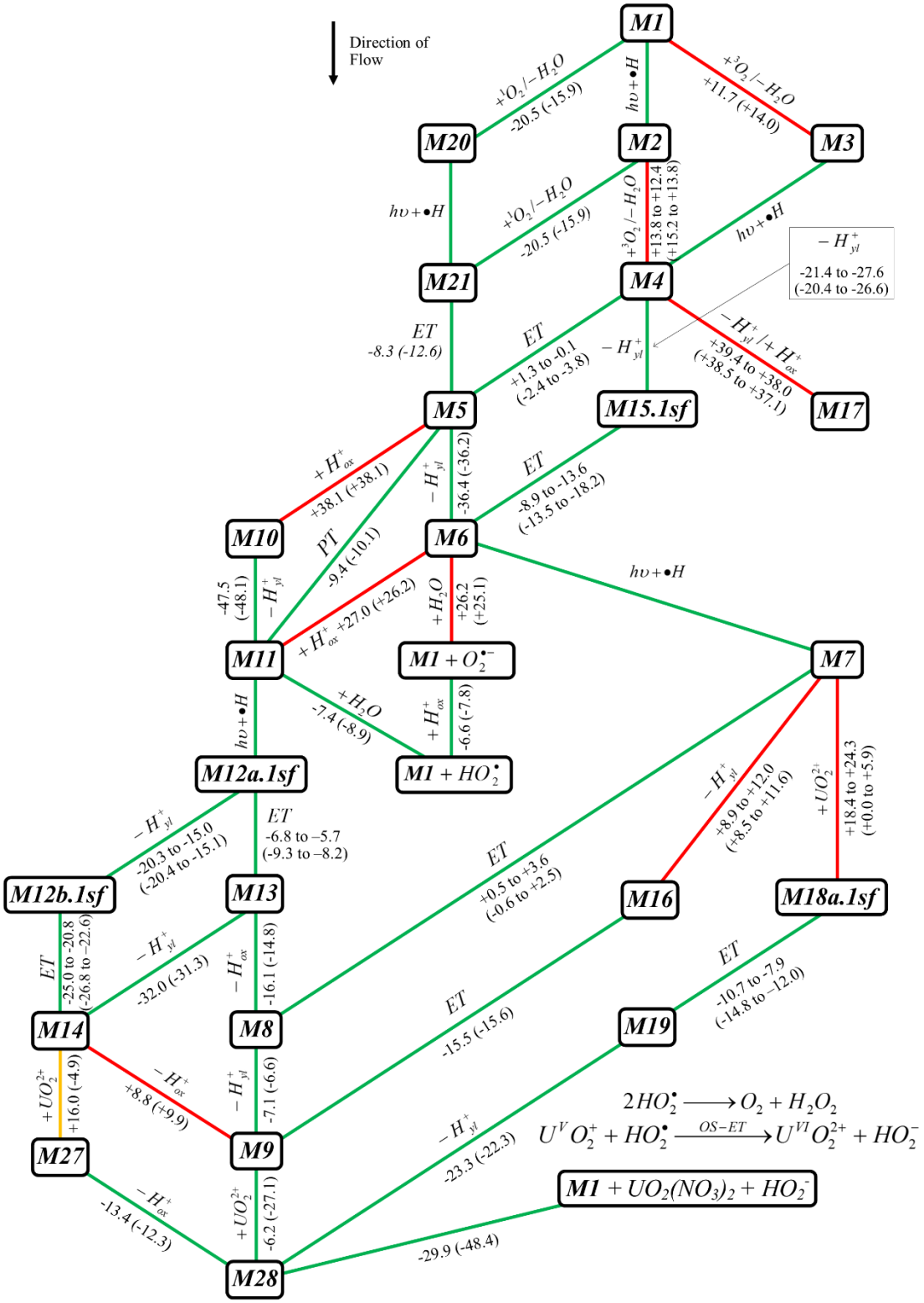

Figure 78: Schematic of the mechanistic web that presents the multiple routes to forming peroxide via inner-sphere photocatalytic electron transfer processes. The boxed ***Mx*** numbers in this schematic represent the names of the computational models used. The lines connecting the boxes represent the reactions occurring that link the models. Each connection is labelled with a brief description of the process occurring along with the ΔG_{solv} (and ΔH_{solv} in parentheses) calculated for the reaction. The sign of the energies quoted refers to the reactions as read as if flowing down the page. In order to aid interpretation of the schematic, reactions predicted to be spontaneous at RT (or have a ΔG_{solv} that is essentially neutral or within the error of the method, i.e. < ~2 kcal mol^{-1}) have been coloured green. Reactions that are predicted not to be spontaneous at RT have been coloured red. An orange line indicates the feasibility of this reaction is undecided, as detailed in the text. It is intended that this schematic is used in conjunction with **Table 33**, which provides a labelled list of the chemical equations that describe each of the transformations included in this mechanistic web schematic.

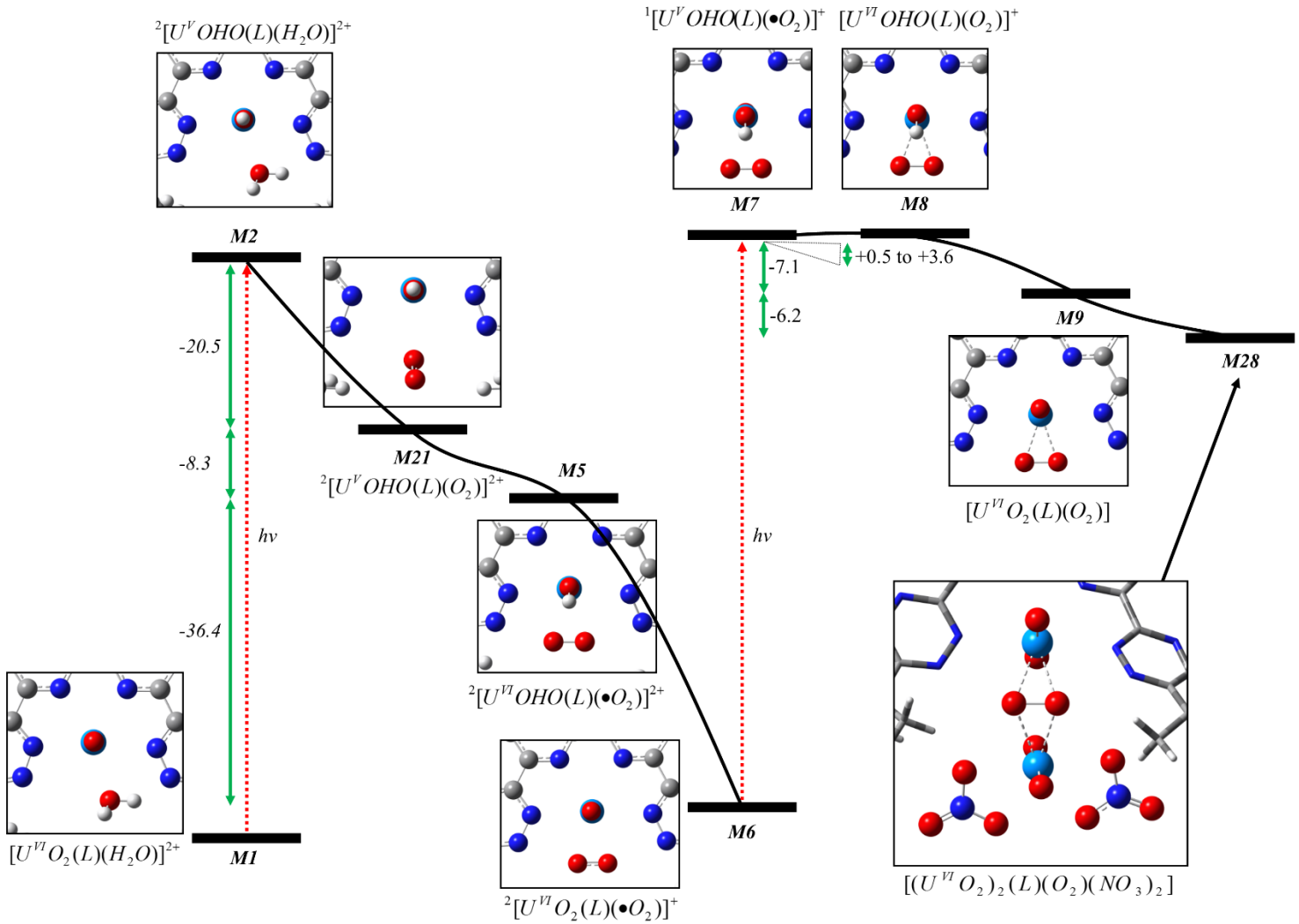

Figure 79: To scale schematic of the reaction profile calculated for the twice photon activated 2-electron transfer mechanism that converts dioxygen to peroxide and ultimately forms a bisuranyl peroxide bridged complex. This schematic represents the mechanism described by **Scheme 8**. The red arrows represent photoexcitation steps and the energies used to define them are equivalent to the λ_{max} for UO_2^{2+}, 414 nm. Green double arrows indicate the free energy released for each of the reactions taking place. All energies are quoted in kcal mol^{-1}.

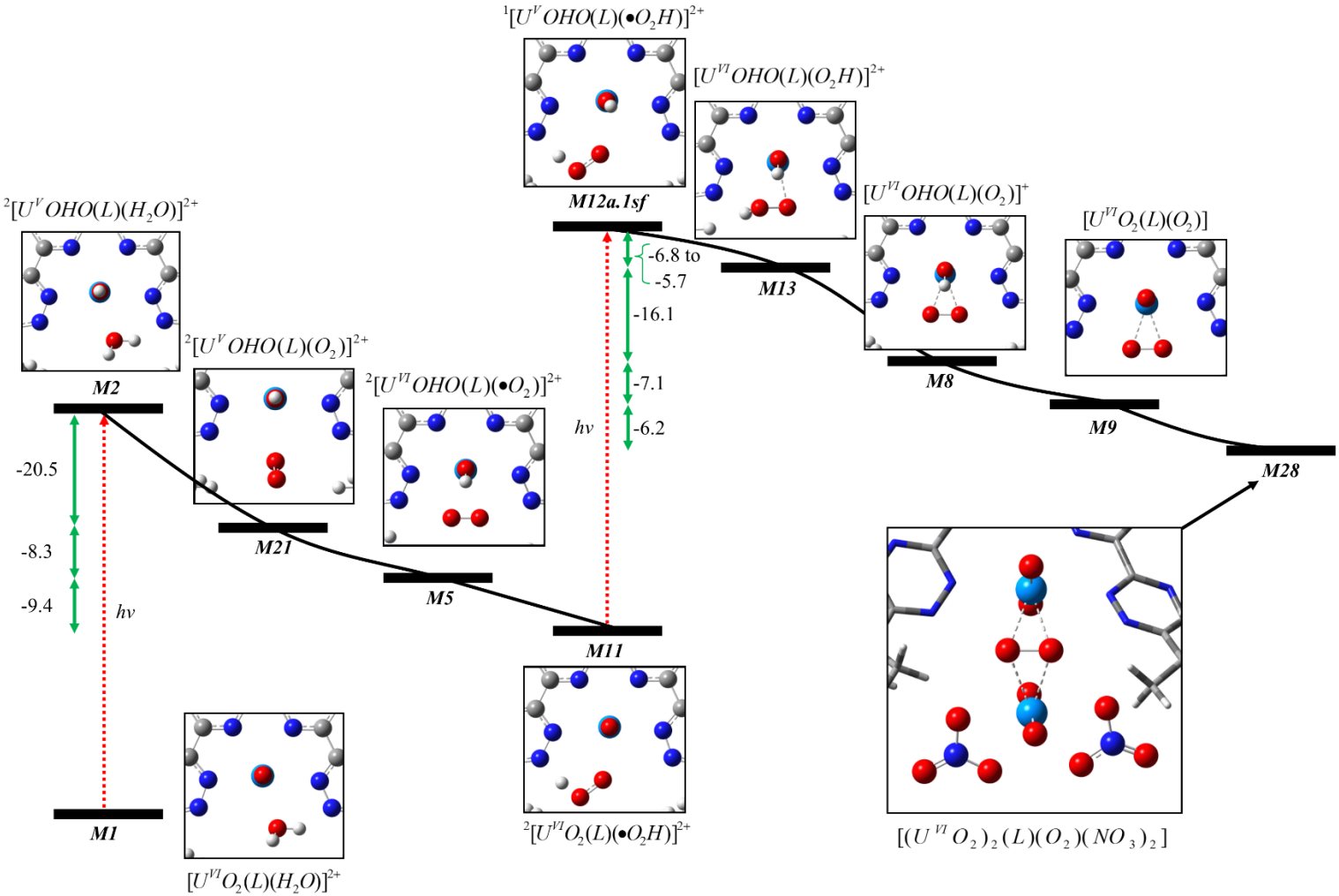

Figure 80: To scale schematic of the reaction profile calculated for the twice photon activated 2-electron transfer mechanism that converts dioxygen to peroxide and ultimately forms a bisuranyl peroxide bridged complex. This schematic represents the mechanism described by **Scheme 10**. The red arrows represent photoexcitation steps and the energies used to define them are equivalent to the λ_{max} for UO_2^{2+}, 414 nm. Green double arrows indicate the free energy released for each of the reactions taking place. All energies are quoted in kcal mol^{-1}.

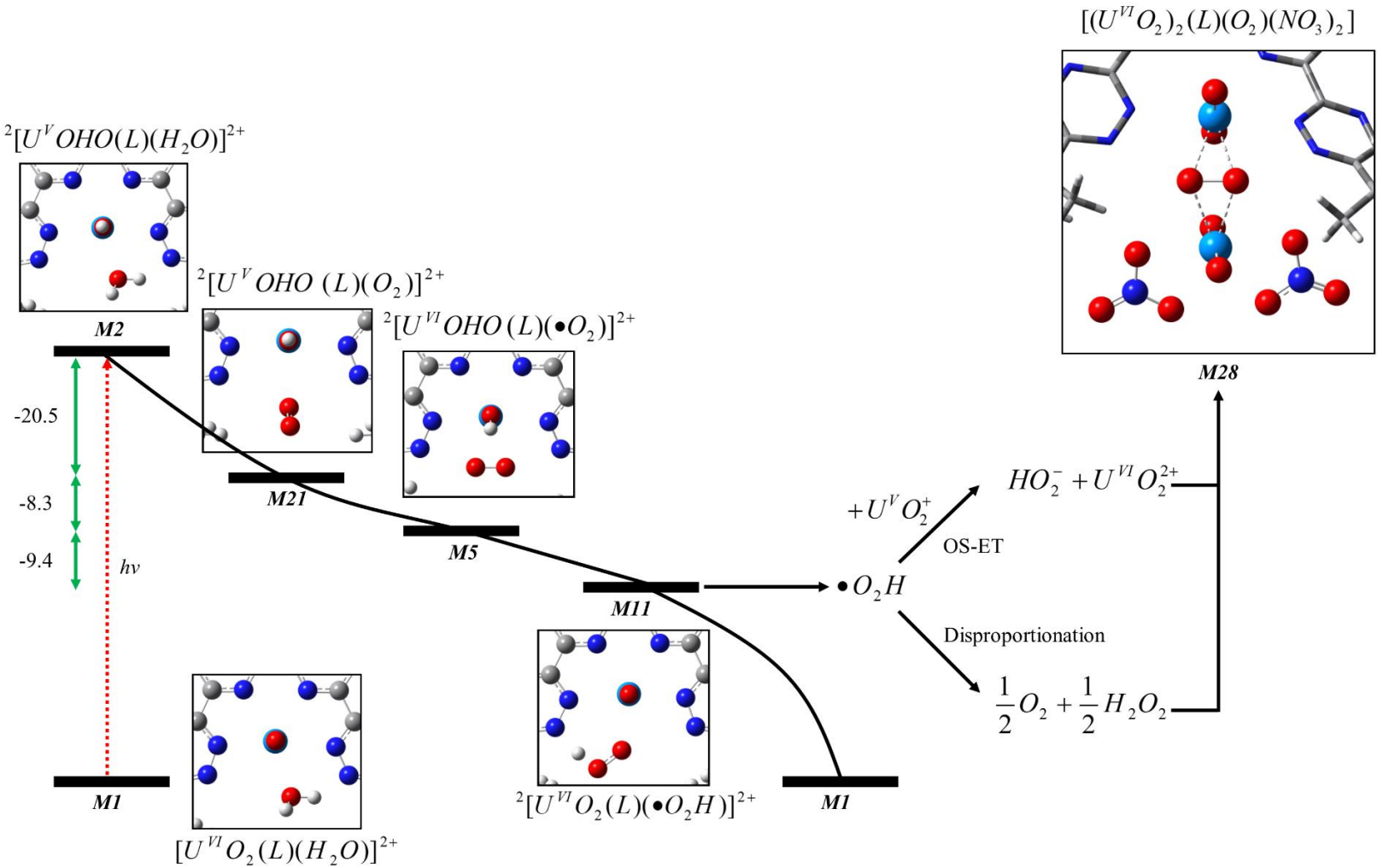

Figure 81: To scale schematic of the reaction profile calculated for the once photon activated single inner sphere ET and single outer sphere ET or disproportionation mechanism that converts dioxygen to peroxide. This schematic represents the mechanism described by **Scheme 9**. The red arrow represents a photoexcitation and the energy used to define it is equivalent to the λ_{max} for UO_2^{2+}, 414 nm. Green double arrows indicate the free energy released for each of the reactions taking place. All energies are quoted in kcal mol^{-1}.

4.4 Conclusion

The reaction possibility space has been scoured for the thermodynamically feasible pathways that may account for the formation of peroxide in solutions containing the uranyl ion and the ligand BTPhen. Two routes to the peroxide bridged product have been identified as favourable. The first is the route proposed by following a kinetic study of the system in the absence of the BTPhen ligand by Bakac et al.[4] and the second is an IS-ET process that proceeds via two iterations of an IS photocatalytic cycle. Both of these processes proced via the initial formation of a transient protonated uranyl(V)-dioxygen complex which subsequently undergoes IS-ET to generate the corresponding protonated uranyl(VI)-superoxide complex, however following this point the two routes diverge. The route favoured by Bakac et al. involves the transfer of the proton on the uranyl(VI) ion to the equatorially bound superoxide anion in a water mediated proton transfer process. The uranyl(VI)-hydroperoxyl radical formed is subsequently only weakly bound and hence favourably dissociates liberating the free hydroperoxyl radical and regenerating the uranyl(VI) catalyst. Following this point a second iteration of the uranyl(VI) excitation and hydrogen atom abstraction steps occur in an aquated uranyl(VI) species to form an aquated uranyl(V) ion which reduces the solvated hydroperoxyl radical via an OS-ET process to form peroxide. The final step of this process required to form the peroxide bridged bisuranyl(VI) product characterised crystallographically by DMW is for two ground state uranyl(VI) ions to spontaneously coordinate a free peroxide anion in solution. The second process identified relates to a process in which both ET reactions occur via IS-ET processes. In this scheme, following the formation of the protonated uranyl(VI)-superoxide complex by the initial IS-ET reaction the uranyl ion spontaneously deprotonates. The uranyl(VI)-superoxide complex formed is calculated to be a relatively stable species in solution and hence it may persist for elongated time periods, during which it is likely to be excited by an incident photon in order to generate the oxidising excited state of this species able to abstract a hydrogen atom from the solvent to generate the corresponding uranyl(V) complex. This species may then undergo an essentially energetically neutral IS-ET process in order to generate a mono-metallic peroxide complex. This mechanism has been identified as the one likely most conservative in energy owing to the fact that no barriers to activation were identified for the ET processes in this route. Furthermore, this reaction mechanism benefits from the fact that deprotonated uranyl(VI)-superoxide complex represents one of the lowest energy superoxide structures and this species is therefore likely to be one of the most abundant in the process, thereby likely leading to a kinetic favourability of this process. The

final step of this twice IS-ET mechanism describes the feasible approach of a uranyl(VI) ion onto this complex in order to form the bisuranyl peroxide bridged complex observed. Schematics outlining the thermodynamic reaction profiles that describe these two processes are presented in **Figure 79** and **Figure 81**, respectively and a schematic detailing the possibility space scoured throughout this study is presented in **Figure 78**.

References

1 F. W. Lewis, L. M. Harwood, M. J. Hudson, M. G. B. Drew, J. F. Desreux, G. Vidick, N. Bouslimani, G. Modolo, A. Wilden, M. Sypula, T.-H. Vu and J.-P. Simonin, *J. Am. Chem. Soc.*, 2011, **133**, 13093–102.

2 K. Kubatko and P. C. Burns, *Inorg. Chem*, 2006, **45**, 6096–6098.

3 D. M. Whittaker, *Ph.D. Thesis, Univ. Manchester*, 2014, 78–87.

4 A. Bakac and J. H. Espenson, *Inorg. Chem.*, 1995, **34**, 1730–1735.

5 H. D. Burrows and T. J. Kemp, *Chem. Soc. Rev.*, 1972, **2**, 139–165.

6 M. J. Frisch, G. W. Trucks, H. B. Schlegel, G. E. Scuseria, M. A. Robb, C. J. R., G. Scalmani, V. Barone, B. Mennucci, G. A. Petersson, H. Nakatsuji, M. Caricato, X. Li, H. P. Hratchian, A. F. Izmaylov, J. Bloino, G. Zheng, J. L. Sonnenberg, M. Hada, M. Ehara, K. Toyota, R. Fukuda, J. Hasegawa, M. Ishida, T. Nakajima, Y. Honda, O. Kitao, H. Nakai, T. Vreven, J. J. A. Montgomery, J. E. Peralta, F. Ogliaro, M. Bearpark, J. J. Heyd, E. Brothers, K. N. Kudin, V. N. Staroverov, T. Keith, R. Kobayashi, J. Normand, K. Raghavachari, A. Rendell, J. C. Burant, S. S. Iyengar, J. Tomasi, M. Cossi, N. Rega, J. M. Millam, M. Klene, J. E. Knox, J. B. Cross, V. Bakken, C. Adamo, J. Jaramillo, R. Gomperts, R. E. Stratmann, O. Yazyev, A. J. Austin, R. Cammi, C. Pomelli, J. W. Ochterski, R. L. Martin, K. Morokuma, V. G. Zakrzewski, G. A. Voth, P. Salvador, J. J. Dannenberg, S. Dapprich, A. D. Daniels, O. Farkas, J. B. Foresman, J. V. Ortiz, J. Cioslowski and D. J. Fox, 2010, Gaussian 09, Revision B.01.

7 World Nuclear Association; Nuclear Power in the UK, *Accessed 15/05/14*, 2011, http://www.world–nuclear.org/info/inf84.html.

8 T. Abram and S. Ion, *Energy Policy*, 2008, **36**, 4323–4330.

9 World Nuclear Association; Processing of Used Nuclear Fuel, *Accessed 16/05/14*, 2014, http://www.world–nuclear.org/info/Nuclear–Fuel–Cyc.

10 N. Kaltsoyannis and P. Scott, *The f-elements*, Oxford Science Publications, 1st edn., 1999.

11 H. G. Friedman, G. R. Choppin and D. G. Feuerbacher, *J. Chem. Educ.*, 1964, 354–358.

12 M. Winter The Periodic Table on the Web, *Accessed 16/05/14*, 2014, www.webelements.com.

13 R. . Dennington, T. . Keith and J. Millam, 2009, GaussView, Version 5.

14 D. L. Clark, S. S. Hecker, G. D. Jarvinen and M. P. Neu, in *The Chemistry of the Actinide and Transactinide Elements*, 2005, pp. 813–1264.

15 R. J. Lemire, J. Fugar, H. Nitsche, P. Potter, M. H. Rand, J. Rydberg, K. Spahiu, J. C. Sullivan, C. Ullman, P. Vitorge and H. Warner, *Chemical Thermodynamics of Plutonium and Neptunium*, Amsterdam, 2001.

16 D. L. Clark, *Los Alamos Sci.*, 2000, **26**, 364–381.

17 W. H. Runde, *Los Alamos Sci.*, 2000, **26**, 391–411.

18 C. E. Housecroft and E. C. Constable, *Chemistry*, Pearson Prentice Hall, 3rd edn., 2006.

19 P. Pyykko, *Chem. Rev.*, 1988, **88**, 563–594.

20 I. Kirker and N. Kaltsoyannis, *Dalton Trans.*, 2011, **40**, 124–31.

21 A. J. Gaunt, S. D. Reilly, A. E. Enriquez, B. L. Scott, J. a Ibers, P. Sekar, K. I. M. Ingram, N. Kaltsoyannis and M. P. Neu, *Inorg. Chem.*, 2008, **47**, 29–41.

22 U. Wahlgren, S. Tsushima and I. Grenthe, *J. Phys. Chem. A*, 2006, **110**, 9025–7.

23 G. Schreckenbach, P. J. Hay and R. L. Martin, *Science (80-.).*, 1998, **20**, 70–90.

24 R. Spezia, B. Siboulet, S. Abadie, R. Vuilleumier and P. Vitorge, *J. Phys. Chem. B*, 2011, **115**, 3560–70.

25 V. Vallet, T. Privalov, U. Wahlgren and I. Grenthe, *J. Am. Chem. Soc.*, 2004, **126**, 7766–7.

26 R. G. Denning, *J. Phys. Chem. A*, 2007, **111**, 4125–43.

27 P. Thuéry, M. Nierlich, N. Keller, M. Lance and J. D. Vigner, *Acta Crystallogr. Sect. C Cryst. Struct. Commun.*, 1995, **51**, 1300–1302.

28 M. P. Wilkerson, C. J. Burns, R. T. Paine and B. L. Scott, *Inorg. Chem.*, 1999, **2**, 4156–4158.

29 J.-C. Berthet, P. Thuéry, M. R. S. Foreman and M. Ephritikhine, *Radiochim. Acta*, 2008, **96**, 189–197.

30 J. Wiebke, A. Weigand, D. Weissmann, M. Glorius, H. Moll, G. Bernhard and M. Dolg, *Inorg. Chem.*, 2010, **49**, 6428–35.

31 N. Kaltsoyannis, *Inorg. Chem.*, 2000, **39**, 6009–17.

32 N. Kaltsoyannis, P. J. Hay, J. Li, J. P. Blaudeau and B. E. Bursten, in *Chemistry of the Actinide and Transactinide Elements*, 2005, pp. 1893–1996.

33 N. Kaltsoyannis, *Chem. Soc. Rev.*, 2003, **32**, 9–16.

34 V. Vallet, U. Wahlgren and I. Grenthe, *J. Phys. Chem. A*, 2012, **116**, 12373–80.

35 M. Bühl, N. Sieffert and G. Wipff, *Dalton Trans.*, 2013, **2**.

36 S. Tsushima and A. Suzuki, *J. Mol. Struct.*, 1999, **487**, 33–38.

37 P. Thuéry, M. Nierlich, B. Masci, Z. Asfari and J. Vicens., *J. Chem. Soc., Dalt. Trans.*, 1999, 3151–3152.

38 C. J. Burns, D. L. Clark, R. J. Donohoe, P. B. Duval, B. L. Scott and C. D. Tait, *Inorg. Chem.*, 2000, **39**, 5464–5468.

39 T. W. Hayton and G. Wu, *Inorg. Chem.*, 2009, **48**, 3065–72.

40 IAEA Assessment of Partitioning Processes for Transmutation of Actinides, 2010, 11–15.

41 D. Magnusson, B. Christiansen, R. Malmbeck and J.-P. Glatz, *Radiochim. Acta*, 2009, **97**, 497–502.

42 PerkinElmer; ChemBioDraw, 2013.

43 M. G. Drew, M. J. Hudson and T. G. Youngs, *J. Alloys Compd.*, 2004, **374**, 408–415.

44 F. W. Lewis, L. M. Harwood, M. J. Hudson, M. G. B. Drew, M. Sypula, J. F. Desreux, N. Bouslimani and G. Vidick, *Synthesis (Stuttg).*, 2010.

45 M. J. Hudson, C. E. Boucher, D. Braekers, J. F. Desreux, M. G. B. Drew, M. R. S. J. Foreman, L. M. Harwood, C. Hill, C. Madic, F. Marken and T. G. a. Youngs, *New J. Chem.*, 2006, **30**, 1171.

46 M. J. Hudson, M. G. B. Drew, M. R. S. Foreman, C. Hill, N. Huet, C. Madic and T. G. A. Youngs, *Dalt. Trans.*, 2003, 1675–1685.

47 M. G. B. Drew, C. Hill, M. J. Hudson, P. B. Iveson, C. Madic and T. G. a Youngs, *Dalton Trans.*, 2004, 244–51.

48 N. Boubals, M. G. B. Drew, C. Hill, M. J. Hudson, P. B. Iveson, C. Madic, M. L. Russell and T. G. A. Youngs, *J. Chem. Soc. Dalt. Trans.*, 2002, **7**, 55–62.

49 M. J. Hudson, L. M. Harwood, D. M. Laventine and F. W. Lewis, *Inorg. Chem.*, 2012, 120806130308003.

50 E. H. K. Aneheim, *Ph.D. Thesis, Chalmers Univ.*, 2012.

51 C. J. Cramer, *Essentials of Computational Chemistry: Theories and Models*, John Wiley & Sons Ltd., 2nd edn., 2004.

52 J. P. Lowe and K. A. Peterson, *Quantum Chemistry*, Elsevier Academic Press, 3rd edn., 2006.

53 P. Atkins and R. Friedman, *Molecular Quantum Mechanics*, .

54 T. H. Dunning, *J. Chem. Phys.*, 1970, **53**, 2823.

55 T. H. Dunning, *J. Chem. Phys.*, 1971, **55**, 716.

56 M. S. Gordon, J. S. Binkley, J. A. Pople, W. J. Pietro and W. J. Hehre, *J. Am. Chem. Soc.*, 1982, **104**, 2797–2803.

57 R. Krishnan, J. S. Binkley, R. Seeger and J. A. Pople, *J. Chem. Phys.*, 1980, **72**, 650.

58 J. S. Binkley, J. A. Pople and W. J. Hehre, *J. Am. Chem. Soc.*, 1980, **102**, 939–947.

59 J. C. Slater, *Phys. Rev.*, 1930, **36**, 57.

60 S. F. Boys, *Proc. R. Soc. London. Ser. A*, 1950, **200**, 542.

61 W. J. Hehre, R. J. Stewart and J. A. Pople, *J. Chem. Phys.*, 1969, **51**, 2657–2664.

62 A. D. Becke, *Phys. Rev. A*, 1988, **38**, 3098–3100.

63 C. Lee, W. Yang and R. G. Parr, *Phys. Rev. B*, 1988, **37**, 785–789.

64 A. D. Becke, *J. Chem. Phys.*, 1993, **98**, 5648–5652.

65 P. J. Stephens, F. J. Devlin, C. F. Chabalowski and M. J. Frisch, *J. Phys. Chem.*, 1994, **98**, 11623–11627.

66 W. Kuchle, M. Dolg, H. Stoll and H. Preuss, *J. Chem. Phys.*, 1994, **100**, 7535–7542.

67 T. R. Cundari and W. J. Stevens, *J. Chem. Phys.*, 1993, **98**, 5555–5565.

68 M. Dolg, *Mod. Methods Algorithms Quantum Chem. Proc.*, 2000, **3**, 507–540.

69 W. Kuchle, M. Dolg, H. Stoll and H. Preuss, *Mol. Phys.*, 1991, **74**, 1245.

70 M. Dolg and X. Cao, *J. Phys. Chem. A*, 2009, **113**, 12573–81.

71 E. D. Glendening, A. E. Reed, J. E. Carpenter and F. Weinhold., 2001, NBO Version 3.1.

72 F. Weinhold and C. R. Landis, *Chem. Educ.*, 2001, **2**, 91–104.

73 D. Ho, 2014, Notepad++.

74 A. D. Becke, *J. Phys. Chem.*, 1993, **98**, 5648–5652.

75 S. H. Vosko, L. Wilk and M. Nusair, *Can. J. Phys.*, 1980, **58**, 1200–1211.

76 X. Cao, M. Dolg and H. Stoll, *J. Chem. Phys.*, 2003, **118**, 487.

77 X. Cao and M. Dolg, *J. Mol. Struct. THEOCHEM*, 2004, **673**, 203–209.

78 P. J. Hay, R. L. Martin and G. Schreckenbach, *J. Phys. Chem. A*, 2000, **104**, 6259–6270.

79 S. Tsushima, U. Wahlgren and I. Grenthe, *J. Phys. Chem. A*, 2006, **110**, 9175–82.

80 R. Ditchfield, W. J. Hehre and J. A. Pople, *J. Phys. Chem.*, 1971, **54**, 724.

81 W. J. Hehre, R. Ditchfield and J. A. Pople, *J. Chem. Phys.*, 1972, **56**, 2257.

82 P. C. Hariharan and J. A. Pople, *Theor. Chem. Acc.*, 1973, **28**, 213–222.

83 P. C. Hariharan and J. A. Pople, *Mol. Phys.*, 1974, **27**, 209–214.

84 M. M. Francl, W. J. Pietro, W. J. Hehre, J. S. Binkley, D. J. DeFrees, J. A. Pople and M. S. Gordon, *J. Chem. Phys.*, 1982, **77**, 3654–3665.

85 K. Raghavachari, J. S. Binkley, R. Seeger and J. A. Pople, *Int. J. Quantum Chem.*, 1981, **20**, 1067–1071.

86 F. Weigend and R. Ahlrichs, *Phys. Chem. Chem. Phys.*, 2005, **7**, 3297–305.

87 F. Weigend, *Phys. Chem. Chem. Phys.*, 2006, **8**, 1057–1065.

88 D. Rappoport and F. Furche, *J. Chem. Phys.*, 2010, **133**, 134105.

89 S. F. Boys and F. Bernardi, *Mol. Phys.*, 1970, **19**, 553.

90 J. W. Ochterski, *Thermochemistry in Gaussian*, 2000.

91 G. Rasul, G. a Olah and G. K. S. Prakash, *PNAS*, 2004, **101**, 10868–71.

92 X. Xu, R. P. Muller and W. a Goddard, *PNAS*, 2002, **99**, 3376–81.

93 B. B. Averkiev and D. G. Truhlar, *Catal. Sci. Technol.*, 2011, **1**, 1526.

94 W. N. Oloo, K. K. Meier, Y. Wang, S. Shaik, E. Münck and L. Que, *Nat. Commun.*, 2014, **5**, 3046.

95 P. Y. Ayala and H. B. Schlegel, *J. Chem. Phys.*, 1998, **108**, 2314.

96 D. J. Grant, Z. Weng, L. J. Jouffret, P. C. Burns and L. Gagliardi, *Inorg. Chem.*, 2012, **51**, 7801–9.

97 F. B. van Duijneveldt, J. G. C. M. van Duijneveldt-van de Rijdt and J. H. van Lenthe, *Chem. Rev.*, 1994, **94**, 1873–1885.

98 M. Bühl, N. Sieffert, A. Chaumont and G. Wipff, *Inorg. Chem.*, 2012, **51**, 1943–52.

99 P. R. Varadwaj and H. M. Marques, *Phys. Chem. Chem. Phys.*, 2010, **12**, 2126–38.

100 Young-Kyu Han, K. H. Kim, S.-K. Son and Y. S. Lee, *Bull. Korean. Chem. Soc.*, 2002, **23**, 1267–1271.

101 V. Barone and M. Cossi, *J. Phys. Chem. A*, 1998, **102**, 404–417.

102 M. Cossi, N. Rega, G. Scalmani and V. Barone, *J. Chem. Phys.*, 2001, **114**, 5691–5701.

103 J. Tomasi, B. Mennucci and R. Cammi, *Chem. Rev.*, 2005, **105**, 2999–3093.

104 G. Schreckenbach and G. a Shamov, *Acc. Chem. Res.*, 2010, **43**, 19–29.

105 S. Tsushima, V. Brendler and K. Fahmy, *Dalton Trans.*, 2010, **39**, 10953–10958.

106 S. Tsushima, *Inorg. Chem.*, 2009, **48**, 4856–62.

107 R. Prabhakar, P. E. M. Siegbahn, B. F. Minaev and H. Ågren, *J. Phys. Chem. B*, 2002, **106**, 3742–3750.

108 K. Yamaguchi, F. Jensen, A. Dorigo and K. N. Houk, *Chem. Phys. Lett.*, 1988, **149**, 537–542.

109 E. Goldstein, B. Beno and K. N. Houk, *J. Am. Chem. Soc.*, 1996, **7863**, 6036–6043.

110 F. Lewis, M. Hudson and L. Harwood, *Synlett*, 2011, **2011**, 2609–2632.

111 F. W. Lewis, L. M. Harwood, M. J. Hudson, M. G. B. Drew, J. F. Desreux, G. Vidick, N. Bouslimani, G. Modolo, A. Wilden, M. Sypula, T. Vu and J. Simonin, *J. Am. Chem. Soc.*, 2011, **133**, 13093–13102.

112 D. Cohen, *J. Inorg. Nuc. Chem.*, 1961, **18**, 211–218.

113 A. Braibanti, G. Ostacoli, P. Paoletti, L. D. Pettit and S. Sammartano, *Pure Appl. Chem.*, 1987, **59**, 1721–1728.

114 M. H. Klaproth, *Chem. Ann. Freunde Naturl.*, 1789, **2**, 387–403.

115 EPA; Radioactive Antiques, *Accessed 20/05/14*, 2014, http://www.epa.gov/radtown/antiques.html.

116 S. Tsushima, C. Götz and K. Fahmy, *Chem. Eur. J.*, 2010, **16**, 8029–33.

117 M. Wilderson and H. J. Dewey, *Actin. Res. Q.*, 2004, **1st**, 2.

118 D. Hobart, *Period. Table Elem.*, 2013.

119 E. Sairenji, R. Soremark, K. Noguchi, M. Shimzu and L. E. Moberg, *Acta Odontol Scand.*, 1982, **40**, 333–339.

120 L. S. Natrajan, *Dalt. Trans.*, 2012, **41**, 13167–13172.

121 I. N. Izosimov, N. G. Firsin, N. G. Gorshkov and S. N. Nekhoroshkov, *Hyperfine Interact.*, 2014, **227**, 271–281.

122 T. M. Mccleskey, T. M. Foreman, E. E. Hallman, C. J. Burns and N. N. Sauer, *Environ. Sci. Technol.*, 2001, **35**, 547–51.

123 J. Bigeleisen, *J. Am. Chem. Soc.*, 1996, **118**, 3676–3680.

124 Y. Mao and A. Bakac, *Inorg. Chem.*, 1996, **35**, 3925–3930.

125 Y. Mao and A. Bakac, *J. Phys. Chem. A*, 1997, **101**, 7929–7933.

126 J. I. Bell and R. E. Biggers, *J. Mol. Spectrosc.*, 1965, **275**, 247–275.

127 S. J. Formosinho, M. D. G. M. Miguel, M. E. D. G. Azenhad, H. D. Burrows, A. P. Daramanyan and K. I. V., *J. Lumin.*, 1991, **49**, 522–526.

128 M. E. D. G. Azenha, H. D. Burrows, S. J. Formosinho and M. D. G. M. Miguel, *J. Chem. Soc. Faraday Trans. 1*, 1989, **85**, 2625.

129 I. Billard, E. Ansoborlo, K. Apperson, S. Arpigny, M. E. Azenha, D. Birch, P. Bros, H. D. Burrows, G. Choppin, L. Couston, V. Dubois, T. Fanghänel, G. Geipel, S. Hubert, J. I. Kim, T. Kimura, R. Klenze, A. Kronenberg, M. Kumke, G. Lagarde, G. Lamarque, S. Lis, C. Madic, G. Meinrath, C. Moulin, R. Nagaishi, D. Parker, G. Plancque, F. Scherbaum, E. Simoni, S. Sinkov and C. Viallesoubranne, *Appl. Spectrosc.*, 2003, **57**, 1027–38.

130 M. Gratzel, *Energy Resources through Photochemistry and Catalysis*, Elsevier Ltd, 1983.

131 D. M. Allen, H. D. Burrows, A. Cox, R. J. Hill, T. J. Kemp and T. J. Stone, *J. Chem. Soc. Chem. Commun.*, 1973, **59**, 59.

132 W. Wang, A. Bakac and J. H. Espenson, *Inorg. Chem.*, 1995, **34**, 6034–6039.

133 S. J. Formosinho and M. D. G. M. Miguel, *J. Chem. Soc. Faraday Trans. 1*, 1984, **80**, 1745.

134 J. Formosinho, *Faraday Trans.*, 1976, **201**, 201–208.

135 V. Balzani, F. Bolletta, M. T. Gandolfi and M. Maestri, in *Topics In Current Chemistry*, Springer, 1978, pp. 1–64.

136 T. M. McCleskey and C. J. Burns, *Inorg. Chem*, 1999, 5924–5925.

137 R. Matsushima, *J. Am. Chem. Soc.*, 1972, **23**, 6010–6016.

138 M. D. Marcantonatos, *J. Chem. Soc. Faraday Trans. 1*, 1980, 1093–1115.

139 H. D. Burrows, *Inorg. Chem.*, 1990, **29**, 1549–1554.

140 R. Nagaishi, Y. Katsumura, K. Ishigure, H. Aoyagi, Z. Yoshida, T. Kimura and Y. Kato, *Photochem. Photobiol.*, 2002, **146**, 157–161.

141 M. Sarakha, H. D. Burrows and M. Bolte, *J. Phys. Chem. A*, 2000, **104**, 3142–3149.

142 D. G. C. A. S. Meisel, *J. Phys. Chem.*, 1973, **1570**, 9–14.

143 D. Meisel, Y. A. Ilan and G. Czapskl, *J. Phys. Chem.*, 1974, 2330–2334.

144 I. Afanas'ev, *Superoxide Ion Chemistry and Biological Implications*, CRC Press, Volume 1., 1989.

145 B. Bielski, D. Cabelli, R. Arudi and A. Ross, *J. Phys. Chem. Ref. Data*, 1985, **14**, 1041–1100.

146 I. Ashur, A. Brandis, M. Greenwald, Y. Vakrat-Haglili, V. Rosenbach-Belkin, H. Scheer and A. Scherz, *J. Am. Chem. Soc.*, 2003, **125**, 8852–61.

147 V. M. Berdnikov, L. L. Makarshin and L. S. Ryvkina, *React. Kinet. Catal. Lett.*, 1978, 281.

148 V. M. Berdnikov, L. L. Makarshin and L. S. Ryvkina, *React. Kinet. Catal. Lett.*, 1978, 205.

149 L. S. Ryvkina and V. M. Berdnikov, *React. Kinet. Catal. Lett.*, 1982, 409.

150 S. Bratsch, *J. Phys. Chem. Ref. Data*, 1989, **18**, 1–21.

151 G. M. Jones, P. L. Arnold and J. B. Love, *Angew. Chem. Int. Ed. Engl.*, 2012, **51**, 12584–7.

152 D. Rose, Y. Chang, Q. Chen and J. Zubieta, *Inorg. Chem.*, 1994, **33**, 5167–5168.

153 G. A. Doyle, D. M. L. Goodgame, A. Sinden and D. J. Williams, *Chem. Commun. (Camb).*, 1993, 1170–1172.

154 G. H. John, I. May, J. Sars, H. M. Steele, D. Collison, M. Helliwell and J. D. Mckinney, *Dalton Trans.*, 2004, **2**, 734.

155 J.-L. Wang, Z.-Y. Deng, S.-B. Duan and Y.-H. Xing, *J. Coord. Chem.*, 2012, **65**, 3546–3555.

156 P. L. Arnold, A.-F. Pécharman and J. B. Love, *Angew. Chemie Int. Ed.*, 2011, **50**, 9456–9458.

157 B. T. McGrail, L. S. Pianowski and P. C. Burns, *J. Am. Chem. Soc.*, 2014, **136**, 4797–800.

158 P. C. Burns and K.-A. Hughes, *Am. Minerol.*, 2003, **88**, 1165–1168.

159 B. K. McNamara, E. C. Buck and B. D. Hanson, in *Scientific Basis for Nuclear Waste Management XXVI. Materials Research Society Symposium Proceedings*, 2003, pp. 401–406.

160 Y. N. Mikhailov, G. M. Lobanova and R. N. Shchelokov, *Zh.Neorg.Khim.(Russ.)(Russ.J.Inorg.Chem.)*, 1981, **26**, 718.

161 W. H. Runde, *Acta Crystallogr. Sect. C*, 2005, **61**, 13–15.

162 K.-A. Kubatko, T. Z. Forbes, A. L. Klingensmith and P. C. Burns, *Inorg. Chem.*, 2007, **46**, 3657–62.

163 G. E. Sigmon, J. Ling, D. K. Unruh, L. Moore-Shay, M. Ward, B. Weaver and P. C. Burns, *J. Am. Chem. Soc.*, 2009, **131**, 16648–9.

164 M. I. Ojovan, *Handbook of Advanced Radioactive Waste Conditioning Technologies*, 2011.

165 C. F. Macrae, I. J. Bruno, J. A. Chisholm, P. R. Edgington, P. McCabe, E. Pidcock, L. Rodriguez-Monge, R. Taylor, J. van de Streek and P. A. Wood, *J. Appl. Cryst*, 2008, **41**, 466–470.

166 C. F. Macrae, P. R. Edgington, P. McCabe, E. Pidcock, G. P. Shields, R. Taylor, M. Towler and J. van de Streek, *J. Appl. Cryst*, 2006, **39**, 453–457.

167 I. J. Bruno, J. C. Cole, P. R. Edgington, M. K. Kessler, C. F. Macrae, P. McCabe, J. Pearson and R. Taylor, *Acta Cryst. B*, 2002, **58**, 389–397.

168 R. Taylor and C. F. Macrae, *Acta Cryst. B*, 2001, **57**, 815–827.

169 B. T. McGrail, G. E. Sigmon, L. J. Jouffret, C. R. Andrews and P. C. Burns, *Inorg. Chem.*, 2014, **53**, 1562–9.

170 B. Vlaisavljevich, L. Gagliardi and P. C. Burns, *J. Am. Chem. Soc.*, 2010, **132**, 14503–8.

171 P. Miró, S. Pierrefixe, M. Gicquel, A. Gil and C. Bo, *J. Am. Chem. Soc.*, 2010, **132**, 17787–94.

172 J. Qiu and P. C. Burns, *Chem. Rev.*, 2013, **113**, 1097–120.

173 I. M. Aladzheva, O. V. Bykhovskaya, Y. V. Nelyubina, Z. S. Klemenkova, P. V. Petrovskii and I. L. Odinets, *Inorganica Chim. Acta*, 2011, **373**, 130–136.

174 I. A. Charushnikova and C. Den Auwer, *Koord. Khim. (Russ.)(Coord. Chem.)*, 2004, **30**, 6.

175 R. Haegele and J. C. A. Boeyens, *Dalt. Trans.*, 1977, 648.

176 N. Akbarzadeh-T and T. Kondori, *Res. Chem. Intermed.*, 2013, **May**.

177 G. H. John, I. May, M. J. Sarsfield, D. Collison and M. Helliwell, *Dalton Trans.*, 2007, **2**, 1603–10.

178 A. R. de Aquino, P. C. Isolani, J. Zukerman-Schpector, L. B. Zinner and C. Vicentini, *J. Alloy. Compd.*, 2001, **323**, 18.

179 K. Takao and Y. Ikeda, *Acta Crystallogr. Sect. E*, 2010, **66**, 539.

180 M. N. Sokolova, A. A. Bessonov and A. M. Fedoseev, *Radiokhimiya (Russ.)(Radiochem.)*, 2012, **54**, 313.

181 I. A. Charushnikova, N. N. Krot and Z. A. Starikova, *Radiokhimiya (Russ.)(Radiochem.)*, 2001, **43**, 448.

182 P. Charpin, G. .Folcher, M. Lance, M. Nierlich and D. Vigner, *Acta Crystallogr. Sect. C Cryst. Struct. Commun.*, 1985, **41**, 1302.

183 P. Thuery, M. Nierlich, B. W. Baldwin, N. Komatsuzaki and T. Hirose, *Dalt. Trans.*, 1999, 1047.

184 B. Masci and P. .Thuery, *Polyhedron*, 2005, **24**, 229.

185 S. Wahu, J.-C. Berthet, P. Thuéry, D. Guillaumont, M. Ephritikhine, R. Guillot, G. Cote and C. Bresson, *Eur. J. Inorg. Chem.*, 2012, **2012**, 3747–3763.

186 R. Burns, in *The Kilmarnock Volume*, Kilmarnock, 1786, p. 138.

187 H. D. Burrows and M. G. Miguel, *Adv. Colloid Interface Sci.*, 2001, **89-90**, 485–96.

188 J. Formosinho, *Faraday Trans.*, 1975, **5**, 1313–1331.

189 S. J. Formosinho, H. D. Burrows, M. da Graca Miguel, M. E. D. G. Azenha, I. M. Saraiva, a. C. D. N. Ribeiro, I. V. Khudyakov, R. G. Gasanov, M. Bolte and M. Sarakha, *Photochem. Photobiol. Sci.*, 2003, **2**, 569.

190 Y. Mao and A. Bakac, *J. Phys. Chem.*, 1996, **100**, 4219–4223.

191 M. C. Derosa and R. J. Crutchley, *Coor. Chem. Rev.*, 2002, **234**, 351–371.

192 L. Martinot, J. Fugar, A. Bard, R. Parsons and J. Jordan, *Standard Potentials in Aqueous Solution*, Mercel Dekker, New Yoek, 1985.

193 A. Bakac, *Inorg. Chem.*, 2010, **49**, 3584–93.

194 H. Steele and R. J. Taylor, *Inorg. Chem.*, 2007, **46**, 6311–8.

195 J. H. Rodriguez, D. E. Wheeler and J. K. Mccusker, *J. Am. Chem. Soc.*, 1998, **120**, 12051–12068.

196 P. E. M. Siegbahn and M. R. a Blomberg, *Dalton Trans.*, 2009, 5832–40.

197 T. Wang, G. Brudvig and V. S. Batista, *J. Chem. Theory Comput.*, 2010, **6**, 755–760.

198 D. Hagberg, G. Karlström, B. O. Roos and L. Gagliardi, *J. Am. Chem. Soc.*, 2005, **127**, 14250–6.

199 M. Bühl and G. Schreckenbach, *Inorg. Chem.*, 2010, **49**, 3821–7.

200 Z. Szabó and I. Grenthe, *Inorg. Chem.*, 2010, **49**, 4928–33.

201 C. Danilo, V. Vallet, J.-P. Flament and U. Wahlgren, *Phys. Chem. Chem. Phys.*, 2010, **12**, 1116–30.

202 X. Yang, X.-B. Wang, L.-S. Wang, S. Niu and T. Ichiye, *J. Chem. Phys.*, 2003, **119**, 8311.

203 L. Noodleman, J. G. Norman, J. H. Osborne, A. Aizman and D. A. Case, *J. Am. Chem. Soc.*, 1985, **107**, 3418.

204 J. E. Crooks, in *Proton Transfer*, 1977, pp. 197–242.

205 H. James, A. Bard, R. Parsons and J. Jordan, *Standard Potentials in Aqueous Solution*, 1985.

206 M. H. Drooker, C. Huang and J. Sylwestrowicz, *J. Inorg. Nuc. Chem.*, 1979, **2**, 1431–1440.

207 O. M. Suleimenov, T. M. Seward and J. K. Hovey, *J. Solution Chem.*, 2007, **36**, 1093–1102.

208 N. A. Smith, *Ph.D. Thesis, Univ. Nevada, Las Vegas*, 2010.

209 S. Tsushima and A. Suzuki, *J. Mol. Struct.*, 2000, **529**, 21–25.

210 V. S. Bryantsev, M. S. Diallo and W. a Goddard, *J. Phys. Chem. B*, 2008, **112**, 9709–19.

211 C.-G. Zhan and D. Dixon, *J. Phys. Chem. A*, 2001, **105**, 11534–11540.

212 G. J. Tawa, I. A. Topol, S. K. Burt, R. A. Caldwell and A. A. Rashin, *J. Chem. Phys.*, 1998, **109**, 4852.

213 M. D. Tissandier, K. A. Cowen, W. Y. Feng, E. Gundlach, M. H. Cohen, A. D. Earhart, J. V Coe and T. R. Tuttle, 1998, **5639**, 7787–7794.

214 C. P. Kelly, C. J. Cramer and D. G. Truhlar, *J. Phys. Chem. B*, 2006, **110**, 16066–81.

215 C. P. Kelly, C. J. Cramer and D. G. Truhlar, *J. Phys. Chem. B*, 2006, **111**, 408–422.

216 S. Hwang and D. S. Chung, *Bull. Korean. Chem. Soc.*, 2005, **26**, 589–593.

217 M. G. Evans and N. Uri, *Trans. Faraday. Soc.*, 1949, **45**, 224–230.

218 W. H. Koppenol and G. Chen, *Oxy Radicals and Their Scavenger Systems. Volume 1: Molecular Aspects*, Elsevier Science, 1983.

219 J. Shen, C. F. Wong and J. A. Mccammont, *J. Comp. Chem.*, 1990, **11**, 1003–1008.

5 APPENDIX 1 – Calculation of BSSE for Systems Incorporating the Peroxide Dianion

When using the standard def2-TZVP basis, BSSEs calculated using the CP method ranged between 1.5 kcal mol^{-1} and 113.0 kcal mol^{-1}, the latter of which is clearly unacceptable when modelling reaction energies that have typical free energy changes on the range of 20 kcal mol^{-1}. It was noted that the models calculated as having the greatest BSSEs contained molecular fragments that by necessity were defined as having anionic charges localised on them. Thereby indicating that their proper treatment would possibly require the presence of diffuse functions in the basis set, in line with typical expectations. The standard incarnation of def2-TZVP contains no such functions, however 'back of a napkin' tests of the KS solution for a sole peroxide anion with the diffuse function augmented def2-TZVP+D basis set, indicated that this too failed to satisfactorily model these anionic species. Such calculations generated solutions that contained unbound electrons i.e. electrons in positive eigenvalue orbitals. In addition to DFT, this was also found to be the case for post-HF methods, culminating in an O_2^{2-} anion optimised at a coupled cluster singles and doubles (CCSD) level with an aug-cc-pVTZ basis also providing a wave function with occupied unbound electronic states. This clearly indicates the instability of the peroxide dianion species in isolation and is likely to be the root cause of the anomalously large BSSE as calculated using the one fragment per molecule approach to the CP calculation utilised in this study. In order to probe this observation further, SP calculations on the DFT and CCSD optimised geometries were repeated employing a CPCM solvation model. The inclusion of a polarisable solvent field with even a single figure dielectric constant was enough to stabilise all occupied orbitals to have negative energies in both CCSD and DFT calculations. This thoroughly suggests that the unbound states observed for the peroxide anion when treated using basis sets up to and including aug-cc-pVQZ in DFT and aug-cc-pVTZ in CCSD is an instability brought about by the extreme charge on the anion and the absence of any polarisable medium in the vicinity that may serve to stabilise it. The presence of occupied positive eigenvalue states when treating the peroxide anion in the gas phase therefore complicates the application of the CP procedure in this study, as the energy of the solution generated for the anionic fragment in its own basis and in the basis of the whole system will not necessarily reflect that of the fragment when treated as part of the system as a whole. The root of this difference being that the anionic charge is necessarily delocalised from the peroxide anion on forming strong coordinate bonds with the uranium species, thereby stabilising the fragment in a way not modelled in the isolated CP calculations. This could

lead to an overestimation of the BSSE in this study, as the charge localised on the anionic unit under the molecular fragmentation scheme employed is inherently delocalised on forming a stable complex. Hence, a proportion of the BSSE correction proposed using the CP method with such a molecular fragmentation scheme may also incorporate a significant degree of the stabilisation energy resulting from the fundamentally valid sharing of the uranium atom basis between the metal and the peroxide anion due to the formation of a partially covalent bond. Despite this rationale, further tests were carried out in order to assess the effect of including diffuse functions on the dioxygen species in the models studied.

The convergence of the BSSE was examined on introducing increasingly diffuse functions into the basis set of the dioxygen ligand species. Three bases were tested, the first two were the standard def2-TZVP and def2-TZVP+D bases as parameterised by Ahlrichs et al.[86,87] Whereas, the third was a bespoke augmented version of the def2-TZVP+D basis to which additional individual diffuse *s*- and *d*- functions had been added along with two extra *p*-functions, designated 'def2-TZVP+D+s+2p+d'. The contraction coefficient for these additional functions followed the trend utilised by Ahlrichs et al.[86,87] when augmenting their standard def2-TZVP basis. This meant that each diffuse function added had a coefficient of one third of the magnitude of the next most diffuse function. In initial tests modifying the basis set of an isolated peroxide dianion, these augmentations proved to provide a reasonable description of the KS orbitals of the dioxygen species without introducing significant SCF convergence issues. The BSSE calculated for a *[UO_2(BTPhen)O_2]* system on changing the peroxide anion basis is presented in **Table 34**.

Table 34: Table of the differences in the calculated single point energies for the 6-31G(d,p) optimised *[UO_2(BTPhen)O_2]* system on increasing the number of diffuse functions on the dioxygen species.[a]

	def2-TZVP	**def2-TZVP+D**	**def2-TZVP+D+s+2p+d**
SP Energy Diff	0.000	-0.746	-0.988
BSSE for O_2	112.702	59.980	3.198
Total BSSE	114.213	61.724	5.191

[a] Energies are quoted in kcal mol^{-1}.

From **Table 34**, it is clear that as more diffuse functions are added, the BSSE calculated for the peroxide fragment decreases significantly. Furthermore, this improvement in the BSSE is almost exclusively due to an improvement in the treatment of the peroxide fragment, as perceived by the CP procedure. Hence, under the fragmentation scheme used in this study, the most diffuse basis set tested does provide an improved estimate of the BSSE in the system than the standard def2-TZVP basis. Despite this apparent failure of the def2-TZVP basis, as will be shown, this improvement is purely of consequence to the CP calculations, as it is an artefact of the fragmentation scheme used. This is demonstrated by the fact that including

the additional functions in the SP calculation of the system as a whole has relatively little influence over the energy of the complex (or their calculated geometries, see below) when BSSE is not considered. This is best exemplified by the fact that the change in the total electronic energy of the system on introducing the diffuse functions is less than 1 kcal mol^{-1}, as shown in the table, above. Therefore, the solution identified when these diffuse functions are absent is not significantly different to that identified when they are included. This is in comparison with the effective change in the BSSE corrected energy on including these functions that results in a change in energy of over 100 kcal mol^{-1} when the most diffuse functions are included. Hence, the inclusion of diffuse functions is only of importance to the calculation of the BSSE as implemented in this study, and reassuringly has very little effect over the properties of the models calculated.

In order to assess the effect of including diffuse functions on the geometry optimisations, the same *[UO_2(BTPhen)O_2]* peroxide bound model system was re-optimised using basis sets containing increasingly diffuse functions on the dioxygen ligand. The basis sets considered were the standard 6-31G(d,p) basis used to optimise all other complexes in this study, the Pople type basis set 6-31+G(d,p) as parameterised in Gaussian 09, a bespoke augmented 6-31+G(d,p) basis set to which an extra *sp* function had been added with a contraction coefficient one third of the magnitude of that of the next most diffuse function and the bespoke augmented def2-TZVP+D+s+2p+d basis used in the SP calculations discussed previously.

The effect of changing the basis of the dioxygen species on important geometric parameters of the optimised complex are detailed in **Table 35**, below. It can be seen that none of the most susceptible geometric parameters were observed to change in magnitude by greater 0.01 Å. The only change that approached this magnitude was that of the peroxide *O*-*O* bond on shifting from the smallest, 6-31G(d,p), to the largest, def2-TZVP+D+s+2p+d, basis set tested. Even this change is actually likely to be an artefact of shifting from a double-ζ basis set to a triple-ζ and is not solely attributed to the addition of diffuse functions. Nevertheless, this change is still small, as quantified in **Table 36** below, in which the energy of each of the structures optimised using the different bases is obtained using SP calculations carried out with the def2-TZVP+D+s+2p+d basis on the peroxide *O* atoms and the standard B1 basis set for all other atoms (see Chapter 2.2). This shows that the energies of the different structures calculated using the various basis set sizes vary by less than 0.05 kcal mol^{-1}, and are therefore insignificant. It is worthwhile to note that the change in the predicted

thermodynamic properties is larger, but still insignificant, with a magnitude on the order of 0.1 kcal mol^{-1}, as shown in **Table 37**.

Table 35: Table of the selected geometric parameters for the *[UO_2(BTPhen)O_2]* model optimised using different basis sets on the dioxygen species.[a, b]

	6-31G(d,p)	**6-31+G(d,p)**	**6-31+G(d,p) + SP**	**def2-TZVP+D+s+2p+d**
O-O	1.414	1.415	1.415	1.404
U-O_{eq1}	2.110	2.113	2.113	2.108
U-O_{eq2}	2.110	2.114	2.114	2.109
U-O_{ax1}	2.047	2.044	2.044	2.049
U-O_{ax2}	1.792	1.791	1.790	1.792

[a] All distances are measured in Angstroms, Å.
[b] The *O-O*, *U-O_{eqx}* and *U-O_{axx}* parameters represent the peroxide bond length, the uranium to peroxide *O*-atom bond distances (where x=1,2) and the uranium to axial oxygen atom distances. Note that axial oxygen atom 1 is protonated in this model.

Table 36: Table of the single point energies calculated using the def2-TZVP+D+s+2p+d basis set for models of the *[UO_2(CyMe$_4$-BTPhen)O_2]* complex optimised using different sized basis sets on the dioxygen species.[a]

Basis Set used for Optimisation	**Difference**
6-31G(d,p)	0.00
6-31+G(d,p)	+0.013
6-31+G(d,p) + SP	+0.016
def2-TZVP+D+s+2p+d	-0.042

[a] All energies are quoted in kcal mol^{-1}.

Table 37: Table of the thermodynamic corrections calculated for the structures of *[UO_2(BTPhen)O_2]* optimised using the different basis sets centred on the dioxygen species.[a]

Basis Set used for Optimisation	**ZPE**	***H***	***G***	**Difference in *H***	**Difference in *G***
6-31G(d,p)	435.33	463.69	386.90	0.00	0.00
6-31+G(d,p)	435.33	463.67	387.01	-0.02	0.12
6-31+G(d,p) + sp	435.31	463.65	387.00	-0.04	0.11
def2-TZVP+D+s+2p+d	435.15	463.50	386.80	-0.19	-0.09

[a] All energies are quoted in units of kcal mol^{-1}.

In order to confirm that the negligible effect of changing the basis was not limited to the *[UO_2(BTPhen)O_2]* peroxide bound species, a selection of other models representing the full spectrum of dioxygen oxidation states to be studied were treated in a manner similar to that described above. In line with the findings for the *[UO_2(BTPhen)O_2]* model, the results suggested that inclusion of diffuse basis functions on the dioxygen unit only marginally

changed the structure of the optimised complex (0.014 Å was the largest deviation observed) and that these changes affected the single point energies calculated using the most diffuse basis set by less than 0.06 kcal mol^{-1}. The greatest change in the thermodynamic corrections calculated was also in line with the previous model at -0.25 kcal mol^{-1}.

Therefore, it is possible to confidently conclude that the only improvement in the calculated energies to be gleaned on including diffuse functions on the formally anionic dioxygen species is an improved estimation of the BSSE energy when using the CP procedure as implemented using a molecular fragmentation scheme. Furthermore, even when using the most diffuse basis studied here, the calculated BSSE correction had not converged, thereby indicating that even the BSSE correction calculated using this most unwieldy basis can still only be considered as an estimate. In addition, this molecular fragmentation scheme will likely overestimate the BSSE for models that localise anionic charge, resulting in the BSSE corrections that unfavourably energetically bias the two electron reduction of dioxygen under study. For this reason, the BSSE corrected reaction energies calculated should be viewed with caution, and are used as a guide to the magnitude of the BSSE in these systems only. In particular, the BSSE corrections calculated for ETs themselves should be discounted since it is in these reactions that the uncertainty in the BSSE correction is magnified. For this reason, the BSSE corrected results are only presented for the initial complexes studied in order to allow the reader to gauge the magnitude of the CP calculated BSSEs in these systems. At later points in the analysis the calculated BSSE corrections have been omitted in the name of clarity.

6 APPENDIX 2 – Modelling the Solvated State of Secondary Species that Play a Role in the Mechanism to Form Peroxide

As stated in Chapter 2.10, in order to model the mechanism of peroxide formation the full range of solvated energies of all of the species that play a role in the mechanism are required. These species are singlet and triplet dioxygen, the superoxide anion, the hydroperoxyl radical, the peroxide anion, the hydroperoxide anion, water and the solvated proton. Unlike the energies of the uranyl coordination complexes modelled, which inherently include the primary solvation sphere of the metal ion in the calculation, should these secondary species be modelled as isolated molecules then it is likely that the predicted solvation energies would be in considerable error. In no other example is this difference more pronounced than for the solvated proton. Fortunately, this species has been the subject of many other studies, and thereby allows the suitability of the functional and solvation model paired in this study to be gauged against the work of others and hence extended with confidence to the remaining species required to describe the desired reaction profiles in this study.

Computational Details

In order to calculate the solvated energy of a proton, a cluster model was employed in which a proton embedded in a cluster of seven water molecules was optimised. The cluster model used followed a procedure outlined in numerous papers in the literature,[210,211,212] modified to be in line with the level of theory used to treat the uranyl-BTPhen complexes in this study. Optimisations were performed using uB3LYP/6-31G(d,p) on all atoms and frequency calculations were carried out at the same level of theory in order to confirm the structures were at a potential minimum. SP calculations were performed using uB3LYP and the def2-TZVP basis on all atoms. Thermal, enthalpic, entropic and free energy corrections calculated using the Gaussian 09 thermochemical analysis were applied to generate the corresponding thermodynamically corrected quantities. Solvation energies for the models were calculated using the CPCM solvation correction, parameterised for a methanol solvent. Methanol was selected as the implicit solvent and water as the explicit solvent in order to coordinate with the conditions of the empirical study, i.e. a mixed methanol-water system. Explicit solvation of the solute by a water cluster was considered to act as an upper limit to the solvation energy. This follows from the reasonable assumption that water will be able to solvate the polar solute more favourably than neat methanol, owing to its greater dielectric constant and its

ability to form stronger *H*-bonds with the solute. Following on, as a model of a mixed aqueous-methanol phase is sought, despite favourable formation of explicitly hydrated clusters, the bulk properties of the solvent would still be governed by the majority species in solution; methanol in this case. Hence, parameters for implicit solvation by methanol were employed. The solvent cavity around the solute was generated using the UA0 model. However, all acidic protons were described by their own explicit spheres, resulting in the cavities formed in these water cluster models being identical to cavities a UFF treatment would provide. BSSE corrections were calculated for these models using the CP method as implemented using a molecular fragmentation scheme. This was done in order to gauge the agreement of these CP-corrected energies with the non-CP corrected hydration free energies calculated in this study, as well as with the most accurate values determined experimentally in various solvation environments. The solvated free energy of the proton was calculated according to the reaction scheme in Equation 130, in which the species $[H(H_2O)_7]^+$ could also be considered as a hydroxonium ion embedded in a cluster of six water molecules i.e. $[H_3O(H_2O)_6]^+$.

$$(H_2O)_{7(aq)} + H^+_{(gas)} \xrightarrow{\Delta G_{hyd}(H^+)} [H(H_2O)_7]^+_{(aq)} \qquad \textbf{(130)}$$

The free energy of hydration of the proton was thus calculated using the equality in **Equation 131**, below,

$$\Delta G_{hyd}(H^+) = G_{gas}([H(H_2O)_7]^+) - G_{gas}(H_2O)_7 - G_{gas}(H^+) + \Delta G_{solv}([H_3O(H_2O)_6]^+) - \Delta G_{solv}(H_2O)_7 \qquad \textbf{(131)}$$

in which $G_{gas}(x)$ represents the gas phase free energy of the optimised species and $G_{solv}(x)$ represents the change in free energy calculated for the same models once immersed in a bath of methanol solvent treated implicitly as a polarisable continuum. As with the uranyl-BTPhen complexes, the free energy of the gas phase species was calculated by applying the free energy correction to the electronic energy for each of each species, as calculated using the harmonic partition functions generated by Gaussian 09.[6]

Calculating the free energy of a proton, $G_{gas}(H^+)$, represents somewhat of a special case, in that it has no electrons and thus an electronic energy of zero. It does however have translational enthalpy and entropy and combined these amount to -6.27 kcal mol^{-1} at 298.15 K. This value was used as the free energy of the gaseous proton in order to calculate its overall free energy of solvation.

Evaluating the equality in **Equation 276**, above, gives a free energy of solvation for the gaseous proton of -262.8 kcal mol^{-1} when a BSSE correction is not included

and -264.8 kcal mol^{-1} when BSSE is accounted for. These values are in good agreement with the most accurate empirical hydration energy of the proton available at the time of writing, -265.9 kcal mol^{-1}.[213,214] In addition, it also corresponds with the work of Kelly et al. who calculate solvation free energies for the proton in neat water and methanol solution of -266.1 kcal mol^{-1} and -263.5 kcal mol^{-1}, respectively.[214,215] The value calculated in this work, in which a mixed explicit-implicit water-methanol solvation model has been used, is also in good agreement with the value of -263.4 kcal mol^{-1} calculated by Hwang et al. [216] who make use of neat methanol to explicitly and implicitly solvate the proton in their studies. The absolute free energies of the component species used to calculate the solvation energies of the proton are included **Table 38** along with solvation free energies of the individual species in order to demonstrate the relative contribution of each of the thermodynamic and solvation corrections to the final calculated quantity. The effect of including a BSSE correction calculated using the CP model has also been included.

Table 38: Table of the individual contributions to the total energy of each model due to ZPE, enthalpy, free energy, solvation and BSSE corrections.[a]

Model	***E*** **(a)**	**ZPE$_{corr}$** **(b)**	***G$_{corr}$ (H$_{corr}$)*** **(c)**	***ΔE$_{solv}$*** **(d)**	***BSSE$_{corr}$*** **(e)**
$(H_2O)_7$	-335927.0	+112.0	+86.2 (+122.4)	-12.1	+8.2
$[H(H_2O)_7]^+$	-336165.3	+118.9	+92.7 (+129.6)	-49.3	+6.1
H^+	0.0	0.0	-6.3 (+1.5)	n/a	n/a

[a] All energies are quoted in kcal mol^{-1}.

Table 39: Table of the calculated (using **Equation 130** in conjunction with the individual contributions in **Table 38**, above) and experimentally determined solvation energies of the proton.[a]

Δ*E*$_{(g)}$ **(a)**	**Δ*G*$_{(g)}$ (Δ*H*$_{(g)}$)** **(a + c)**	**Δ*E* + ZPE$_{(aq)}$** **(a + b + d)**	**Δ*G*$_{(aq)}$ (Δ*H*$_{(aq)}$)** **(a + c + d)**	**Δ*G*$_{(aq)}$ (Δ*H*$_{(aq)}$) + BSSE** **(a + c + d + e)**	**Experimental** ***H$_2$O - MeOH***
-238.3	-225.6 (-232.6)	-268.6	-262.8 (-269.8)	-264.8 (-270.4)	-265.9 – N/A 266.1 – 263.5 N/A – 263.4

[a] All energies in kcal mol^{-1}.

As can be seen in **Table 38**, the difference between the ZPE, enthalpy and free energy corrections for both the protonated and non-protonated water clusters are very similar, differing by less than 10 kcal mol^{-1} between the models. Although relatively small, the trend in the figures is as would be expected, in that the enthalpy and free energy corrections of the more strongly bound and ordered protonated complex are greater than the non-protonated analogue. By far the largest driving force for the protonation of the water cluster is the

solvation energy, which favours solvation of the charged protonated cluster over the non-protonated cluster by 37.2 kcal mol^{-1}.

As shown in **Table 39**, correcting the internal electronic energy for the effects of temperature and disorder brings the calculated free energy between those calculated by Kelly et al. for neat water and methanol systems, -266.1 kcal mol^{-1} and -263.5 kcal mol^{-1}, respectively.[214,215] Conceptually, being within the limits of the neat water and methanol phase solvation energies of the proton, the BSSE corrected value of -264.8 kcal mol^{-1} presents an agreeable solvation energy for the proton in a mixed aqueous-methanol phase modelled. However, despite this close agreement, the difference between the BSSE corrected and non-corrected solvation energies of 2.1 kcal mol^{-1} is in line with reasonable uncertainty in such a crude model of solvation and so it is reasonable that both values are considered equally reliable for the purposes required.

As stated previously, the energetic correction that outweighs all others in this model is observed to be the CPCM solvation energy, which favours the formation of the solvated $[H(H_2O)_7]^+$ cluster by 37.2 kcal mol^{-1}. The importance of treating solvation effectively in this particular example is demonstrated by the graph in **Figure 82**, in which it is possible to see the gradual convergence of the proton solvation free energy as the number of water molecules treated explicitly is increased. This demonstrates that in this particular system explicit solvation is required to accurately describe the directional nature of the solvation between the proton and the solvent. However, once a critical number of these interactions have been included there is relatively little accuracy to be gained on increasing the number further as the remaining effects are adequately described by an implicit solvation model. This mirrors the findings by multiple other groups.[212,210,211]

Summary

The close agreement between literature values and those calculated here using a gas phase optimised cluster model, followed by application of an implicit methanol solvation model at the level of theory used in the study of the uranyl complexes, provides confidence in the applicability of the computational approach to be employed. Importantly, the close agreement between the solvation energy of the proton predicted using this model and that gleaned from experiment suggests that optimisation of all the structures with implicit solvation is not necessary, given the increased time it would take to perform these types of calculations primarily due to difficulties with convergence. This study suggests that a large proportion of the solvation energy can be recovered by merely calculating the effect of

solvent on the gas phase optimised geometry. This finding has also been echoed by the work of others.[211]

Extension of this Study to Model the Remaining Secondary Species

Building on this success, the computational protocol described for the solvation of the proton was extended to treat the other species that play a secondary role in the catalytic reaction mechanism under study. This was conducted in order to allow the construction of stoichiometric reaction schemes that describe specific reaction pathways, such as PT reactions and ligand substitutions in the mechanism to be modelled, thereby allowing thermodynamic reaction paths to be constructed. The secondary species considered were singlet dioxygen, triplet dioxygen, superoxide, the hydroperoxyl radical (the conjugate acid of superoxide), the peroxide dianion and the hydroperoxide anion (the conjugate acid of the peroxide dianion). The solvent cluster explicitly defined for each of these models contained five water molecules. The models were optimised using the same level of theory and methodology as for the proton model described previously and a reasonable initial guess for the lowest energy structure of each cluster was inferred from the most stable analogous water only clusters identified by Bryantsev et al.[210] Images of the optimised geometries of these clusters are included in **Figure 83**.

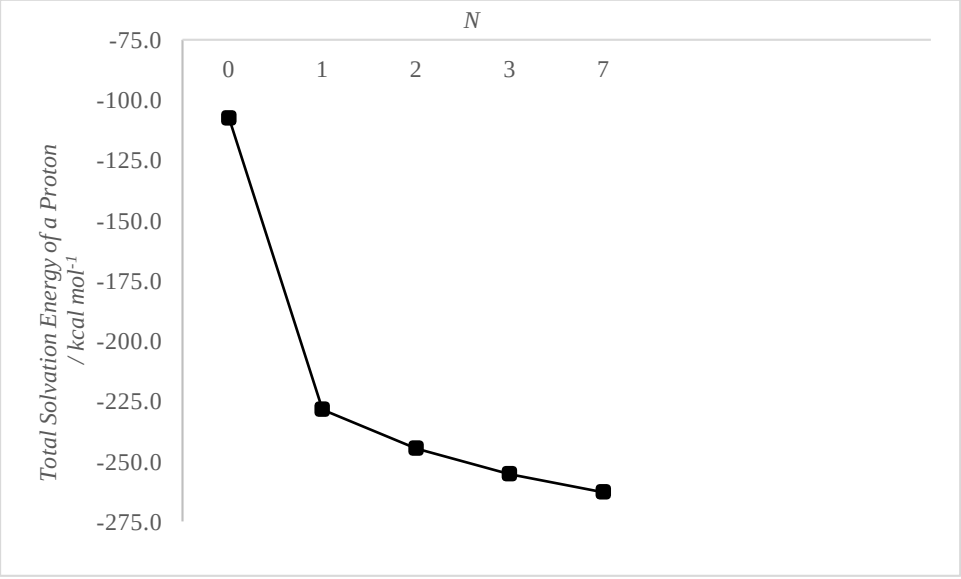

Figure 82: Graph of the total solvation energy of a proton as modelled using an explicitly defined small cluster model embedded in a bath of implicitly considered solvent, where *N* is the number of water molecules explicitly modelled, as per $[H(H_2O)_n]^+$.

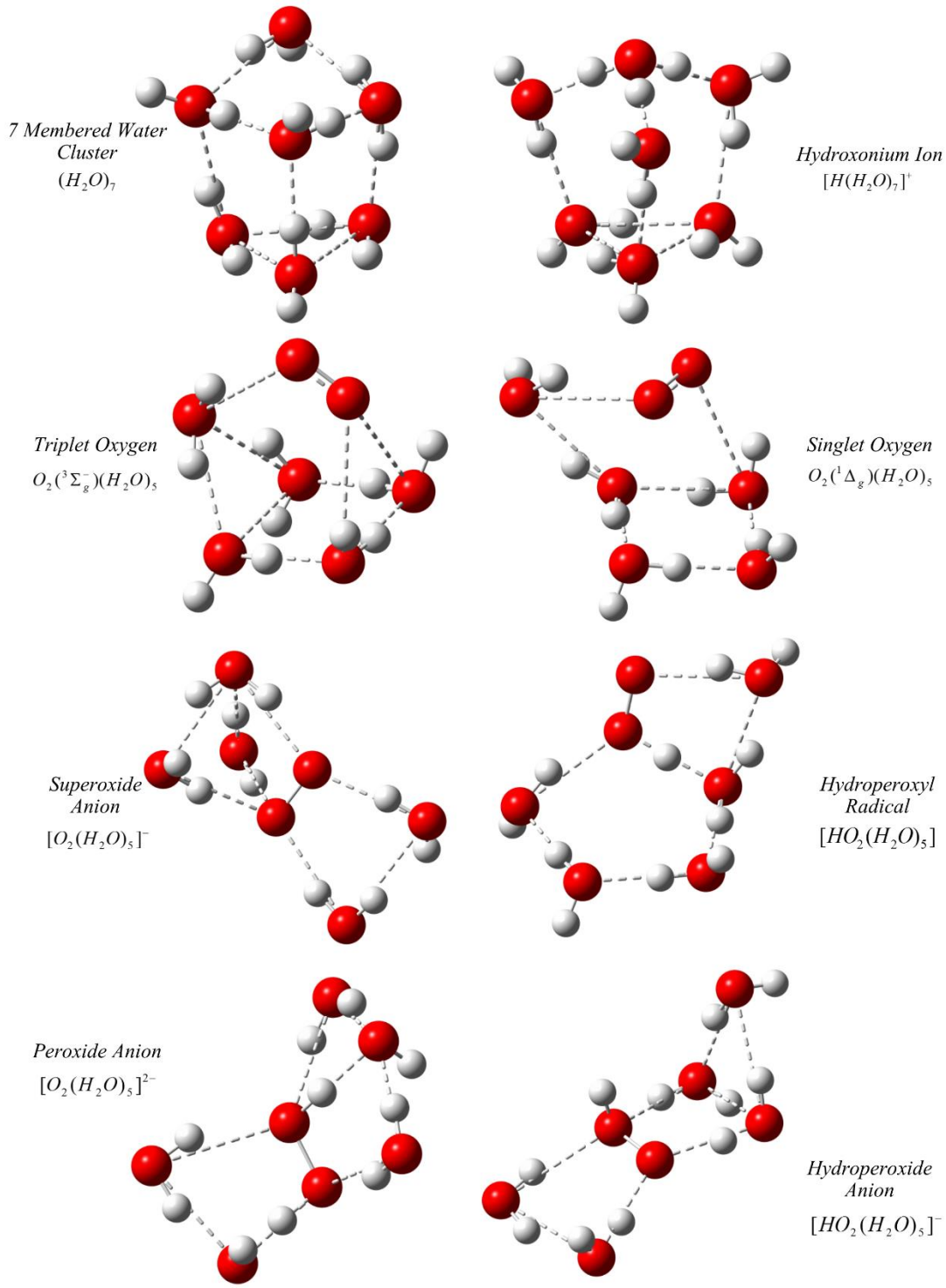

Figure 83: Optimised structures of the solvated clusters of the secondary species considered in this mechanism.

The single point energies of these structures including ZPE, enthalpic, free energy, BSSE and solvation corrections are presented in **Table 40**.

Table 40: Internal electronic energies and component thermodynamic, solvation and BSSE corrections for the auxiliary molecules that play a part in the proposed mechanism for the two electron reduction of dioxygen by the uranyl(VI). All energies are quoted in kcal mol^{-1}.

Species Description	**Formula**	***E***	ZPE_{corr}	G_{corr} (H_{corr})	ΔE_{solv}	$BSSE_{corr}$
Singlet Dioxygen	$O_2(^1\Delta_g)(H_2O)_5$	-334276.0	+82.2	+56.0 (+92.2)	-9.2	+7.8
Triplet Dioxygen	$O_2(^3\Sigma g^-)(H_2O)_5$	-334315.6	+81.7	+53.0 (+92.2)	-9.5	+7.7
Superoxide	$[O_2(H_2O)_5]^-$	-334370.6	+82.0	+54.3 (+92.1)	-47.4	N/A
Hydroperoxyl Radical	$[HO_2(H_2O)_5]^{2-}$	-334696.1	+88.7	+61.2 (+98.6)	-10.5	+7.3
Peroxide Dianion	$[O_2(H_2O)_5]^{2-}$	-334324.6	+80.1	+54.0 (+89.1)	-170.4	+35.8
Hydroperoxide Anion	$[HO_2(H_2O)_5]^-$	-334756.2	+89.4	+62.3 (+99.2)	-51.6	N/A
Proton	$[H(H_2O)_7]^+$	-336165.3	+118.9	+92.7 (+129.6)	-49.3	+6.2
7 Membered Water Cluster	$(H_2O)_7$	-335927.0	+112.0	+86.3 (+122.4)	-12.1	+8.2
6 Membered Water Cluster	$(H_2O)_6$	-287936.5	+94.1	+67.2 (+104.0)	-10.1	+5.2
5 Membered Water Cluster	$(H_2O)_5$	-239945.8	+78.4	+54.6 (+86.5)	-9.6	N/A

It should be noted, in agreement with the predicted instability of the isolated peroxide dianion in solution reported in Appendix 1, that on optimisation within a cluster of water molecules it became clear that the energetic minimum structure of the peroxide dianion was one in which it had abstracted protons from the surrounding water molecules. In doing this it was able to dissipate its excess anionic charge somewhat, thereby leading to a converged model that more accurately resembles a structure of $[H_2O_2(OH)_2(H_2O)_3]^{2-}$ than $[O_2(H_2O)_5]^2$, **Figure 83**. This change in the chemical identity of the complex is reflected by the excessively large BSSE calculated using a molecular fragmentation scheme that assumes a $[O_2(H_2O)_5]^{2-}$ cluster, of +35.8 kcal mol^{-1}. This large BSSE is remedied somewhat on changing the fragmentation scheme to represent a chemical model of the species $[H_2O_2(OH)_2(H_2O)_3]^{2-}$, for which a value of +6.7 kcal mol^{-1} was calculated. The instability

of the peroxide dianion in solution is reflected by the high acid dissociation constant of H_2O_2 in water, pK_a = 11.7, and the unquantified pK_a of the second dissociation.[217]

Using the models discussed above, it is possible to calculate the free energies of protonation for the peroxide dianion and the superoxide anion using **Equations 132** and **133** in combination with the energies of the species discussed to this point.

$$[O_2(H_2O)_5]^{2-} + [H_3O(H_2O)_6]^{+} \leftrightarrow [HO_2(H_2O)_5]^{-} + (H_2O)_7 \quad \textbf{(132)}$$

$$[O_2(H_2O)_5]^{-} + [H_3O(H_2O)_6]^{+} \leftrightarrow [HO_2(H_2O)_5] + (H_2O)_7 \quad \textbf{(133)}$$

Such models predict that both protonation reactions are spontaneous, with energies of -35.4 kcal mol^{-1} and -12.6 kcal mol^{-1}, respectively. Despite this agreement with experiment over the feasibility of these reactions, on comparing the magnitude of the corresponding calculated *dissociation* free energy change for the $HO_2^{\bullet}$ radical (+12.6 kcal mol^{-1}) and the corresponding experimental free energy calculated from its pK_a of 4.8, ΔG = +6.6 kcal mol^{-1}, it is clear the computational model is overestimating the free energy for this transition by approximately 6 kcal mol^{-1}. This inaccuracy is echoed when calculating the solvation energy of the superoxide anion using a method analogous to that laid out for the proton above. The experimentally determined hydration free energy of $O_2^{\bullet -}$ is presented in the literature with values ranging from -78.0 kcal mol^{-1} to -86.0 kcal mol^{-1}.[218,219] However, the energies calculated by this study indicate values of ΔH_{solv} and ΔG_{solv} of -81.2 kcal mol^{-1} and -72.6 kcal mol^{-1}, respectively. Therefore there is a discrepancy in the calculated free energy of solvation in the range of 5.4 kcal mol^{-1} to 13.4 kcal mol^{-1} depending on the reference chosen. This underestimation in the solvation energy of the anionic superoxide species, directly affects the calculated pK_a value, as an underestimation of the solvation of the charged species will artificially shift the equilibrium calculated to favour the neutral $^{\bullet}O_2H$ species and hence predict a more basic pK_a than is physical. In order to account for this shortcoming in the solvation model for this negatively charged species, whenever free energies of reaction are presented in this study that employ the clustered $^{\bullet}O_2^-$ model, two free energies of reaction are provided. The first represents the raw free energy calculated using the pure computational model as described above, whereas the second includes a -6 kcal mol^{-1} empirical correction factor to solvation energy of the superoxide anion to curb the unphysical basicity of this species as modelled here.